UC Berkeley
UC Berkeley Electronic Theses and Dissertations

Title
Solving the Air Pollution Crisis: Mitigation and Monitoring

Permalink
https://escholarship.org/uc/item/3bt0b8xw

Author
Caubel, Julien J

Publication Date
2018

Peer reviewed|Thesis/dissertation

eScholarship.org Powered by the California Digital Library
University of California

Solving the Air Pollution Crisis: Mitigation and Monitoring

by

Julien Jacques Caubel

A dissertation submitted in partial satisfaction of the

requirements for the degree of

Doctor of Philosophy

in

Engineering – Mechanical Engineering

in the

Graduate Division

of the

University of California, Berkeley

Committee in charge:

Professor Alice Agogino, Co-Chair
Professor Ashok Gadgil, Co-Chair
Professor Costas Grigoropoulos
Professor Robert Harley

Fall 2018

Solving the Air Pollution Crisis: Mitigation and Monitoring
© 2018
by Julien Jacques Caubel

Abstract

Solving the Air Pollution Crisis: Mitigation and Monitoring

by

Julien Jacques Caubel

Doctor of Philosophy in Engineering – Mechanical Engineering

University of California, Berkeley

Professor Alice Agogino, Co-Chair
Professor Ashok Gadgil, Co-Chair

Air pollution is one of the world's greatest environmental health risks, responsible for over 7 million premature deaths annually. Around half of these premature mortalities are linked to biomass cooking fires that release harmful air pollutants into people's homes, such as particulate matter (PM). Although nearly 3 billion people worldwide depend on biomass cooking fuels, relatively little scientific research exists on mitigating the smoke they generate. One promising approach for reducing emissions is the injection of secondary air into the biomass cookstove's combustion chamber. However, cold secondary air can also quench the combustion process when improperly injected, and so many secondary air injection cookstove designs do not actually reduce harmful smoke emissions relative to a traditional three stone fire (TSF).

Since wood is a common cooking fuel throughout the world, this dissertation presents an experimental wood-burning cookstove platform, dubbed the 'Modular (MOD) stove', to identify and optimize secondary air injection parameters that reduce the emission of harmful pollutants. The MOD stove enables systematic, repeatable experiments in which various secondary air injection design features, such as flow rate and location, can be quickly and easily adjusted. Over 130 experimental trials were conducted, demonstrating that wood combustion is highly sensitive to small changes in the secondary air injection parameters. Using a systematic experimental approach, an optimal design configuration was identified that reduces mass emissions of $PM_{2.5}$, carbon monoxide (CO), and black carbon (BC) by ~90% relative to a traditional TSF, while also improving thermal efficiency.

Using an updated version of the MOD stove, an additional 111 performance tests were conducted to quantify the practical design requirements (e.g., secondary air pressure and temperature) to achieve ≥ 90% mass emission reductions relative to a TSF. Using this experimental data, I demonstrate that low-cost (<$10) fans and blowers are currently available to drive the secondary flow, and this hardware can be independently powered using an inexpensive thermoelectric generator mounted nearby. Furthermore, size-resolved PM measurements demonstrate that secondary air injection effectively inhibits particle growth, but the total number of particles generated remains relatively unaffected. I investigate the potential impacts for human health and explore methods to mitigate the PM formation mechanisms that persist. As a whole, the MOD stove platform demonstrates that secondary air injection is a practical, effective, and

potentially economical method for meaningfully reducing smoke emissions from biomass cookstoves. However, designs should be experimentally validated and optimized, and further research is needed to eliminate the persistent formation of ultrafine particles that are particularly harmful to human health.

Ambient air pollution is also widespread, and linked to significant adverse health outcomes. Over 90% of the world's population lives in areas where ambient air pollution concentrations exceed World Health Organization recommendations, resulting in ~4 million premature deaths annually. The health impacts of ambient air pollution are particularly acute in urban settings. In 2010, premature deaths due to ambient air pollution were about 50% more common in urban than in rural environments, and this could increase to nearly 90% by 2050. Although ground-based air quality measurements are needed to address this growing health crisis, traditional regulatory monitoring networks do not provide sufficient spatial coverage and resolution to adequately assess air pollution exposures in urban environments. Distributed networks of low-cost air quality sensors are emerging to fill this gap.

Black carbon (BC) is an important component of PM pollution, strongly linked to adverse human health outcomes and climate change, but low-cost sensors for monitoring this critical pollutant are lacking. This dissertation presents the Aerosol Black Carbon Detector (ABCD), specifically designed for distributed air quality monitoring networks. As such, the ABCD integrates a compact weatherproof enclosure, solar-powered rechargeable battery, and cellular communication to enable long-term, outdoor deployments. Most importantly, the ABCD incorporates a number of novel design features to provide uniquely accurate BC concentration measurements in tough operating environments that debilitate existing commercial instruments. Over 100 ABCDs were operated outdoors, and their measurement performance was comparable to that of a commercial BC instrument collocated inside a regulatory monitoring station.

The validated fleet of ABCDs was deployed to 100 sampling sites in West Oakland, California – a neighborhood disproportionately affected by air pollution associated with the nearby Port of Oakland and surrounding highways. Over 100 days, the wireless sensor network successfully collected 84.0% of the 240,000 hourly BC concentration measurements desired (100 sampling sites × 2,400 hours). The widespread failure of miniature vacuum pumps was responsible for most missing measurements. The resulting BC concentration maps demonstrate that concentrations vary sharply over short distances (~100 m) and timespans (~1 hour), and generally depend on surrounding land use, traffic patterns, and location relative to prevailing winds. BC concentrations at each sampling site are highly repeatable over the diurnal and weekly cycles, and periodic trends are analyzed throughout the community. Using these trends as a reference, unusually polluted locations are detected, and likely emissions sources nearby are identified. In this way, the 100x100 Network demonstrates the value of low-cost sensor networks to accurately characterize urban air pollution distributions, and provide regulatory agencies, governments, and community stakeholders with actionable insights to mitigate the sources.

Air pollution is a pervasive and persistent health threat that can only be tackled if we work to both mitigate and monitor emission sources. As such, the MOD stove studies presented here are targeted towards abating the world's deadliest polluters. However, even the best of emissions reduction efforts are left blind without accurate measurements of the resulting air quality. The ABCD meets this need, providing accurate BC monitoring capabilities in a uniquely practical and economical package. Together, these complementary technologies will help underpin more comprehensive, data-driven efforts to quantifiably reduce harmful air pollution exposure throughout the world, and ultimately prevent millions of premature deaths.

We still think of air as free. But clean air is not free, and neither is clean water. The price tag on pollution control is high. Through our years of past carelessness we incurred a debt to nature, and now that debt is being called.

- Richard M. Nixon

Table of Contents

List of Figures

List of Tables

Acknowledgements

Throughout my PhD, I was surrounded by kind, talented, and motivated individuals, whose steady professional and moral support made this work possible. I would like to express my sincere gratitude to my academic advisors: Professors Alice Agogino, Ashok Gadgil, and Thomas Kirchstetter. Over the last five years, these individuals have been a constant source of inspiration and encouragement, pushing me to pursue research opportunities that have expanded my professional and personal horizons in countless unexpected and rewarding ways. Each one of my advisors truly dedicated themselves to nurturing my growth as an engineer and researcher, and I am sincerely grateful. I would also like to acknowledge Professor Toby Cumberbatch, who got me hooked on engineering for the greater good and taught me that human and cultural interactions are the foundation to lasting innovation – your mentorship set me on the path I am on today. Furthermore, I would like to sincerely thank the faculty members who served on my Qualifying Exam and Dissertation Committees, and whose expertise and feedback greatly strengthened this work: Professors Sara Beckman, Steven Glaser, Robert Harley and Costas Grigoropoulos. Finally, I would like to specifically recognize Thomas Kirchstetter's central participation as a virtual fifth member to my Dissertation Committee, who co-authored many of the chapters in this manuscript and was a foundational support to the body of work presented.

My colleagues, coauthors, and collaborators lent intellectual, technical, and emotional support that enabled this work: Vi Rapp, Troy Cados, Sharon Chen, Daniel Wilson, Chelsea Preble, Allen Boltz, Jonathan Slack, Gary Hubbard, and Rebecca Sugrue. I thank these individuals for the steadfast friendships, honest feedback, and hard work that underpinned our research together.

This dissertation is extremely data-intensive, relying upon hundreds of biomass cookstove tests and millions of air quality measurements. These datasets are the result of many undergraduate students spending countless hours in the laboratory and the field, and I would like to recognize their central contribution to this research: Brahim Idrissi Kaitouni, Marion Laglaive, Guillaume Charbonnel, Arjun Kaul, Varun Khurana, Maelle Seigle, Anouar Mabrouki, Annie Rosen, Shannon Chang, Carter Keeling, Kelly Archer, Tobin Holcomb, and Caroline Loffredo. Through their relentless dedication, work ethic, and good humor, these individuals greatly brightened my time as a graduate student and I am truly thankful.

The fabrication of the hardware presented in this dissertation was possible thanks to the expertise and craftsmanship of the amazing engineering staff at UC Berkeley and Lawrence Berkeley National Lab: Alex Jordan, Tom Clark, Jacob Gallego, Michael Neufer, Mick Franssen, Dennis Lee, Jesse Lopez, Gordon Long, Scott McCormick, Jeffrey Olson, Tim Williams, and Rick Kraft. I would also like to thank the administrative staff that kept our crazy projects up and running: Natasha Nelson and Maram Canawati. Public organizations and non-profits also played a significant role in the successful deployment and operation of the 100x100 BC Network: Ms. Margaret Gordon and Brian Beveridge at the West Oakland Environmental Indicators Project; Phil Martien, Steven Randall and many others at the Bay Area Air Quality Management District; and the staff at the Port of Oakland.

I want to thank the many generous organizations that enabled my PhD research. The National Science Foundation's Graduate Research Fellowship Program funded the majority of my doctoral studies, and gave me the financial and intellectual independence to freely pursue diverse research topics. The initial development of the black carbon sensor was funded by the Center for Effective Global Action at UC Berkeley. The Department of Energy (DOE) funded

instrument validation efforts under Lawrence Berkeley National Laboratory (LBNL) Contract No. DE-AC02-05CH11231. The Environmental Defense Fund funded the 100x100 Network through a generous grant from Signe Ostby and Scott Cook, and we sincerely thank program manager Ramon Alvarez for his guidance and support. The biomass cookstove research was also performed at LBNL, under DOE Contract No. DE-AC02-05CH11231. I gratefully acknowledge the DOE's Biomass Energy Technologies Office and program manager Elliott Levine for their forward-looking support of biomass cookstove research in our group and many others.

My family has always believed in me and kept me believing in myself – I would not be here without their constant love and support. My friends, Geoff Wehmeyer, Steve Truncale, and Maddie Foster kept me grounded and were always around when I needed a laugh. Finally, my girlfriend Cameron Tattle brightens my life everyday, your love (and cookies) made this manuscript possible. I love you all so much; you are the foundation upon which this work is built.

Chapter 1 – Introduction

1.1 The Air Pollution Crisis

Over 90% of the world's population breathes polluted air, residing in areas where air pollution concentrations persistently exceed World Health Organization (WHO) recommendations.[1] Chronic exposure to airborne pollutants, particularly $PM_{2.5}$ (particulate matter with an aerodynamic diameter $\leq$ 2.5 μm) increases the incidence of respiratory and cardiovascular diseases that reduce life expectancy.[2-4] As a result, air pollution is a leading environmental health risk, responsible for over 7 million premature deaths annually (or ~1 in 9 deaths, globally).[1,5] Low- and middle-income countries (LMICs) are disproportionately burdened by the health impacts of air pollution, and account for over 90% of premature deaths attributable to air pollution.[1,5-7] In these developing regions, ambient air pollution concentrations have increased over the last several decades, particularly in growing urban centers.[6,8,9] Furthermore, billions of poor households depend on crude biomass fires for heating and cooking, and suffer from the toxic smoke released into their homes.[9-11] If current trends continue, ambient air pollution's global contribution to premature mortality could double by 2050.[8] Moreover, the number of people who rely on solid biomass fuels for household energy is predicted to increase in many LMICs, and so the health impacts associated with indoor air pollution can also be expected to increase unabated.[10,12]

While global air pollution concentrations have generally increased over the last several decades, high income countries (HICs) have made considerable strides in improving air quality.[6,9] In the United States and the European Union, effective regulatory measures have helped to drive significant reductions in the ambient concentration of harmful air pollutants, and premature deaths attributable to air pollution exposure have correspondingly diminished.[1,13,14] These regulatory measures, such as the United States' Clean Air Act of 1970, specify maximum acceptable concentrations of key air pollutants, outline standard methods for monitoring these pollutant levels, and provide the legislative mandate to implement and enforce policies targeted towards their reduction.[15-17] Furthermore, households in HICs generally have access to clean sources of household energy (e.g. electricity).[10,18] As a result, over half of infantile respiratory infections in LMICs are attributable to air pollution, but this health risk is negligible in HICs.[19]

Despite the significant air quality gains achieved in many HICs, air pollution continues to be a major environmental health risk in even the most economically developed regions.[20] In the US, nearly 100,000 premature deaths are still linked to air pollution every year, largely in urban areas exposed to harmful emissions from transportation and power generation.[8,14,21] Globally, urban populations are particularly vulnerable to ambient air pollution. In 2010, premature deaths due to ambient air pollution were about 50% more common in urban than in rural environments, and this could increase to nearly 90% by 2050, if urban populations and air pollution concentrations both continue to grow at current rates.[8] Ambient air quality measurements are needed to address this rising number of mortalities, but traditional monitoring technologies, such as dedicated ground stations and satellites, do not provide measurements with sufficient spatial and temporal resolution to accurately quantify the highly variable air pollution concentrations typical of urban environments.[22-24] In most LMICs, air quality monitoring infrastructure is entirely lacking, largely due to the prohibitive purchase and operational costs associated with traditional air pollution measurement technologies.[25] As a result, air quality management policies

in LMICs and cities around the world have suffered for lack of accurate, actionable information on air pollution exposure. [1,15,25]

In order to tackle the mounting air pollution crisis facing our global society, current mitigation and monitoring techniques must be expanded and adapted to address a new set of polluters and infrastructural challenges, particularly in today's rapidly developing regions. Perhaps most importantly, new clean combustion technologies should be developed to significantly reduce toxic pollutant emissions from biomass cooking fuels, as these account for over half of all premature deaths attributable to air pollution exposure.[5,26] Furthermore, economical, practical, and scalable air quality monitoring techniques are needed to inform and validate emissions reduction interventions. Without accurate and expansive monitoring of air pollution levels, governments and regulatory agencies are effectively left blind, and mitigation efforts necessarily suffer. However, by working to both mitigate and monitor air pollution emissions simultaneously, an information feedback loop is established, whereby the benefits of technological interventions and regulatory actions can be immediately quantified, and thereby further improved. In this dissertation, I explore how this comprehensive, data-driven approach can help to quantifiably reduce harmful air pollution exposure throughout the world, and mitigate millions of preventable deaths.

1.2 Targeting the Deadliest Polluters: Biomass Cookstoves

Over 3 billion people (~40% of the world's population) rely on solid biomass fuels, such as wood or charcoal, for their daily cooking needs.[10,18,27,28] Often, households use traditional cookstoves, consisting of little more than a cooking pot crudely supported above a burning bed of biomass with stones or clay supports (e.g. a three stone fire, or TSF). These traditional stoves are highly fuel inefficient, and are significant sources of harmful air pollution, such as carbon monoxide (CO) and $PM_{2.5}$.[12,29] When these traditional biomass fires are used in poorly ventilated homes, indoor concentrations of air pollutants can be 10 to 100 times higher than those recommended by the WHO.[29-31] Consequently, indoor exposure to harmful emissions from biomass cookstoves is one of the world's greatest environmental health burdens, causing nearly 4 million premature deaths annually.[11,26]

Many stoves have been designed and developed to reduce the harmful emissions generated while cooking with solid biomass fuels.[32-34] Generally, these improved cookstoves are natural draft designs that only provide ~50% emissions reductions relative to a traditional three-stone fire (TSF) – not enough to significantly alleviate health impacts.[11,12,32] Some natural draft stoves also use processed biomass fuels, such as pellets or briquettes, to achieve further emission reductions, but the additional manufacturing and distribution costs severely limits the adoption of these fuels in the poor, rural communities most at risk.[33,35,36]

Although significant resources have been dedicated to mitigating air pollution emissions from industrial and transportation sources, there is comparatively little scientific research on harmful pollution from biomass cookstoves. A cursory search on Google Scholars reveals only ~7,000 articles for a query of 'biomass cookstove pollution', while well over a million articles are provided for both 'transportation pollution' and 'electrical power pollution', though the health burden attributable to these pollution sources is significantly lower than that associated with biomass cookstoves. However, a robust body of research exists on the improvement of industrial appliances that rely on solid biomass combustion, such as water boilers and heaters. This research shows that the careful injection of secondary air into the combustion chamber can significantly reduce harmful smoke emissions from biomass combustion, while also improving

thermal performance (e.g. fuel consumption).[34,35,37-40] In this dissertation, I use experimental methods to systematically adapt and apply these industrial emission reduction methods to the residential biomass cookstoves responsible for millions of premature deaths every year.

1.3 Tracking and Driving Progress: Distributed Air Quality Monitoring

Air quality measurements are critical to the assessment and management of air pollution's adverse health impacts. Traditionally, cities and regulatory agencies operate dedicated air quality monitoring stations that house laboratory-grade instruments and continuously generate accurate air pollution records at central locations.[41] However, high purchase and operational costs severely limit the number of sampling sites that can be established, and in even the most developed networks, the average spatial density is < 1 monitoring station per 10 km^2.[24,25,42] In contrast, urban concentrations of $PM_{2.5}$ and other pollutants vary significantly over distances of just 0.01 to 0.1 km, and therefore air quality measurements collected at central monitoring sites are not adequate to assess the surrounding populations' pollution exposures.[43-46] Furthermore, expensive and complex monitoring stations are out reach of the developing regions where the health impacts of air pollution are most acute, and where air quality measurements are consequently most needed.[8,25] Satellite measurements provide air pollution concentration measurements over large geographical areas, including developing or remote regions, but again spatial resolution is lacking, generally ranging from around 1 to 10 km.[47,48]

Distributed networks of low-cost air quality sensors have emerged to address the lack of spatial coverage and resolution associated with traditional air quality monitoring techniques.[24,49,50] These distributed sensing platforms usually rely on inexpensive electrochemical cells to measure the concentration of gaseous pollutants, such as ozone. [51-55] Since adverse health impacts are most closely linked to $PM_{2.5}$ exposure, low-cost sensors that measure the light scatted by airborne particles to estimate $PM_{2.5}$ mass concentrations have become increasingly popular.[56-61] Sensing platforms also include communication hardware, so that data can be wirelessly transmitted and collected in near real-time. This integrated hardware enables practical and economical monitoring of air pollution concentrations with unprecedented spatiotemporal resolution, but the accuracy of the measurements generated has been called into question.[58,62] In particular, light-scattering sensors are highly sensitive to a number of external factors, such as environmental conditions and particle composition, which can severely limit the accuracy of the PM mass concentration measurements collected.[56-61] Furthermore, there are no low-cost sensors currently on the market to monitor black carbon (BC), an important component of PM pollution.

BC is a primary component of PM pollution generated during the incomplete combustion of biomass and fossil fuels, and prolonged exposure to these combustion emissions is particularly harmful to human respiratory health.[63-68] BC is also short-lived, but potent climate forcer.[63,69] While PM is generated by a wide variety of anthropogenic and natural sources, BC is almost exclusively emitted by combustion processes, and is consequently a useful proxy for monitoring diesel trucks, biomass stoves, and other combustion applications.[63,68,70-73] For example, Figure 1 provides monthly-average $PM_{2.5}$ and BC mass concentrations recorded at two regulatory sampling sites in Oakland, California. One sampling site is located in a residential neighborhood, while the other is directly adjacent to a major highway (< 50 m away). The figure shows that BC concentrations are markedly higher near the highway, clearly reflecting the air quality impact of nearby traffic emissions, but only account for < 10% of total $PM_{2.5}$ mass concentrations.

Therefore, $PM_{2.5}$ concentrations across both sites are nearly identical, as the contribution from combustion sources is small. Similarly, Figure 2 provides daily-average BC and $PM_{2.5}$ concentrations at the near-highway site throughout the weekly cycle, normalized by the yearly average concentrations in 2011 (when the data was collected). The figure shows that BC concentrations are > 1.5 times greater during on weekdays than on Sunday, in accordance with nearby traffic patterns, while $PM_{2.5}$ concentrations remain comparatively constant. In this way, BC concentration measurements can more effectively illuminate the spatiotemporal variability of health and environmental impacts associated with combustion emissions.[72,73] In this dissertation, I present a new BC sensor that can be practically and economically deployed in large numbers, and incorporates a number of novel design features to enable uniquely accurate BC concentration measurements in tough operating environments that debilitate existing commercial instruments. This low-cost BC sensor will be a valuable addition to emerging sensor networks for air quality monitoring.

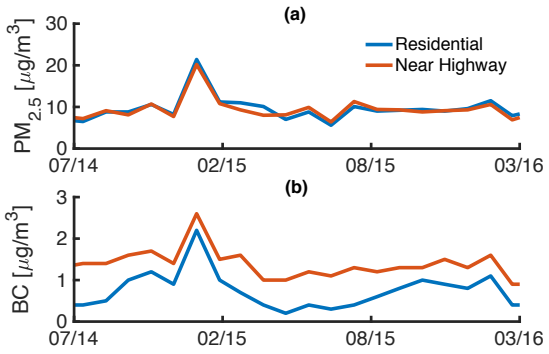

Figure 1. Monthly-average (a) particulate matter ($PM_{2.5}$) and (b) black carbon (BC) concentrations recorded at two regulatory monitoring stations in Oakland, California, from July 2014 to March 2016. One station is located in a residential neighborhood, while the other is directly adjacent to a major highway. (Data source: Bay Area Air Quality Management District)

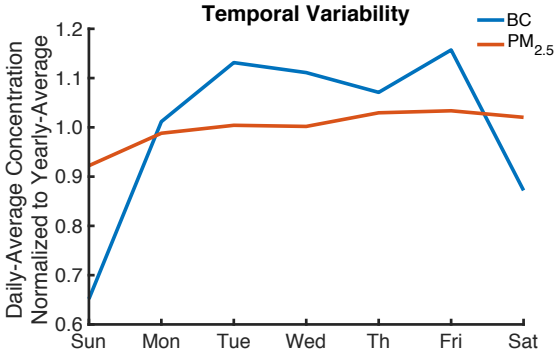

Figure 2. Daily-average particulate matter ($PM_{2.5}$) and black carbon (BC) concentrations recorded at regulatory monitoring directly adjacent to a major highway in Oakland, California. Daily-average values throughout the weekly cycle are calculated using data collected in 2011, and normalized by the corresponding yearly-average concentrations. (Data source: Bay Area Air Quality Management District)

1.4 Overview of Dissertation

This dissertation presents research on two separate but complementary topics, each focusing on the mitigation and monitoring of air pollution, respectively. Chapters 2 and 3 present the design, experimental optimization, and practical evaluation of high-efficiency biomass cookstoves that implement secondary air injection to significantly reduce the emission of harmful air pollutants. Chapters 4 and 5 focus on the design, validation, and deployment of a low-cost BC sensor for distributed air quality monitoring networks. In both research topics, design theory and scientific experimentation are combined to develop new, innovative solutions for the reduction and measurement of air pollution.

1.4.1 Secondary Air Injection in Wood-Burning Cookstoves

For many biomass combustion appliances, an effective and simple method for reducing unwanted emissions is to carefully inject secondary air into the combustion chamber.[34,35,37-40] The jets of secondary air promote more complete fuel oxidation by providing oxygen to the combustion zone, and enhancing turbulent mixing of air and gas-phase fuel.[37-39,74-76] However, many cookstoves with secondary air injection do not actually emit fewer harmful pollutants than a traditional TSF (where emissions are evaluated in terms of the mass of pollutant emitted per kilowatt of heat delivered to the thermal load, usually a cooking pot).[32,77] The flow of secondary air is generally much colder than the combustion gases, and so when improperly injected, it can effectively quench the flames and lower combustion temperatures below the pollutants' oxidation threshold.[75,78-80] Furthermore, existing secondary air injection studies have almost solely focused on biomass cookstoves that use processed biomass fuels (e.g. pellets), which may not be affordable or accessible in the poor, isolated regions most dependent on biomass for household energy.[10,32,34,80] In order to fill this gap, Chapters 2 and 3 of my dissertation focus on the implementation, optimization, and evaluation of secondary air injection in cookstoves fueled with unprocessed firewood, as this is a common primary cooking fuel throughout the world. For these studies, I designed and built two modular stove platforms, dubbed the 'MOD stoves'. The MOD stoves enable systematic, repeatable experiments in which various secondary air injection design features, such as flow rate and location, can be quickly and easily adjusted.

Chapter 2 presents the experimental MOD stove platform, and a parametric testing approach to identify and optimize critical secondary air injection design parameters that reduce harmful emissions and improve cooking performance. Over 130 experimental trials were conducted, systematically varying air injection design parameters to evaluate their effect on the cookstove's combustion performance. Using this experimental dataset, emission reduction mechanisms are investigated, and fundamental design principles are inferred and developed. Since the performance of biomass cookstoves is highly variable, effectively evaluating the impact of any given design modification can be time-intensive, as many replicate tests are typically required.[81] Therefore, I outline a streamlined parametric procedure that reduces the total requisite number of full-length performance tests, and enables the rapid experimental characterization of numerous, co-dependent design factors. Furthermore, secondary air injection has been shown to increase the emission of ultrafine particles (UFP) with aerodynamic diameters < 100 nm. These UPFs may be particularly harmful to human respiratory health, as they can penetrate more deeply into the lungs. Chapter 2 uses size-resolved particle emission measurements to analyze how secondary air injection influences the formation and growth of particulate matter, and investigates the potential implications for human health.

While Chapter 2 establishes the feasibility of using secondary air injection to reduce harmful smoke emissions from biomass cookstoves, Chapter 3 uses an updated MOD stove design to determine whether performance improvements demonstrated in the laboratory can be practically and economically translated to the field. The updated MOD stove has a smaller combustion chamber to increase the effectiveness of the secondary air injection jets, and implements several other design improvements derived from the experimental development of the first MOD stove. Using this updated platform, the study explores the practical design requirements to reduce mass emissions of $PM_{2.5}$, CO, and BC by ≥ 90% (relative to a traditional TSF). Over 110 experimental trials were conducted to optimize the cookstove design, and the resulting data are used to accurately quantify the emissions reductions that could be achieved using low-cost hardware currently the market. For example, I evaluate the commercial availability of miniature fans/blowers to drive the secondary air injection flow, and thermoelectric generators to independently power this hardware. Furthermore, the MOD stove's particle emissions are analyzed, and particle size ranges are identified where additional reductions are required to further mitigate potential health impacts. This set of experimental studies will help to guide and inform the development of practical and affordable wood-burning cookstoves that can be manufactured, distributed, and adopted on a large scale, using secondary air injection to meaningfully reduce harmful smoke exposure in billions of households worldwide.

1.4.2 Low-Cost Black Carbon Sensor

Black carbon (BC) is a major component of PM pollution, strongly linked to adverse human health outcomes and climate change, but low-cost sensors for monitoring this critical pollutant are lacking.[63-69] Current BC instruments generally consist of large bench top models that cost >$10,000, and generate inaccurate or erroneous measurements when ambient conditions (e.g., temperature and relative humidity) fluctuate.[82,83] Consequently, existing BC instruments must be housed indoors or incorporate pre-treatment of the sampled air (such as drying or heating), significantly increasing the complexity and cost of their implementation. Due to these limitations, it is not practical or economical to deploy existing BC instruments in large numbers.

In order to fill this gap, Chapters 4 and 5 present the Aerosol Black Carbon Detector (ABCD), a low-cost sensor specifically designed for distributed air quality monitoring networks. The ABCD measures the optical absorption of PM collected on a fibrous filter to estimate BC mass concentrations in real-time – a simple and robust principle of operation shared with many other commercial BC monitors.[84,85] Furthermore, the ABCD is packaged in a compact weatherproof enclosure that houses a solar-powered rechargeable battery and cellular communication module to enable remote, wireless operation over extended periods. Most importantly, the ABCD incorporates several innovative design features and data processing methods that reduce the sensor's inherent sensitivity to ambient temperature fluctuations, and therefore improve measurement performance in unconditioned operating environments (e.g., outdoors).

Chapter 4 focuses on the design, development, and validation of the ABCD. The ABCD's principle of operation and design features are fully detailed. Furthermore, the ABCD's unique temperature compensation methodology is outlined and illustrated using data collected in the field. Over 100 ABCDs were constructed and deployed outdoors in collocation with a commercial BC instrument operating inside a regulatory monitoring station. Using BC measurements from the commercial monitor as a reference, the precision and accuracy of the

ABCD fleet is evaluated both with and without the temperature compensation algorithm enabled. The measurement artifacts that plague existing BC instruments are effectively identified, modeled, and corrected under realistic operating conditions.

Chapter 5 presents the 100x100 Network, a distributed network of ABCDs deployed to 100 sampling sites in West Oakland, California, for a period of 100 days (from May 19 to August 27, 2017). West Oakland is a San Francisco Bay Area neighborhood that is adjacent to the Port of Oakland and surrounded by major highways. As such, the community is disproportionately affected by PM emissions from heavy-duty diesel trucks, locomotives, and ships. In order to better understand the resulting air quality impacts, local residents and businesses were recruited to host ABCDs at 100 distinct sampling sites dispersed throughout the 15-km^2 neighborhood. Each sampling site in the network resultantly monitors an average area of ~0.15 km^2, an effective spatial density that is ~100 times higher than that achieved by today's most highly developed regulatory networks (e.g., those operated in London, Hong Kong, and other wealthy cities).[25,42] At each hour of the 100-day campaign, ABCDs wirelessly transmitted BC concentration measurements to an online server (on a one-minute time base), thereby generating highly resolved air quality maps in near real-time.

Chapter 5 presents the data collection and network maintenance methods that enabled the distributed measurement campaign, such a custom website that we created to provide real-diagnostic information on all sensors and thereby facilitate the coordination of maintenance activities. I also assess the reliability of the sensor hardware and data collection systems throughout the duration of the measurement campaign, and identify major modes of failure to both quantify and qualify the network's overall data collection efficiency. Prevalent failure modes are investigated to help inform the operation of future monitoring networks. Furthermore, major spatiotemporal BC trends observed in West Oakland are presented, and the minimum measurement resolution required to adequately capture the BC concentration gradients is investigated. Finally, I identify geographical areas where unusually elevated BC concentrations were detected, and attribute likely emission sources nearby. In this way, the study provides preliminary insight into how data gathered using distributed networks of low cost sensors can be leveraged to rapidly identify, and ultimately mitigate, local sources of air pollution in urban communities.

Chapter 2 – Experimental Optimization of Secondary Air Injection in a Wood-Burning Cookstove

2.1 Abstract

Nearly 40% of the world's population regularly cooks on inefficient biomass stoves that emit harmful airborne pollutants, such as particulate matter (PM). Secondary air injection can significantly reduce PM mass emissions to mitigate the health and climate impacts associated with biomass cookstoves. However, secondary air injection can also increase the number of ultrafine particles emitted, which may be more harmful to health. This research investigates the effect of secondary air injection on the mass and size distribution of PM emitted during solid biomass combustion. An experimental biomass cookstove platform and parametric testing approach are presented to identify and optimize critical secondary air injection parameters that reduce PM and other pollutants. Size-resolved measurements of PM emissions were collected and analyzed as a function of parametric stove design settings. The results show that PM emissions are highly sensitive to secondary air injection flow rate and velocity. Although increasing turbulent mixing (through increased velocity) can promote more complete combustion, increasing the total flow rate of secondary air may cause localized flame quenching that increases particle emissions. Therefore, biomass cookstoves that implement secondary air injection should be carefully optimized and validated to ensure that PM emission reductions are achieved throughout the particle size range.

2.2 Introduction

Nearly 40% of the world's population relies on biomass stoves for their daily cooking needs.[10] These stoves are often three stones supporting a cooking pot above a burning bed of solid biomass, known as a three stone fire (TSF). These rudimentary stoves are significant sources of harmful airborne pollutants, such carbon monoxide (CO) and particulate matter (PM).[12] Exposure to indoor air pollution from solid biomass combustion is the world's greatest environmental health risk, causing nearly 4 million premature deaths annually.[26] Many clean and efficient biomass stoves have been designed to reduce exposure to these harmful emissions. Since wood is a common primary cooking fuel, many improved cookstoves are natural draft, wood-burning designs that provide around 50% mass emission reductions relative to a TSF (when normalized by cooking power).[18,28,32] The World Health Organization (WHO) recommends that 24-hour average PM concentrations remain below 25 $\mu g/m^3$.[86] However, a TSF can generate average indoor concentrations exceeding 1000 $\mu g/m^3$, and many natural draft, wood-burning cookstoves do not adequately reduce emissions to meet WHO guidelines and significantly alleviate health impacts.[30,31]

Since harmful emissions from biomass stoves are generated by incomplete fuel oxidation, emission reduction strategies generally rely on improvements in the combustion process. Complete fuel oxidation requires an adequate supply of oxygen in the combustion zone, and benefits from: (1) Combustion temperatures above ~850°C, (2) Sufficient residence time for the gas-phase fuel in the combustion zone, and (3) Turbulence to promote mixing of gas-phase fuel and oxygen.[87] In natural draft cookstoves, combustion of the gas-phase fuel is a buoyancy- and diffusion-driven process that generates little turbulence, leading to fuel-rich combustion zones where oxidation is incomplete. Although natural draft cookstoves designed to consume improved

biomass fuels (such as pellets) can reduce harmful emissions, the additional fuel processing cost and lack of distribution infrastructure limit adoption in the poor, remote communities most at risk.[29,32]

In many applications of solid fuel combustion, such as boilers, heaters, and cookstoves, an effective method for reducing unwanted emissions is injecting secondary air into the combustion chamber.[34,35,37-40] Carefully positioned, high-velocity jets of secondary air generate turbulent mixing that is typically lacking in naturally drafted, diffusion flames. Air injection also provides oxygen directly to fuel-rich zones, thereby promoting more complete oxidation and higher combustion temperatures.[37,74,80] However, non-preheated secondary air is much cooler than the combustion gases, and when improperly injected, can lead to lower combustion temperatures that result in incomplete fuel oxidation and more pollutant emissions.[79] Furthermore, researchers have shown that secondary air injection can reduce the mass of PM emitted during cooking, but may increase the number of ultrafine particles generated.[75] Inhalation of these ultrafine particles (i.e., with diameters smaller than 100 nm) may lead to long-term respiratory illness.[88] Consequently, it is important to ensure that secondary air injection designs achieve emission reductions throughout the particle size range.

Achieving comprehensive emission reductions using secondary air injection requires many design parameters to be optimized. For example, the airflow rate should be set at an optimal value that promotes effective turbulent mixing, but does not lower combustion zone temperatures excessively. Several publications demonstrate the importance of secondary air injection optimization in combustion appliances that utilize pelletized biomass fuels.[37,38,74,78,80] However, over 2 billion people do not have access to processed fuels, and must instead rely on unprocessed biomass, such as wood and dung.[33] Despite the potential benefits of air injection, systematic studies of this technology in cookstoves that use unprocessed biomass fuels are not readily available.

In this Chapter, we present an experimental biomass cookstove platform and parametric testing approach to identify and optimize critical secondary air injection parameters that reduce CO, PM, and black carbon (BC) emissions from unprocessed wood combustion. We conducted over 130 experimental trials, systematically varying several air injection design parameters (e.g., flow rate, velocity, position) to evaluate their effect on cooking performance and emissions. Size-resolved measurements of particle emissions were analyzed as a function of parametric cookstove settings to provide insight on the effects of secondary air injection on particle formation mechanisms, and inform future improved biomass cookstove designs.

2.3 Materials and Methods

2.3.1 Modular Air Injection Cookstove Design (MOD).

The MOD stove, shown in Figure 3, is a continuously fed, wood-burning cookstove designed to enable rapid adjustments of critical air injection design features. The MOD stove's general architecture is based on the Berkeley-Darfur Stove (BDS), using the same firebox design and accommodating the same cast-aluminum Darfuri cooking pot.[32,75] The MOD stove has a cylindrical firebox that is 178 mm (7 inch) in diameter with a front-facing fuel feed, and a cast-iron fuel grate. Above the firebox, there is a conical chimney (see Figure 3(c)) that reduces to a cylindrical extension, or 'throat', 76 mm (3 inch) in diameter. The pot is supported above the throat, and surrounded by a skirt to increase heat transfer efficiency.

Primary air enters the firebox through the open fuel feed and adjustable openings in the stove body located below the fuel grate. Secondary air from a compressed air cylinder flows into a manifold inside the stove and is injected into the firebox through holes in the conical chimney, as shown in Figure 4. The conical chimney is a removable pipe reducer known as a 'cone'. These removable cones (one of which is shown in Figure 3(c)) allow for various air injection designs to be implemented and tested rapidly. In order to create new air injection patterns, holes are simply drilled into a new cone, and the cone is then mounted inside the manifold.

The MOD stove also incorporates design features to adjust the following parameters: (1) Primary air intake: the size of the opening in the stove body for primary air entrainment can be adjusted using a sliding ring, (2) Grate height: the fuel grate can be moved up and down, adjusting the distance between the fuel bed and the air injection holes in the conical manifold, and (3) Pot height: the pot sits on three bolts to adjust the height of the pot above the throat. Using these design features, shown in Figures A1 to A3, rapid, repeatable, and consistent parametric experiments can be conducted. However, the stove's complex modular design and reliance on a compressed air cylinder make it uneconomical and impractical for field use. Instead, the lessons learned and design principles extracted from testing of the MOD stove are intended to inform future clean biomass cookstove designs for mass production and distribution.

Figure 3. (a) MOD stove (b) Air injection manifold (c) Air injection cone

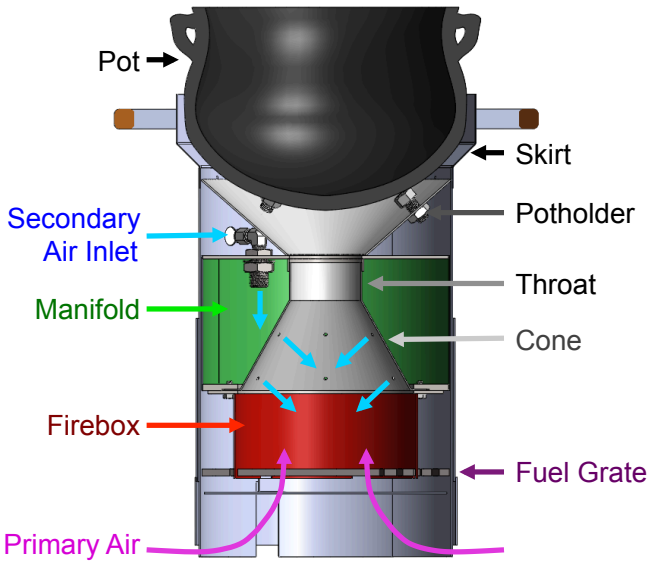

Figure 4. Cut view of MOD stove

2.3.2 Experimental Set Up

All experiments were conducted at the cookstove testing facility at Lawrence Berkeley National Laboratory (LBNL), schematically represented in Figure A4. Cookstoves are tested under a steel exhaust hood that completely captures pollutant emissions. Electric blowers exhaust emissions outside the building using a steel duct system. The flow rate through the duct is calculated using differential pressure measurements across a calibrated iris damper, and set to 5660 LPM (200 CFM) throughout testing to ensure replicability of measurements.

Particulate and gaseous emission concentrations in the duct are measured every second (1 Hz) using a suite of real-time instruments. Carbon monoxide (CO) and carbon dioxide (CO_2) volume concentrations are measured using a California Analytical Instruments 600 Series gas analyzer. Real-time PM instruments sample emissions from the duct isokinetically using a secondary diluter (see Appendix A5). Particle number concentrations are measured as a function of particle diameter from 5 nm to 2.5 µm using a TSI 3091 Fast Mobility Particle Sizer (FMPS), and a TSI 3321 Aerodynamic Particle Sizer (APS). BC mass concentrations are measured using a Magee Scientific AE-22 Aethalometer. The total mass of PM with aerodynamic diameter ≤ 2.5 µm ($PM_{2.5}$) emitted during each cookstove experiment is measured gravimetrically using 47-mm filters. The gravimetric filter system samples PM emissions from the duct isokinetically using a dedicated probe. Detailed overviews of the experimental set-up and gravimetric $PM_{2.5}$ measurement procedures are provided in Appendix A1.2.

2.3.3 Stove Testing Procedure

Cookstove performance and emissions were measured during the high power, cold start phase of the Water Boiling Test (WBT) 4.2.3.[89] During this test phase, a fire is lit inside a stove that is initially at ambient temperature ('cold'), and operated at a high firepower to boil 5 L of water. The test ends when a full rolling boil is reached at a measured water temperature of 99°C (the nominal local boiling point). Pollutant emissions are typically more elevated during this phase of stove use because: (1) the cold stove and pot of water quench flames and absorb heat,

thereby lowering combustion temperatures, (2) the cold fuel bed combusts poorly during initial lighting, and (3) the mass of harmful emissions released per energy delivered to the pot of water typically increases with firepower.[32] In this way, the cold start phase represents a 'worst-case' emissions scenario, and the design principles derived can be applied to other phases of stove use that are more forgiving to performance (e.g., hot start or simmer).

For each experiment, the stove was fueled with Douglas Fir wood cut into uniform pieces and dried to 7-9% moisture content on a wet basis. All tests were conducted at a constant high firepower setting of 5 kW to enable the immediate comparison of stove configurations.[75] A compressed air cylinder provided secondary air for the MOD stove using a two-stage regulator. The volumetric flow rate of secondary air was measured using a rotameter and adjusted using a valve. During preliminary trials, we observed that turning on the secondary air injection too soon after ignition caused the fire to smolder or go out entirely. Consequently, air injection was initiated about 2 minutes after fuel ignition to ensure the fire was well established, thereby preventing quenching and extinction.

2.3.4 Parametric Testing Procedure

Five MOD stove design parameters were identified for experimental optimization: (1) Pot height, (2) Grate height, (3) Primary air intake size, (4) Secondary air injection pattern (number and arrangement of holes), and (5) Secondary air flow rate. Since testing results from solid biomass stoves are highly variable, replicate tests are required to accurately determine performance and emission levels at any given parametric stove configuration. In order to reduce the total testing time required to optimize the stove, exploratory trials were conducted using a simplified cold start procedure (see Appendix A1.4).

During exploratory testing, stove design parameters were methodically adjusted to reduce pollutant emissions while maintaining high thermal efficiency. Using data from 71 exploratory trials, optimal settings were identified for the following air injection design parameters: The gap between the pot and skirt is set to 15 mm (0.60 inch), the grate height is set to 57 mm (2.25 inch) below the air injection manifold, and the primary air intake is set to roughly 70% of the fully open position (an opening with an area of 4800 mm^2 (7.4 $inch^2$)). Furthermore, two clean and efficient air injection patterns were identified for further parametric testing (shown in Figure A6). All exploratory testing results are provided in Appendix A.

Following exploratory testing, the two optimal air injection patterns were tested at flow rates of 21, 28, and 35 LPM (0.75, 1, and 1.25 CFM), for a total of six parametric configurations; all other parameters were maintained at the optimal values identified during exploratory testing. For each parametric configuration, 6 to 7 replicate tests were conducted. By adjusting the stove parameters in evenly distributed increments, parametric curves were generated to illuminate how secondary air injection influences the stove's emissions and performance. Results from these initial 39 trials suggest that an air injection flow rate of 28 LPM is most effective, and so an additional 12 trials were conducted at this flow rate using both air injection patterns. These two final sets of 12 replicate tests enable the identification and validation of the optimal parametric stove configuration with a higher degree of confidence.

2.3.5 Data Analysis and Metrics

All stove performance and emissions metrics were calculated in accordance with the methods presented in Appendix A1.6. Emission factors are normalized by the average thermal

power delivered to the pot, known as cooking power, in units of kW-delivered (kWd). Cooking power is defined as the product of firepower and thermal efficiency, and represents the useful thermal power output of the cookstove. All data are presented with 90% confidence intervals calculated using Student's t-distribution.[81,90]

The MOD stove's performance and emissions are compared to those of a TSF using cold start testing data collected by Rapp et al. (2016) at the LBNL cookstove facility. The TSF was also tested at a firepower of 5 kW, with the same pot, fuel, experimental procedures, and instruments as used for the MOD stove testing.[75]

2.4 Results and Discussion

2.4.1 Parametric Performance Metrics

A total of 63 WBT cold start tests were conducted to identify the cleanest, most efficient combination of secondary air injection pattern and flow rate. The thermal efficiency and emissions of six MOD stove configurations are evaluated as a function of air injection flow rate and velocity, as shown in Figure 3. The air injection velocity is calculated using the air injection flow rate and total area of the holes in the air injection pattern, as outlined in Appendix A1.6. Emission factors represent the total mass of pollutant emitted during the cold start test, normalized by the cooking power.

Firepower, shown in Figure 5(a), was maintained at 5.1±0.1 kW throughout parametric testing to provide consistency between experiments. Figure 5(b) shows that thermal efficiency remains around 27% for flow rates of 21 and 28 LPM, and decreases to about 24% at 35 LPM. The decrease in thermal efficiency at 35 LPM is likely caused by the abundance of injected air cooling the combustion zone, thereby reducing the stove's exhaust temperature even as firepower is held constant. The drop in exhaust temperature reduces the rate of heat transfer to the pot, and degrades the thermal performance of the stove.

Increasing CO emissions, shown in Figure 5(c), also suggest that air injection at 35 LPM is quenching the flame and cooling the combustion zone.[74,91] CO emissions from biomass combustion increase dramatically when combustion temperatures drop below ~800°C, but remain relatively constant above this critical oxidation temperature.[39,79] Correspondingly, Figure 5(c) shows that CO emissions are relatively constant as air injection increases from 21 to 28 LPM, but more than double when flow rate increases from 28 to 35 LPM. Additionally, as air injection velocity increases from 20 to 25 m/s at 35 LPM, the magnitude and variability of CO emissions both increase substantially, suggesting that enhanced turbulent mixing of excess secondary air is quenching the flame.

$PM_{2.5}$ emissions follow the same trend as CO emissions: When the flow rate is increased from 28 to 35 LPM at a constant velocity of 20 m/s, $PM_{2.5}$ emissions nearly double, and continue to rise as air injection velocity increases at 35 LPM (see Figure 5(d)). PM formation and growth occur when volatile gases in the exhaust cool and nucleate into solid particles or condense onto existing particles.[92] Similarly to CO, many volatile organic compounds that form PM, such as polycyclic aromatic hydrocarbons (PAH), oxidize around 750-800°C. At a flow rate of 35 LPM, excessive secondary air injection likely lowers the combustion zone temperature below this critical oxidation point, thereby enhancing particle nucleation and condensation.[79] Earlier studies have also shown that high CO emissions are usually accompanied by higher emissions of volatile organic compounds and other carbonaceous species that contribute to $PM_{2.5}$ mass emissions.[79,91]

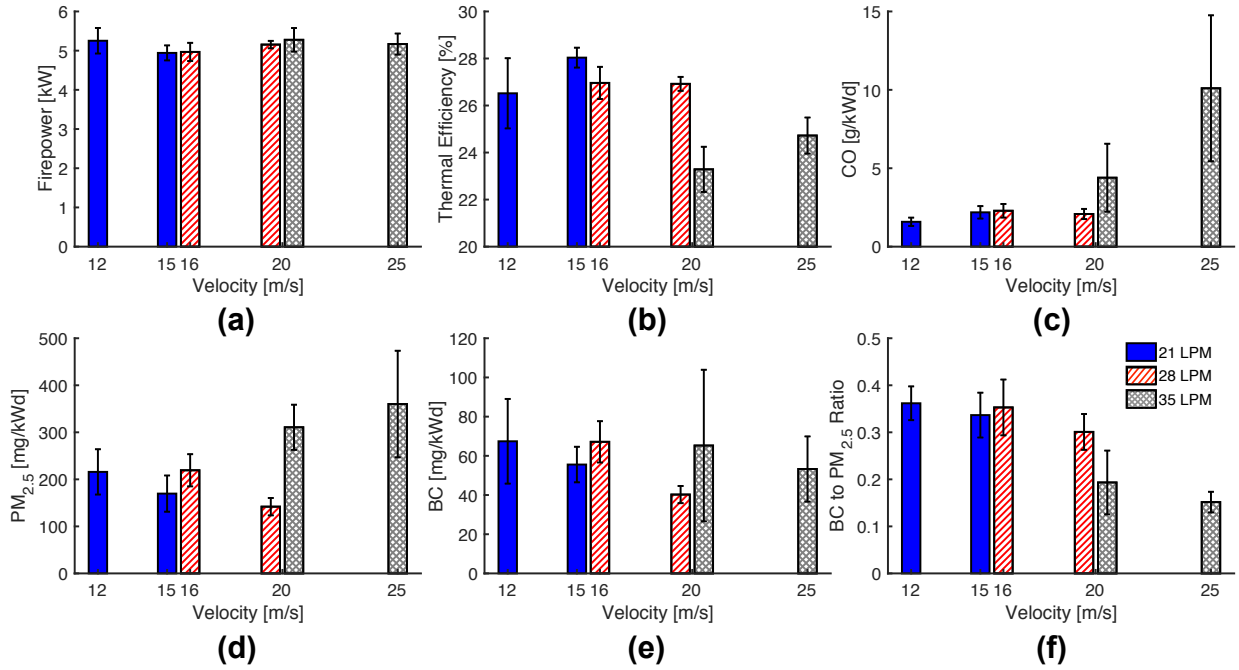

Figure 5. Cold start performance and emissions of the MOD stove as a function of secondary air injection flow rate (represented by bar color) and velocity (shown on the horizontal axis): (a) Firepower (kW); (b) Thermal efficiency (%), (c) Carbon monoxide (CO) emissions (g/kWd), (d) Particulate matter ($PM_{2.5}$) emissions (mg/kWd), (e) Black carbon (BC) emissions (mg/kWd), (f) BC to $PM_{2.5}$ ratio. Bar heights represent the metric mean at each stove configuration, and error bars represent the corresponding 90% confidence interval. Emissions are reported as the total mass of pollutant emitted during the cold start test normalized by the cooking power.

$PM_{2.5}$ composition can also provide insight into combustion conditions. $PM_{2.5}$ emissions from biomass combustion contain both inorganic particles, such as salt compounds and heavy metals, and organic particles consisting of either BC or tars.[93] The effect of air injection flow rate and velocity on BC emissions – optically absorbing soot that forms directly in the flame – is shown in Figure 5(e). At each flow rate setting, BC emissions decrease with increasing air injection velocity, as additional oxygen and turbulent mixing help to eliminate fuel-rich zones where BC is formed.[94] However, BC emissions at the low velocity setting for each air injection flow rate remain nearly constant (~70 mg/kWd). As flow rate increases, combustion zone temperatures are lowered, and the rate of BC oxidation decreases.[95,96] For these combustion conditions, the resulting increase in BC emissions effectively negates the reductions incurred from increasing turbulent mixing.[39,97]

Unlike CO and $PM_{2.5}$, BC emissions at a secondary air flow rate of 35 LPM generally decrease when injection velocity increases from 20 to 25 m/s, suggesting that combustion zone temperatures are sufficiently elevated to oxidize BC. BC from biomass combustion has been shown to oxidize around 350 °C.[97,98] This oxidation temperature is much lower than that of CO and many of the volatile compounds that form $PM_{2.5}$ (around 750 - 800 °C), and enables BC reductions throughout the parametric range.

In order to better understand the effect of secondary air injection on $PM_{2.5}$ composition, the ratio of BC to $PM_{2.5}$ emissions is shown in Figure 5(f). The figure shows that the BC to $PM_{2.5}$

ratio is stable at air injection flow rates of 21 and 28 LPM, but decreases sharply at 35 LPM. This trend further illustrates that BC is effectively oxidized throughout the parametric range, but excessive cooling at a flow rate of 35 LPM quenches the flame and increases overall $PM_{2.5}$ mass emissions. Furthermore, the BC to $PM_{2.5}$ ratio at each flow rate setting remains relatively constant as air injection velocity increases, suggesting that $PM_{2.5}$ composition is more dependent on combustion temperature than turbulent mixing.

Overall, the metrics in Figure 5 indicate that a flow rate of 28 LPM at an air injection velocity of 20 m/s is the optimal configuration for this stove. In this configuration, the stove minimizes emissions of pollutants, while maintaining high thermal efficiency. Although thermal efficiency and CO emissions improve slightly at a flow rate 21 LPM, the metrics show that 28 LPM at 20 m/s provides an optimal balance between maintaining high thermal performance and lowering pollutant emissions. Compared to a TSF, the optimal configuration of the MOD stove uniformly reduces CO, $PM_{2.5}$, and BC emissions by about 90%, while increasing thermal efficiency from 23.3 ± 0.7% to 26.4 ± 0.4% (see Appendix A2.3).

2.4.2 Size-Resolved Particle Emissions with Varying Air Injection Flow Rate

The optimal injection pattern identified in Figure 5 (Cone 1, shown in Figure A6) was tested at 21, 28, and 35 LPM (corresponding to air injection velocities of 15, 20, and 25 m/s, respectively). Figure 6 shows the mean particle distribution of replicate trials conducted at each air injection flow rate, with shaded areas representing 90% confidence intervals of the set. Each distribution represents the total particle number and volume emitted over the cold start, normalized by the cooking power. FMPS measurements span from 6 to 295 nm, while APS measurements span from 351 to 2500 nm. The last four bins of the FMPS measurement span (from 341 to 524 nm) are omitted, and the APS measurements have been converted from aerodynamic to electrical mobility particle diameter (see Appendix A1.7).[99]

Figure 6(a) reveals that the number distribution at each secondary air injection flow rate setting has a maximum peak at a particle diameter of around 10 nm, representing primary particles formed by the nucleation of volatile gases in the exhaust or soot generation in the flame.[100-102] Furthermore, the figure illustrates that as flow rate increases, the number of particles from 10 to 50 nm also increases. These results suggest that combustion zone temperatures decrease with increasing flow rate, thereby inhibiting the oxidation of volatile organic gases and other PM-forming species.[39] The increased emission of volatile gases and lower combustion zone temperatures both promote more PM nucleation.[79,91] Counterintuitively, PM nucleation is also encouraged by the stove's emission reductions themselves. Volatile compounds in the exhaust preferentially condense onto existing particles, thereby driving their growth. However, as secondary air injection controls emissions, the lack of existing particles promotes more nucleation in the volatile gases that persist, as there is less particle surface area available for condensation. The number distribution at a flow rate of 35 LPM has two prominent peaks at particle diameters of around 20 and 30 nm that diminish as flow rate decreases. These two peaks likely represent primary particle species that begin to form as combustion zone temperatures decrease at higher air injection flow rates.[94,102]

The particle volume distributions in Figure 6(b) show a unimodal peak centered at a particle diameter of around 100 nm, closely mirroring particle distribution measurements from other biomass combustion studies.[39,76,91,101] The figure also shows that a secondary air injection flow rate of 28 LPM yields the lowest volume distribution, indicating that this provides sufficient turbulent mixing to promote better fuel oxidation without lowering combustion zone

temperatures excessively. The increased particle volume generation at both 21 LPM and 35 LPM suggests that 21 LPM does not provide enough turbulent mixing while 35 LPM cools the combustion zone.

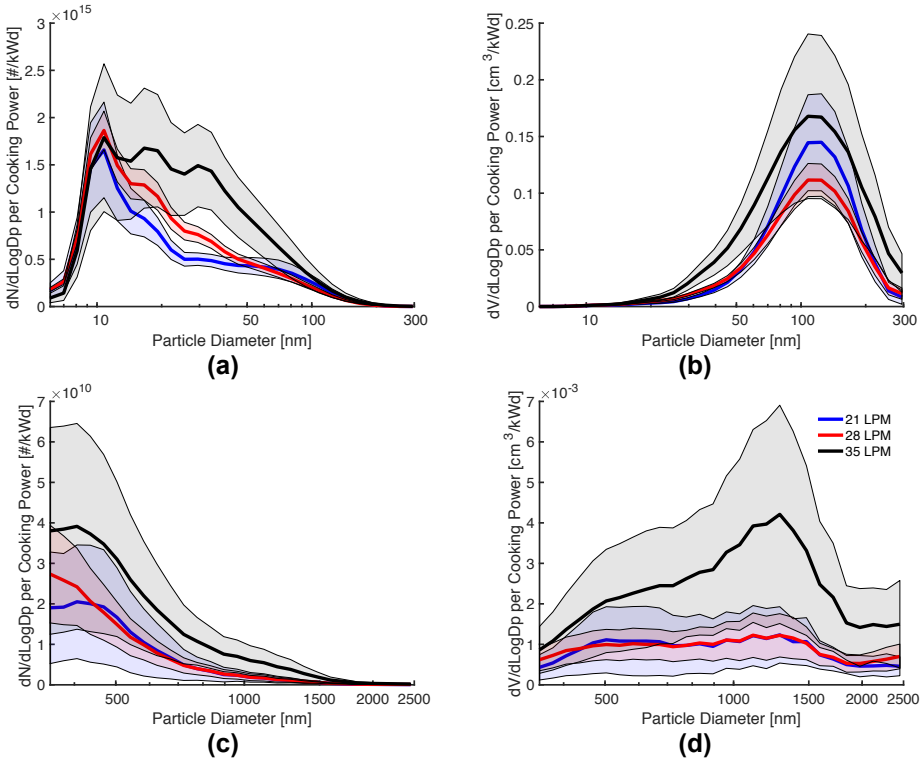

Figure 6. Size-resolved distribution of total particle number or volume emitted during the cold start, normalized by the average cooking power, for three air injection flow rate settings: (a) FMPS particle number distribution, (b) FMPS particle volume distribution, (c) APS particle number distribution, (d) APS particle volume distribution

Figure 6(c) and 6(d) show that the number and volume distributions of particles larger than 350 nm (up to 2500 nm) are roughly similar for flow rates of 21 and 28 LPM, but increase appreciably at 35 LPM, further indicating that combustion zone temperatures drop below the critical oxidation temperature of certain PM forming species.[91] The distinct peak in the volume distribution at 1280 nm (see Figure 6(d)) is the result of primary particle growth through condensation and agglomeration, promoted by the low combustion temperatures and high turbulent mixing at a flow rate of 35 LPM.[101,102]

2.4.3 Size-Resolved Particle Emissions with Varying Air Injection Velocity

Air injection flow rate was maintained at the optimal 28 LPM setting, while velocity was varied using the two different air injection patterns. Figure 7 provides the resulting particle number and volume distributions at secondary air injection velocities of 16 and 20 m/s. For both air injection velocities, the peaks in the particle number distributions at a diameter of 10 nm are nearly identical (see Figure 7(a)). However, increasing air injection velocity reduces particle number emissions above 30 nm. Additionally, the peaks at particle diameters of 20 nm and 30 nm become less distinguishable as air injection velocity increases from 16 m/s to 20 m/s. These

results indicate that additional turbulent mixing at higher air injection velocity promotes more oxidation of volatile gases, and reduces the formation of primary particles and subsequent particle growth through condensation.[39,91] Correspondingly, Figure 7(b) shows that increasing air injection velocity reduces the particle volume distribution by almost 50%.

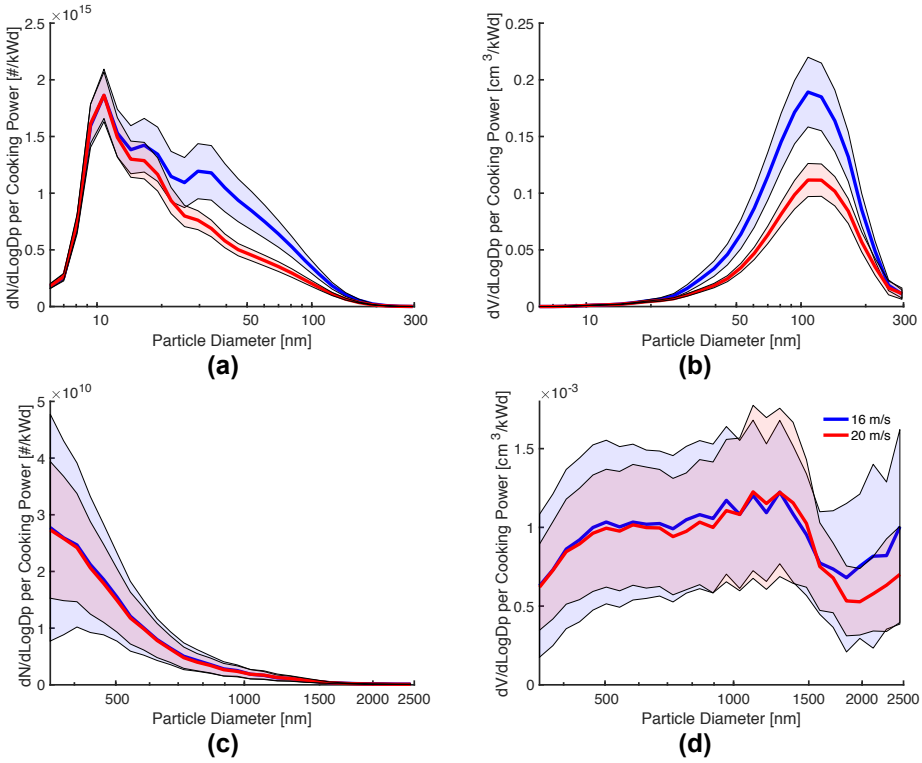

Figure 7. Size-resolved distribution of total particle number or volume emitted during the cold start, normalized by the average cooking power, for two air injection velocity settings at a flow rate of 28 LPM: (a) FMPS particle number distribution, (b) FMPS particle volume distribution, (c) APS particle number distribution, (d) APS particle volume distribution

For particles larger than 350 nm (up to 2500 nm), the particle number and volume distributions at both air injection velocities are nearly identical (see Figure 7(c) and 5(d)). These results indicate that air injection at 28 LPM promotes more complete fuel oxidation and reduces particle growth above 350 nm, independently of air injection velocity. However, for a flow rate of 21 LPM, the number of particles larger than 350 nm increases significantly as air injection velocity decreases, suggesting that a lack of turbulent mixing can promote particle growth under certain conditions (see Figure A9). Particle number and volume distributions for the air injection velocities tested at 21 LPM and 35 LPM are provided in section Appendix A2.4.

2.4.4 Size-Resolved Particle Emissions Compared to Three-Stone Fire

Figure 6 and 7 show that the MOD stove provides the greatest particle emission reductions at a secondary air injection flow rate of 28 LPM and injection velocity of 20 m/s (which agrees with the gravimetric $PM_{2.5}$ measurements provided in Figure 3(d)). However, it should also be noted that the emission of particles smaller than 50 nm in diameter are somewhat lower for an air injection flow rate of 21 LPM, highlighting the importance of maintaining high combustion zone temperatures to minimize ultrafine particle emissions.

Figure 8 compares FMPS particle number and volume distributions of the optimal MOD stove configuration (28 LPM and 20 m/s) to the TSF. Figure 8(a) shows that the MOD stove reduces the total number of ultrafine particles (with a diameter less than 100 nm) by about 75% relative to the TSF. However, for particles less than 10 nm in diameter, the MOD stove generates roughly the same number of particles as the TSF. Given the MOD stove's improved combustion conditions (as demonstrated by the significant emissions reductions), it is possible that these 10 nm particles nucleate from inorganic volatile gases, such as salts. These inorganic compounds volatilize more readily at higher fuel bed temperatures, and result in particle emissions that cannot be reduced through improvements in the combustion process.[37,40,76,93]

Figure 8(b) shows that volumetric particle emissions are reduced by an order of magnitude throughout the diameter range provided, which agrees with the gravimetric particle measurements provided in Table A2. For particles larger than 350 nm in diameter, the MOD stove uniformly reduces particle number and volume generation by nearly two orders of magnitude. Number and volume distributions for particles larger than 350 nm can be found in Appendix A2.5.

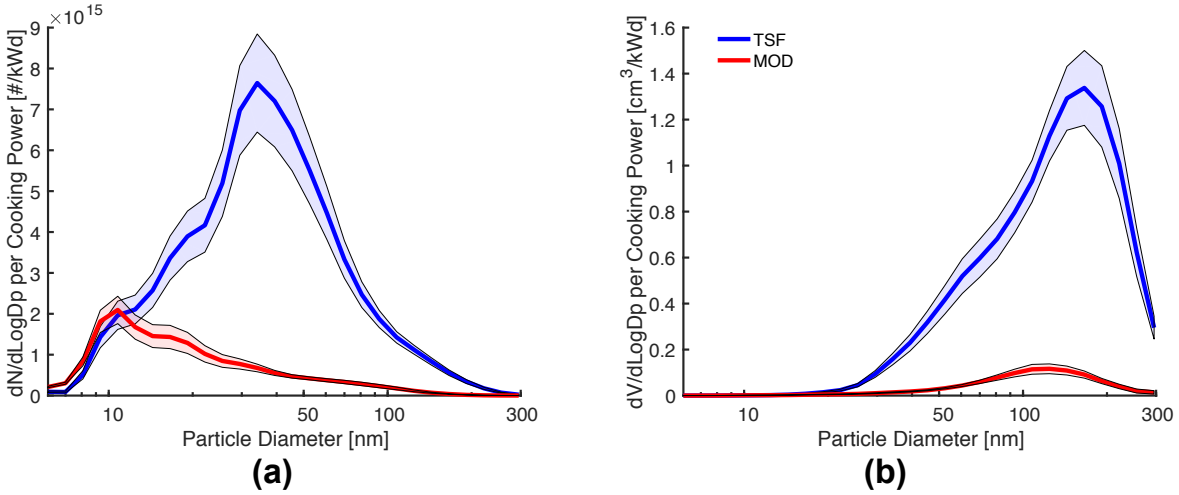

Figure 8. Size-resolved distribution of total particle number or volume emitted during the cold start, normalized by the average cooking power for a three-stone fire (TSF) and the MOD stove operating at an air injection flow rate of 28 LPM and velocity of 20 m/s: (a) FMPS particle number distribution, (b) FMPS particle volume distribution

Using the experimentally optimized configuration, the MOD stove reduces CO, $PM_{2.5}$, and BC mass emissions by about 90%, and reduces ultrafine particle number emissions by about 75%, compared to a TSF. The results also demonstrate that pollutant emissions are highly sensitive to secondary air injection design parameters, such as flow rate and velocity. Therefore, improved cookstove designs that implement air injection should be experimentally optimized and validated to ensure that pollutant mass emissions are minimized, and particle emissions are reduced across the full range of PM diameters. While this study focuses on modulating five stove design parameters to reduce emissions, it is also important to investigate other operational factors, such as firepower, fuel condition (moisture content, size, surface area), and secondary air temperature. Furthermore, future studies should incorporate additional instrumentation to enable deeper investigation of the combustion process, such as thermocouples to measure combustion temperatures, and/or a thermal-optical analyzer to examine the composition of PM emitted.

Overall, this study demonstrates that experimental optimization enables the design of wood-burning stoves that both reduce pollutant emissions and improve cooking performance. The experimental approach and results presented can inform the development of air injection stoves that reduce harmful smoke exposure in the one billion households currently relying on biomass cooking fuels.

Chapter 3 - Practical Design Considerations for Secondary Air Injection in a Wood-Burning Cookstove

3.1 Abstract

Billions of households worldwide cook with solid biomass fuels (often wood), and suffer from the toxic smoke emitted into their homes and kitchens. Laboratory studies of wood-burning cookstoves demonstrate that secondary air injection into the combustion chamber can significantly reduce the emission of harmful air pollutants, but critical engineering considerations, such as the pressure and power required to drive the secondary flow, are omitted. As a result, emission reductions achieved in the laboratory are not easily translated into practical cookstove designs that households can afford and adopt on a large scale. In this study, we use a modular cookstove platform to experimentally quantify the practical secondary air injection design requirements (e.g., pressure and temperature) to reduce the mass emission of harmful pollutants by 90% relative to a traditional cooking fire. Over the course of 111 experimental trials, we illuminate the underlying physical mechanisms that drive emission reductions, and outline design principles to optimize cookstove performance. Using this experimental data, we demonstrate that low-cost (<$10) fans and blowers are currently available to drive the secondary flow, and this hardware can be independently powered using an inexpensive thermoelectric generator mounted nearby. Furthermore, size-resolved particulate matter (PM) emission measurements show that secondary air injection effectively inhibits particle growth, but the total number of particles generated remains relatively unaffected. This study investigates the potential impacts for human health and explores methods to mitigate the PM formation mechanisms that persist.

3.2 Introduction

Over 2 billion people cook using solid biomass fuels, such as wood and dung.[10,28] Typically, households rely on traditional biomass cookstoves that are highly inefficient and polluting.[12,33] When these cookstoves are used in poorly ventilated homes, indoor concentrations of harmful pollutants, such as particulate matter (PM) and carbon monoxide (CO), can be up to 100 times higher than levels recommended by the World Health Organization (WHO).[29-31] As a result, chronic exposure to indoor air pollution from solid biomass cookstoves is a leading environmental health risk, causing nearly 4 million premature deaths annually.[26,36] In order to address this global health crisis, many clean and efficient biomass cookstoves have been developed and distributed.[32-34]

Some biomass cookstoves are designed to reduce unwanted emissions by using a small fan or blower to inject secondary air into the combustion chamber.[32,34,35,103,104] When properly injected, the jets of secondary air increase the turbulent mixing and residence time of gas-phase fuel in the combustion zone, while providing oxygen directly to fuel-rich regions.[37-39,74,75,78,105] As a result, fuel oxidation is more complete, and fewer harmful pollutants are emitted into the environment. Air injection can also enhance the cookstove's thermal performance, thereby reducing fuel consumption.[34,37] However, secondary air is typically much cooler than the combustion exhaust gases and improper injection can result in lower combustion temperatures that limit fuel oxidation and heat transfer to the thermal load (e.g. a cooking pot).[75,78-80,105] For example, Jetter et al. evaluated the performance of several secondary air injection cookstoves and show that half do not reduce PM or CO emissions (evaluated as the mass of pollutant

emitted per kilowatt of thermal power delivered) relative to a traditional three stone fire (TSF).[32] To enable greater emissions reductions, many air injection stoves rely on processed biomass fuels (e.g. pellets or briquettes), but the additional fuel production and distribution costs limit adoption in the poor, rural regions most dependent on biomass for household energy.[10,29,32,35,37]

Wood is a common primary cooking fuel throughout the world,[18,28] and though several studies demonstrate that secondary air injection can significantly reduce unwanted emissions from wood-burning stoves, many design parameters must be carefully considered and validated. For example, Caubel et al. show that unprocessed wood combustion is highly sensitive to secondary air injection flow rate, location, and other factors. Methodical experimental optimization of these design parameters enables 90% reductions of CO, PM, and black carbon (BC) mass emissions relative to a traditional TSF while also improving thermal efficiency.[105] However, critical operational parameters, such as the pressure required to drive the secondary air flow, are not provided to appropriately size the components (e.g. fans or blowers) needed in a practical, stand-alone cookstove that does not rely on an external power source. Consequently, emission reductions achieved in the laboratory are not easily translated into practical and economical cookstove designs that can be manufactured, distributed, and adopted on a large scale.

In this study, we use an experimental cookstove platform to investigate the practical secondary air injection design requirements for achieving significant emission reductions from unprocessed wood combustion. We conducted 111 experimental trials, systematically varying critical secondary air injection parameters (e.g. flow rate and location) to identify a design configuration that achieves $\geq$ 90% average emission reductions relative to a TSF, and also improves thermal performance. Throughout the experimental optimization, we recorded critical operational parameters, such as the secondary air injection supply flow rate and pressure, to evaluate whether the performance improvements are practically achievable using inexpensive, off-the-shelf components that can be powered independently (e.g., small fans powered by a thermoelectric generator). Furthermore, we use size-resolved PM measurements to investigate the physical mechanisms contributing to the reduction of total PM mass emissions, and identify particle size ranges where further emission reductions are needed.

3.3 Materials and Methods

3.3.1 Modular Air Injection Cookstove Design: Version 2 (MOD2)

The MOD2 stove, presented in Figure 9, is a continuously fed, wood-burning cookstove that enables critical secondary air injection parameters to be modulated easily and repeatably. The MOD2 stove is the second design iteration of the modular stove (MOD) described in Caubel et al.,[105] and therefore shares the same general design architecture and accommodates the same cast-aluminum Darfuri cooking pot. The MOD2 stove has a circular firebox, 15 cm (6 inch) in diameter, with an open fuel feed at the front. Above the firebox, a conical chimney reduces to a 6.4-cm (2.5-inch) diameter throat located directly below the pot. An integrated air manifold surrounds the firebox and conical chimney assembly (Figure 9(c)). Secondary air is supplied to a port at the back on the manifold and is injected into the firebox through orifices drilled into the conical chimney. The conical chimney is removable, such that different air injection patterns can easily be drilled, installed, and tested (Figure 9(b)). Primary air enters the firebox through the open fuel feed, and adjustable openings below the grate. The pot supports allow for the

adjustment of the pot's height above the chimney's throat. The stove also incorporates a steel skirt that closely surrounds the pot to enhance the rate of heat transfer from the exhaust gases.

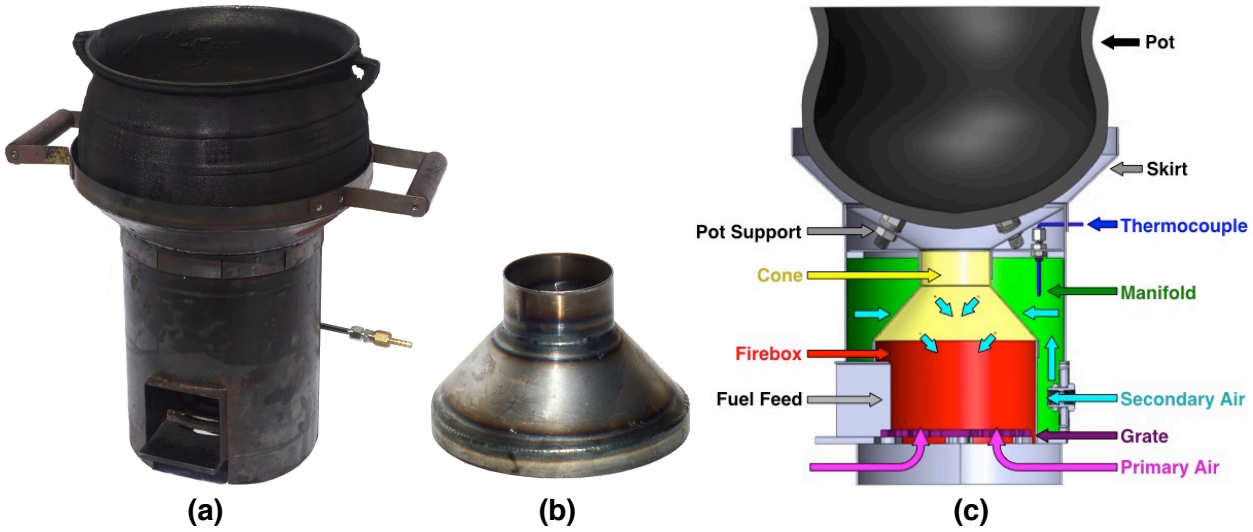

Figure 9. (a) The MOD2 stove with cast-aluminum Darfuri pot; (b) Removable conical chimney, into which secondary air injection patterns are drilled; (c) Cross-sectional view of the MOD2 stove showing the firebox, conical chimney, secondary air manifold, secondary air flow path, and other design features.

Previous research on the MOD stove (version 1) demonstrated that higher secondary air injection velocities improved stove performance, but excessive secondary air flow quenches the combustion.[105] The velocity of the secondary air jets decreases rapidly after injection into the firebox. For the 1.59-mm (0.0625-inch) diameter secondary air injection orifices used throughout the study, the average jet velocity diminishes by 90% over a normal distance of just 4 cm,[106,107] or less than half of the distance required to reach the center of the MOD stove firebox.

The MOD2 stove builds upon the lessons learned during the development and testing of the MOD stove (version 1) design. In order to ensure that secondary air jets better reach the flames, the MOD2's firebox and conical chimney are approximately 15% smaller than in the MOD stove, putting the secondary air injection orifices closer to the fuel bed. By reducing the distance from the orifice to the combustion zone, the effective velocity of the air jets increases, thereby promoting more turbulent mixing and oxygen injection at lower secondary flow rates that do not prohibitively cool the combustion. MOD2 stove dimensions were not reduced further, as a 15-cm diameter firebox was deemed to be the smallest size for practical feeding and tending of firewood at a high firepower. Other stove dimensions, such as the size of the fuel feed, were scaled down similarly. Additional details regarding the MOD2 stove design are provided in the SI.

3.3.2 Experimental Set-Up and Stove Testing Procedure

The MOD2 stove was developed at Lawrence Berkeley National Laboratory's (LBNL) cookstove testing facility. The experimental setup and the testing procedure for the MOD2 stove are the same as that described by Caubel et al. for the MOD stove (version 1),[105] and a brief

overview is provided here. During testing, emissions from the MOD2 stove are completely captured using a steel hood, and exhausted outdoors using a steel ducting system and blowers. The flow rate of air through the duct is measured using an orifice flow meter and set to ~5660 LPM (200 CFM) throughout. Air pollution instruments sample the duct flow and provide emission concentration measurements every second (1 Hz). A California Analytical Instruments 600 Series gas analyzer measures the volumetric concentrations (ppmv) of carbon monoxide (CO), carbon dioxide (CO_2), and oxygen (O_2). The total mass of $PM_{2.5}$ (PM with aerodynamic diameter $\leq$ 2.5 μm) emitted during the test phase is measured gravimetrically. A suite of real-time PM instruments sample emissions from the duct using a secondary diluter, usually set to operate at a dilution ratio of ~20:1. Using the diluted sample flow, a TSI 3091 Fast Mobility Particle Sizer (FMPS) and a TSI 3321 Aerodynamic Particle Sizer (APS) together provide size-resolved particle number concentration measurements from 5 to 2500 nm, while a Magee Scientific AE-22 Aethalometer provides black carbon (BC) mass concentration measurements.

The MOD2 stove was tested using the cold start, high power phase of the Water Boiling Test (WBT) 4.2.3,[89] as pollutant emissions are usually highest during this phase of stove use.[105,108] For each test, the MOD2 stove was initially at ambient temperature ("cold"), and a new fire was lit in a cold fuel bed (kindling). The fire was operated at a high firepower setting of ~5 kW to bring 5 L of cold water to a temperature of 99°C, the nominal local boiling point. The stove was fueled with uniformly cut pieces of dry Douglas Fir (7−9% moisture content on a wet basis), and secondary air came from a compressed air cylinder. The standard volumetric flow rate (SLPM) of secondary air was measured using a rotameter, and adjusted using a valve. In order to prevent quenching and extinction of the combustion during start-up, the secondary air flow was usually initiated ~2 min after fuel ignition, once the kindling was observed to be fully lit and the fire well established, and was held constant throughout the remainder of the cold start.

The temperature of the secondary air was monitored in real time using two K-type thermocouples. One thermocouple was installed inside the manifold, as shown in Figure 9, while the other was mounted at the secondary air inlet. A pressure tap was also installed inside the manifold, and manifold pressures were measured as a function of secondary flow rate using a digital manometer (The Energy Conservatory, model DG700).

3.3.3 Parametric Testing Procedure

Four design MOD2 stove parameters were systematically varied over a total of 111 tests: (1) Secondary air injection pattern (2) Secondary air injection flow rate (3) Primary air intake, and (4) Pot height. The first 52 tests were conducted to constrain the parametric space. During these preliminary tests, a constant 4 to 5 kW firepower setting was difficult to maintain and the combustion efficiency was low, indicating that the stove lacked primary air. Consequently, the adjustable air intakes below the grate were fully opened, and when this did not prove sufficient, the stove was also elevated on three bricks, such that primary air could flow more freely through the grate and into the bottom of the firebox. Two promising air injection patterns were identified during the preliminary tests, shown in Figure B4 (a total of 7 injection patterns were tested). Pattern 1 consists of two concentric rows, each with three orifices evenly spaced around the circumference of the conical chimney. The bottom row of holes is located near the juncture of the conical chimney and firebox, while the top row is located below the throat. Pattern 2 is identical to the Pattern 1, except that the bottom row has six evenly spaced orifices, rather than three. In both patterns, all air injection orifices have a diameter of 1.59 mm (0.0625 in). The

stove was not fitted with a pot skirt during preliminary testing. Additional details of the preliminary testing procedure and results are provided in the Appendix B.

For the remaining 59 parametric tests, each air injection pattern was tested at six secondary air flow rate settings ranging from 14 to 50 SLPM (0.5 to 1.75 SCFM), for a total of 12 parametric configurations. At each design configuration, 4 to 8 replicate tests were conducted (except for Pattern 2 at 50 SLPM, where 2 tests were conducted). During testing, we discovered that the stove's air manifold leaked significantly at the juncture between the removable conical chimney and the stove body. However, the leakage was consistent and replicable, and so the secondary air flow actually injected into the firebox could be calculated (see the procedure outlined in Appendix B). The calculations show that 27% to 39% of the total secondary air flow was injected through the holes in the conical chimney, while the remaining air leaked through the juncture at the top of the manifold, away from the firebox and combustion process. All results are presented in terms of the standard flow rate (SLPM) of air injected through the holes in the conical chimney at each setting, ranging from 5.5 to 14 SLPM, rather than the total flow into the manifold.

During the first 15 parametric tests, the height of the pot above the chimney throat was incrementally increased from ~1.59 to 2.5 cm (0.625 to 1.0 inch) to reduce the impingement of flames on the bottom of the pot, and was maintained at this setting for all subsequent experiments. The pot height was not increased past this set point because larger gaps between the pot and skirt diminish convective heat transfer from the exhaust gases. Throughout the parametric trials, the temperature of the secondary air was measured in the manifold and inlet every second (1 Hz). For both air injection patterns, the manifold pressure was measured at each secondary air flow rate setting while the stove was cold (manifold pressure measurements were not collected during stove testing). A single set of manifold pressure measurements was collected for each pattern.

3.3.4 Data Analysis and Performance Metrics

All stove performance and emission metric calculations are presented in section B1.4 of Appendix B. Emission factors are normalized by the average thermal power delivered to the pot, known as cooking power. Using real-time manifold temperature measurements, stove manifold pressures during each test were extrapolated from the corresponding pressure measurement recorded while the stove was cold. All data are presented with 90% confidence intervals calculated using Student's t-distribution. [81,90] The MOD2 stove's performance and emissions are compared to those of the MOD stove (version 1) and a TSF, both tested using the same experimental procedure, fuel, cooking pot, and firepower setting (~5 kW).[75,105]

3.4 Results and Discussion

3.4.1 Stove Performance and Emissions: Air injection pattern and flow rate

For both air injection patterns, Figure 10 shows that the MOD2 stove's overall performance improves significantly as the secondary flow rate increases from 5.3 to 8.5 SLPM. Since firepower was held constant throughout testing, the average stoichiometric flow of air into the combustion is around 70 SLPM for all 12 design configurations (Figure B12), and the total flow of air through the stove may be 2-5 times higher than this stoichiometric value, as the wood combustion draws excess primary air.[87,109,110] As secondary flow rate rises, the average air

injection velocity through each pattern increases proportionally (Figure B12). Over this range of secondary flow rates, accounting for 7.5 to 12% of the average stoichiometric flow, CO, $PM_{2.5}$,, and BC emissions drop by around 55% to 75% (Figure B12), while combustion efficiency rises from about 95% to 98%. These improvements demonstrate that unprocessed wood combustion is highly sensitive to small increases in secondary flow (relative to the total combustion flow), as higher air jet velocities provide more turbulent mixing and oxygen in the combustion zone.[74] The improvement of combustion conditions also translates to thermal efficiency gains, which increases from about 29% to 32%.

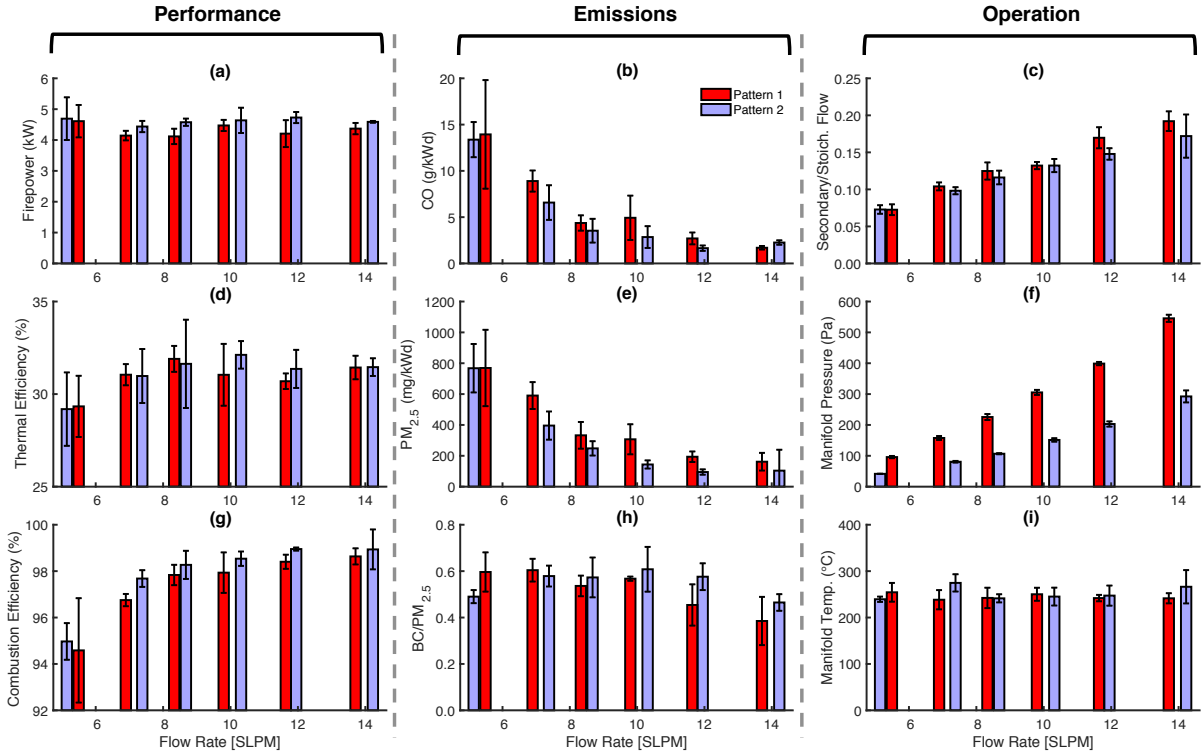

Figure 10. MOD2 stove performance, emissions, and operational metrics during high-power cold start testing, presented as function of secondary air injection flow rate and air injection pattern: (a) Firepower (kW); (b) Carbon Monoxide (CO) emissions (g/kWd); (c) Ratio of the secondary to stoichiometric flow rate of air; (d) Thermal efficiency (%); (e) Particulate matter ($PM_{2.5}$) emissions (mg/kWd); (f) Average manifold pressure (Pa); (g) Combustion efficiency (%); (h) Black Carbon (BC)/$PM_{2.5}$ ratio; (i) Average manifold temperature (°C). Bars represent the mean of replicate test data collected for each stove configuration, while error bars represent the corresponding 90% confidence interval.

For secondary flow rates > 8.5 SLPM, combustion efficiency ranges from 98 to 99%, increasing only slightly with more secondary air flow, while thermal efficiency remains constant around 31%. At these settings, the secondary flow represents 12 to 18 % of the average stoichiometric flow of air into the combustion and is much colder than the combustion gases. Figure 10 shows that the average manifold temperature is around 250 °C for all configurations, while biomass combustion temperatures typically exceed 850 °C. [38,87] Although the secondary air injection flow still represents a small fraction of the total air flow into the stove, it may be

sufficient at these settings (> 8.5 SLPM) to cool the exhaust gases appreciably, thereby limiting the rate of fuel oxidation and heat transfer to the pot. Other biomass cookstove studies show that exhaust temperatures drop with increased secondary flow.[38,79,111]

Some heat from the fire is also used to heat the secondary air in the manifold. Since average secondary air temperatures remain approximately constant for all stove design configurations, more heat from the fire is necessarily transferred to the manifold as secondary flow increases. However, Figure B12 shows that less than 0.1 kW is lost to heating the secondary air at all flow rates, which is small compared to the total power being delivered to the pot (~1.4 kW). Therefore, secondary air flow does not need to be constrained to maintain high air injection temperatures or prevent the diversion of output heat from the pot to the secondary air manifold, though some restraint is required to prevent excessive cooling of the exhaust gases and combustion chamber.

Although thermal performance gains diminish with secondary flow rates above 8.5 SLPM, CO, $PM_{2.5}$, and BC emissions generally decrease steadily throughout the parametric range (Figure 10 and Figure B12), thereby suggesting that combustion temperatures remain sufficiently elevated to oxidize harmful pollutants, and higher air injection velocities continue to enhance mixing of the air and gas-phase fuel. However, average emissions of CO and $PM_{2.5}$ from Pattern 2 increase slightly at a flow rate of 14 SLPM. Although only two tests were conducted at this stove configuration (4 to 8 tests were conducted at all other configurations), the results suggest that secondary flow rates greater than 12 SLPM through Pattern 2 may quench the flame, and reduce combustion zone temperatures below the 850 °C required to oxidize CO and many of the volatile organic species that form PM.[38,74,79] However, BC emissions and the corresponding BC to total $PM_{2.5}$ ratio both clearly continue to decrease in this configuration, as the oxidation temperature of BC is much lower (~350 °C) than that of CO and other pollutants,[95,98,112] and higher air injection velocities inhibit the formation of fuel-rich flame zones where BC forms.[63,94]

The ratio of BC to total $PM_{2.5}$ emissions from the MOD2 stove ranges from around 0.4 to 0.6, which is higher than that typically reported for biomass cookstoves, both traditional and improved.[113-115] Emissions from the BioLite™ HomeStove™, a wood-burning cookstove with secondary air injection similar to the MOD2 stove, have comparably elevated $BC/PM_{2.5}$ ratios (>0.7),[103] suggesting that this design architecture may effectively oxidize most PM-forming species, but BC generation somehow persists. A likely explanation for these persistent BC emissions is that the water-filled cooking pot is quenching flames protruding from the chimney throat. When the MOD2 stove was operated without a pot skirt during preliminary tests, Figure B10 shows that the $BC/PM_{2.5}$ ratio was significantly lower (<0.25), though thermal efficiency also suffered (< 29%). The pot skirt restricts the exhaust flow to enhance heat transfer, but the resulting higher exhaust velocities entrain more flames through the chimney throat, where they quench against the pot and generate BC. Emissions from the MOD stove (version 1) also had markedly lower $BC/PM_{2.5}$ ratios (< 0.4), likely because the pot is higher above the fuel grate, the chimney throat is ~15% larger, and the skirt fits more loosely around the pot. Therefore, exhaust velocity and flame impingement are both reduced, but again, thermal efficiency deteriorates (< 28%).[105]

MOD2 stove emission reductions are not solely dependent on higher secondary air injection velocities to enhance the combustion process. At each air flow rate setting, the average injection velocity is roughly 1.5 times greater through Pattern 1 than Pattern 2 (Figure B12), and yet Figure 10 shows that Pattern 2 generally outperforms Pattern 1, thereby suggesting that the addition of air jets near the fuel bed promotes more effective turbulent mixing in the combustion

zone, despite the drop in injection velocity. Correspondingly, it was previously observed that as secondary flow increases to 14 SLPM, emissions from Pattern 2 tend to rise while emissions from Pattern 1 continue to drop, as the more effective orifice placement also enables quenching of the combustion at lower flow rates. In this way, wood combustion is also highly sensitive to the number of secondary air injection orifices and their location relative to the fuel bed, and this sensitivity can be exploited to more effectively enhance stove performance. For example, Figure 9 shows that the manifold pressure at each flow rate setting is 1.9 to 2.3 times lower for Pattern 2 (compared to a theoretical reduction of 2.25 times), thereby enabling greater performance improvements at lower secondary flow rates and pressures that can be more easily achieved by the miniature fans and blowers typically implemented in improved cookstoves.

Figure 10 shows that a secondary flow rate of 12 SLPM through Pattern 2 effectively minimizes the MOD2 stove's CO and $PM_{2.5}$ emissions, while maximizing combustion efficiency. Although thermal efficiency and BC emissions improve slightly (≤10%) at other flow rate settings, this configuration likely provides an optimal balance between reducing harmful emissions and improving thermal performance. In this configuration, the MOD2 stove emits 90% less CO, $PM_{2.5}$, and BC than a TSF (on average), and thermal efficiency increases from 23±1% to 31±1% (Table S1).

Compared to the MOD stove (version 1), the MOD2 stove achieves similar emission reductions at half the secondary air injection flow rate. Furthermore, when the secondary flow rate was set 25% higher than the optimal setting, $PM_{2.5}$ and CO emissions from the MOD stove more than doubled.[105] MOD2 stove emissions, on the other hand, increase only slightly (<40%) when the flow rate rises by ~17%, from 12 SLPM to 14 SLPM. Together, these trends illustrate that the MOD2 stove's smaller firebox and chimney dimensions allow the secondary air jets to be more effective at lower flow rates, penetrating further into the firebox to enable significant emission reductions while preventing excessive cooling or quenching of the combustion. Additionally, the lower secondary flow rates likely contribute to the MOD2 stove's higher thermal efficiency, as cooling of the exhaust flow diminishes.

Overall, the testing results indicate that secondary flow rate must be optimized to maximize injection velocity but prevent flame quenching. Additionally, cookstove designs should employ the smallest firebox that still allows for user-friendly tending and feeding of fuel, so that air injection orifices are located closer the combustion zone. Secondary air injection patterns should also be experimentally validated, as small design changes can significantly impact cookstove performance and operational requirements (e.g., pressure). Furthermore, design compromises are sometimes required to enhance both the stove's thermal and emissions performance. In this case, adding a pot skirt to the MOD2 stove enhanced thermal efficiency but also increased the BC/$PM_{2.5}$ ratio. Since the MOD2 stove still achieves significant (90±10%) BC mass emission reductions relative to a TSF, the elevated BC/$PM_{2.5}$ ratio may be justified by the increase in thermal efficiency afforded.

Having identified the optimal MOD2 stove design configuration and established the underlying physical mechanisms responsible for the performance improvements, it is important to determine whether these experimental results can be translated into a practical cookstove design that households can afford and adopt.

3.4.2 Secondary Air Injection Design Requirements: Flow, Pressure and Power

The MOD2 stove receives pressurized air from a cylinder, such that the secondary flow can be adjusted accurately and consistently over the course of many experimental trials, but this

approach is clearly not practical or economical on a large scale. Instead, many commercial biomass cookstoves rely on a small axial fan or centrifugal blower to drive the secondary flow of air, often drawing power from a thermoelectric generator (TEG).[34,103] TEGs convert heat from the biomass combustion directly to electricity, thereby providing an independent, reliable, and convenient source of power at little cost (often < $10/W of power generated).[116-119] TEG modules mounted to biomass cookstoves have been shown to generate as much as 10 W of electrical power, although an output of 1 to 5 W is more typical.[116,118-120] There are also some biomass cookstoves on the market powered by solar panels or simple wall chargers, but unlike TEGs, these alternatives are dependent on operational factors external to the cookstove, such as sufficient insolation or access to electricity.[34,104]

Figure 10 shows that MOD2 performance is optimal when injecting a secondary flow rate of 12 SLPM through Pattern 2. In this configuration, an average manifold pressure of ~200 Pa is required. It is important to note that as the stove heats up during normal use, more manifold pressure is required to maintain a constant mass flow of secondary air through the injection pattern. Air is injected into the MOD stove around room temperature (~25 to 30 °C) throughout, but heats up significantly over the course of the cold start, ultimately reaching manifold temperatures of 300 to 400 °C (Figure 13). The density of air at these elevated temperatures is around half that of the air initially flowing into the manifold, and so the volumetric flow rate of air passing through the injection pattern effectively doubles, as does the manifold pressure required. Consequently, when sizing a fan or blower to drive secondary air injection in a biomass cookstove, it is important to consider the manifold pressure required at typical operating conditions, rather than when the stove is cold (at ambient temperature). In this study, we defined the operating temperature as the average secondary air temperature in the manifold during the cold start, and therefore present the corresponding average manifold pressure. Manifold pressure measurements gathered at ambient conditions are extrapolated to the operating temperature, as outlined in the Appendix B.

Figure 11 provides the maximum (static) pressure, maximum (free) flow rate, and rated electrical power consumption of 1,157 miniature fans and blowers stocked by Digikey Electronics®, a major electronic parts supplier. All available models costing < $10 (when ordering 1000 units) are presented, as the minimization of manufacturing costs is crucial to the development of affordable cookstoves. To reflect the MOD2 stove's operational requirements, reference lines are provided at a static pressure of 200 Pa and rated electrical power of 5 W (the maximum power typically output by a stove-mounted TEG module).[116,118-120] In order to generate the maximum pressures presented in Figure 11, the devices must operate near static conditions, or at a flow rate below ~10% of the maximum value specified by the manufacturer (measured with no flow resistance). The MOD2 stove requires 12 SLPM in the optimal configuration, so the free flow rate should be at least ~100 LPM for the fan or blower to operate near static conditions, and the markers in Figure 11 are colored to reflect this requirement. Since secondary air is drawn into the stove from the environment near standard conditions, the rated volumetric flow rate (LPM) is analogous to the stove's mass flow rate (SLPM) requirements, identified experimentally. It should also be noted that the rated power consumption is often measured at free flow conditions, and though this may not be exactly representative of power consumption at the requisite operating conditions, it provides a valid estimate.

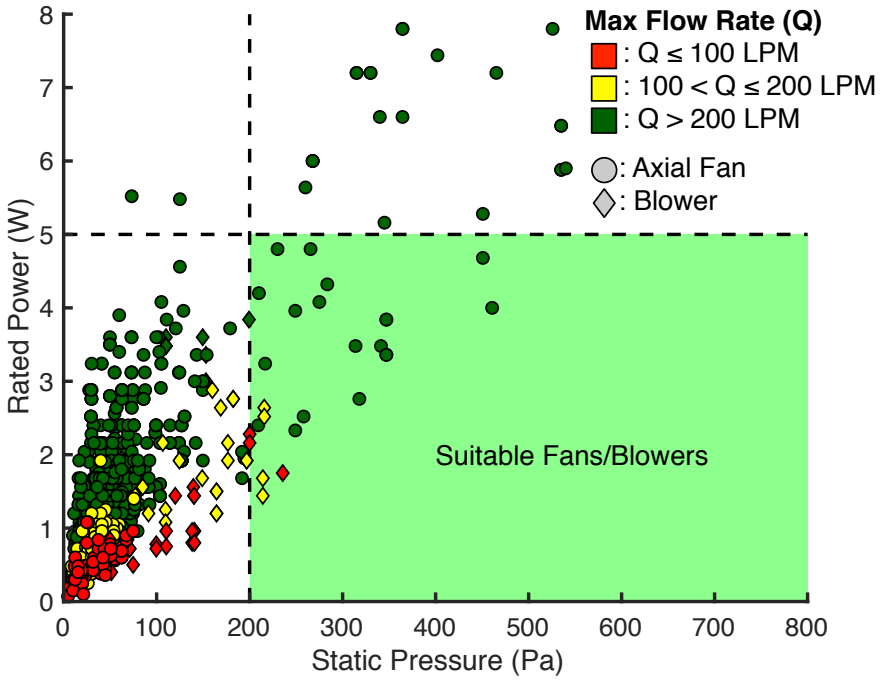

Figure 11. Static pressure, free flow rate, and rated electrical power consumption of 1,135 miniature axial fans and centrifugal blowers that are stocked by Digikey Electronics ® and cost < $10 per unit (when ordering 1000 units). Fans and blowers that meet the MOD2 stove's operational requirements (in the optimal design configuration) are indicated. Marker colors indicate the devices' ability to operate near static flow conditions while providing the stove's required flow rate (12 SLPM).

Only 23 (~2%) of the 1,135 fans and blowers presented in Figure 11 meet the MOD2 stove's static pressure (>200 Pa), free flow (>100 SLPM), and electrical power (<5 W) requirements. Miniature fans and blowers are typically designed for cooling electronics, and therefore provide high air flow rates at low pressures – around 70% of the devices shown in Figure 11 generate maximum flow rates > 100 LPM using < 5 W of power, but at static pressures < 100 Pa. However, the MOD2 stove requires relatively low flow rates of air, driven through small injection orifices that generate high velocity air jets in the combustion chamber, but require significant input pressures. Of the 23 viable devices identified, Figure 11 shows that suitable blowers generally require less power than axial fans, as they are better suited to high pressure, low flow applications. It is also important to note that as the stove heats up during normal use and manifold pressures rise, the electrical power input to the fan or blower must also increase to maintain a constant mass flow of secondary air into the firebox. Overall, Figure 11 illustrates that low-cost fans and blowers are currently available to achieve effective and practical secondary air injection in wood-burning cookstoves, but they must be carefully chosen and evaluated thoroughly, as the vast majority are not intended to meet the flow, pressure, and energy consumption conditions required.

3.4.3 Room for Improvement: Start Up and Ultrafine Particle Emissions

Health guidelines from the WHO, EPA, and other organizations generally recommend maximum $PM_{2.5}$ pollution levels in terms of mass concentration (e.g., $\mu g/m^3$).[86,121] By this measure, the MOD2 stove significantly alleviates health impacts from biomass combustion, as it reduces $PM_{2.5}$ mass emissions by an order of magnitude relative to a traditional TSF. However, Figure 12 shows that the vast majority (>80%) of $PM_{2.5}$ emissions from the MOD2 stove consist of ultrafine particles (UFP) with a diameter < 100 nm, which may be particularly harmful to human respiratory health, as their small size enables deeper penetration into the lungs.[88,122-124] Consequently, it is important not only to reduce the mass of PM, but also the number of UFPs that is emitted and potentially inhaled.

Secondary air injection does not significantly reduce the total number of particles generated by biomass combustion, but instead shifts the PM size distribution towards smaller, less massive particles.[75,105,125,126] As the secondary flow rate increases from 7.2 to 12 SLPM, Figure 12 shows that the total number of particles emitted from 5 to 2500 nm remains relatively steady, ranging from 5.5×10^{14} to 6.9×10^{14} particles/kWd. Total $PM_{2.5}$ volume, on the other hand, decreases over the range of secondary flow rates presented, as particle size diminishes. Given that $PM_{2.5}$ density remain nearly constant (Figure B12), the particle volume measurements are directly proportional to particle mass, and therefore closely mirror the $PM_{2.5}$ mass emission measurements shown in Figure 10.

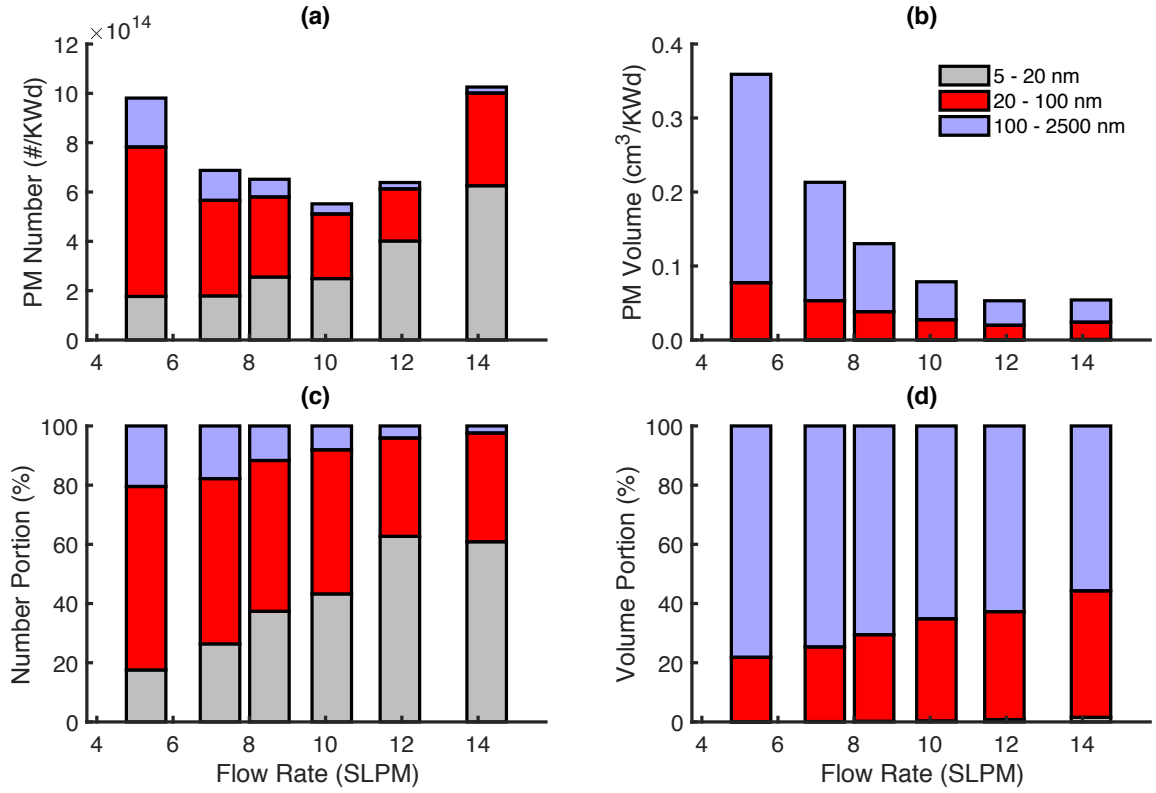

Figure 12. (a) Total $PM_{2.5}$ number and (b) volume emissions from the MOD2 stove over the cold start (normalized by cooking power), as a function of particle diameter and secondary air flow rate through injection Pattern 2. (c) Portion of the total number, and (d) volume of particles

emitted in each size range: 5 to 20 nm, 20 to 100 nm, and 100 to 2500 nm. Each bar represents the mean of replicate test data collected for each stove configuration. Confidence intervals are here omitted for clarity, and instead provided in Figure B13.

Figure 12 shows that secondary air injection effectively inhibits particle growth, but does not significantly reduce their formation. Particles form either through nucleation, as volatile organic and inorganic compounds emitted during wood pyrolysis cool in the exhaust, or through soot (BC) generation in the flame, during quenching of fuel-rich combustion zones.[37,93,94,102] Typically, these primary particles grow through agglomeration and condensation of volatile compounds. However, Figure 10 shows that CO and $PM_{2.5}$ mass reductions closely mirror one another as secondary flow rate increases, likely because CO and many-PM forming volatile organic compounds (e.g. PAH) oxidize under similar conditions.[91,92,127] As volatile organic gas emissions diminish at higher secondary flow rates, primary particles no longer grow through their condensation. As a result, the portion of PM in the nucleation mode (5 – 20 nm) increases from 20 to 60% as secondary air flow through Pattern 2 increases, but these small particles account for less than 2 % of the total PM volume (and therefore mass). Figure B16 provides the size distribution of particle number emissions, and shows a distinct peak at a particle diameter of ~12 nm, which increases with secondary air flow rate.

In the absence of volatile organic gases in the exhaust, inorganic and BC particles generally grow to sizes <100 nm through agglomeration. [63,76,92,128] Figure 12 shows that the fraction of ultrafine particles (5 – 100 nm) grows from 80 to 97% as secondary flow increases, and accounts for 20 to 40% of the PM volume generated. As the size distribution shifts towards smaller particles, the fraction of particles in the accumulation mode (100 – 2500 nm) correspondingly decreases from 20 to 3% over the parametric range presented, but still accounts for most (60 to 80%) of the emitted volume. Particles in the accumulation mode form as some growth pathways persist, such the condensation of gases in cool regions of the exhaust flow or agglomeration of particles under turbulent mixing conditions. Some of the larger particle (>1000 nm) may also consist of fly ash generated in the fuel bed and entrained in the exhaust flow.[94]

Total particle number emissions are lowest for a secondary flow rate of 10 SLPM (Figure 12), suggesting that this configuration may provide the optimal balance of turbulent mixing and high combustion temperatures to inhibit particle formation. However, total PM volume generation continues to decrease at higher flow rates, as particles continue to grow smaller. Furthermore, $PM_{2.5}$ number emissions increases sharply from 12 to 14 SLPM, again indicating that excessive secondary flow in this configuration quenches the combustion zone,[39] but total $PM_{2.5}$ volume changes little, as particle emissions in the accumulation mode persist. Together, these trends demonstrate that $PM_{2.5}$ mass emission reductions can be achieved while simultaneously generating more UFPs.

When secondary air flow rate is sufficient, the particle size distribution shifts towards smaller, less massive particles as the stove, fuel, and exhaust gases warm up during the cold start test.[129] As the secondary flow rate through Pattern 2 increases, Figure 13 shows that the particle volume generation is increasingly attenuated over the first 18 minutes of the cold start test, although the number of emitted particles accumulates steadily for all configurations. The $PM_{2.5}$ number and volume accumulation rates reflect the secondary rate flow dependence illustrated in Figure 12 and outlined above. Manifold temperatures rise more rapidly at higher flow rate settings (Figure 13(c)), thereby hastening the inhibition of particle growth. For flow rates $\geq$ 10 SLPM, the count median diameter (CMD) of particle emissions decreases from around 60 nm to

20 nm over the first 18 minutes of the cold start (Figure B17), and so most volume emissions are consequently emitted during this start up period. At the optimal secondary flow rate setting of 12 SLPM, half of total volume emissions are emitted within the first ~7 minutes following ignition, representing only ~30% of the total test length (in this configuration, the average time to boil is 24±2 min). Consequently, if further PM mass reductions are sought, methods should be developed to enhance combustion conditions during the start up phase.

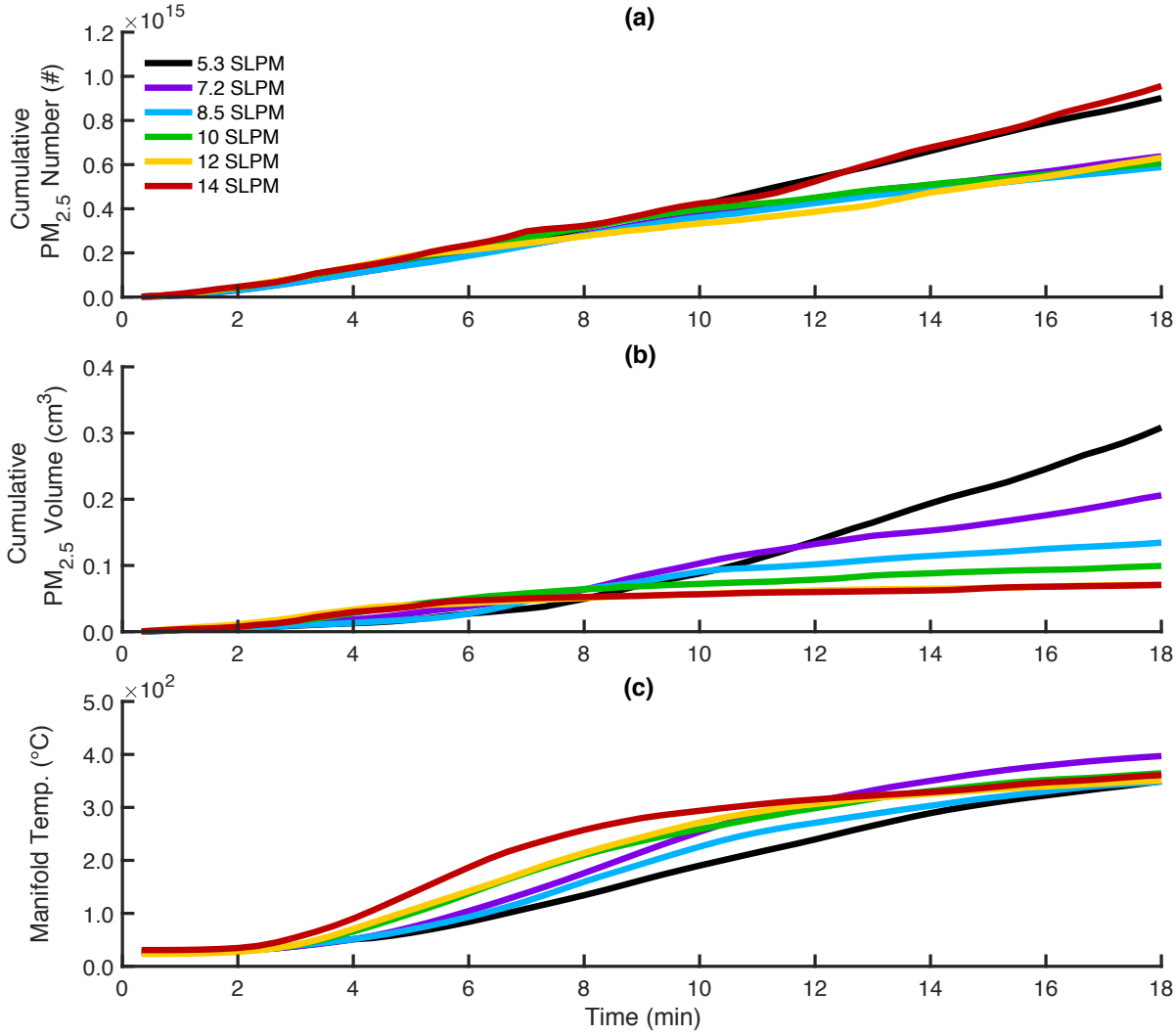

Figure 13. (a) Accumulation of $PM_{2.5}$ number and (b) volume emissions from the MOD2 stove over the first 18 minute of the cold start. (c) Temperature of secondary air in the MOD2 stove manifold over the first 18 minute of the cold start. Each line represents the mean of replicate test measurements collected at each of the six secondary flow settings (using injection Pattern 2). Confidence are omitted here for clarity, and instead provided in Figure B14 and Figure B15 for all secondary flow rate settings. All data presented is block-averaged on a 20-sec time base.

Although volume emissions are effectively attenuated over time, the number of particles continues to accumulate steadily for all configurations, and the CMD is less < 80 nm throughout (Figure B17), well within the ultrafine range that is of particular concern for human health. As a result, it is important that future research efforts investigate methods for inhibiting particle formation entirely, rather than simply limiting particle growth. For example, methods of restricting the fuel bed temperature could be devised to limit the volatilization of inorganic compounds that nucleate into incombustible particles.[37] Since BC represents a significant portion of the PM generated by the MOD2 stove, methods should also be developed to prevent quenching of flames against the pot and other surfaces, but while also maintaining high thermal efficiency.

While further improvements are needed to reduce UFP emissions, the MOD2 stove generally illustrates that secondary air injection is a practical and effective method for reducing harmful air pollution from wood combustion. Most importantly, the emission reductions demonstrated experimentally are achievable using inexpensive hardware currently on the market, and can be driven independently using a TEG or other low-cost power source. However, stove performance is highly sensitive to secondary air injection design parameters, and so it is important that new designs be validated and optimized experimentally. The experimental results presented here illustrate several important design principles, such that combustion chamber dimensions should be minimized so as to increase the effectiveness of secondary air jets. When applied together, these design principles and the experimental optimization procedure will help to inform and improve the design of clean, efficient, and practical wood-burning cookstoves to mitigate harmful air pollution exposure in the billions of households that depend on solid biomass for their daily cooking needs.

Chapter 4 - A New Black Carbon Sensor for Dense Air Quality Monitoring Networks

4.1 Abstract

Low-cost air pollution sensors are emerging and increasingly being deployed in densely distributed wireless networks that provide more spatial resolution than is typical in traditional monitoring of ambient air quality. However, a low-cost option to measure black carbon (BC) – a major component of particulate matter pollution associated with adverse human health risks – is missing. This Chapter presents a new BC sensor designed to fill this gap, the Aerosol Black Carbon Detector (ABCD), which incorporates a compact weatherproof enclosure, solar-powered rechargeable battery, and cellular communication to enable long-term, remote operation. This Chapter also demonstrates a data processing methodology that reduces the ABCD's sensitivity to ambient temperature fluctuations, and therefore improves measurement performance in unconditioned operating environments (e.g., outdoors). Over 100 ABCDs were operated outdoors in collocation with a commercial BC instrument (Magee Scientific, Model AE33) housed inside a regulatory air quality monitoring station. The measurement performance of 105 ABCDs is comparable to the AE33. The fleet-average precision and accuracy, expressed in terms of mean absolute percentage error, are 9.2 ± 0.8 % (relative to the fleet average data) and 24.6 ± 0.9 % (relative to the AE33 data), respectively (fleet-average ± 90% confidence interval).

4.2 Introduction

Air quality monitoring networks operated by regulatory agencies traditionally rely on a small number of measurement sites centrally located within large geographical areas. For example, the European Union only requires one sampling site to monitor an area of 100,000 km^2.[17] The number of monitoring sites is primarily restricted by the cost of expensive regulatory-grade air pollution analyzers housed in environmentally controlled structures.[24,41] Monitoring at central locations is highly valuable for establishing air pollution concentration trends[130], but pollutant concentrations measured at a single monitoring location do not necessarily accurately describe the pollution exposures of individuals located around the central monitor.[22,23] This is particularly true for primary pollutants, whose concentrations tend to vary widely with location.[66,131]

Emerging low-cost sensors offer the opportunity to monitor air pollution with much greater spatial resolution.[49,58] Low-cost sensors that cost a few hundred dollars or less are available for many pollutant gases, such as electrochemical sensors for nitrogen dioxide or ozone.[54,55,62,132] Low-cost sensors that measure particulate matter (PM) are also available, where mass concentration is typically based on the amount of light scattered by the airborne particles.[56,59,61] Combinations of these low-cost sensors are increasingly deployed in densely distributed sensor networks to provide greater spatial resolution than traditional regulatory monitoring networks.[52,53,133-135] One notable gap, however, is the absence of a black carbon (BC) monitor in these networks.

BC, a primary air pollutant, is the main light-absorbing component of PM generated by fossil fuel combustion (notably diesel engines) and biomass burning (such as woodstoves).[136]

Exposure to particulate matter from these sources is associated with increased risk of pulmonary and cardiovascular diseases, cancer, and premature death.[3,4,67] BC is also a potent short-lived climate pollutant.[63,69] BC analyzers employing different measurement principles exist.[84,85] However, most cost on the order of $10,000 to $20,000 (USD) and are thus too expensive to be deployed in large numbers.

This Chapter presents a new BC sensor – the aerosol black carbon detector (ABCD) – designed for dense deployment in air quality monitoring networks. In addition to providing an overview of the ABCD's design architecture, this Chapter presents a detailed evaluation of the sensor's native sensitivity to ambient temperature fluctuations, and demonstrates a novel data processing methodology to correct this temperature dependence. This data processing method greatly reduces inaccurate or erroneous BC measurements that plague other BC analyzers.[83,137] To validate the performance of this new sensor, we constructed over 100 ABCDs and operated this sensor fleet outdoors in collocation with a commercial BC instrument housed inside a regulatory air quality monitoring station in Oakland, California.

4.3 Materials and Methods

4.3.1 Aerosol Black Carbon Detector (ABCD)

The ABCD belongs to a class of instruments known as aerosol absorption photometers, which include the particle soot absorption photometer, the aethalometer, and the multi-angle absorption photometer.[138-140] These instruments measure the light absorption of ambient PM collected on a fibrous filter. The ABCD converts measured light absorption to BC mass concentration. The central component of the ABCD is the optical cell, shown in Figure 14.

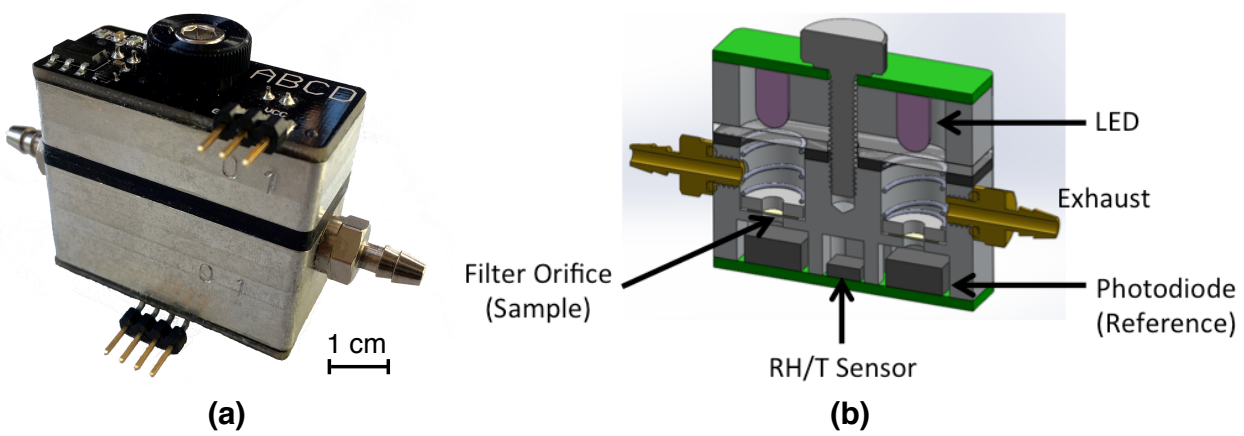

Figure 14. Aerosol Black Carbon Detector: (a) Optical cell; (b) Section view of optical cell

Air is a drawn into the cell with a rotary vane pump, and through two Teflon-coated glass-fiber filters (Pallflex® Emfab™) that lie between light emitting diodes (LEDs) and photodiodes, as illustrated in Figure 15. The LEDs operate at a central wavelength of 880 nm, where BC is the predominant PM species to absorb light.[141-144] The photodiodes generate electrical voltages that are linearly proportional to the intensity of light transmitted through each filter. The analog voltage measurements from the photodiodes are digitized using a 24-bit analog-to-digital converter (ADC) and processed by a microcontroller unit (MCU). A relative

humidity and temperature (RH/T) sensor is mounted directly in the sample flow path between the sample and reference photodiodes. A differential pressure sensor downstream of the optical cell measures the volumetric flow rate of the sampled air (see Appendix C3). The MCU generates a pulse-width modulated signal to control the electrical power delivered to the rotary vane pump and maintain a desired flow rate between 100 and 250 cc min^{-1}.

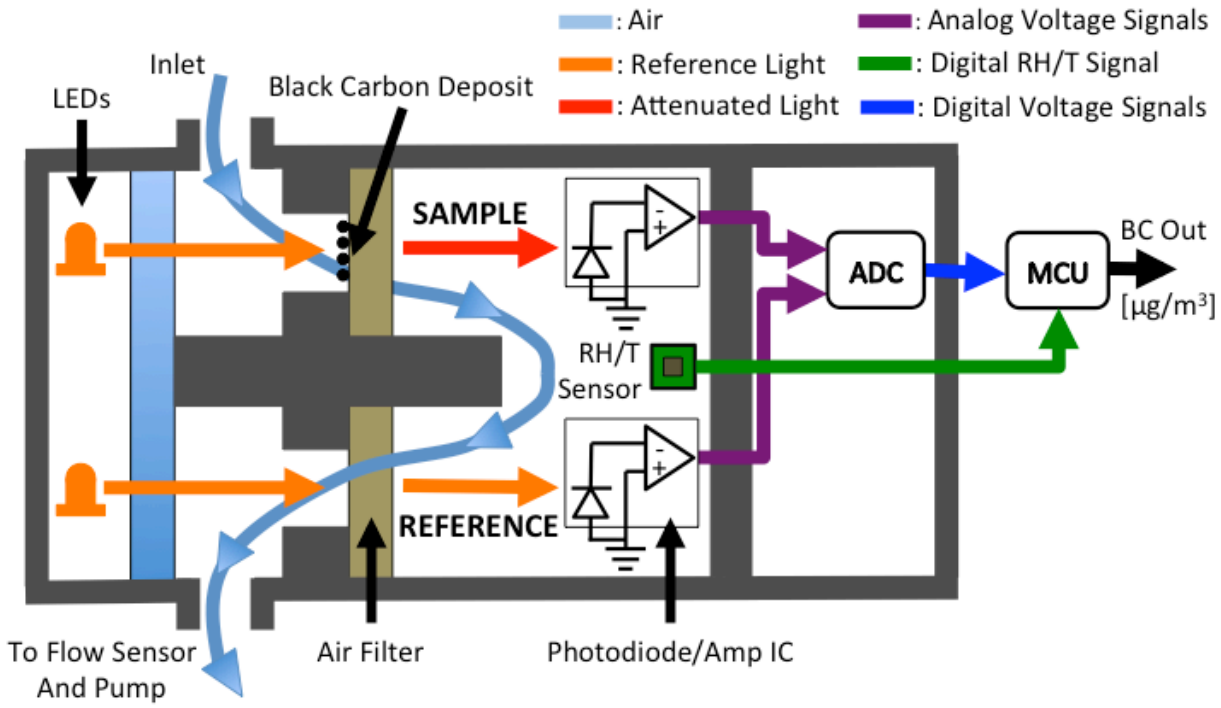

Figure 15. Functional diagram of the ABCD optical cell

The intensity of light reaching the photodiode below the first filter in series (i.e., the sample filter) is attenuated by the accumulation of BC. Emfab™ filters have a particle removal efficiency of 99.9%,[145] so the air reaching the second filter does not contain any light-absorbing BC. BC mass concentration is computed from measured optical attenuation, which is continually evaluated as the natural log ratio of the reference to sample voltage outputs. Air is drawn through both the reference and sample filters with the intention of minimizing the influence of environmental conditions on measured BC concentrations, such as changes in the relative humidity of the sampled air and temperature of the electrical components. To further reduce the BC sensor's environmental sensitivity, a real-time temperature compensation method was developed, as described in detail below.

The optical cell is enclosed with all the components required for the ABCD to serve as a self-contained, wireless sensor node, as shown in Figure 16. This outdoor monitoring package includes rotary vane vacuum pump, air flow sensor, rechargeable battery (12-volt, 10-amp-hour), and an integrated electronics board, known as the AUX board. The AUX board is a printed circuit board that integrates the MCU, real-time clock, SD memory card slot, 2G cellular modem, power management electronics, and hardware for all required input and output connections. The enclosure is a weatherproof, insulated box onto which a photovoltaic panel (18-volt, 8-watt) is mounted. A charge controller regulates the power generated to recharge the battery. Additional

details of these components are provided in Appendix C4. The ABCD's MCU processes and stores data to the SD memory card at 0.5 Hz, and for this study, the ABCD was programmed to wirelessly transmit 60 one-minute average values every hour to an online database using the 2G cellular modem. Appendix C5 provides details on the data collection and analysis methods.

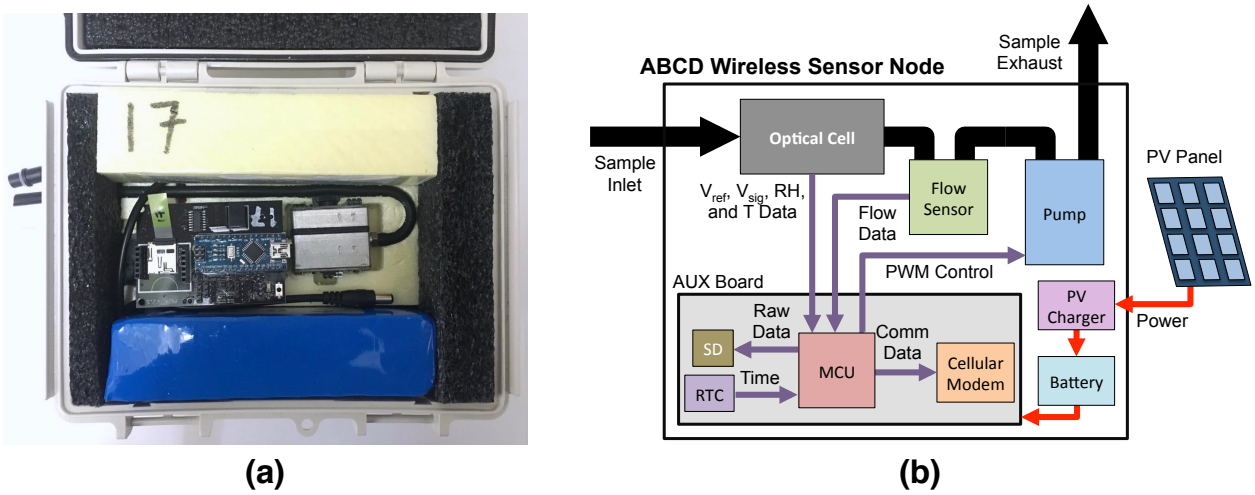

Figure 16. Complete ABCD in outdoor monitoring package: (a) Interior view; (b) Functional diagram.

The complete ABCD has dimensions of 18 × 23 × 10 cm, weighs 1.5 kg, and consumes 0.6-watt of electrical power at a sample flow rate of 110 cc min^{-1}. Under this condition, the onboard battery can power the ABCD for ~8 days. The photovoltaic panel extends this operational period indefinitely if weather conditions and instrument placement allow sufficient insolation. Internal insulation is intended to prevent condensation when sampling cold, moist air by keeping the optical cell above the dew point temperature. The optical cell is positioned in the enclosure for easy removal and is readily opened using a single thumbscrew. These features allow for easy replacement of the sample filter after it becomes excessively loaded with BC.

The custom optical cell is designed with a minimal number of parts to simplify the fabrication process and reduce manufacturing costs. The MCU, flow sensor, charge controller, battery, and pump are commercially available components. This design approach enables the construction of a complete ABCD sensor at material cost of roughly $400 for a production batch of around 150 units. The pump ($125) and custom optical cell ($100) account for about half of this cost (see Appendix C4 for comprehensive list of components).

4.3.2 Field Validation

BC concentrations measured with ABCD units were compared to those measured with an aethalometer (Magee Scientific, Model AE33) operated by the Bay Area Air Quality Management District at a monitoring station adjacent to a major highway in Oakland, California. The AE33 is operated inside the monitoring station using a sampling probe that extends outdoors, and used as a reference against which ABCD performance is evaluated. ABCDs were hung from railings on the roof of the station, as shown in Figure C1.

4.4 Results and Discussion

4.4.1 Measurement Bias from Environmental Fluctuations

The response of an ABCD operating outdoors with a High Efficiency Particulate Air (HEPA) filter on its inlet for a two-week period is shown in Figure 17. The output voltages (Figure 17a) are clearly dependent on ambient conditions, oscillating in sync with the diurnal trends in temperature and relative humidity (Figure 17c). These output voltage oscillations are likely the result of the optical electronics' temperature sensitivity. The LEDs are rated to dim 0.3% for every 1°C temperature rise [146], which is approximately what is observed (0.1 V reduction relative to a 1.5 V baseline with a 20°C temperature increase), suggesting that the temperature sensitivity of the LEDs plays a major role. Photodiode sensitivity (the voltage output per watt of incident light intensity) decreases by 0.01% for every 1°C temperature rise [147], and likely also contributes to the diurnal voltage oscillations. It should be noted that the ABCD measures the temperature of the air flowing through the optical cell, but it is assumed that the electronics nearby are at a similar temperature. Expected variations in the optical thickness of the fibrous filters due to sorption and desorption of water vapor from the sampled air are opposite to the observed voltage oscillations, suggesting that RH sensitivity is smaller than the temperature dependence of the optical electronics.

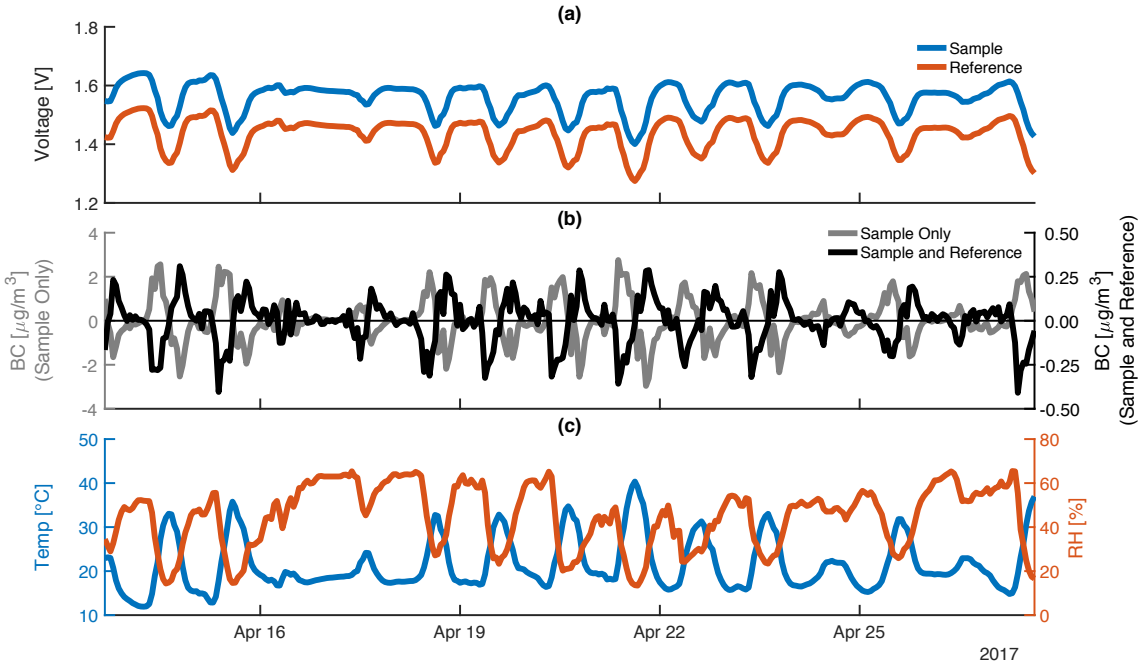

Figure 17. The response of an ABCD operating outdoors with a HEPA filter on its air inlet for two weeks: (a) Sample (blue) and reference (red) voltage outputs from optical cell; (b) Black carbon (BC) concentration calculated using only sample voltage (gray), and using both the sample and reference voltages (black); (c) Optical cell temperature (blue) and relative humidity (RH) (red). All data is provided on a 60-minute time base.

Although the sample and reference output voltage oscillations track one another closely, the rates of voltage change over time are not identical. Consequently, reported BC concentrations

are not zero, as would be expected for a sensor sampling particle-free air. Rather BC concentrations exhibit a diurnal trend typically in the ± 0.3 μg m^{-3} range (Figure 17b, black), with a mean absolute error (MAE) on the order of 0.1 μg m^{-3} and a two-week average BC concentration of −0.003 μg m^{-3}. BC concentrations computed using only the output from the photodiode monitoring the sample filter are much larger, in the ± 2 μg m^{-3} range (Figure 17b, gray), which illustrates that computing BC concentrations using both the reference and sample signals significantly reduces, but does not completely eliminate environmental effects. If ambient BC concentrations are much larger than ± 0.3 μg m^{-3}, then further compensation may not be necessary. However, in many locations, ambient BC concentrations are comparable to 0.3 μg m^{-3} and, thus, temperature compensation is employed to further reduce the environmental sensitivity.

4.4.2 Temperature Compensation

The temperature response of each ABCD optical cell was determined by operating each instrument outdoors with a HEPA filter on the inlet for at least 24 hours. In all cases, sample and reference photodiode voltage outputs display a highly linear dependence on the recorded cell temperature. In order to quantify this temperature dependence, the relative change (*RC*) in each photodiode's output voltage is calculated as:

$$RC(t) = \frac{V(t) - V(0)}{V(0)} \qquad (1)$$

where *V(t)* is the photodiode voltage (V) at time *t*, and *V(0)* is the first voltage logged during the particle-free sampling event. In Figure 18, *RC* is plotted as a function of sensor temperature for three ABCD optical cells, and linear regression factors (slope, intercept, and R^2) are shown. The temperature sensitivities of an optical cell's sample and reference channels (i.e., the slopes of the linear regressions, m_{smpl} and m_{ref}) are often not equal. Therefore, the ratio of these slopes (m_{smpl}/m_{ref}, hereafter referred to as "slope ratio") is often either greater than or less than unity. For example, ABCD 1 has a slope ratio of 0.57, indicating that the sample voltage output is less temperature sensitive than the reference. Consequently, as the temperature fluctuates over time, the sample and reference voltage outputs do not change at an equal rate. The result is non-zero BC measurements, as the effect of changing temperature on the sample voltage output is not exactly compensated by the effect of changing temperature on the reference voltage output. For example, the optical cell referenced in Figure 17 has a slope ratio of 0.89, and the reference voltage output significantly reduces, but does not completely eliminate, the environmental influence on reported BC concentrations.

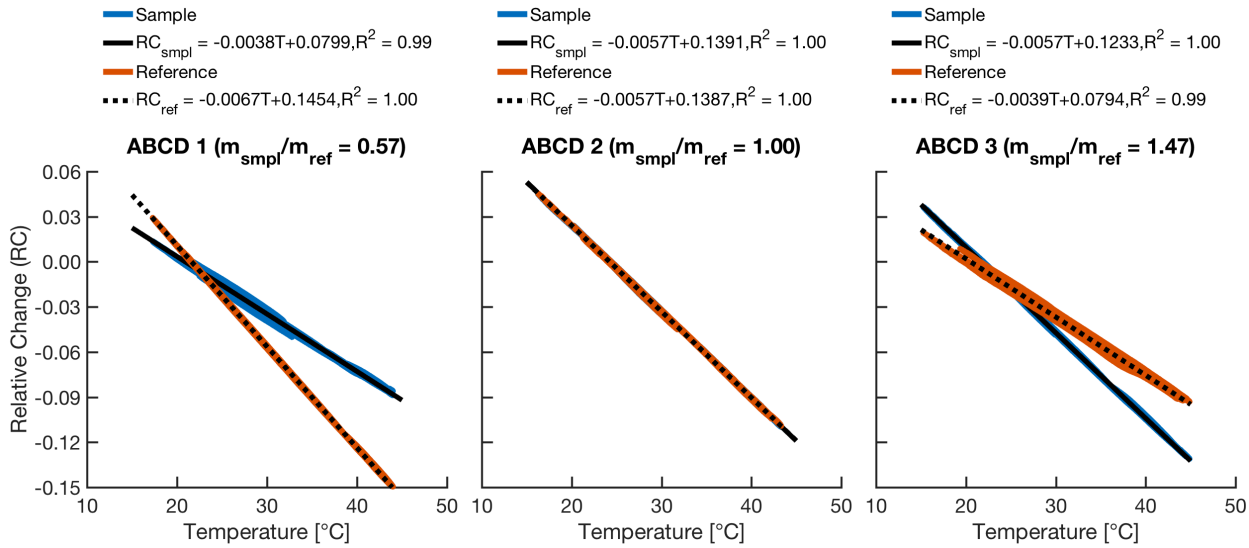

Figure 18. Relative change (RC) in the sample (blue) and reference (red) voltage outputs of three ABCD optical cells as a function of sample flow temperature, along with corresponding linear regression equations and coefficients of determination. The ratio of the sample to reference temperature sensitivities (m_{smpl}/m_{ref}) of each optical cell is noted above each plot.

In Equation (2), the linear regression equations for each photodiode output are set equal to Equation (1), except that the voltage change is now evaluated relative to the temperature compensated voltage:

$$RC(t) = \frac{V(t) - V_{comp}(t)}{V_{comp}(t)} = \quad mT(t) + b \qquad (2)$$

where $V_{comp}(t)$ is the temperature compensated voltage output (V), $T(t)$ is the sample flow temperature (^{o}C), and m ($^{o}C^{-1}$) and b are the slope and intercept of the linear regression, respectively. Rearranging Equation (2) yields an equation that allows the photodiode voltage, $V(t)$, to be compensated using real-time temperature measurements:

$$V_{comp}(t) = \frac{V(t)}{mT(t) + b + 1}. \qquad (3)$$

BC concentrations calculated using the temperature compensated sample and reference voltage outputs from Equation 3 are generally significantly less sensitive to temperature fluctuations.

We observed considerable variability in the temperature sensitivity the optical cells (e.g., as illustrated in Figure 18), likely because of variations in the LEDs, photodiodes, and related circuitry. Consequently, we evaluated the temperature sensitivity and determined the linear regression coefficients in Equation 3 uniquely for each individual ABCD optical cell. The slope and intercept for both photodiode outputs are stored on SD cards assigned to each optical cell. The SD card is inserted into the ABCD's AUX board, and the respective linear regression coefficients are uploaded to the MCU to compensate BC measurements in real time as a function of measured temperature.

In Figure 19, temperature compensated (TComp) responses are shown in addition to the uncompensated (Raw) responses for the ABCD shown in Figure 17b. Throughout the trial, temperature compensated voltage outputs steadily maintain their initial values (Figure 19a) and temperature compensated BC concentrations (Figure 19b) exhibit a diurnal trend typically in the ± 0.1 μg m^{-3} range (compared to ± 0.3 μg m^{-3} when uncompensated) with a MAE of 0.02 μg m^{-3} (compared to 0.1 μg m^{-3} when uncompensated).

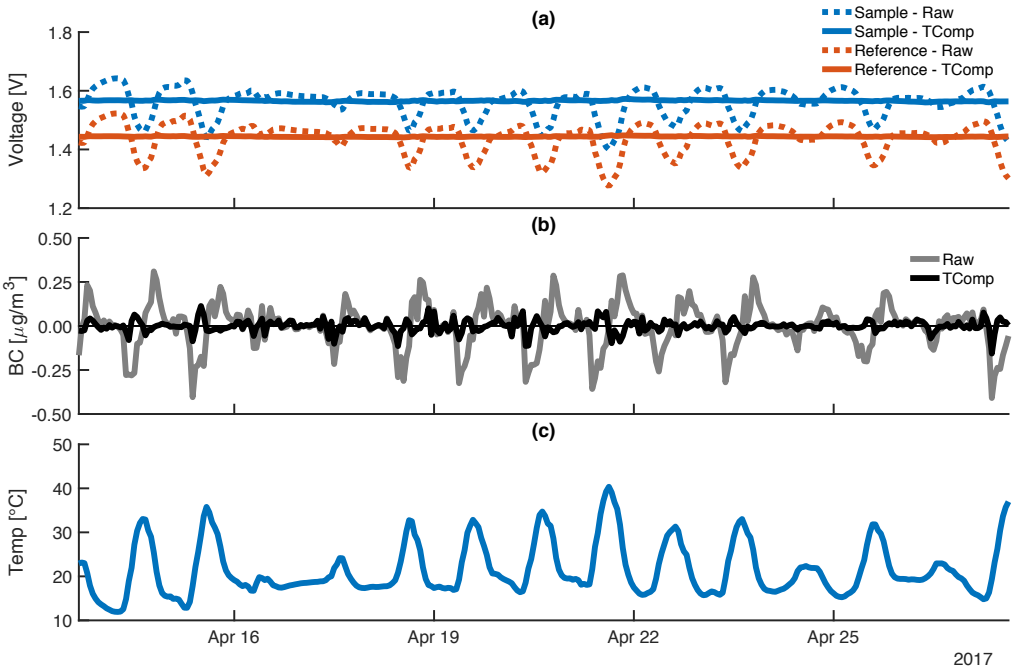

Figure 19. The response of an ABCD operating outdoors with a HEPA filter on its air inlet for two weeks. Temperature compensated responses (solid) are shown in addition to the uncompensated responses (dashed) previously provided in Figure 17: (a) Sample (blue) and reference (red) voltage outputs from optical cell; (b) Uncompensated (gray) and temperature compensated (black) black carbon (BC) concentrations; (c) Optical cell temperature. All data is provided on a 60-minute time base.

To further illustrate the implementation of the temperature compensation method, both uncompensated and temperature compensated BC concentrations are shown in Figure 20 for five ABCDs with HEPA-filtered inlets. The slope ratios for these cells ranges from 0.57 to 1.47 and uncompensated BC concentrations ranged between ± 2 μg m^{-3}. As shown in Figure 20a, uncompensated diurnal BC oscillations and corresponding MAE values are largest for ABCD optical cells whose slope ratios are farthest from unity (cells 1 and 5) and smallest for the cell with a slope ratio of 1.00 (cell 3). Furthermore, as a consequence of the temperature dependence illustrated in Figure 18, BC oscillations for optical cells with slope ratios less than unity (cells 1 and 2) are opposite those for optical cells with slope ratio greater than unity (cells 4 and 5).

As shown in Figure 20b, all temperature compensated BC concentrations are very close to the true zero, with MAE values on the order of 0.02 μg m^{-3} irrespective of the optical cell's slope ratio. BC concentrations and MAE for cell 3 whose slope ratio is ~1 are essentially unaltered by the procedure, as expected.

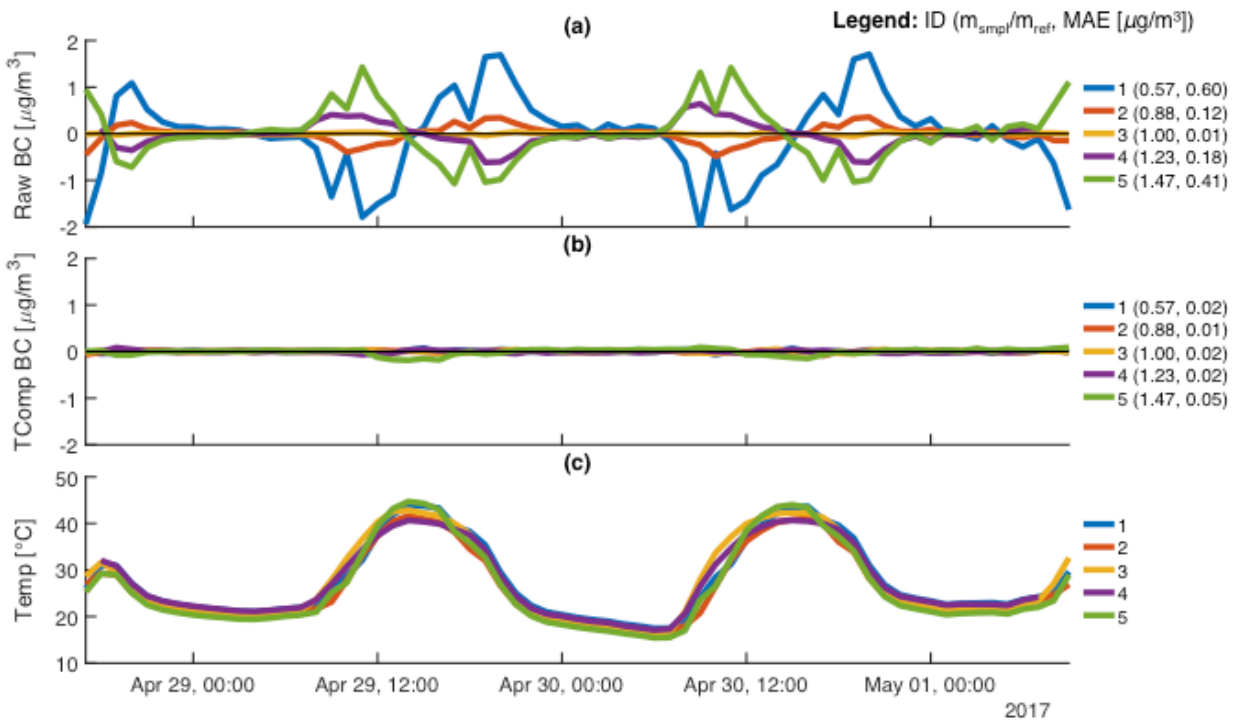

Figure 20. The response of five ABCD units operating outdoors with HEPA filters on the air inlets: (a) Uncompensated black carbon (BC) concentrations; (b) Temperature compensated BC concentrations; (c) Optical cell temperatures. All data is provided on a 60-minute time base. For each ABCD, the slope ratio of the optical cell and mean absolute error (MAE) of BC concentration measurements are shown in the legends. The MAE of BC measurements is evaluated relative to the desired zero output (0 μg m^{-3}).

Figure 21 summarizes the zero response of all 150 ABCD optical cells manufactured in this study. MAEs of uncompensated and temperature compensated BC concentrations are plotted against the absolute deviation of each cell's slope ratio from unity ($|m_{smpl}/m_{ref} - 1|$). As illustrated, MAE generally increases proportionally with increasing absolute slope ratio deviation for uncompensated cells. In contrast, temperature compensation works to significantly improve performance: all ABCD optical cells report BC concentrations near zero such that, across the fleet of 150 cells, the MAE averages 0.016 ± 0.001 μg m^{-3} (mean ± 90% confidence interval).

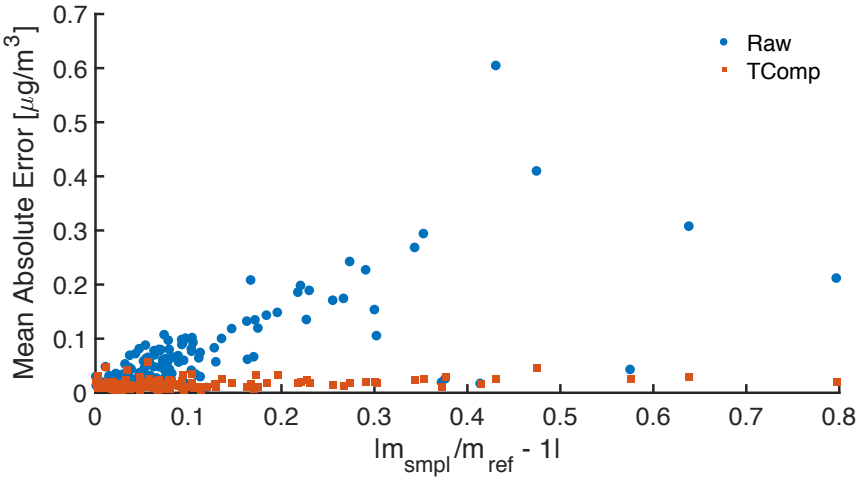

Figure 21. Mean absolute error (MAE) of uncompensated (Raw) and temperature compensated (TComp) black carbon concentrations reported by 150 ABCD optical cells with HEPA-filtered inlets, as a function of the slope ratio's absolute deviation from unity ($|m_{smpl}/m_{ref} - 1|$). The MAE of 60-minute time base BC concentrations is evaluated relative to 0 μg m^{-3}.

4.4.3 Field Validation

Following acquisition of temperature compensation parameters for all optical cells, ABCDs were operated outdoors for one week atop the Bay Area Air Quality Management District's near-roadway monitoring station (see Figure C1). Figure 22 shows time series of uncompensated and temperature compensated BC concentrations for five ABCDs with optical cell slope ratios ranging from 0.66 to 1.69. BC concentrations reported by the aethalometer (Magee Scientific, Model AE33) housed inside the monitoring station are shown for comparison.

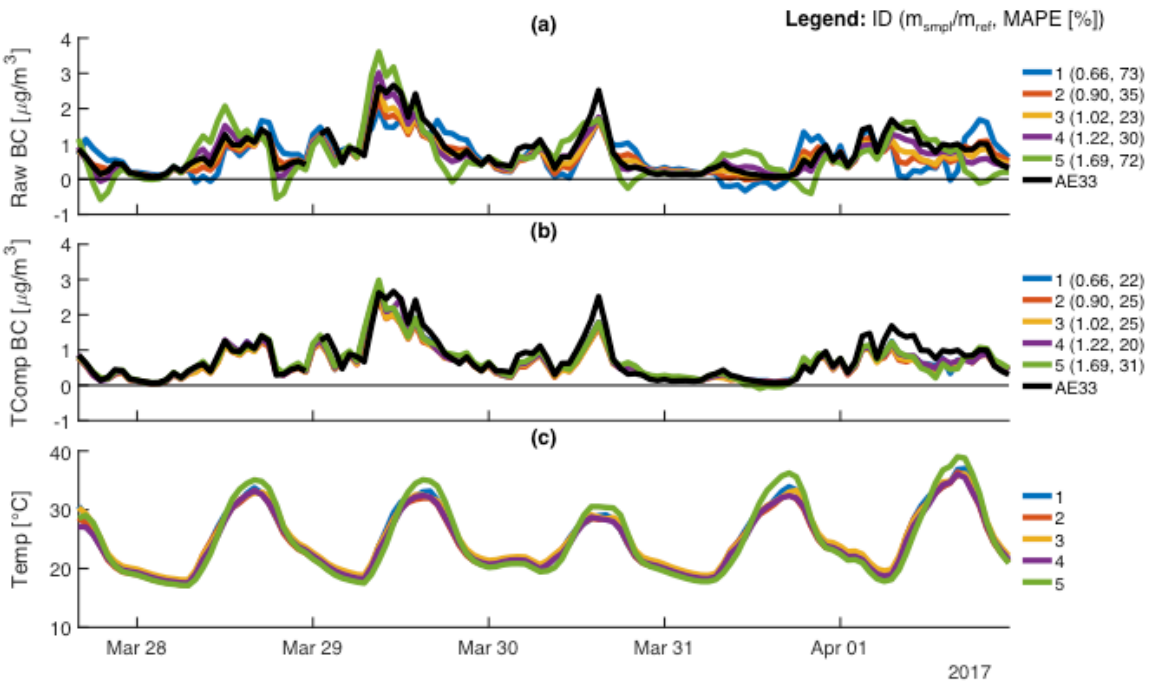

Figure 22. Five ABCD units operating outdoors atop a Bay Area Air Quality Management District roadside monitoring station: (a) Uncompensated black carbon (BC) concentrations; (b) Temperature compensated BC concentrations; (c) Optical cell temperatures. Also shown are BC concentrations reported by a Magee Scientific AE33 housed inside the monitoring station (black). All data is provided on a 60-minute time base. For each ABCD, the legend shows the slope ratio of the optical cell and mean absolute percent error (MAPE) of the BC concentrations, the latter of which is based on deviations from BC concentrations reported by the AE33 reference instrument. The ABCDs shown in this figure are different than those presented in Figure 20.

Uncompensated BC concentrations deviate more notably from the AE33 reference for ABDCs with optical cell slope ratios that are significantly offset from unity (Figure 22a). Uncompensated BC concentrations include erroneous negative values over substantial portions of the sampling period. For ABCD optical cells with slope ratios of 0.66 and 1.69, the corresponding mean absolute percent error (MAPE) in BC concentration relative to the AE33 (~70 %) is three times larger than the MAPE for the ABCD optical cell with a slope ratio of 1.02 (23%). Furthermore, optical cells with slope ratios less than unity tend to overestimate BC concentrations when the temperature increases (and vice-versa). Temperature compensation reduces measurement bias (Figure 22b). The five ABCDs have temperature compensated MAPEs ranging from 22 to 31%, and negative BC measurements are nearly eliminated.

Figure 23 shows the precision and accuracy of these ABCDs during this field evaluation period. The precision of each ABCD is evaluated relative to the mean of BC concentrations from the five ABCDs, while accuracy is evaluated relative to the AE33. Sensor precision (compare Figure 23a and Figure 23b) and accuracy (compare Figure 23c and Figure 23d) are much improved through the temperature compensation method. Temperature compensated data are less scattered and have lower MAPE. For example, uncompensated BC concentrations from optical cells with slope ratios farthest from unity have MAPEs of ~70% relative to both the mean BC concentration of the aggregate ABCDs and the AE33 reference. In contrast, most temperature compensated ABCDs have a precision error of ~8% and accuracy error of ~25%. However,

temperature compensated hourly data from ABCD 5, whose optical cell slope ratio is 1.69, still contains a few negative BC measurements that significantly increase the precision and accuracy error. This suggests that the method presented does not fully compensate the temperature dependence of optical cells with slope ratios that deviate excessively from unity. On the other hand, the precision and accuracy of ABCD 3, whose optical cell slope ratio is 1.02, are essentially unaltered by temperature compensation, as expected.

The field performance of 105 ABCD optical cells is plotted in Figure 24 as a function of the slope ratios' absolute deviation from unity ($|m_{smpl}/m_{ref} - 1|$). The precision and accuracy of uncompensated BC concentrations diminishes as the slope ratio increasingly deviates from unity, but temperature compensation generally improves measurement performance throughout. Similar to the 5 ABCDs featured in Figure 23, the temperature compensated fleet-average precision and accuracy MAPE of the 105 ABCD optical cells, respectively, are 9.2 ± 0.8 % and 24.6 ± 0.9 % (mean ± 90% confidence interval).

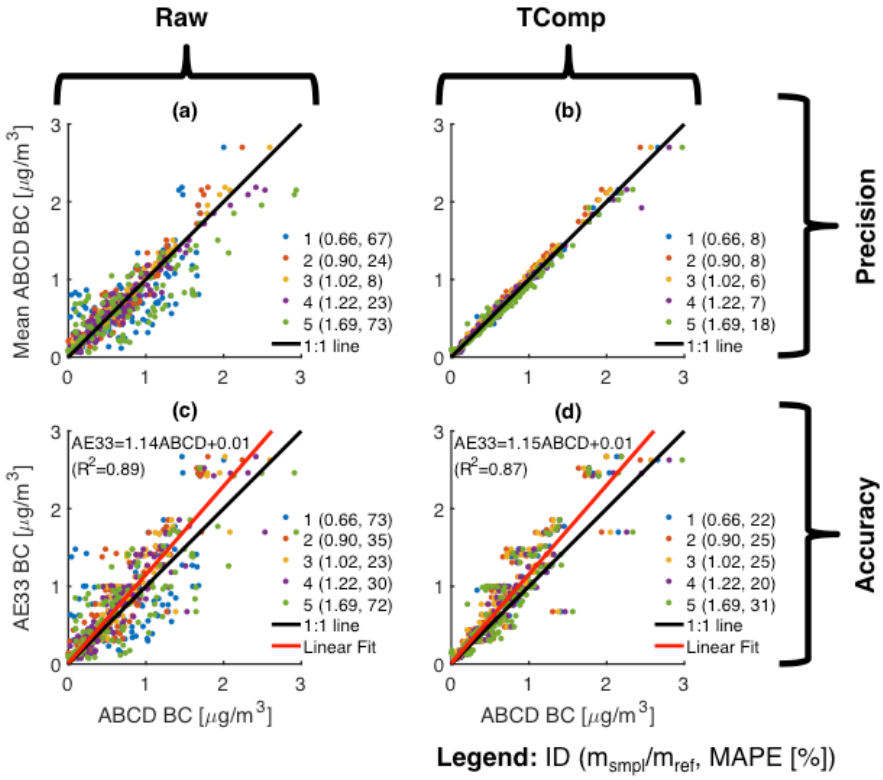

Figure 23. Five ABCD units operating atop a Bay Area Air Quality Management District roadside monitoring station: (a) Precision of uncompensated black carbon (BC) concentrations; (b) Precision of temperature compensated BC concentrations; (c) Accuracy of uncompensated BC concentrations; (d) Accuracy of temperature compensated BC concentrations. All data is provided on a 60-minute time base. Precision is evaluated relative to the mean of BC measurements from all 5 ABCD units, while accuracy is evaluated relative to the AE33 reference instrument. Accuracy plots (c) and (d) also provide the least-square linear regression of the aggregate ABCD data set to the AE33.

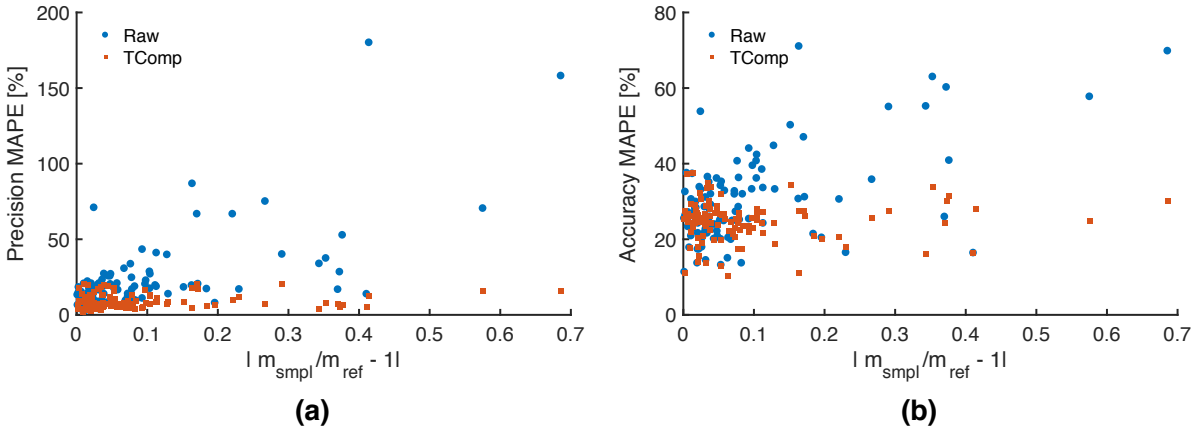

Figure 24. Mean absolute percentage error (MAPE) of uncompensated (Raw) and temperature compensated (TComp) black carbon (BC) concentrations reported during field operation of 105 ABCD optical cells, as a function of the slope ratio's absolute deviation from unity ($|m_{smpl}/m_{ref} - 1|$): (a) Precision evaluated relative to the mean ABCD response; (b) Accuracy evaluated relative to the AE33 reference instrument.

Uncompensated and temperature compensated ABCD BC concentrations are ~15% lower than those reported by the AE33 (see linear regressions in Figure 23c and Figure 23d), and even after temperature compensation, the MAPEs of most ABCDs are above 20% relative to the AE33 (Figure 24b). This bias may be related to the value chosen to convert ABCD optical absorption to BC mass concentration (i.e., the mass attenuation coefficient in Equation C1) or the so-called "loading artifact." The loading artifact causes underestimation of BC concentrations with increased loading of the sample filter [148-150]. Whereas the AE33 periodically changes its filter and incorporates a software algorithm to correct for the loading artifact [151], the ABCDs use only a single filter and the data presented here have not been adjusted for a loading artifact.

4.4.4 Low Cost Air Quality Sensors: Lessons Learned and Future Work

The ABCD's low-cost design, compact weatherproof enclosure, solar-powered rechargeable battery, and cellular communication enable its remote operation. The temperature compensation method presented in this study significantly diminishes the ABCD's sensitivity to varying ambient temperature, thereby increasing the precision and accuracy of measured BC mass concentrations in unconditioned indoor and outdoor operating environments. ABCDs deployed outdoors at a Bay Area Air Quality Management District monitoring station demonstrate a precision error of ~9% and an accuracy error of ~25% when evaluated relative to the commercial instrument (Magee Scientific, Model AE33). To provide a benchmark against which to compare this measurement performance, two AE33 instruments were operated side-by-side in the monitoring station for 20 days (see Figure C3). During this period, the precision error of the AE33 instruments was 9% (the MAPE of each AE33 relative to the mean of both instrument measurements). Therefore, the ABCD's measurement precision, while operating outdoors under fluctuating ambient conditions, generally matches that of the commercial instrument operating inside the monitoring station.

Ongoing research includes comparison of the ABCD and AE33 instruments at additional sampling locations, further investigation of the loading artifact, and a citywide deployment of the ABCDs in an air quality monitoring network to provide insights into BC emissions sources and spatiotemporal patterns in BC concentrations.

Chapter 5 - A Distributed Network of 100 Black Carbon Sensors for 100 Days of Air Quality Monitoring in West Oakland, California

5.1 Abstract

Urban populations are particularly vulnerable to the adverse health impacts of ambient particulate matter (PM) pollution exposure. Air quality measurements are needed to address this growing health risk, but traditional regulatory monitoring at central sites does not provide sufficient spatial coverage and resolution to adequately characterize the highly heterogeneous pollution distributions typical of urban settings. Distributed networks of low-cost air quality sensors are emerging to fill this gap. In this study, we present the 100×100 BC Network, a 100-day deployment of low-cost black carbon (BC) sensors across 100 sampling sites in West Oakland, California – an urban community disproportionately affected by diesel BC emissions associated with nearby port facilities and highways. We assess the reliability of the sensor hardware and data collection systems, and identify major modes of failure to both quantify and qualify the network's performance. Overall, we successfully collected 84.0% of the 240,000 hourly BC concentration measurements desired (100 sampling sites × 2,400 hours), and the widespread failure of the sensors' miniature vacuum pumps was responsible for most missing measurements. The hourly dataset is used to generate highly resolved BC maps throughout West Oakland, demonstrating that concentrations vary sharply over short distances (~100 m) and timespans (~1 hour), depending on surrounding land use, traffic patterns, and location relative to prevailing winds. BC concentrations at each sampling site are highly repeatable over the diurnal and weekly cycles, and periodic pollution trends are characterized throughout the neighborhood. Using these general trends as a reference, unusually polluted locations are detected, and likely emissions sources nearby are identified.

5.2 Introduction

Ambient particulate matter (PM) pollution is a major environmental health risk, responsible for over 4 million premature deaths annually.[152] Urban populations are particularly affected. In 2010, premature deaths due to air pollution were about 50% more common in urban than in rural settings, and this could increase to 90% by 2050 if urban populations and pollutant concentrations both continue to grow at current rates.[8]

Although air pollution measurements are needed to address this health crisis, ground-based air quality monitoring is generally sparse or completely lacking throughout the world.[25,153] In even the most developed air quality monitoring networks, such as those operated in London and Hong Kong, the spatial density of sampling sites is less than 1 per 10 km^2.[42] In contrast, primary air pollutant concentrations can fluctuate by an order of magnitude over distances of just ~0.1 to 1 km in urban settings.[43,45,46,154-157] Consequently, the pollution exposures of urban community members may not be well described by the concentrations measured by traditional air monitoring at central sites.[22,23,158]

New low-cost PM sensors that infer particle mass from a simple light scattering measurement are emerging[56-61], and together with inexpensive electrochemical sensors that measure gaseous pollutants,[53-55,62,132,159,160] are being deployed in urban air quality monitoring networks that provide much greater spatial resolution and coverage than is attainable with expensive regulatory-grade monitors.[22-24,49,130,154] However, there is a gap in the market for low-

cost sensors that discriminate among the components of PM. With this in mind, Caubel et al. developed the Aerosol Black Carbon Detector (ABCD).[161] Black carbon (BC) is an important component of PM emitted during the incomplete combustion of biomass and fossil fuels (e.g., diesel engines) that is strongly linked to adverse health impacts.[3,4,63-65,67,72,153,162] BC is also a short-lived but potent climate forcer.[63,73,136] Thus, a low-cost BC sensor would be a valuable addition to emerging sensor networks for monitoring combustion emissions and quantifying their impact on human health and the environment.[68,70-73,136]

This chapter presents the 100×100 BC Network, a deployment of ABCDs across 100 sampling sites in West Oakland, California, for a period of 100 days (from May 19 to August 27, 2017). In partnership with several community organizations, residents and businesses were recruited to host ABCD units at 100 distinct sampling locations in the 15 km^2 neighborhood.[163] The resulting average network density of 6.7 sampling sites/km^2 was ~100 times greater than that currently achieved by traditional regulatory networks.[25,42] Together, the networked sensors generated a map of BC concentrations with high spatial and temporal resolution. This chapter describes the operation and maintenance of the 100×100 BC Network, and presents major spatiotemporal BC concentration trends observed during the campaign in West Oakland.

5.3 Materials and Methods

5.3.1 Aerosol Black Carbon Detector (ABCD)

Caubel et al. provide a thorough description of the ABCD's operating principle, design features, and measurement performance.[161] A brief overview is also presented here. The ABCD is an aerosol photometer that continuously draws air through a white fibrous filter, measures the rate of 880-nm radiation attenuated by BC accumulating on the filter, and computes the corresponding BC mass concentration in the air. Housed in a compact weatherproof enclosure, the ABCD incorporates a 2G cellular modem for wireless communication and draws power from an onboard battery and photovoltaic (PV) panel (Figure D1). A key feature of the ABCD is a software algorithm that diminishes the sensor's temperature sensitivity, thereby increasing the precision and accuracy of BC mass concentrations measured outdoors when ambient temperature fluctuates.

For this study, we constructed 128 ABCDs to enable collocation at some of the 100 sites and replacement in the event of sensor loss or damage. Prior to network deployment, all ABCDs were operated outdoors at one of three validation sites (Figure D4). At each validation site, a commercial BC monitor (Model AE33, Magee Scientific) was housed indoors, sampling outdoor air through a dedicated conduit. ABCDs that agreed closely with the collocated AE33s were certified for network deployment, while faulty sensors were repaired and returned to the validation site. Collectively, the validated ABCD fleet demonstrated an average precision and accuracy, expressed in terms of mean absolute percentage error, of 8.5 ± 0.7% relative to the fleet average data and 26 ± 1% relative to the AE33 data, respectively (fleet-average ± 90% confidence interval). A thorough overview of the fleet's validation and measurement performance is provided in Appendix D.

5.3.2 Network Deployment in West Oakland, California

West Oakland is a mixed residential/industrial neighborhood in the San Francisco Bay Area that is adjacent to regional port and rail yard facilities and surrounded by major highways.

As such, the air quality in this community of 42,000 residents is influenced by BC emissions from heavy-duty diesel trucks, locomotives, and marine vessels.[163-165] In partnership with the Environmental Defense Fund (EDF), the Bay Area Air Quality Management District (BAAQMD), the Port of Oakland, and the West Oakland Environmental Indicators Project (WOEIP), 55 West Oakland residents, 19 local businesses, and 8 community organizations (such as schools) were recruited to host ABCDs. Hosts were provided with a $50 gift card for each month of their participation. We also located sensors along a main road on the Port of Oakland boundary and at two BAAQMD air monitoring stations. All sampling sites are shown in Figure 25 and categorized by host type on the map in Figure D3.

Most ABCDs were zip-tied to accessible fences, porches, or trees on the front, street-facing side of residences and businesses, approximately 1.5m above the ground (e.g., head height). Mounting sites were chosen to maximize the insolation of the sensor's PV panel – facing south, and away from shaded areas whenever possible. Seven hosts provided access to an outdoor power outlet, allowing those sensors to be plugged in. At 12 network sites (Figure D4), ABCDs were collocated in pairs, and each sensor in the pair set to different sample flow rate. The collocation data was used to verify the sensors' precision and allowed for the investigation of BC measurement artifacts (discussed below). At the three field validation sites mentioned above, we collocated two ABCD pairs (four sensors total) with the commercial BC monitor.

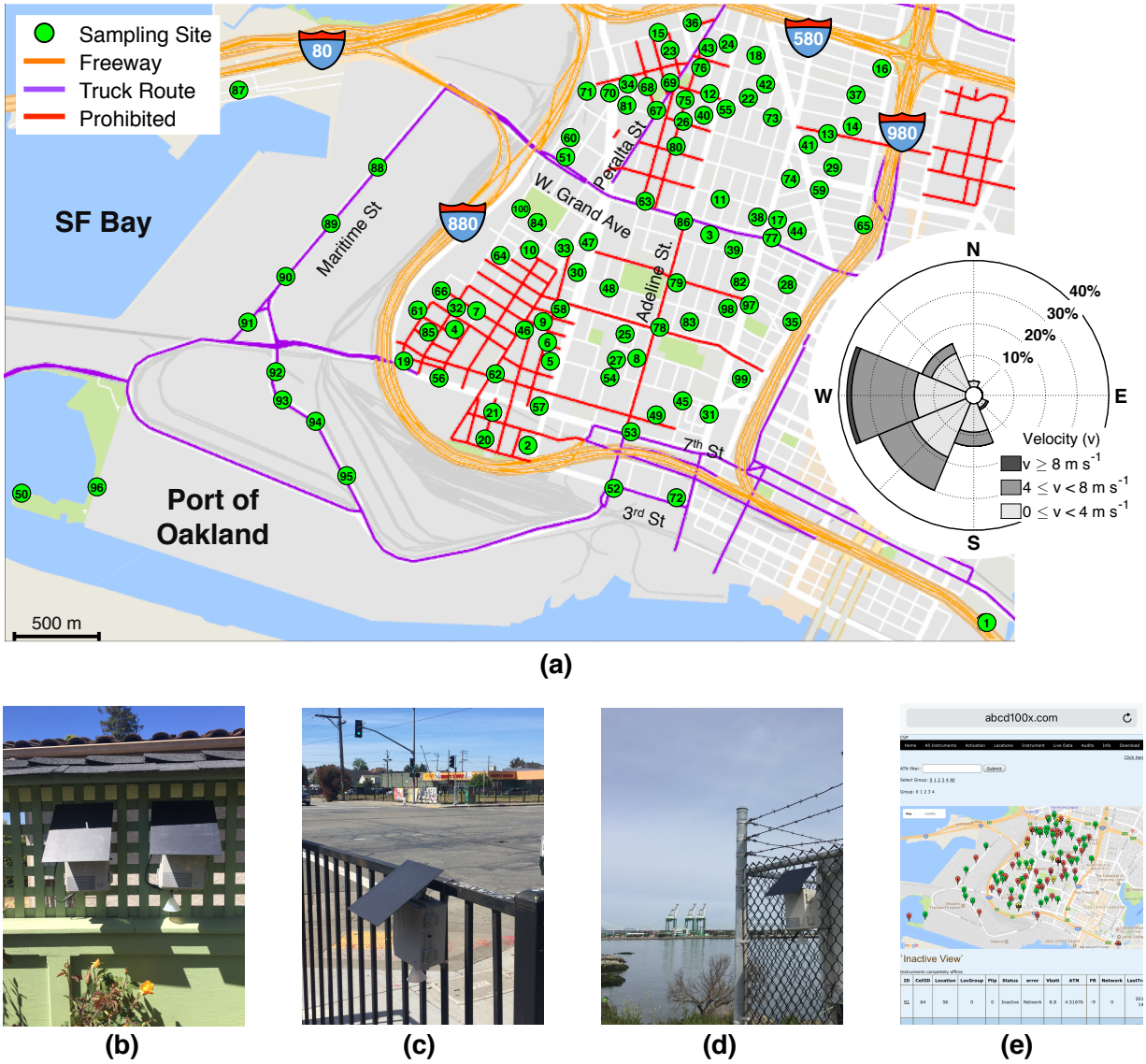

Figure 25. (a) Map of West Oakland indicating the location of all sampling sites in the 100×100 BC Network in relation to designated truck routes, freeways, and streets where truck traffic is prohibited (as provided by the City of Oakland). A wind rose of hourly wind direction and velocity measured at the BAAQMD monitoring station (site 3) during the 100-day study is also shown. Pictures of ABCDs deployed at: (b) a residential collocation site, (c) a traffic intersection, (d) an upwind site near the San Francisco Bay. (e) Screenshot of sensor status map from the network maintenance website, as accessed on a mobile device in the field.

5.3.3 Data Transmission, Management and Analysis

Every hour, each ABCD in the 100×100 BC Network wirelessly transmitted sixty 1-minute average BC concentration values to an online database purpose-built for this study. Onboard SD cards from each ABCD were also collected regularly and the data was uploaded to the online database. The SD card data, recorded at a measurement rate of 0.5 Hz, was averaged

down to a 1-minute time base and combined with the data collected wirelessly. During periods when redundant data was collected, SD card data was retained and wireless data was discarded. This combined dataset, containing ~15 million lines of 1-minute data, was filtered programmatically to remove erroneous or inaccurate BC mass concentrations recorded by sensors suffering from pump failures, excessively loaded filters, or other technical issues. The filtered dataset was then manually inspected using a custom Graphical User Interface (GUI) to remove any remaining erroneous measurements and validate the programmatic filtering. After manual inspection, BC data was corrected for a filter loading artifact,[166,167] and errors in sample flow rate measurements. The corrected 1-minute data was averaged down to an hourly time base using a 90% data retention threshold, and so hourly averages calculated using < 54 1-minute measurements were discarded. BC concentrations measured simultaneously by collocated ABCD units were averaged, such that there is a single BC time series for each sampling site in the network. The resulting dataset consists of up to 240,000 hourly BC mass concentration measurements collected at 100 sampling sites over 2400 hours (100 days). This hourly dataset is used for all analyses presented in this study. A more detailed overview of the programmatic filtering, GUI, and data corrections is provided in Appendix D.

5.3.4 Network Operation and Maintenance

The study team maintained the ABCDs with the aid of a custom-made website that displayed near real-time diagnostics from all sensors in the network and issued alerts on an interactive map (Figure 25(e)), such as low battery voltage or high filter loading. Routine maintenance included replacement of fibrous filters and downloading SD card data. High filter loading alerts were issued when optical attenuation exceeded a value of 80 (relative to a clean-filter value of 0), consistent with common practice.[166,167] The required frequency of filter replacement was twice a week for sensors located along busy truck routes and once every 1-2 weeks for sensors in residential areas. In most cases, PV panels fully recharged the onboard batteries every day. At a few locations, insufficient solar insolation or theft of PV panels required that discharged batteries be replaced on a weekly basis. Additionally, field maintenance included sensor flow rate verification and recalibration, performed using a primary standard air flow calibrator (Gilian, Gilibrator-2). Many ABCDs required repair during the study, as discussed below. Following maintenance, team members used the website to catalog activity notes and reactivate the sensors for normal sampling.

5.3.5 Network Site Categorization

To analyze BC concentration trends in the context of surrounding land use and location relative to prevailing winds, most sampling sites are classified into six distinct location categories: (1) Upwind, (2) Residential, (3) Industrial, (4) Near Highway, (5) Truck Route, and (6) Port, as shown in Figure 26. Since winds predominantly come from the west (Figure 25), the 3 western-most sampling sites in the network are assigned to the upwind category. Similarly, 8 sites located on/near Maritime Street are assigned to the Port category. Of the 100 sites in the network, 88 were located within the West Oakland neighborhood, the area bounded area on all sides by freeways in Figure 25(a). Using a map of West Oakland's land use designations (Figure D13), 27 sites were categorized as residential, 8 were categorized as industrial, 10 were identified within 50 meters of designated truck routes, and 11 were identified within 150 meters of freeways (Figure 25). In total, 68 sampling sites were assigned to represent the 6 location

categories. Other sites in the network remain uncategorized because they did not meet any of the individual criteria detailed above. Additional details on site categorization are provided in Appendix D.

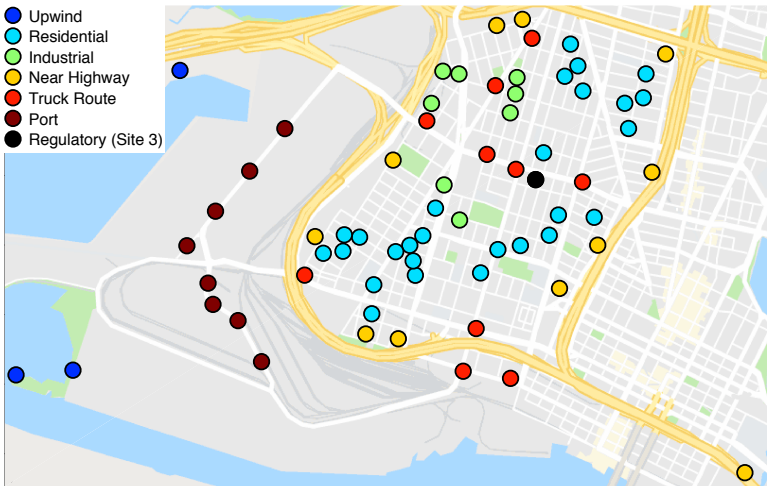

Figure 26. 100×100 BC Network sites assigned to each of the six location categories: (1) Upwind, (2) Residential, (3) Industrial, (4) Near Highway, (5) Truck Route, and (6) Port. The location of the BAAQMD's regulatory monitoring station (site 3) in West Oakland is also shown.

5.4 Results And Discussion

5.4.1 Network and Sensor Performance

The network data collection performance over the 100 days is illustrated in Figure 27. 84.0% of the possible 240,000 hourly BC concentration measurements were successfully collected and validated. The inability to continuously deploy working sensors at all 100 sampling sites was the greatest single cause of data loss (6.7%). Sites were increasingly left unmonitored over the 100 days (Figure D15), mostly because nearly half of the sensors' miniature vacuum pumps failed and could not all be readily replaced. Whereas only 1 sampling site was left unmonitored on the first day of the network (May 20), over 30 sampling sites were left unmonitored by the end of the deployment period (August 27). The high rate of pump failure is likely due to operation past the 3000-hour rating and/or outside the recommended temperature range (10 to 30°C). Other sensor components, such as flow sensors and control boards, failed much less frequently than the pumps. However, the lack of replacement pumps was not responsible for all incomplete site deployments. For instance, one site (99) was left unmonitored for the last 70 days of the campaign because the residential host dropped out of the study, and two sites (72 and 100) were discarded from the network following the theft of several sensors (Figure D14).

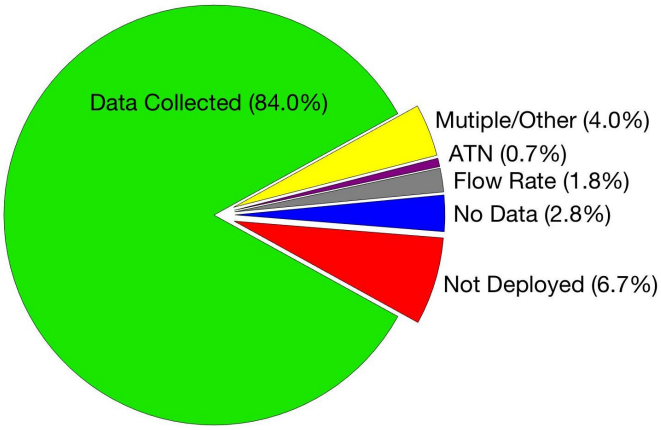

Figure 27. Network data collection performance, shown as the fractions of hourly BC mass concentration measurements collected, lost, or discarded over the 100-day campaign. All percentages are evaluated relative to the 240,000 hourly-average BC measurements ideally generated by 100 sampling sites over 100 days (2400 hours).

A small amount of data (2.8%) was lost to technical errors preventing sensors deployed in the network from measuring or recording BC mass concentrations. Missing measurements were often the result of hardware failures (e.g. inadvertent disconnection of electrical components) or sensors losing power as inclement weather or poor sensor placement inhibited proper PV panel insolation. Furthermore, some BC measurements were neither wirelessly transmitted nor collected from the SD cards, as some sampling sites had poor cellular reception and the corresponding SD cards were accidentally overwritten.

Using programmatic filtering, inaccurate or invalid BC mass concentration measurements were detected and removed from the dataset. Sample flow rate measurements deviating from the nominal set point by ≥ 3 cc min^{-1} were detected in 1.8% of the hourly dataset, with pump failures responsible for most flow rate errors. Less than 1% of hourly BC mass concentrations were measured with excessively loaded aerosol filters (optical attenuation > 100) and discarded. The programmatic data filter was also configured to detect additional sensor errors like loss of digital communication with the optical cell and instances of multiple errors, while the GUI was used to manually remove any remaining invalid measurements that were not detected programmatically. For example, nearly half of the data from site 76 was manually discarded because the ABCD's inlet tubing was accidentally disconnected and air was not drawn through the optical cell; otherwise the sensor was operating nominally, so no errors were detected programmatically. Collectively, these remaining faults affected 4% of the hourly measurements.

Since collocated ABCD measurements are averaged to yield a single BC time series at each site, the data collection rate was very high for the network's 12 collocation sites. At each of the three validation sites (1, 2, and 3) where four ABCDs were collocated, at least one sensor was operating correctly for over 95 of the 100 days (Figure D14 and Figure D15).

5.4.2 Black Carbon Concentrations in West Oakland: Spatiotemporal Trends and Outliers

Diurnal and weekly patterns in BC concentrations at the 100 sampling sites varied depending on surrounding land use, local traffic patterns, and prevailing wind direction, as illustrated in Figure 28 and Figure 29. The lowest concentrations were measured at the 3 upwind

sites (50, 87, and 96) located near the San Francisco Bay. Average evening concentrations at these sites were as low as ~0.2 µg m^{-3} and daytime concentrations approached 0.4 µg m^{-3}. All other category-averaged BC concentrations were higher. Thus, these upwind concentrations represent the regional background on top of which dynamic, local emission sources build.

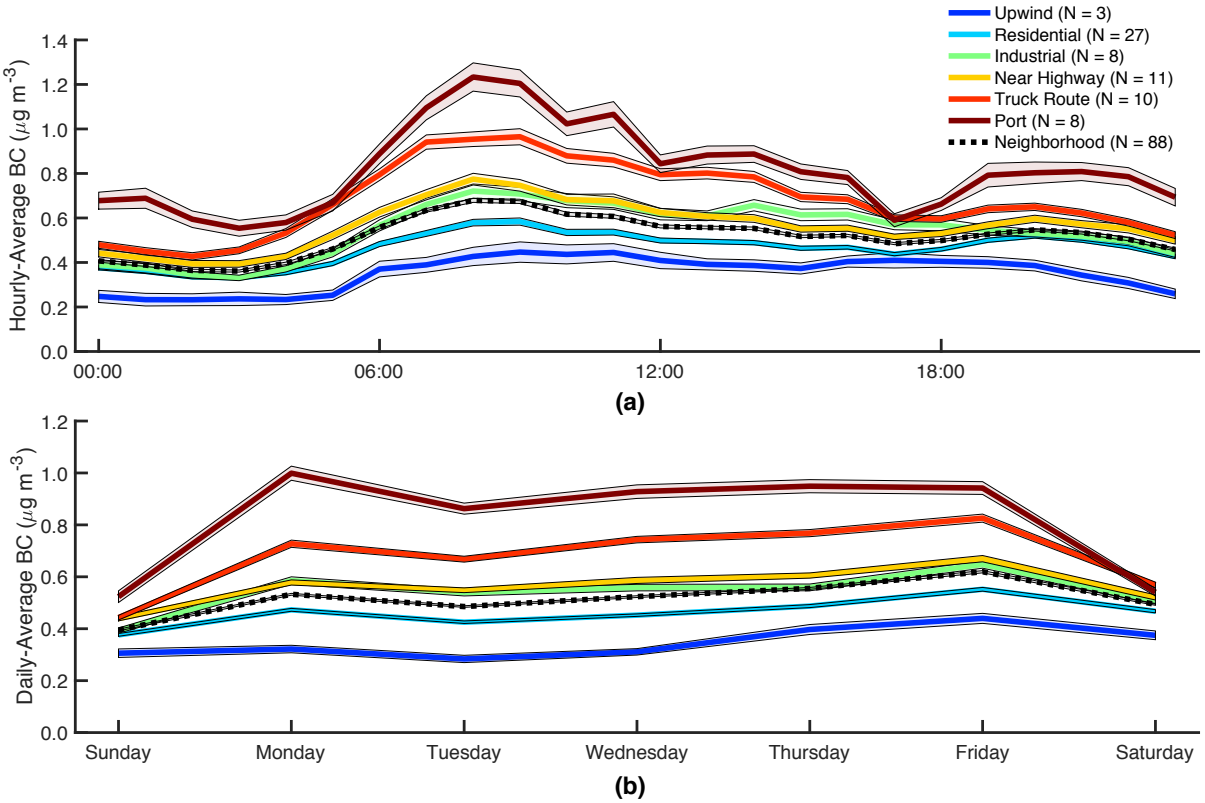

Figure 28. BC concentration trends at the six location categories: (a) Hourly-average BC concentrations over the diurnal cycle, (b) Daily-average concentrations over the weekly cycle. Bold lines represent the mean of hourly- or daily-average BC concentrations measured at all sites assigned to each location category and shaded areas representing the corresponding 90% confidence intervals. Average BC concentrations are also shown for the West Oakland neighborhood as a whole. The number of sites assigned to each category (N) is provided in the legend. Plot generation details are provided in Appendix D.

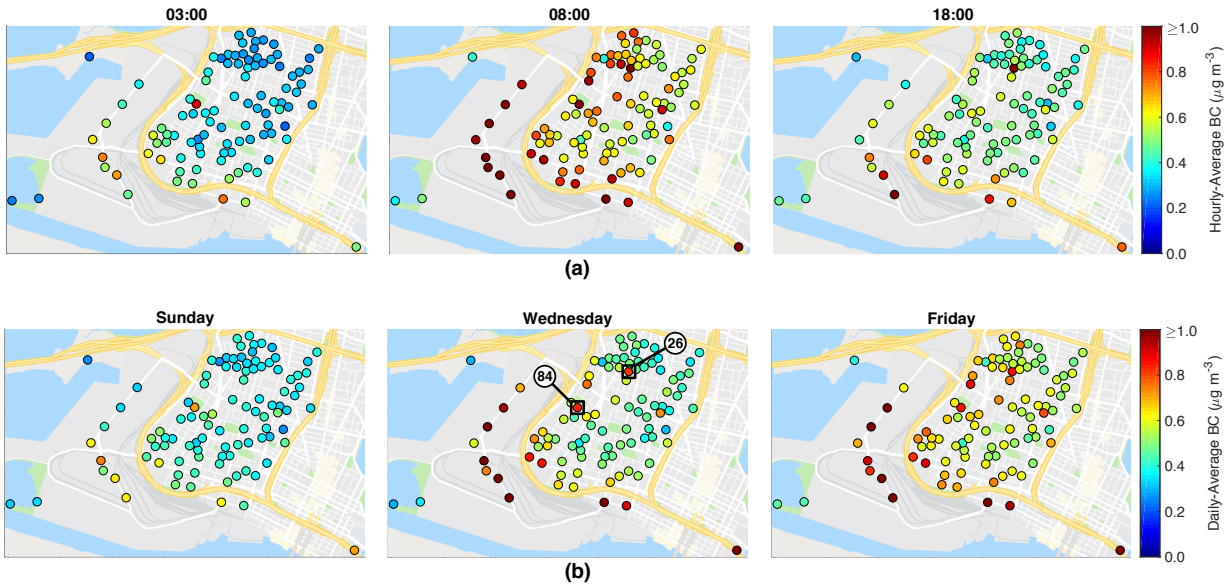

Figure 29. BC concentrations in West Oakland over the 100-day sampling campaign: (a) Hourly-average BC distributions measured at 00:00, 8:00 and 18:00; (b) Daily-average distributions measured on Sunday, Wednesday, and Friday. Some sampling sites were shifted slightly from their true geographical location to ensure that all BC concentration markers are clearly visible.

BC concentrations were highest and most variable along Maritime Street in the Port of Oakland, where ABCDs were located a few meters away from heavy-duty diesel trucks accessing Port terminals. Truck traffic volume on this road is high, with ~7,300 trucks transiting through the Port on an average weekday.[168] BC concentrations in the Port were 200 ± 10% higher than those measured at the upwind sites (mean difference of category-average concentrations measured at each hour of the 100-day campaign ± 90% confidence interval). The Port-category BC concentrations varied in accordance with business operations. Hourly BC concentrations were lowest at 3:00 (0.55 ± 0.04 μg m^{-3}) when terminals were usually closed, peaked as terminal gates opened around 8:00 (1.23 ± 0.06 μg m^{-3}), and gradually decreased to a daytime minimum at 17:00 upon closing of the dayshifts.[169,170] Accordingly, Shah et al.'s mobile monitor shows that the primary fraction of organic aerosols in the Port of Oakland is ~20% at 8:00 and increases to > 40% from 11:00 to 17:00, as local daytime emissions build on top of the nighttime background.[171] Similarly, daily-average concentrations were about twice as high on Monday (1.00 ± 0.03 μg m^{-3}) than on Saturday and Sunday (~0.53 ± 0.02 μg m^{-3}). From 19:00 to 1:00, elevated BC concentrations ranging from 0.70 ± 0.09 to 1.3 ± 0.2 μg m^{-3} were recorded along three and four lane sections of Maritime Street (sampling sites 90, 92, 94, and 95), as a result of truck activity associated with some terminals' nighttime shifts. BC concentrations during the nighttime shift were higher at sites located along the multilane section of Maritime Street, where trucks were observed to park (Figure D16), than at other sections of the same street (≤ 0.7 μg m^{-3}) where trucks cannot park (sites 88, 89, 91, and 93, Figure D17). Although total port-related truck activity levels are likely much lower at night than in the daytime, wind speeds and atmospheric mixing heights are also lower and may also contribute to the elevated evening concentrations (Figure D18).

In the West Oakland community, hourly BC concentrations measured at residential sites were 29.1 ± 0.6% and 9.7 ± 0.9% lower than those measured near designated truck routes and highways, respectively, and 67 ± 5% greater than those measured at the three upwind sites. It is estimated that ~7,200 diesel trucks operate on the neighborhood's designated routes on an average weekday, roughly half of which are associated with the Port of Oakland.[168] BC concentrations measured near designated truck routes were 150 ± 10% greater than those measured upwind, and generally mirror the diurnal and weekly patterns observed at the Port. However, concentrations measured along designated truck routes increased only slightly from 18:00 to 21:00, while Port concentrations rose sharply. After 21:00, nighttime BC concentrations measured near most truck routes and industrial sites were similar to those measured in residential areas nearby, indicating that most local commercial/industrial activity subsided. Outside the West Oakland community, elevated evening concentrations persisted at site 52, located on a designated truck route near I-880 and a major Port entrance, and site 1, directly downwind of I-880. These indicate that nighttime truck traffic is mainly restricted to the highway and nearby Port access corridors, and generally avoids designated routes in the neighborhood.[168]

Neighborhood concentrations at most sites decreased overnight and reached a diurnal minimum at 3:00 (Figure 28). In the absence of nighttime emission sources, a smooth gradient of decreasing BC concentrations from the southwest to the northeast of the neighborhood was observed, in the downwind direction from I-880 and the Port. Site 84 stands out as one location within the freeway-bounded neighborhood where middle-of-the-night concentrations were unusually elevated (Figure 29(b)). BC concentrations at this site did not follow the generally observed diurnal and weekly trends. Rather, concentrations were higher at night than during the day, and daily-average BC concentrations only decreased by ~10% over the weekend, as opposed the > 40% decrease typically measured at other neighborhood sites (Figure 30). Furthermore, BC concentrations at this site were 120 ± 20% greater than those measured at nearby site 100, although it was located 150 meters further from I-880 (mean difference of hourly site concentrations measured over the 100-day campaign ± 90% confidence interval). This hyperlocal elevation in BC concentrations can most likely be attributed to activity at a trucking company directly across the street (Figure D19), where residents noted the presence of refrigerated trucks that park overnight and power their refrigeration units using auxiliary diesel ('reefer') engines. Goods may need to be refrigerated over the weekend, resulting in the consistently high BC concentrations observed throughout the week.

In the morning, hourly-average BC concentrations rise sharply throughout West Oakland, usually reaching a diurnal maximum during the rush hour at 8:00 (Figure 28). Strong spatial gradients in daytime concentrations were observed along streets where trucks are permitted, particularly near major intersections or access points to the Port and surrounding highways. For example, sites 52 and 72 are < 500 m apart on the same designated truck route (3rd Street), but concentrations were 60 ± 2% higher at site 52 because it was located on a busy four-way intersection near a major Port entrance and access ramps to I-880. Similarly, BC concentrations measured from 7:00 to 19:00 at site 77 on a busy truck route intersection were 180 ± 20% greater than that measured on a residential street ~75 m away (site 17). After the ABCD at industrial site 70 was stolen from a fence ~2.5 m from Mandela Parkway, the replacement sensor was mounted only 25 m away (~20 m from the roadway) and recorded BC concentrations that were 28 ± 4% lower (Figure D21 and Figure D22). Elevated concentrations measured near highways also decay sharply over short distances – Sampling sites 20 and 21 were located only ~200 m apart on

the same residential street downwind of I-880, but daytime BC concentrations were 30 ± 6% higher at the site closest to the highway (site 20).

In contrast to these examples, BC concentrations in areas where truck traffic is prohibited are usually lower and more uniform. For example, sites 78 and 79 are located along Adeline Street, an arterial road where trucks are not allowed, and daytime-average concentrations were identical (0.57 ± 0.02 μg m^{-3}, the average ± 90% confidence interval of all hourly measurements collected from 7:00 to 19:00 at each site). One notable exception is industrial site 26, where average BC concentrations were 130 ± 20% greater than that measured < 100 m away at site 75, although both sites were on the same residential street where trucks are not permitted. These elevated BC concentrations follow a diurnal pattern consistent with normal business hours (Figure 30), and so are likely the result of emissions from industrial processes (e.g., smelting) and truck traffic associated with a metals recycling plant located ~100 m upwind of site 26 (Figure D20).[172]

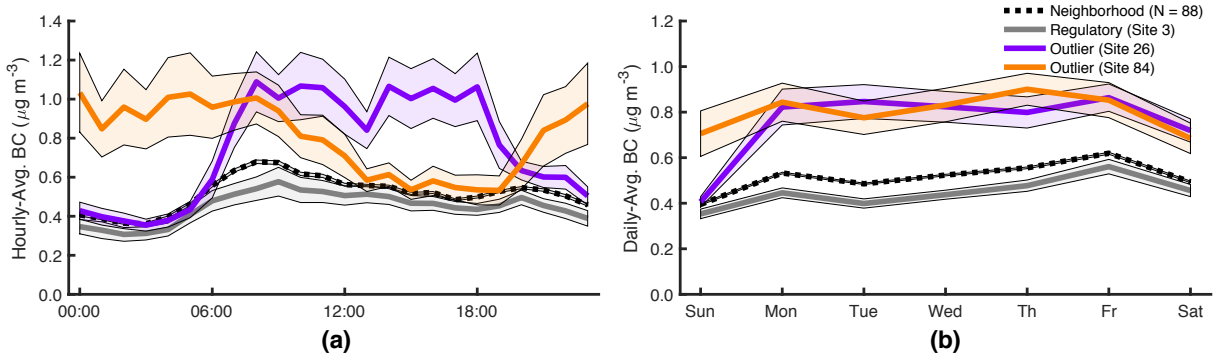

Figure 30. Average BC concentration trends in the West Oakland neighborhood, at the BAAQMD regulatory monitoring location (site 3), and two sites that stand out amongst the others: (a) Hourly-average BC concentrations over the diurnal cycle, (b) Daily-average concentrations over the weekly cycle. Bold lines represent the mean of hourly- or daily-average BC concentrations measured at each site or set of sites, with shaded areas representing the corresponding 90% confidence intervals. Site ID numbers and the number of sampling sites in the neighborhood (N) are indicated in the legend.

5.4.3 Air Quality Monitoring Networks: Lessons Learned and Future Work

The spatiotemporal variability of BC concentrations measured by the 100x100 BC Network in West Oakland (Figure 28 and Figure 29) illustrates the high spatial density of fixed-location monitors required to accurately capture the heterogeneous air pollution distributions typical of urban settings. Especially for primary air pollutants, it is not surprising that a single monitor cannot tell the whole story: BC concentrations at site 3 – which is collocated with the local air district's sole monitoring station in West Oakland – are 30 ± 1% lower than those measured < 400 m away at site 77, located < 5 m downwind of a busy truck route intersection. The sharp decay in BC concentrations often observed over distances of 100 m or less demonstrate that sensors must be very close to combustion sources to quantify their influence on local air quality.

Even with inexpensive sensors, the cost of dense monitoring networks can build quickly, especially the effort related to data management, quality assurance, and interpretation. However, the diurnal and weekly BC concentration cycles tend to be highly repeatable, suggesting that long-term deployments may not be necessary to characterize periodic patterns. Figure D23 and

Figure D24 show that 2 to 4 weeks of continuous BC concentration measurements are sufficient to calculate hourly- and daily-average values very similar to those derived over ~14 weeks. These results suggest that a deployment of fewer sensors for shorter durations (several weeks) might be equally informative if the sensors were regularly repositioned to new sampling sites. However, it should be noted that since BC concentration levels are highly seasonal,[173] the trends observed here strictly apply to the summertime in West Oakland.

Air quality monitoring with mobile sampling platforms is a complementary approach that offers greater spatial resolution but less temporal coverage.[174-176] Apte et al. mapped concentrations of BC and other pollutants in West Oakland using cars equipped with air quality monitoring equipment.[155] Similar to our study, they find high spatial variation in BC concentrations and identify the area around site 26 (the metals recycling plant) as a 'hotspot' where BC concentrations are particularly elevated. However, the mobile platforms didn't operate at night and on weekends and, therefore, did not produce diurnal or weekly trends nor reveal unusually elevated evening BC concentrations, such as that associated with truck refrigeration activity at site 84. This lack of temporal coverage is worrisome, as Figure 28 illustrates that BC concentrations at the 6 location categories in West Oakland fluctuate by 75% to 120% over the diurnal cycle, while daily concentrations vary by 50% to 90% during the week.

Analytical methods, such as land use regression (LUR) models, are being developed to extrapolate highly resolved pollution distributions from sparse datasets.[44,46,177] Nevertheless, these analytical methods cannot account for the systematic loss of data over certain time periods (e.g. nighttime) or geographical locations. Therefore, time-continuous air pollution records from distributed networks of low-cost sensors should be combined with spatially-resolved mobile measurements, effectively leveraging the advantages of each approach to produce more comprehensive and representative datasets that can be better analyzed using LUR and other models.[178-180] Using a versatile portfolio of complementary monitoring and modeling methods, it will be practical and economical to describe air pollution more granularly than ever before, and leverage the insights to mitigate the severe health impacts resulting from air pollution exposure.

Chapter 6 – Conclusion

6.1 Summary of Major Findings

Traditional approaches to air quality management are ill-suited to mitigating emissions from today's deadliest polluters, and monitoring air quality in a rapidly urbanizing world. A new generation of technologies and policies is emerging to address the growing health threat posed by air pollution, and this dissertation contributes to this effort. Harmful emissions from biomass cooking fuels are the world's greatest environmental health risk, and yet scientific research on the development of clean biomass cooking technologies remains scarce. Using the MOD stove, my dissertation attempts to fill this gap in the scientific literature. To the best of my knowledge, the MOD stove is the first continually fed, wood-burning cookstove to reduce mass emissions of CO, $PM_{2.5}$, and BC by 90% relative to a traditional cooking fire. The study demonstrates that wood combustion is highly sensitive to key secondary air injection design parameters, such as the location and arrangement of the secondary air jets in the combustion chamber. As a result, an experimental optimization procedure is developed to identify and validate cookstove designs that are both clean and efficient. Using the experimental data, crucial secondary air injection design principles are illustrated and explained, so they can be applied to the development of future cookstoves. Although the MOD stove significantly reduces the total mass of $PM_{2.5}$ emitted during cooking, size-resolved $PM_{2.5}$ measurements reveal that more ultra-fine particles (UFPs) are generated (relative to a traditional cooking fire). UFPs are particularly harmful to the human respiratory system, and so adverse health impacts could potentially persist despite the reduction in $PM_{2.5}$ mass emissions.

Though the MOD stove effectively demonstrates that secondary air injection can significantly reduce emissions from a wood-burning cookstove in the laboratory, it is an experimental platform wholly unsuited for mass production or deployment. Using an updated MOD stove design, I characterize the practical secondary air injection design requirements (e.g., flow rate, pressure, and temperature) to achieve $\geq$ 90% emissions reductions. With this experimental performance data, I identify inexpensive (<$10) miniature fans and blowers that meet the MOD stove's secondary flow rate and pressure requirements. However, only 2% of over 1000 models investigated meet all performance requirements, illustrating the importance of conducting thorough experimental characterization prior to engineering system components. I also show that these fans and blowers can be powered using low-cost thermoelectric modules mounted to the side of the stove. In this way, the study demonstrates the availability of low cost hardware capable of driving a stand-alone (independently powered) secondary air injection system that practically and effectively reduces harmful smoke emissions, while also improving cooking performance.

While emission reduction technologies like the MOD stove are critical to improving global air quality, their implementation should be informed, focused, and validated using accurate measurements of ambient air pollution concentrations. Distributed networks of low-cost sensors are emerging to address the lack spatial coverage and resolution associated with traditional air quality monitoring techniques, but no low-cost sensors are currently available to monitor BC, an important component of combustion PM pollutant closely linked to adverse health and environmental impacts. In order to fill this space in the field, I designed and developed the ABCD: the first low-cost BC sensor specifically intended for long-term outdoor deployments in spatially dense, wireless sensor networks.

A fleet of over 100 ABCDs was operated outdoors, and their measurement performance was comparable to that of a commercial BC monitor collocated inside a regulatory air quality monitoring station. The fleet-average precision and accuracy, expressed in terms of mean absolute percentage error, are 9.2 ± 0.8% (relative to the fleet average data) and 24.6 ± 0.9% (relative to the commercial BC monitor), respectively (fleet-average ± 90% confidence interval). The validation study demonstrates that the ABCD's unique temperature compensation algorithm and hardware features provide regulatory-grade BC mass concentration measurements in tough operational conditions that debilitate existing instruments.

The validated fleet of ABCDs was deployed to 100 sampling sites throughout West Oakland, California. This air quality network, dubbed the 100x100 BC Network, is likely the most extensive and spatially dense fixed-site monitoring effort ever undertaken. The distributed fleet of sensors successfully collected 84.0% of the 240,000 hourly-average BC concentration measurements ideally generated at 100 sampling sites over 100 days (2,400 hours). Most missing data resulted from the widespread failure of the sensors' vacuum pumps, while all other hardware and data collection methods proved to be extremely reliable. The sensor network shows that BC concentrations in West Oakland vary greatly over short distances and timespans, and are strongly dependent on surrounding land use, traffic patterns, and location relative to prevailing winds. For example, average BC concentrations are highest in the Port of Oakland, largely as a result of diesel emissions from heavy truck traffic nearby. Using these general trends as a reference, sampling sites were detected with unusually elevated BC concentrations. By analyzing diurnal and weekly concentration trends at these sites, I identify likely polluters nearby. For instance, I show that high nighttime concentrations near a neighborhood park are likely the result of refrigerated trucks parked and idling at a facility across the street. In this way, the 100x100 BC Network demonstrates the value of distributed networks of low-cost sensors at fixed monitoring sites to accurately characterize urban air pollution trends, and provide actionable information to identify and mitigate local polluters.

As a whole, the BC concentration maps suggest that a minimum spatial resolution of around 100 m is required to completely capture dynamic BC concentration gradients typical of urban environments like West Oakland. However, the collection of continuous pollution records with this degree of spatial resolution may be redundant over long periods, as BC concentrations at each sampling site tend to follow highly repeatable, periodic trends over the diurnal and weekly cycles. At selected sites, it was shown that 2 to 4 weeks of continuous BC concentration measurements are sufficient to derive hourly- and daily-average trends very similar to those resulting from the entire ~14 weeks of continuous monitoring. These types of practical observations gleaned from the 100x100 BC Network will help to inform and improve the design and development of future air quality monitoring efforts.

6.2 Future Research

Although both the MOD stove and the ABCD have been thoroughly validated, the impact of these technologies is ultimately dependent on their widespread utilization and integration within existing efforts to address the adverse health and environmental impacts outcomes associated with air pollution. Below, I outline the next phases of development and implementation.

6.2.1 Modular Secondary Air Injection Cookstove Platform

Though the MOD stove reduces $PM_{2.5}$ mass emissions by 90% relative to a traditional cooking fire, the generation of UFPs persists and must be mitigated. Future studies of secondary air injection in wood-burning cookstoves should investigate the chemical composition of these UFPs using an aerosol mass spectrometer or other analytical methods. Using this speciation data, it will be possible to better identify and actively target the physical mechanisms responsible for UFP formation. For example, past research has shown that particulate emissions from biomass stoves with secondary air injection stoves are largely inorganic, consisting of salts and heavy metals that volatilize from the fuel bed and nucleate into particles as the volatile vapors cool in the exhaust.[37,40,76,93] In order to impede this formation pathway, methods should be developed to cool the fuel bed below the volatilization threshold of inorganic species, while simultaneously maintaining sufficient combustion temperatures to ensure complete oxidation of the gas-phase fuel. In this way, information on the chemical composition of UFPs can be effectively leveraged to enable further emission reductions.

The second design iteration of the MOD stove shows that low-cost hardware is available to meet the secondary air injection flow requirements, but does not actually implement or validate this hardware experimentally. The next logical step in the MOD stove's development is to integrate a low-cost blower and thermoelectric generator that independently drive the secondary air injection flow needed to achieve > 90% emission reductions relative to a traditional cooking fire. This next iteration of the MOD stove design should remain modular, such that different combinations of blowers and thermoelectric generators can be characterized rapidly, and an optimal configuration determined. By integrating this hardware and validating its operation experimentally, the MOD stove will be a robust, stand-alone device that can be practically adopted in the field.

Though it is crucial to properly validate clean cooking technologies in the laboratory, the mitigation of health impacts is ultimately contingent on households' willingness to welcome these technologies into their homes and kitchens. Many clean cookstoves have been designed and distributed, but studies show that they often aren't widely adopted in the long term.[181-184] Cooking styles and fuel preferences vary widely around the world, and so cookstoves that may have proven popular in one region, can be rejected in another. Another common problem with cookstove adoption is 'stacking', wherein households use the clean cooking technology in conjunction with a traditional fire, and so harmful smoke exposure does not diminish.[183,184] With the MOD stove's emissions reduction technology fully developed and validated, implementation studies should be conducted to identify communities whose cooking needs are fully met by the MOD stove's fundamental design architecture. For example, regions where firewood is scarce would not be appropriate. Similarly, regions where local cuisine is not primarily dependent on cooking pots, such as Central American countries where flat-topped 'plancha' stoves are prevalent, should also be excluded from consideration. With appropriate target communities identified, user-centric design studies should be conducted to determine whether stove modifications could significantly improve adoption. [185,186] For example, the MOD stove should be adapted to better accommodate local pots and cookware. Since the MOD stove was originally derived from the Berkeley Darfur Stove (BDS), it currently accommodates the same round-bottomed, Darfuri-style pot, which is unlikely to be culturally appropriate in other regions.

During the initial distribution process, quantifiable measures of the cookstove's adoption and health impacts should be collected, as user surveys are often skewed by courtesy bias and

other factors.[184,187] For example, stove-use monitors are now increasingly emerging to directly measure the frequency and duration of cooking with improved technologies. Furthermore, the ABCD and other low-cost air quality sensors should also be deployed to accurately quantify any potential improvements in air quality, and help determine whether traditional cookstove use persists.[187-189] By integrating sensor data and direct feedback from local stakeholders into the design and dissemination process, an iterative and interactive design loop is established to help ensure that clean cooking technologies developed in the laboratory can more effectively meet the cultural and practical expectations of host communities who currently suffer from chronic smoke inhalation in their homes. Only once adoption and integration have been firmly established should a cookstove design be finalized and mass-produced for widespread distribution in the target community for which it has been optimized.

6.2.2 Aerosol Black Carbon Detector

Though the 100x100 Network demonstrated the ABCD's core ability to gather accurate BC measurements over long-term outdoor deployments, it also revealed several major weaknesses in the sensor hardware and network maintenance methods. The ABCDs' rotary vane pumps were the primary cause of hardware failure, and so other devices should be investigated to draw a continuous sample flow of air through the instrument. Of particular interest are miniature piezoelectric blowers currently emerging on the market.[190] Piezoelectric blowers have very few moving parts, and so may prove to be more durable than traditional diaphragm or rotary vane pumps. Furthermore, they are extremely small, inexpensive, and power efficient, and so are ideally suited for incorporation into compact, low-cost platforms for air quality monitoring.

The current ABCD design is also not well suited to mass manufacturing, as it consists of many disparate components that must be painstakingly assembled by hand. For example, the assembly of 127 ABCDs took our 100x100 Network team (of six people) over four weeks to complete. Furthermore, separate ABCD components are connected together using electrical wires and rubber tubes that were prone to failure or malfunction. Future versions of the sensor should incorporate all components onto a single printed-circuit board (PCB) that can be inexpensively produced in large numbers, and easily mounted in a weatherproof casing with minimal assembly. Wherever possible, the instrument's manifold (which guides the flow of sample air through the various sensor components) should be mated directly to the monolithic PCB, thereby reducing the need for tubing.

Currently, the ABCD's sample filter must be replaced manually when it becomes excessively loaded with BC. Across a network comprising over 100 individual sensors, periodic filter replacement proved to a very labor-intensive task throughout the 100x100 Network deployment. While most sensors in the network required filter replacement every week or so, sensors in highly polluted areas usually required filter replacements every few days, further exasperating the maintenance load. As a result, future versions of the ABCD should incorporate a mechanism to replace or rejuvenate the fibrous filter automatically. The ABCD's optical cell has a symmetrical design that can be exploited for this purpose: after passing through the sample filter, where BC collects, the particle-free flow of air passes through an identical reference filter. Using a simple software adjustment to account for the reversal, the optical cell can effectively operate with air flowing in either direction. Therefore, when the sample filter becomes excessively loaded with BC, the flow of air can be reversed, such that the clean reference filter now becomes the sample (collecting ambient BC), and the loaded filter becomes the reference. This feature has been validated experimentally, and effectively doubles the operational lifetime

of the ABCD. To further minimize maintenance, many existing BC instruments incorporate a reel of clean filter material that automatically cycles through the instrument's optical head when excessive loading is detected. In order to enable practical and economical monitoring across hundreds or thousands of sensor nodes, future versions of the ABCD should incorporate features that enable continuous operation for several months without maintenance.

While BC is useful for monitoring combustion emissions, other critical air pollutants should also be measured concurrently to provide a more complete picture of air quality. For example, it would be straightforward to incorporate electrochemical gas sensors in the ABCD's sample flow path to measure the concentrations of ozone, carbon monoxide, and other gaseous pollutants. Similarly, the integration of a light-scattering PM sensor would be beneficial. Different combinations of air quality sensors could be tailored to specific applications – a carbon monoxide sensor may be valuable for measuring indoor air quality, but not worth the additional cost when operating outdoors. In addition, the integration of multiple air quality sensors could enhance the measurement of each individual species. For instance, it may be possible to adjust the light scattering PM sensor's calibration factor (e.g., the assumed index of refraction) based on BC concentrations measured simultaneously.

The data collected by the 100x100 Network suggests that average diurnal and weekly BC concentration trends at each sampling site can be determined from only 2 to 4 weeks of continuous data collection. As a result, stationary pollution sensors could be deployed to sampling sites for short periods (several weeks) and regularly moved throughout the monitored area, thereby increasing the spatial density of periodic concentration trends without requiring additional sensors. Furthermore, areas with unusually elevated BC concentrations can be identified and better studied by re-deploying sensors from less polluted sectors of the network to sampling sites located near likely emissions sources. For future studies to implement this semi-mobile monitoring approach, a more rigorous analysis is needed to determine the minimum site deployment required to accurately characterize local pollution trends at the desired timescale. For example, it should be noted that pollution concentrations usually fluctuate seasonally over the course of the year. For example, BC concentrations in Oakland are much higher during the winter than the summer.[173] Therefore, diurnal and weekly trends must be determined using measurements collected throughout the year so as to capture these seasonal fluctuations. The trends presented in this dissertation only apply to the summer months during which the data was collected. If monthly or annual concentration trends are desired, it is likely that a semi-mobile monitoring approach would be inappropriate, as the discontinuous measurements collected might obscure or skew long-term pollution patterns at each location.

The BC concentration maps in West Oakland demonstrate that a spatial resolution of ~100 m is needed completely capture BC concentration gradients in urban environments. However, the number of sensors and sampling sites needed to establish monitoring networks with this degree of spatial density is likely to remain prohibitively expensive and impractical. Mobile monitoring platforms, usually consisting of automobiles outfitted with air quality instruments, provide measurements with a spatial resolution on the order of 10 m over large geographical areas. However, they only record pollution concentrations during the discrete instances when they pass by a given geographical location, and so temporal coverage is lacking.[155,174] Satellites provide unparalleled spatial coverage at low resolution (>1 km), and temporal resolution suffers as they typically only pass over a given location once a day. [47,48,191] In this way, existing monitoring methods each present a distinct set of advantages and disadvantages.

Analytical methods, such as land use regression (LUR) models, are increasingly being developed to extrapolate highly resolved air pollution distributions from sparse datasets.[44,46,177] However, these analytical methods cannot account for the systematic loss of data over certain time periods (e.g. nighttime) or locations. Therefore, time-continuous pollution record from distributed networks of low-cost sensors should be combined with spatially resolved and extensive measurements collected by mobile monitors and satellites, effectively leveraging the advantages of each approach to produce a more comprehensive and representative dataset that can be further analyzed using LUR or other models.[178,179] In order to expand and improve air quality monitoring throughout the world, it is critical that regulatory agencies, governments, and environmental organizations continue to diversify the portfolio of monitoring and modeling methods at their disposal, and the ABCD is well equipped to play an integral role in this effort.

References

(1) Gumy, S.; Prüss-Ustün, A.; Adair-Rohani, H.; Dora, C.; Fletcher, E.; PhD, P. G. S.; PhD, M. T. *Ambient Air Pollution: A Global Assessment of Exposure and Burden of Disease*; World Health Organization (WHO), 2016; pp 1–121.

(2) Anderson, J. O.; Thundiyil, J. G.; Stolbach, A. Clearing the Air: A Review of the Effects of Particulate Matter Air Pollution on Human Health. *J. Med. Toxicol.* **2011**, *8* (2), 166–175.

(3) Landrigan, P. J.; Fuller, R.; Adeyi, O.; Arnold, R.; Boufford, J. I. The Lancet Commission on pollution and health. *The Lancet* **2017**, 1–51.

(4) Brunekreef, B.; Holgate, S. T. Air pollution and health. *The Lancet* **2002**, *360* (9341), 1233–1242.

(5) *Burden of disease from the joint effects of Household and Ambient Air Pollution for 2012*; World Health Organization (WHO): Geneva, 2016; pp 1–4.

(6) Brauer, M.; Freedman, G.; Frostad, J.; van Donkelaar, A.; Martin, R. V.; Dentener, F.; Dingenen, R. V.; Estep, K.; Amini, H.; Apte, J. S.; et al. Ambient Air Pollution Exposure Estimation for the Global Burden of Disease 2013. *Environ. Sci. Technol.* **2016**, *50* (1), 79–88.

(7) Apte, J. S.; Marshall, J. D.; Cohen, A. J.; Brauer, M. Addressing Global Mortality from Ambient PM 2.5. *Environ. Sci. Technol.* **2015**, *49* (13), 8057–8066.

(8) Lelieveld, J.; Evans, J. S.; Fnais, M.; Giannadaki, D.; Pozzer, A. The contribution of outdoor air pollution sources to premature mortality on a global scale. *Nature* **2015**, *525* (7569), 367–371.

(9) Cohen, A. J.; Brauer, M.; Burnett, R. T.; Anderson, H. R.; Frostad, J.; Estep, K.; Balakrishnan, K.; Brunekreef, B.; Dandona, R.; Feigin, V.; et al. Estimates and 25-year trends of the global burden of disease attributable to ambient air pollution: an analysis of data from the Global Burden of Diseases Study 2015. *The Lancet* **2017**, *389* (10082), 1907–1918.

(10) Bonjour, S.; Adair-Rohani, H.; Wolf, J.; Bruce, N. G.; Mehta, S.; Prüss-Ustün, A.; Lahiff, M.; Rehfuess, E. A.; Mishra, V.; Smith, K. R. Solid Fuel Use for Household Cooking: Country and Regional Estimates for 1980–2010. *Environ. Health Perspect.* **2013**, *121* (7), 784–790.

(11) Bruce, N.; Adair-Rohani, H.; Puzzolo, E.; Dora, C. *WHO Guidelines for Indoor Air Quality: Household Fuel Combustion*; World Health Organization (WHO): Geneva, 2014; pp 1–172.

(12) Bruce, N. G.; Perez-Padilla, R.; Albalak, R. Indoor air pollution in developing countries: a major environmental and public health challenge. *Bulletin of the World Health Organization* **2000**, *78* (9), 1078–1092.

(13) Zhang, X. Y.; Wang, Y. Q.; Zhang, X. C.; Guo, W.; Niu, T.; Gong, S. L.; Yin, Y.; Zhao, P.; Jin, J. L.; Yu, M. Aerosol monitoring at multiple locations in China: contributions of EC and dust to aerosol light absorption. *Tellus B: Chemical and Physical Meteorology* **2017**, *60* (4), 647–656.

(14) Caiazzo, F.; Ashok, A.; Waitz, I. A.; Yim, S. H. L.; Barrett, S. R. H. Air pollution and early deaths in the United States. Part I: Quantifying the impact of major sectors in 2005. *Atmospheric Environment* **2013**, *79*, 198–208.

(15) Kuklinska, K.; Wolska, L.; Namiesnik, J. Air quality policy in the U.S. and the EU – a

review. *Atmospheric Pollution Research* **2015**, *6* (1), 129–137.
(16) Gulia, S.; Nagendra, S. M. S.; Khare, M.; Khanna, I. Urban air quality management-A review. *Atmospheric Pollution Research* **2015**, *6* (2), 286–304.
(17) European Parliament. *Directive 2008/50/EC of the European Parliament and of the Council of 21 May 2008 on Ambient Air Quality and Cleaner Air for Europe*; 2008.
(18) Birol, F.; Argiri, M.; Cozzi, L.; Dowling, P.; Emoto, H.; Lyons, L.; Malyshev, T. *World Energy Outlook 2006*; Priddle, R., Ed.; International Energy Agency, 2006; pp 1–601.
(19) Prüss-Ustün, A.; Wolf, J.; Corvalan, C.; Bos, R.; Neira, M. *Preventing Disease Through Healthy Environments: A Global Assessment of the Burden of Disease From Environmental Risks*; World Health Organization (WHO), 2016; pp 1–176.
(20) Pascal, M.; Corso, M.; Chanel, O.; Declercq, C.; Badaloni, C.; Cesaroni, G.; Henschel, S.; Meister, K.; Haluza, D.; Martin-Olmedo, P.; et al. Assessing the public health impacts of urban air pollution in 25 European cities: Results of the Aphekom project. *Science of the Total Environment* **2013**, *449*, 390–400.
(21) Zhang, Y.; West, J. J.; Mathur, R.; Xing, J.; Hogrefe, C.; Roselle, S. J.; Bash, J. O.; Pleim, J. E.; Gan, C.-M.; Wong, D. C. Long-term trends in the ambient $PM_{2.5}$- and O3-related mortality burdens in the United States under emission reductions from 1990 to 2010. *Atmos. Chem. Phys.* **2018**, *18* (20), 15003–15016.
(22) Steinle, S.; Reis, S.; Sabel, C. E. Quantifying human exposure to air pollution—Moving from static monitoring to spatio-temporally resolved personal exposure assessment. *Science of the Total Environment* **2013**, *443*, 184–193.
(23) de Nazelle, A.; Seto, E.; Donaire-Gonzalez, D.; Mendez, M.; Matamala, J.; Nieuwenhuijsen, M. J.; Jerrett, M. Improving estimates of air pollution exposure through ubiquitous sensing technologies. *Environmental Pollution* **2012**, *176*, 92–99.
(24) Snyder, E. G.; Watkins, T. H.; Solomon, P. A.; Thoma, E. D.; Williams, R. W.; Hagler, G. S. W.; Shelow, D.; Hindin, D. A.; Kilaru, V. J.; Preuss, P. W. The Changing Paradigm of Air Pollution Monitoring. *Environ. Sci. Technol.* **2013**, *47* (20), 11369–11377.
(25) Carvalho, H. The air we breathe: differentials in global air quality monitoring. *The Lancet Respiratory* **2016**, *4* (8), 603–605.
(26) Lim, S. S.; Vos, T.; Flaxman, A. D.; Danaei, G.; Shibuya, K.; Adair-Rohani, H.; AlMazroa, M. A.; Amann, M.; Anderson, R. H.; Andrews, K. G.; et al. A Comparative Risk Assessment of Burden of Disease and Injury Attributable to 67 Risk Factors and Risk Factor Clusters in 21 regions, 1990–2010: A Systematic Analysis for the Global Burden of Disease Study 2010. *The Lancet* **2012**, *380* (9859), 2224–2260.
(27) WEO. Energy for Cooking in Developing Countries. **2007**, 1–27.
(28) Legros, G.; Havet, I.; Bruce, N. G.; Bonjour, S. *The Energy Access Situation in Developing Countries*; United Nations Development Programme (UNDP): New York, 2009; pp 1–142.
(29) Edwards, R.; Karnani, S.; Fisher, E. M.; Johnson, M.; Naeher, L.; Smith, K. R.; Morawska, L. *WHO Indoor Air Quality Guidelines: Household fuel Combustion*; World Health Organization, 2014; pp 1–42.
(30) Smith, K. R.; Dutta, K.; Chengappa, C.; Gusain, P. P.; Masera, O.; Berrueta, V.; Edwards, R.; Bailis, R.; Shields, K. N. Monitoring and evaluation of improved biomass cookstove programs for indoor air quality and stove performance: conclusions from the

Household Energy and Health Project. *Energy for Sustainable Development* **2007**, *11* (2), 5–18.
(31) Chen, C.; Zeger, S.; Breysse, P.; Katz, J.; Checkley, W.; Curriero, F. C.; Tielsch, J. M. Estimating Indoor PM2.5 and CO Concentrations in Households in Southern Nepal: The Nepal Cookstove Intervention Trials. *PLoS ONE* **2016**, *11* (7), e0157984–17.
(32) Jetter, J.; Zhao, Y.; Smith, K. R.; Khan, B.; Yelverton, T.; DeCarlo, P.; Hays, M. D. Pollutant Emissions and Energy Efficiency under Controlled Conditions for Household Biomass Cookstoves and Implications for Metrics Useful in Setting International Test Standards. *Environ. Sci. Technol.* **2012**, *46* (19), 10827–10834.
(33) Malla, S.; Timilsina, G. R. *Household Cooking Fuel Choice and Adoption of Improved Cookstoves in Developing Countries*; The World Bank, 2014; pp 1–52.
(34) Sutar, K. B.; Kohli, S.; Ravi, M. R.; Ray, A. Biomass cookstoves: A review of technical aspects. *Renewable and Sustainable Energy Reviews* **2015**, *41*, 1128–1166.
(35) Still, D.; Bentson, S.; Li, H. Results of Laboratory Testing of 15 Cookstove Designs in Accordance with the ISO/IWA Tiers of Performance. *EcoHealth* **2015**, *12*, 12–24.
(36) Foell, W.; Pachauri, S.; Spreng, D.; Zerriffi, H. Household cooking fuels and technologies in developing economies. *Energy Policy* **2011**, *39* (12), 7487–7496.
(37) Lamberg, H.; Sippula, O.; Tissari, J.; Jokiniemi, J. Effects of Air Staging and Load on Fine-Particle and Gaseous Emissions from a Small-Scale Pellet Boiler. *Energy Fuels* **2011**, *25* (11), 4952–4960.
(38) Lyngfelt, A.; Leckner, B. Combustion of wood-chips in circulating fluidized bed boilers — NO and CO emissions as functions of temperature and air-staging. *Fuel* **1999**, No. 78, 1065–1072.
(39) Nuutinen, K.; Jokiniemi, J.; Sippula, O.; Lamberg, H.; Sutinen, J.; Horttanainen, P.; Tissari, J. Effect of air staging on fine particle, dust and gaseous emissions from masonry heaters. *Biomass and Bioenergy* **2014**, *67*, 167–178.
(40) Carroll, J. P.; Finnan, J. M.; Biedermann, F.; Brunner, T.; Obernberger, I. Air staging to reduce emissions from energy crop combustion in small scale applications. *Fuel* **2015**, *155*, 37–43.
(41) Chow, J. C. Measurement Methods to Determine Compliance with Ambient Air Quality Standards for Suspended Particles. *Journal of the Air & Waste Management Association* **1995**, *45* (5), 320–382.
(42) Yi, W.; Lo, K.; Mak, T.; Leung, K.; Leung, Y.; Meng, M. A Survey of Wireless Sensor Network Based Air Pollution Monitoring Systems. *Sensors* **2015**, *15* (12), 31392–31427.
(43) Zhou, Y.; Levy, J. I. Factors influencing the spatial extent of mobile source air pollution impacts: a meta-analysis. *BMC Public Health* **2007**, *7* (1), 122–11.
(44) Jerrett, M.; Arain, A.; Kanaroglou, P.; Beckerman, B.; Potoglou, D.; Sahsuvaroglu, T.; Morrison, J.; Giovis, C. A review and evaluation of intraurban air pollution exposure models. *J Expo Sci Environ Epidemiol* **2004**, *15* (2), 185–204.
(45) Karner, A. A.; Eisinger, D. S.; Niemeier, D. A. Near-Roadway Air Quality: Synthesizing the Findings from Real-World Data. *Environ. Sci. Technol.* **2010**, *44* (14), 5334–5344.
(46) Marshall, J. D.; Nethery, E.; Brauer, M. Within-urban variability in ambient air pollution: Comparison of estimation methods. *Atmospheric Environment* **2008**, *42* (6), 1359–1369.

(47) Chudnovsky, A. A.; Kostinski, A.; Lyapustin, A.; Koutrakis, P. Spatial scales of pollution from variable resolution satellite imaging. *Environmental Pollution* **2013**, *172*, 131–138.
(48) Lin, C.; Li, Y.; Lau, A. K. H.; Deng, X.; Tse, T. K. T.; Fung, J. C. H.; Li, C.; Li, Z.; Lu, X.; Zhang, X.; et al. Estimation of long-term population exposure to PM2.5 for dense urban areas using 1-km MODIS data. *Remote Sensing of Environment* **2016**, *179*, 13–22.
(49) Kumar, P.; Morawska, L.; Martani, C.; Biskos, G.; Neophytou, M.; Di Sabatino, S.; Bell, M.; Norford, L.; Britter, R. The rise of low-cost sensing for managing air pollution in cities. *Environment International* **2015**, *75*, 199–205.
(50) Popoola, O. A. M.; Carruthers, D.; Lad, C.; Bright, V. B.; Mead, M. I.; Stettler, M. E. J.; Saffell, J. R.; Jones, R. L. Use of networks of low cost air quality sensors to quantify air quality in urban settings. *Atmospheric Environment* **2018**, *194*, 58–70.
(51) Bart, M.; Williams, D. E.; Ainslie, B.; McKendry, I.; Salmond, J.; Grange, S. K.; Alavi-Shoshtari, M.; Steyn, D.; Henshaw, G. S. High Density Ozone Monitoring Using Gas Sensitive Semi-Conductor Sensors in the Lower Fraser Valley, British Columbia. *Environ. Sci. Technol.* **2014**, *48* (7), 3970–3977.
(52) Kanaroglou, P. S.; Jerrett, M.; Morrison, J.; Beckerman, B.; Arain, M. A.; Gilbert, N. L.; Brook, J. R. Establishing an air pollution monitoring network for intra-urban population exposure assessment: A location-allocation approach. *Atmospheric Environment* **2005**, *39* (13), 2399–2409.
(53) Mead, M. I.; Popoola, O. A. M.; Stewart, G. B.; Landshoff, P.; Calleja, M.; Hayes, M.; Baldovi, J. J.; McLeod, M. W.; Hodgson, T. F.; Dicks, J.; et al. The use of electrochemical sensors for monitoring urban air quality in low-cost, high-density networks. *Atmospheric Environment* **2012**, *70*, 186–203.
(54) Lewis, A. C.; Lee, J. D.; Edwards, P. M.; Shaw, M. D.; Evans, M. J.; Moller, S. J.; Smith, K. R.; Buckley, J. W.; Ellis, M.; Gillot, S. R.; et al. Evaluating the performance of low cost chemical sensors for air pollution research. *Faraday Discussions* **2016**, *189*, 85–103.
(55) Masson, N.; Piedrahita, R.; Hannigan, M. Quantification Method for Electrolytic Sensors in Long-Term Monitoring of Ambient Air Quality. *Sensors* **2015**, *15* (10), 27283–27302.
(56) Budde, M.; Busse, M.; Beigl, M. Investigating the Use of Commodity Dust Sensors for the Embedded Measurement of Particulate Matter; 2012; pp 1–4.
(57) Singer, B. C.; Delp, W. W. Response of consumer and research grade indoor air quality monitors to residential sources of fine particles. *Indoor Air* **2018**, *28* (4), 624–639.
(58) Castell, N.; Dauge, F. R.; Schneider, P.; Vogt, M.; Lerner, U.; Fishbain, B.; Broday, D.; Bartonova, A. Can commercial low-cost sensor platforms contribute to air quality monitoring and exposure estimates? *Environment International* **2017**, *99*, 293–302.
(59) Joel Kuula; Timo Mäkelä; Risto Hillamo; Hilkka Timonen. Response Characterization of an Inexpensive Aerosol Sensor. *Sensors* **2017**, *17* (12), 2915–14.
(60) Mukherjee, A.; Stanton, L.; Graham, A.; Roberts, P. Assessing the Utility of Low-Cost Particulate Matter Sensors over a 12-Week Period in the Cuyama Valley of California. *Sensors* **2017**, *17* (8), 1805–1816.
(61) Williams, R.; Kaufman, A.; Hanley, T.; Rice, J.; Garvey, S. *Evaluation of Field-*

deployed Low Cost PM Sensors; EPA/600/R-14/464; US Environmental Protection Agency (EPA), 2014.

(62) Cross, E. S.; Williams, L. R.; Lewis, D. K.; Magoon, G. R.; Onasch, T. B.; Kaminsky, M. L.; Worsnop, D. R.; Jayne, J. T. Use of electrochemical sensors for measurement of air pollution: correcting interference response and validating measurements. *Atmos. Meas. Tech.* **2017**, *10* (9), 3575–3588.

(63) Bond, T. C.; Doherty, S. J.; Fahey, D. W. Bounding the role of black carbon in the climate system: A scientific assessment. *J. Geophys. Res. Atmos.* **2013**, *118* (11), 5380–5552.

(64) Gan, W. Q.; Koehoorn, M.; Davies, H. W.; Demers, P. A.; Tamburic, L.; Brauer, M. Long-Term Exposure to Traffic-Related Air Pollution and the Risk of Coronary Heart Disease Hospitalization and Mortality. *Environ. Health Perspect.* **2010**, *119* (4), 501–507.

(65) Highwood, E. J.; Kinnersley, R. P. When smoke gets in our eyes: The multiple impacts of atmospheric black carbon on climate, air quality and health. *Environment International* **2006**, *32* (4), 560–566.

(66) Janssen, N. A. H.; van Vliet, P. H. N.; Arts, F.; Harssema, H.; Brunekreef, B. Assessment of exposure to traffic related air pollution of children attending schools near motorways. *Atmospheric Environment* **2001**, *35*, 3875–3884.

(67) Kim, J. J.; Smorodinsky, S.; Lipsett, M.; Singer, B. C.; Hodgson, A. T.; Ostro, B. Traffic-related Air Pollution near Busy Roads. *Am J Respir Crit Care Med* **2004**, *170* (5), 520–526.

(68) Janssen, N. A. H.; Gerlofs-Nijland, M. E.; Lanki, T.; Salonen, R. O.; Cassee, F.; Hoek, G.; Fischer, P.; Brunekreef, B.; Krzyzanowski, M. *Health Effects of Black Carbon*; The WHO European Centre for Environment and Health (WHO): Bonn, 2012; pp 1–96.

(69) Intergovernmental Panel on Climate Change (IPCC). *Climate Change 2007*; Solomon, S., Qin, Manning, M., Eds.; Cambridge University Press: Cambridge, UK, 2007; pp 1–1007.

(70) Cyrys, J.; Heinrich, J.; Hoek, G.; Meliefste, K.; Lewné, M.; Gehring, U.; Bellander, T.; Fischer, P.; Vliet, P. V.; Brauer, M.; et al. Comparison between different traffic-related particle indicators: Elemental carbon (EC), PM2.5 mass and absorbance. *J Expo Sci Environ Epidemiol* **2003**, *13* (2), 134–143.

(71) Reche, C.; Querol, X.; Alastuey, A.; Viana, M.; Pey, J.; Moreno, T.; Rodríguez, S.; González, Y.; Fernández-Camacho, R.; la Rosa, de, J.; et al. New considerations for PM, Black Carbon and particle number concentration for air quality monitoring across different European cities. *Atmos. Chem. Phys.* **2011**, *11* (13), 6207–6227.

(72) Janssen, N. A. H.; Hoek, G.; Simic-Lawson, M.; Fischer, P.; van Bree, L.; Brink, ten, H.; Keuken, M.; Atkinson, R. W.; Anderson, H. R.; Brunekreef, B.; et al. Black Carbon as an Additional Indicator of the Adverse Health Effects of Airborne Particles Compared with PM_{10} and $PM_{2.5}$. *Environ. Health Perspect.* **2011**, *119*, 1691–1699.

(73) Lükewille, A. *Status of black carbon monitoring in ambient air in Europe*; 18/2013; European Environmental Agency (EEA) : Luxembourg, 2013; pp 1–48.

(74) Okasha, F. Staged combustion of rice straw in a fluidized bed. *Experimental Thermal and Fluid Science* **2007**, *32* (1), 52–59.

(75) Rapp, V. H.; Caubel, J. J.; Wilson, D. L.; Gadgil, A. J. Reducing Ultrafine Particle

Emissions Using Air Injection in Wood-Burning Cookstoves. *Environ. Sci. Technol.* **2016**, *50* (15), 8368–8374.
(76) Wiinikka, H.; Gebart, R. The Influence of Air Distribution Rate on Particle Emissions in Fixed Bed Combustion of Biomass. *Combustion Science and Technology* **2005**, *177* (9), 1747–1766.
(77) Shen, G.; Tao, S.; Wei, S.; Zhang, Y.; Wang, R.; Wang, B.; Li, W.; Shen, H.; Huang, Y.; Chen, Y.; et al. Reductions in Emissions of Carbonaceous Particulate Matter and Polycyclic Aromatic Hydrocarbons from Combustion of Biomass Pellets in Comparison with Raw Fuel Burning. *Environ. Sci. Technol.* **2012**, *46* (11), 6409–6416.
(78) Wiinikka, H.; Gebart, R. Critical Parameters for Particle Emissions in Small-Scale Fixed-Bed Combustion of Wood Pellets. *Energy Fuels* **2004**, *18* (4), 897–907.
(79) Pettersson, E.; Lindmark, F.; Öhman, M.; Nordin, A.; Westerholm, R.; Boman, C. Design Changes in a Fixed-Bed Pellet Combustion Device: Effects of Temperature and Residence Time on Emission Performance. *Energy Fuels* **2010**, *24* (2), 1333–1340.
(80) Tryner, J.; Tillotson, J. W.; Baumgardner, M. E.; Mohr, J. T.; DeFoort, M. W.; Marchese, A. J. The Effects of Air Flow Rates, Secondary Air Inlet Geometry, Fuel Type, and Operating Mode on the Performance of Gasifier Cookstoves. *Environ. Sci. Technol.* **2016**, *50* (17), 9754–9763.
(81) Wang, Y.; Sohn, M. D.; Wang, Y.; Lask, K. M.; Kirchstetter, T. W.; Gadgil, A. J. How many replicate tests are needed to test cookstove performance and emissions? — Three is not always adequate. *Energy for Sustainable Development* **2014**, *20*, 21–29.
(82) Cai, J.; Yan, B.; Kinney, P. L.; Perzanowski, M. S.; Jung, K.-H.; Li, T.; Xiu, G.; Zhang, D.; Olivo, C.; Ross, J.; et al. Optimization Approaches to Ameliorate Humidity and Vibration Related Issues Using the MicroAeth Black Carbon Monitor for Personal Exposure Measurement. *Aerosol Science and Technology* **2013**, *47* (11), 1196–1204.
(83) Arnott, W. P. Photoacoustic and filter-based ambient aerosol light absorption measurements: Instrument comparisons and the role of relative humidity. *J. Geophys. Res.* **2003**, *108* (D1), 1042–11.
(84) Lack, D. A.; Moosmüller, H.; McMeeking, G. R.; Chakrabarty, R. K.; Baumgardner, D. Characterizing elemental, equivalent black, and refractory black carbon aerosol particles: a review of techniques, their limitations and uncertainties. *Anal Bioanal Chem* **2013**, *406* (1), 99–122.
(85) Watson, J. G.; Chow, J. C.; Chen, L. W. A. Summary of Organic and Elemental Carbon/Black Carbon Analysis Methods and Intercomparisons. *Aerosol Air Qual. Res.* **2005**, *5* (1), 65–102.
(86) *WHO Air quality guidelines for particulate matter, ozone, nitrogen dioxide and sulfur dioxide*; World Health Organization, 2005.
(87) Nussbaumer, T. Combustion and Co-combustion of Biomass: Fundamentals, Technologies, and Primary Measures for Emission Reduction †. *Energy Fuels* **2003**, *17* (6), 1510–1521.
(88) Valavanidis, A.; Fiotakis, K.; Vlachogianni, T. Airborne Particulate Matter and Human Health: Toxicological Assessment and Importance of Size and Composition of Particles for Oxidative Damage and Carcinogenic Mechanisms. *Journal of Environmental Science and Health, Part C* **2008**, *26* (4), 339–362.
(89) *The Water Boiling Test*, 4 ed.; Global Alliance for Clean Cookstoves, 2014; pp 1–89.
(90) Taylor, J. R. *An introduction to error analysis: The study of uncertainties in physical*

measurements; University Science Books: Sausalito, CA, 1997; pp 1–1.
(91) Johansson, L. S.; Leckner, B.; Gustavsson, L.; Cooper, D.; Tullin, C.; Potter, A. Emission characteristics of modern and old-type residential boilers fired with wood logs and wood pellets. *Atmospheric Environment* **2004**, *38* (25), 4183–4195.
(92) Torvela, T.; Tissari, J.; Sippula, O.; Kaivosoja, T.; Leskinen, J.; Virén, A.; Lähde, A.; Jokiniemi, J. Effect of wood combustion conditions on the morphology of freshly emitted fine particles. *Atmospheric Environment* **2014**, *87*, 65–76.
(93) Kelz, J.; Brunner, T.; Obernberger, I.; Jalava, P.; Hirvonen, M. R. PM emissions from old and modern biomass combustion systems and their health effects. **2010**.
(94) Obaidullah, M.; Bram, S.; Verma, V. K.; De Ruyck, J. A Review on Particle Emissions from Small Scale Biomass Combustion. *International Journal of Renewable Energy Research* **2012**, *2* (1), 1–13.
(95) Jiang, M.; Wu, Y.; Lin, G.; Xu, L.; Chen, Z.; Fu, F. Pyrolysis and thermal-oxidation characterization of organic carbon and black carbon aerosols. *Science of the Total Environment* **2011**, *409* (20), 4449–4455.
(96) Brunner, T.; Barnthaler, G.; Obernberger, I. Evaluation of Parameters Determining PM Emissions and their Chemical Composition in Modern Residential Biomass Heating Appliances; 2008; pp 81–86.
(97) Petzold, A.; Ogren, J. A.; Fiebig, M.; Laj, P.; Li, S. M.; Baltensperger, U.; Holzer-Popp, T.; Kinne, S.; Pappalardo, G.; Sugimoto, N.; et al. Recommendations for reporting "black carbon" measurements. *Atmos. Chem. Phys.* **2013**, *13* (16), 8365–8379.
(98) Elmquist, M.; Cornelissen, G.; Kukulska, Z.; Gustafsson, Ö. Distinct oxidative stabilities of char versus soot black carbon: Implications for quantification and environmental recalcitrance. *Global Biogeochem. Cycles* **2006**, *20* (2), 1–11.
(99) Khlystov, A.; Stanier, C.; Pandis, S. N. An Algorithm for Combining Electrical Mobility and Aerodynamic Size Distributions Data when Measuring Ambient Aerosol. *Aerosol Science and Technology* **2004**, *38* (S1), 229–238.
(100) Just, B.; Rogak, S.; Kandlikar, M. Characterization of Ultrafine Particulate Matter from Traditional and Improved Biomass Cookstoves. *Environ. Sci. Technol.* **2013**, *47*, 3506–3512.
(101) Jöller, M.; Brunner, T.; Obernberger, I. Modeling of aerosol formation during biomass combustion for various furnace and boiler types. *Fuel Processing Technology* **2007**, *88*, 1136–1147.
(102) Obernberger, I.; Brunner, T.; Barnthaler, G. Fine Particulate Emissions From Modern Austrian Small-Scale Biomass Combustion Plants; 2011; Vol. 15, pp 1–12.
(103) Jetter, J.; Ebersviller, S. *Test Report: BioLite HomeStove with Woof Fuel*; U.S. Environmental Protection Agency, 2015; pp 1–33.
(104) Delapena, S.; Garland, C.; Jagoe, K.; Okada, E.; Ouk, S.; Pennise, D.; Pillarisetti, A.; Steele, J. *Quantifying the health impacts of ACE-1 biomass and biogas stoves in Cambodia*; Berkeley Air Monitoring Group, 2016; pp 1–52.
(105) Caubel, J. J.; Rapp, V. H.; Chen, S. S.; Gadgil, A. J. Optimization of Secondary Air Injection in a Wood-Burning Cookstove: An Experimental Study. *Environ. Sci. Technol.* **2018**, *52* (7), 4449–4456.
(106) Lienhard, J. H., V; Lienhard, J. H., IV. Velocity Coefficients For Free Jets FromSharp-Edged Orifices. *Journal of Fluids Engineering* **1984**, *106* (13), 1–5.

(107) Cushman-Roisin, B. Turbulent Jets. In *Environmental Fluid Mechanics*; New York, 2014; pp 1–9.
(108) Bilsback, K. R.; Eilenberg, S. R.; Good, N.; Heck, L.; Johnson, M.; Kodros, J. K.; Lipsky, E. M.; L'Orange, C.; Pierce, J. R.; Robinson, A. L.; et al. The Firepower Sweep Test: A novel approach to cookstove laboratory testing. *Indoor Air* **2018**, *28* (6), 936–949.
(109) Bäfver, L. S.; Leckner, B.; Tullin, C.; Berntsen, M. Particle emissions from pellets stoves and modern and old-type wood stoves. *Biomass and Bioenergy* **2011**, *35* (8), 3648–3655.
(110) Houshfar, E.; Skreiberg, Ø.; Løvås, T.; Todorović, D.; Sørum, L. Effect of Excess Air Ratio and Temperature on NOx Emission from Grate Combustion of Biomass in the Staged Air Combustion Scenario. *Energy Fuels* **2011**, *25* (10), 4643–4654.
(111) Kirch, T.; Birzer, C. H.; Medwell, P. R.; Holden, L. The role of primary and secondary air on wood combustion in cookstoves. *International Journal of Sustainable Energy* **2017**, *37* (3), 268–277.
(112) Petzold, A.; Schloesser, H.; Sheridan, P. J.; Arnott, W. P.; Ogren, J. A.; Virkkula, A. Evaluation of Multiangle Absorption Photometry for Measuring Aerosol Light Absorption. *Aerosol Science and Technology* **2005**, *39* (1), 40–51.
(113) Garland, C.; Delapena, S.; Prasad, R.; L'Orange, C.; Alexander, D.; Johnson, M. Black carbon cookstove emissions: A field assessment of 19 stove/fuel combinations. *Atmospheric Environment* **2017**, *169*, 140–149.
(114) Soneja, S. I.; Tielsch, J. M.; Curriero, F. C.; Zaitchik, B.; Khatry, S. K.; Yan, B.; Chillrud, S. N.; Breysse, P. N. Determining Particulate Matter and Black Carbon Exfiltration Estimates for Traditional Cookstove Use in Rural Nepalese Village Households. *Environ. Sci. Technol.* **2015**, *49* (9), 5555–5562.
(115) Vicente, E. D.; Alves, C. A. An overview of particulate emissions from residential biomass combustion. *Atmospheric Research* **2018**, *199*, 159–185.
(116) Champier, D.; Bédécarrats, J. P.; Kousksou, T.; Rivaletto, M.; Strub, F.; Pignolet, P. Study of a TE (thermoelectric) generator incorporated in a multifunction wood stove. *Energy* **2011**, *36* (3), 1518–1526.
(117) Champier, D.; Bedecarrats, J. P.; Rivaletto, M.; Strub, F. Thermoelectric power generation from biomass cook stoves. *Energy* **2010**, *35* (2), 935–942.
(118) Gao, H. B.; Huang, G. H.; Li, H. J.; Qu, Z. G.; Zhang, Y. J. Development of stove-powered thermoelectric generators: A review. *Applied Thermal Engineering* **2016**, *96*, 297–310.
(119) Nuwayhid, R. Y.; Shihadeh, A.; Ghaddar, N. Development and testing of a domestic woodstove thermoelectric generator with natural convection cooling. *Energy Conversion and Management* **2005**, *46* (9-10), 1631–1643.
(120) Mal, R.; Prasad, R.; Vijay, V. K.; Verma, A. R. The Design, Development and Performance Evaluation of Thermoelectric Generator(TEG) Integrated Forced Draft Biomass Cookstove. *Procedia - Procedia Computer Science* **2015**, *52*, 723–729.
(121) National Ambient Air Quality Standards Table. *epa.gov*. October 25, 2016, pp 1–3.
(122) Martins, L. D.; Martins, J. A.; Freitas, E. D.; Mazzoli, C. R.; Gonçalves, F. L. T.; Ynoue, R. Y.; Hallak, R.; Albuquerque, T. T. A.; Andrade, M. de F. Potential health impact of ultrafine particles under clean and polluted urban atmospheric conditions: a model-based study. *Air Qual Atmos Health* **2009**, *3* (1), 29–39.

(123) Chen, R.; Bin Hu; Liu, Y.; Xu, J.; Yang, G.; Xu, D.; Chen, C. Beyond PM2.5: The role of ultrafine particles on adverse health effects of air pollution. *BBA - General Subjects* **2016**, *1860* (12), 2844–2855.
(124) Clifford, S.; Mazaheri, M.; Salimi, F.; Ezz, W. N.; Yeganeh, B.; Low-Choy, S.; Walker, K.; Mengersen, K.; Marks, G. B.; Morawska, L. Effects of exposure to ambient ultrafine particles on respiratory health and systemic inflammation in children. *Environment International* **2018**, *114*, 167–180.
(125) Just, B.; Rogak, S.; Kandlikar, M. Characterization of Ultrafine Particulate Matter from Traditional and Improved Biomass Cookstoves. *Environ. Sci. Technol.* **2013**, *47* (7), 3506–3512.
(126) Shen, G.; Gaddam, C. K.; Ebersviller, S. M.; Vander Wal, R. L.; Williams, C.; Faircloth, J. W.; Jetter, J. J.; Hays, M. D. A Laboratory Comparison of Emission Factors, Number Size Distributions, and Morphology of Ultrafine Particles from 11 Different Household Cookstove-Fuel Systems. *Environ. Sci. Technol.* **2017**, *51* (11), 6522–6532.
(127) Tissari, J.; Lyyränen, J.; Hytönen, K.; Sippula, O.; Tapper, U.; Frey, A.; Saarnio, K.; Pennanen, A. S.; Hillamo, R.; Salonen, R. O.; et al. Fine particle and gaseous emissions from normal and smouldering wood combustion in a conventional masonry heater. *Atmospheric Environment* **2008**, *42* (34), 7862–7873.
(128) Nielsen, I. E.; Eriksson, A. C.; Lindgren, R.; Martinsson, J.; Nyström, R.; Nordin, E. Z.; Sadiktsis, I.; Boman, C.; Nøjgaard, J. K.; Pagels, J. Time-resolved analysis of particle emissions from residential biomass combustion - Emissions of refractory black carbon, PAHs and organic tracers. *Atmospheric Environment* **2017**, *165*, 179–190.
(129) Hosseini, S.; Li, Q.; Cocker, D.; Weise, D.; Miller, A.; Shrivastava, M.; Miller, J. W.; Mahalingam, S.; Princevac, M.; Jung, H. Particle size distributions from laboratory-scale biomass fires using fast response instruments. *Atmos. Chem. Phys.* **2010**, *10* (16), 8065–8076.
(130) US Environmental Protection Agency EPA. DRAFT Roadmap for Next Generation Air Monitoring. **2013**.
(131) Van Roosbroeck, S.; Wichmann, J.; Janssen, N. A. H.; Hoek, G.; van Wijnen, J. H.; Lebret, E.; Brunekreef, B. Long-term personal exposure to traffic-related air pollution among school children, a validation study. *Science of The Total Environment* **2006**, *368* (2-3), 565–573.
(132) Tsujita, W.; Yoshino, A.; Ishida, H.; Moriizumi, T. Gas sensor network for air-pollution monitoring. *Sensors and Actuators B: Chemical* **2005**, *110* (2), 304–311.
(133) Jiao, W.; Hagler, G.; Williams, R.; Sharpe, R.; Brown, R.; Garver, D.; Judge, R.; Caudill, M.; Rickard, J.; Davis, M.; et al. Community Air Sensor Network (CAIRSENSE) project: evaluation of low-cost sensor performance in a suburban environment in the southeastern United States. *Atmos. Meas. Tech.* **2016**, *9* (11), 5281–5292.
(134) Gao, M.; Cao, J.; Seto, E. A distributed network of low-cost continuous reading sensors to measure spatiotemporal variations of PM2.5 in Xi'an, China. *Environmental Pollution* **2015**, *199*, 56–65.
(135) Heimann, I.; Bright, V. B.; McLeod, M. W.; Mead, M. I.; Popoola, O. A. M.; Stewart, G. B.; Jones, R. L. Source attribution of air pollution by spatial scale separation using high spatial density networks of low cost air quality sensors. *Atmospheric Environment*

2015, *113* (C), 10–19.
(136) Sasser, E.; Hernby, J. *Report to Congress on Black Carbon*; EPA-450/R-12-001; US Environmental Protection Agency (EPA), 2012.
(137) Cai, J. Validation of MicroAeth® as a Black Carbon Monitor for Fixed-Site Measurement and Optimization for Personal Exposure Characterization. *Aerosol Air Qual. Res.* **2014**, 1–18.
(138) Springston, S. *Particle Soot Absorption Photometer Instrument Handbook*; DOE/SC-ARM-TR-176; US Department of Energy, 2016; pp 1–28.
(139) Hansen, A. D. A.; Rosen, H.; Novakov, T. The Aethalometer - An Instrument for the Real-Time Measurement of Optical Absorption by Aerosol Particles. *The Science of the Total Environment* **1984**, *36*, 191–196.
(140) Petzold, A.; Schönlinner, M. Multi-angle absorption photometry—a new method for the measurement of aerosol light absorption and atmospheric black carbon. *Journal of Aerosol Science* **2004**, *35* (4), 421–441.
(141) Kirchstetter, T. W.; Thatcher, T. L. Contribution of organic carbon to wood smoke particulate matter absorption of solar radiation. *Atmos. Chem. Phys.* **2012**, *12* (14), 6067–6072.
(142) Ramachandran, S.; Rajesh, T. A. Black carbon aerosol mass concentrations over Ahmedabad, an urban location in western India: Comparison with urban sites in Asia, Europe, Canada, and the United States. *J. Geophys. Res.* **2007**, *112* (D6), 817–819.
(143) Bodhaine, B. A. Aerosol Absorption Measurements at Barrow, Mauna Loa and the South Pole. *J. Geophys. Res.* **1995**, *100* (D5), 8967–8975.
(144) Yang, M.; Howell, S. G.; Huebert, B. J. Attribution of aerosol light absorption to black carbon, brown carbon, and dust in China – interpretations of atmospheric measurements during EAST-AIRE. *Atmos. Chem. Phys.* **2009**, *9*, 1–16.
(145) Pallflex® Filters: Emfab™, Fiberfilm™, and Tissuquartz™ Filters, 2002.
(146) *QED121, QED122, QED123 Plastic Infrared Light Emitting Diode*; Fairchild Semiconductor Corporation, 2008; pp 1–8.
(147) *OPT101 Monolithic Photodiode and Single-Supply Transimpedance Amplifier*; OPT101; Texas Instruments, 2015.
(148) Jimenez, J.; Claiborn, C.; Larson, T.; Gould, T.; Kirchstetter, T.; Gundel, L. Loading Effect Correction for Real-Time Aethalometer Measurements of Fresh Diesel Soot. *Journal of the Air & Waste Management Association* **2007**, *57* (7), 868–873.
(149) Cheng, Y. H.; Yang, L. S. Correcting aethalometer black carbon data for measurement artifacts by using inter-comparison methodology based on two different light attenuation increasing rates. *Atmos. Meas. Tech. Discuss.* **2015**, *8* (3), 2851–2879.
(150) Virkkula, A.; Mäkelä, T.; Hillamo, R.; Yli-Tuomi, T.; Hirsikko, A.; Hämeri, K.; Koponen, I. K. A Simple Procedure for Correcting Loading Effects of Aethalometer Data. *Journal of the Air & Waste Management Association* **2007**, *57* (10), 1214–1222.
(151) Drinovec, L.; Močnik, G.; Zotter, P.; Prévôt, A. S. H.; Ruckstuhl, C.; Coz, E.; Rupakheti, M.; Sciare, J.; Müller, T.; Wiedensohler, A.; et al. The "dual-spot" Aethalometer: an improved measurement of aerosol black carbon with real-time loading compensation. *Atmos. Meas. Tech.* **2015**, *8* (5), 1965–1979.
(152) Gakidou, E.; Afshin, A.; Abajobir, A. A.; Abate, K. H.; Abbafati, C.; Abbas, K. M.; Abd-Allah, F.; Abdulle, A. M.; Abera, S. F.; Aboyans, V.; et al. Global, regional, and national comparative risk assessment of 84 behavioural, environmental and

occupational, and metabolic risks or clusters of risks, 1990 to 2016: a systematic analysis for the Global Burden of Disease Study 2016. *The Lancet* **2017**, *390* (10100), 1345–1422.

(153) Cohen, A. J.; Ross Anderson, H.; Ostro, B.; Pandey, K. D.; Krzyzanowski, M.; Künzli, N.; Gutschmidt, K.; Pope, A.; Romieu, I.; Samet, J. M.; et al. The Global Burden of Disease Due to Outdoor Air Pollution. *Journal of Toxicology and Environmental Health, Part A* **2005**, *68* (13-14), 1301–1307.

(154) Saraswat, A.; Apte, J. S.; Kandlikar, M.; Brauer, M.; Henderson, S. B.; Marshall, J. D. Spatiotemporal Land Use Regression Models of Fine, Ultrafine, and Black Carbon Particulate Matter in New Delhi, India. *Environ. Sci. Technol.* **2013**, *47* (22), 12903–12911.

(155) Apte, J. S.; Messier, K. P.; Gani, S.; Brauer, M.; Kirchstetter, T. W.; Lunden, M. M.; Marshall, J. D.; Portier, C. J.; Vermeulen, R. C. H.; Hamburg, S. P. High-Resolution Air Pollution Mapping with Google Street View Cars: Exploiting Big Data. *Environ. Sci. Technol.* **2017**, *51* (12), 6999–7008.

(156) Boogaard, H.; Kos, G. P. A.; Weijers, E. P.; Janssen, N. A. H.; Fischer, P. H.; van der Zee, S. C.; de Hartog, J. J.; Hoek, G. Contrast in air pollution components between major streets and background locations: Particulate matter mass, black carbon, elemental composition, nitrogen oxide and ultrafine particle number. *Atmospheric Environment* **2011**, *45* (3), 650–658.

(157) Olson, D. A.; Hammond, D. M.; Seila, R. L.; Burke, J. M.; Norris, G. A. Spatial gradients and source apportionment of volatile organic compounds near roadways. *Atmospheric Environment* **2009**, *43* (35), 5647–5653.

(158) Jerrett, M.; Arain, A.; Kanaroglou, P.; Beckerman, B.; Potoglou, D.; Sahsuvaroglu, T.; Morrison, J.; Giovis, C. A review and evaluation of intraurban air pollution exposure models. *J Expo Sci Environ Epidemiol* **2004**, *15* (2), 185–204.

(159) Bart, M.; Williams, D. E.; Ainslie, B.; McKendry, I.; Salmond, J.; Grange, S. K.; Alavi-Shoshtari, M.; Steyn, D.; Henshaw, G. S. High Density Ozone Monitoring Using Gas Sensitive Semi-Conductor Sensors in the Lower Fraser Valley, British Columbia. *Environ. Sci. Technol.* **2014**, *48* (7), 3970–3977.

(160) Schneider, P.; Castell, N.; Vogt, M.; Dauge, F. R.; Lahoz, W. A.; Bartonova, A. Mapping urban air quality in near real-time using observations from low-cost sensors and model information. *Environment International* **2017**, *106*, 234–247.

(161) Caubel, J.; Cados, T.; Kirchstetter, T. A New Black Carbon Sensor for Dense Air Quality Monitoring Networks. *Sensors* **2018**, *18* (3), 738–18.

(162) Alexeeff, S. E.; Roy, A.; Shan, J.; Liu, X.; Messier, K.; Apte, J. S.; Portier, C.; Sidney, S.; Van Den Eeden, S. K. High-resolution mapping of traffic related air pollution with Google street view cars and incidence of cardiovascular events within neighborhoods in Oakland, CA. **2018**, 1–13.

(163) West Oakland neighborhood: Detailed profile. *City-Data.com*. September 5, 2018.

(164) Palaniappan, M.; Wu, D.; Kohleriter, J. *Clearing the Air: Reducing Diesel Pollution in West Oakland*; West Oakland Environmental Indicators Project : Oakland, 2003; pp 1–16.

(165) Di, P. *Diesel Particulate Matter Health Risk Assessment for the West Oakland Community*; Oakland, 2008; pp 1–48.

(166) Good, N.; lter, A. M. O.; Peel, J. L.; Volckens, J. An accurate filter loading correction

is essential for assessing personal exposure to black carbon using an Aethalometer. **2016**, *27* (4), 409–416.
(167) Kirchstetter, T. W.; Novakov, T. Controlled generation of black carbon particles from a diffusion flame and applications in evaluating black carbon measurement methods. *Atmospheric Environment* **2007**, *41* (9), 1874–1888.
(168) Lau, V.; Martien, P.; Fairley, D. *West Oakland Truck Survey*; Bay Area Air Quality Management District: San Francisco, 2010; pp 1–89.
(169) *Port of Oakland Marine Terminal Information for Truck Appointments*; Bay Area Air Quality Management District : San Francisco, 2007; pp 1–7.
(170) Port of Oakland - Trucker Resources: Oakland Portal. *portofoakland.emodal.com*. Oakland November 12, 2018.
(171) Shah, R. U.; Robinson, E. S.; Gu, P.; Robinson, A.; Apte, J. S.; Presto, A. A. High spatial resolution mapping of aerosol composition and sources in Oakland, California using mobile aerosol mass spectrometry. *Atmos. Chem. Phys. Discuss.* **2018**, 1–31.
(172) *Custom Alloy Scrap Sales, Inc. : BAAQMD Fact Sheet*, 146 ed.; Bay Area Air Quality Management District (BAAQMD): Oakland, 2009; pp 1–4.
(173) Kirchstetter, T. W.; Aguiar, J.; Tonse, S.; Fairley, D.; Novakov, T. Black carbon concentrations and diesel vehicle emission factors derived from coefficient of haze measurements in California: 1967–2003. *Atmospheric Environment* **2008**, *42* (3), 480–491.
(174) Van den Bossche, J.; Peters, J.; Verwaeren, J.; Botteldooren, D.; Theunis, J.; De Baets, B. Mobile monitoring for mapping spatial variation in urban air quality: Development and validation of a methodology based on an extensive dataset. *Atmospheric Environment* **2015**, *105*, 148–161.
(175) Hasenfratz, D.; Saukh, O.; Walser, C.; Hueglin, C.; Fierz, M.; Arn, T.; Beutel, J.; Thiele, L. Deriving high-resolution urban air pollution maps using mobile sensor nodes. *Pervasive and Mobile Computing* **2015**, *16*, 268–285.
(176) Van Poppel, M.; Peters, J.; Bleux, N. Methodology for setup and data processing of mobile air quality measurements to assess the spatial variability of concentrations in urban environments. *Environmental Pollution* **2013**, *183*, 224–233.
(177) Ryan, P. H.; LeMasters, G. K. A Review of Land-use Regression Models for Characterizing Intraurban Air Pollution Exposure. *Inhalation Toxicology* **2008**, *19* (1), 127–133.
(178) Adams, M. D.; Kanaroglou, P. S. Mapping real-time air pollution health risk for environmental management: Combining mobile and stationary air pollution monitoring with neural network models. *Journal of Environmental Management* **2016**, *168*, 133–141.
(179) Schneider, P.; Castell, N.; Vogt, M.; Dauge, F. R.; Lahoz, W. A.; Bartonova, A. Mapping urban air quality in near real-time using observations from low-cost sensors and model information. *Environment International* **2017**, *106*, 234–247.
(180) Riley, E. A.; Schaal, L.; Sasakura, M.; Crampton, R.; Gould, T. R.; Hartin, K.; Sheppard, L.; Larson, T.; Simpson, C. D.; Yost, M. G. Correlations between short-term mobile monitoring and long-term passive sampler measurements of traffic-related air pollution. *Atmospheric Environment* **2016**, *132*, 229–239.
(181) Lewis, J. J.; Pattanayak, S. K. Who Adopts Improved Fuels and Cookstoves? A Systematic Review. *Environ. Health Perspect.* **2012**, *120*, 637–645.

(182) Pillarisetti, A.; Vaswani, M.; Jack, D.; Balakrishnan, K.; Bates, M. N.; Arora, N. K.; Smith, K. R. Patterns of Stove Usage after Introduction of an Advanced Cookstove: The Long-Term Application of Household Sensors. *Environ. Sci. Technol.* **2014**, *48* (24), 14525–14533.
(183) Smith, K. R. Changing Paradigms in Clean Cooking. *EcoHealth* **2015**, 1–4.
(184) Ruiz-Mercado, I.; Masera, O.; Zamora, H.; Smith, K. R. Adoption and sustained use of improved cookstoves. *Energy Policy* **2011**, *39* (12), 7557–7566.
(185) Shan, M.; Carter, E.; Baumgartner, J.; Deng, M.; Clark, S.; Schauer, J. J.; Ezzati, M.; Li, J.; Fu, Y.; Yang, X. A user-centered, iterative engineering approach for advanced biomass cookstove design and development. *Environ. Res. Lett.* **2017**, *12* (9), 095009–095012.
(186) Kshirsagar, M. P.; Kalamkar, V. R. User-centric approach for the design and sizing of natural convection biomass cookstoves for lower emissions. *Energy* **2016**, *115* (Part 1), 1202–1215.
(187) Wilson, D. L.; Monga, M.; Saksena, A.; Kumar, A.; Gadgil, A. Effects of USB port access on advanced cookstove adoption. *Development Engineering* **2018**, *3*, 209–217.
(188) Hostettler, S.; Hazboun, E.; Bolay, J.-C. *Technologies for Development: What is Essential?*; Springer, 2015; pp 1–223.
(189) Pillarisetti, A.; Allen, T.; Ruiz-Mercado, I.; Edwards, R.; Chowdhury, Z.; Garland, C.; Hill, L.; Johnson, M.; Litton, C.; Lam, N.; et al. Small, Smart, Fast, and Cheap: Microchip-Based Sensors to Estimate Air Pollution Exposures in Rural Households. *Sensors* **2017**, *17* (8), 1879–18.
(190) Volckens, J.; Quinn, C.; Leith, D.; Mehaffy, J.; Henry, C. S.; Miller-Lionberg, D. Development and evaluation of an ultrasonic personal aerosol sampler. *Indoor Air* **2016**, *27* (2), 409–416.
(191) Marc, M.; Tobiszewski, M.; a, B. Z.; la Guardia, de, M.; nik, J. N. Current air quality analytics and monitoring: A review. *ACA* **2015**, *853*, 116–126.
(192) Pope, S. B. *Turbulent Flows*; Cambridge University Press, 2005; pp 1–810.
(193) Wilson, D. L.; Wilson; Rapp, V. H.; Caubel, J. J.; Chen, S. S.; Gadgil, A. J. *Verifying mixing in dilution tunnels*; LBNL-2001088; Lawrence Berkeley National Laboratory, 2017.
(194) D07 Committee. *Standard Test Methods for Direct Moisture Content Measurement of Wood and Wood- Base Materials*; D4442-07; ASTM International: West Conshohocken, PA, 2015; pp 1–6.
(195) Bengston, H. Iris Flow Meter Discharge Coefficient Values Using ISO 5167. *Bright Hub Engineering*. September 21, 2010.
(196) The Energy Conservatory. *FlowBlaster - Operation Manual*; DG-700; The Energy Conservatory: Minneapolis, 2014.
(197) TrueFlow - Measuring Air Handler Flow Accurately. **2014**, 1–3.
(198) Fox, R. W.; McDonald; Pritchard, P. J. *Introduction to Fluid Mechanics*, 7 ed.; John Wiley & Sons: Hoboken, 2017.
(199) Dixon, J. C. *The Shock Absorber Handbook*, 2nd ed.; John Wiley & Sons: Chichester, 2007.
(200) fantech. *IR Series Iris Dampers*; 411736; fantech, 2016; pp 1–4.
(201) Conservation Strategies. Specifications for the APT System and Accessories. *Conservation Strategies*. February 26, 2010, pp 1–3.

(202) Hay, N.; Spencer, A. Discharge Coefficients of Cooling Holes With Radiused and Chamfered Inlets. *Journal of Turbomachinery* **1992**, *114* (701), 1–6.
(203) Taslim, M.; Ugarte, S. Discharge Coefficient Measurements for Flow Through Compound-Angle Conical Holes with Cross-Flow. *The International Journal of Rotating Machinery* **2004**, *10* (2), 145–153.
(204) Incropera, F.; Dewitt, D.; Bergman, T.; Levine, A. *Fundamentals of Heat and Mass Transfer*, 6 ed.; John Wiley & Sons : Hoboken, 2007; pp 1–10.
(205) Frigge, M.; Hoaglin, D. C.; Iglewicz, B. Some Implementations of the Boxplot. *The American Statistician* **1989**, *43* (1), 50–54.
(206) Cheng, Y.-H. Real-Time Performance of the microAeth® AE51 and the Effects of Aerosol Loading on Its Measurement Results at a Traffic Site. *Aerosol Air Qual. Res.* **2013**, 1–11.
(207) *West Oakland Specific Plan: Land Use*; City of Oakland: Department of Building and Planning : Oakland, 2014; pp 1–104.

Appendix A – Supporting Information: Experimental Optimization of Secondary Air Injection in a Wood-Burning Cookstove

A1 – Materials and Methods

A1.1 Modular Stove (MOD)

The MOD stove, shown in Figure 1, is a continuously fed, wood-burning cookstove that enables rapid, parametric adjustments of five critical air injection design features: (1) Pot height, (2) Fuel grate height, (3) Size of the opening in the stove body for primary air entrainment (known as the primary air intake), (4) Secondary air injection pattern (number and arrangement of holes), and (5) Secondary air injection flow rate. Three bolts are mounted through a conical potholder, as shown in Figure A1, to support the pot. Washers are placed under the bolts to change the height of the pot relative to the throat opening in the stove.

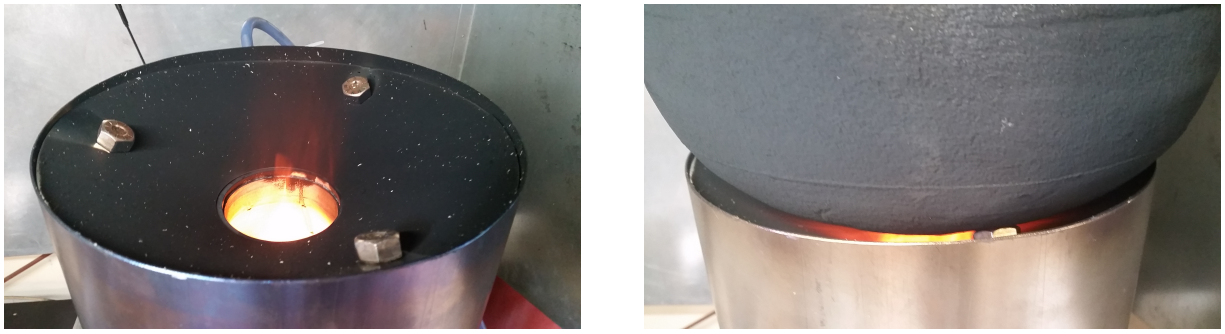

Figure A1. Three adjustable bolts that support the pot (left). Bolt height can be adjusted to modulate the gap between the pot and stove (right).

The grate is mounted along a series of 'tracks' in the stove body, as shown in Figure A2. These tracks allow the grate to be moved up and down relative to the air injection manifold. After adjustment, the grate is secured at the height setting using a pipe clamp.

Figure A2. Grate tracks on MOD stove, allowing grate height to be easily adjusted.

The primary air intake consists of an opening located at the front of the stove body, below the grate. The size of the primary intake is adjusted using a ring that rotates to allow the size of the opening to be varied, as shown in Figure A3.

Figure A3. Primary air intake on the front of the MOD stove, with adjustable ring (mounted using hose clamp)

A1.2 Experimental Setup

All experiments were conducted in the Lawrence Berkeley National Laboratory cookstove research facility, schematically represented in Figure A4. With this laboratory system, we have found that an air flow rate of 5660 LPM (200 CFM) through the duct is sufficient to ensure complete capture of emissions at the hood, but also low enough that it does not induce any drafting of the stove being tested. Two blowers in parallel are required to draw this volumetric flow rate of air through the duct. The flow rate is set to 5660 LPM by adjusting the blowers' speed with a motor controller.

The duct system has an initial 3-m (10-foot) length of 254-mm (10-inch) diameter ducting (known as the 'dilution tunnel') that is directly connected to the apex of the smoke hood using a ninety-degree elbow with a 152-mm (6-inch) diameter. Three sampling probes, constructed from flexible copper or stainless steel tubing of varying diameters, are mounted to the dilution tunnel using an access panel located 2 m (80 inches) downstream of the hood. At the nominal flow rate of 5660 LPM, the Reynolds number in the dilution tunnel is 3.9×10^4, well within the turbulent regime. Assuming fully developed turbulent flow in a duct, the characteristic mixing length of air in air is simply equal to the duct diameter.[192,193] Therefore, the laboratory's dilution tunnel provides about 8 characteristic mixing lengths, ensuring that the flow is well mixed prior to sampling by the instruments.

Sampling probes for gravimetric and real-time PM measurements are parallel to the longitudinal axis of the dilution tunnel (with their openings facing directly into the flow), and located on the horizontal plane at the center of the tunnel, offset by about 50 mm (2 inches) from either side of the tunnel's central axis. The sampling probe for gaseous emission measurements is mounted behind the PM sampling probes, but not directly downstream. The gas sampling probe extends about 100 mm (4 inches) into the duct and the opening is transverse to the flow (to

reduce the amount of ash and debris that is aspirated). The mounting arrangement of the three sampling probes in the duct is illustrated in Figure A5.

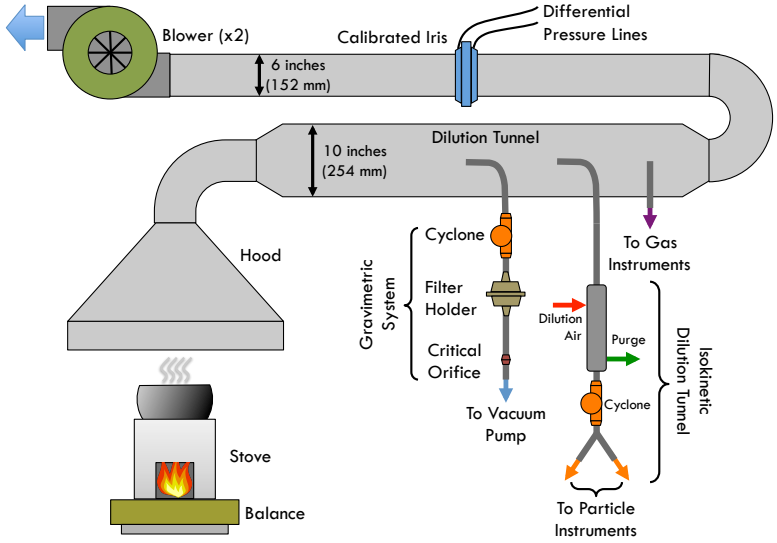

Figure A4. Schematic of cookstove testing facility at Lawrence Berkeley National Laboratory

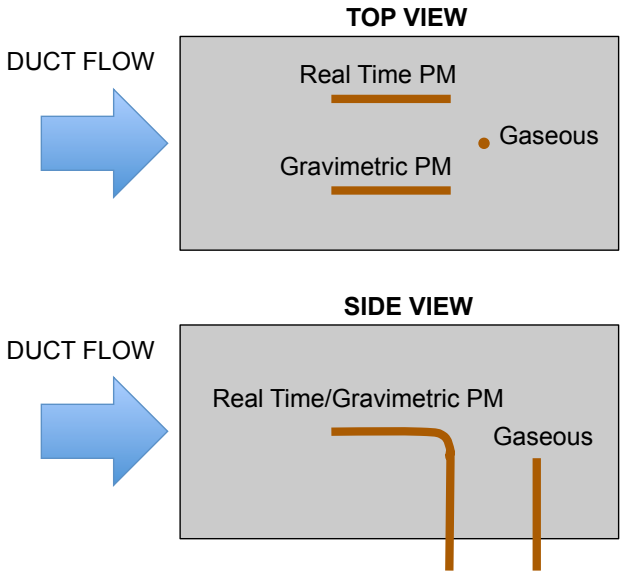

Figure A5. Schematic representation of instrument sampling probes (real time PM, gravimetric PM and gaseous emissions measurements) in the exhaust duct's dilution tunnel. Both top and side views of the tunnel are provided.

Both PM probes sample exhaust from the duct isokinetically, such that the velocity of the sample flow in the probes matches the velocity of the duct flow. Isokinetic sampling ensures that particle distributions are not biased by changes in particle momentum imparted during sampling. The exhaust flow velocity through the 254-mm (10-inch) duct at the nominal 5660 LPM (200 CFM) flow rate is 1.87 m/s. The gravimetric PM measurement system, shown in Figure A4, samples at a constant 16.7 LPM using a probe with a 14-mm (0.55-inch) inner diameter,

providing a sample flow velocity of 1.82 m/s that closely matches the nominal duct velocity. The sample flow subsequently passes through a BGI Very Sharp Cut Cyclone (VSCC) with a nominal cut point of 2.5 μm prior to collection on a 47-mm filter. Filter flow rate is driven by a vacuum pump and maintained at a constant 16.7 LPM using a critical orifice. In an effort to reduce testing costs, Quartz filters (~$0.50 each) were used for exploratory and initial parametric testing of the MOD stove, while PTFE-coated glass fiber filters (~$5.00 each) were used for final replicate testing of optimized cookstove configurations. The filters are humidity conditioned and weighed on a calibrated microbalance both before and after each test. The difference in the filter's mass before and after testing is used to calculate the total mass of $PM_{2.5}$ emitted during the test sequence.

Pollutant concentrations in the duct are typically an order of magnitude greater than the ambient concentrations for which the real-time PM measurement instruments are designed. Consequently, a secondary diluter was designed to reduce PM concentrations in the sampled flow, while maintaining isokinetic sampling conditions. A detailed overview of the secondary diluter's operation is provided in Appendix A5. The diluted flow passes through a cyclone with a nominal cut point of 2.5 μm prior to measurement by the TSI 3091 Fast Mobility Particle Sizer, TSI 3321 Aerodynamic Particle Sizer and Magee Scientific AE-22 Aethalometer.

Moisture content of the fuel wood was measured using a Delmhorst J-2000 moisture meter (calibrated using an oven-drying technique).[194] A thermocouple data logger was used to measure water, duct, and ambient temperature. An Energy Conservatory Automated Performance Testing system (APT-8) equipped with eight pressure sensors and a relative humidity sensor was used to measure duct humidity, differential pressure between the room and various locations in the exhaust duct, and differential pressure across the adjustable iris damper in the exhaust duct for determining duct flow rate. Real time fuel consumption and water evaporation were measured with an electronic platform scale (64 kg capacity and 0.1 g resolution) and a small scale was used for measuring unburned wood, char, and water loss from boiling (6 kg capacity and 0.1 g resolution). During each experiment, all exhaust sample flows (gaseous and aerosol) were periodically validated with a primary airflow calibrator (a Gilian Gilibrator that meets National Institute for Occupational Safety and Health (NIOSH) accuracy requirements).

At the beginning of each experiment day, all instruments were calibrated for offset using ultra high purity (99.999%) nitrogen for gas analyzers and ultra-zero air for particle instruments. The CAI-600 gas analyzer was also calibrated for span using 1000-ppm CO and 5000-ppm CO_2 calibration gases, and room air for O_2 calibration (assuming a constant ambient concentration of 21.0%). At the end of each experiment day, calibration of the instruments was validated to ensure accuracy.

A1.3 Cold Start Procedure

Cookstove performance and emissions are tested at a constant 5 kW firepower using the cold start phase of the Water Boiling Test (WBT) 4.2.3.[89] The 5-KW firepower set point was chosen because it represents the lowest achievable and maintainable firepower at which the TSF successfully boils 5 L of water. Due to the inherent difficulty of tending a TSF, it should be noted that the TSF's firepower varies more than the engineered stoves' firepower. For instance, the 90% confidence intervals of the mean firepower maintained during 10 replicate TSF and MOD stove tests are ± 0.4 and ± 0.06 KW, respectively.

During testing, firepower is monitored in real time using CO_2 concentration measurements from the duct. Since CO_2 is a primary product of combustion, CO_2 concentrations in the duct are directly dependent on the stove's firepower. The cookstove operator adjusts the fuel feed rate to reach and maintain a constant CO_2 concentration of 3000 ± 500 ppm, as this correlates to a firepower of roughly 5 kW (under our laboratory conditions).

Prior to each cold start test, the pot is cleaned of soot, and the stove completely emptied of char and ash. A fire is started in the stove using 15 g of pine shavings, and 60 g of Douglas Fir kindling cut uniformly into 6 x 6 x 72-mm (0.25 x 0.25 x 3-inch) pieces. Throughout the test, the stove is fueled using Douglas Fir wood cut into uniform 25 x 25 x 152-mm (1 x 1 x 6-inch) pieces and allowed to dry to 7-9% moisture content on a wet basis. Following test completion, the remaining water, unburned fuel, and char are weighed.

A1.4 Exploratory Testing Procedure

In order to reduce the total number of tests required to optimize the stove, the experimental testing procedure was divided into two distinct phases. The first phase of testing consisted of rapid, exploratory trials for operators to become familiar with the stove, investigate preliminary air injection flow rates and patterns, and enable initial bounding of the design parameters. These initial trials consist of a simplified cold start procedure that uses fewer emissions instruments to reduce preparation time. Although some basic performance and emissions metrics were calculated for these initial trials, stove parameters were mostly bounded as a result of visual observations and practical testing considerations. For example, it was found that air injection holes in the conical manifold should have a maximum diameter of 3.18 mm (0.125 inches) to create observable mixing jets in the firebox, and a minimum diameter of 1.59 mm (0.0625 inches), as smaller holes are difficult to drill and create excessive back pressure in the manifold. Similarly, secondary airflow rate was bounded to a minimum of 14 LPM (0.5 CFM), where mixing from the jets is first observed in the firebox, and maximum of 43 LPM (1.5 CFM), where direct jet impingement on the fuel starts to occur (which quenches the flame).

The placement of air injection holes in the vertical throat section of the conical manifold was found to prohibitively reduce thermal efficiency. In some tests that implemented air injection in the vertical throat, the water could not be brought to a full boil within 45 minutes. It is likely that the air injected directly into the throat section simply cools the exhaust, thereby reducing the rate of heat transfer to the pot. Consequently, all injection holes are drilled on the conical portion of the manifold, facing downwards into the firebox such that the air jets are aimed directly at the center of the burning fuel bed. After several trials, it was found that injecting air directly into the firebox significantly improves thermal efficiency relative to trials that implement injection in the vertical throat section.

The pot height was increased by stacking washers under the three support bolts until the stove operated consistently at 5 kW firepower without the flames protruding from the throat and touching the pot (thereby quenching the flames). The final setting, consisting of 9 washers stacked under the bolts, maintains a nearly constant gap of 15 mm (0.60 inches) between the pot and stove skirt. The pot-skirt gap was not increased past this set point to improve convective heat transfer from the exhaust gases to the pot.

Although most of the primary air enters the stove through the open fuel feed, and the resulting draft draws flames safely into the firebox, the adjustable intake at front of the stove body is intended to promote better air distribution in the firebox by allowing some air to enter through the fuel bed. However, if primary air intake through this adjustable opening is too large,

the remaining draft through the fuel feed can be insufficient to draw flames safely into to the firebox. Consequently, the adjustable primary air intake below the grate was progressively opened over several trials until flames just began escaping the fuel feed at 5 kW operation. The resulting intake is an opening with an area of roughly 4800 mm^2 (7.4 in^2).

The grate height was also adjusted using simple observations of combustion conditions in the firebox. After initial bounding of the injection flow rate to around 28 LPM (1 CFM), the grate was progressively moved upwards, closer to the air injection manifold, until the air injection jets were observed to cause visible mixing in the combustion zone without allowing flames to touch the manifold itself. After some experimentation, it was found that the vertical distance between the grate and lowest air injection holes should be set to roughly 57 mm (2.25 inches). It should be noted that grate height adjustments sometimes required corresponding adjustments in pot height. For example, when the grate was moved upwards towards the manifold, a washer or two would be added to the bolts supporting the pot to compensate from the heightened fuel bed and prevent flames from touching the pot directly.

In this way, simple experimental observations and practical testing considerations were used to find optimal settings for several air injection design parameters. Furthermore, these exploratory tests showed that the air injection pattern should be parameterized as three concentric rows arranged along the conical portion of the removable manifold cone.

Following 21 initial trials, optimal settings were identified for the pot height, grate height, primary air intake size, and air injection hole diameter, and these parameters were generally held constant for the remaining exploratory trials. The number and arrangement of air injection holes in the conical manifold was widely varied, with 12 distinct air injection patterns tested over 50 trials. Detailed descriptions of each injection pattern, and the resulting data from this testing phase are provided in Appendix A3. Furthermore, performance and emission metrics were calculated for all trials.

The shortened cold start procedure implemented during these exploratory trials omits several experimental measurements to accelerate the rate of testing. In order to execute complete calculations, the following assumptions were made to account for these omitted measurements:

- Water was measured volumetrically to 5 L, and assumed to have a constant mass of 5000 g.
- All kindling was measured out to a total mass of roughly 75 g using a balance, but the exact mass was not recorded. The kindling is assumed to have a constant mass of 75 g throughout.
- All fuel wood is assumed to have a moisture content of 9% on a wet basis.
- It is assumed that no wood or char left are left over in the stove at the end of the cold start.
- During the first 21 trials of the test phase, the water remaining at the end of the test and the pot are assumed to have a combined mass of 6760 g, while the pot alone is assigned a constant mass of 1713 g. These values are the mean values recorded for last 50 trials of exploratory testing, during which these measurements were taken. During this phase, the mass of the remaining water/pot and pot alone are 6760±10 g and 1713 ±1 g, respectively (mean ± 90% confidence interval over 50 trials).

Given the assumptions listed above, the results should not be compared directly to results from other test phases in this study. Instead, the results are intended to provide a comparative measure of performance and emissions for the parametric stove settings evaluated using the procedure and assumptions implemented during this phase alone. Three main metrics were analyzed to identify highly performing air injection patterns: Thermal efficiency (%), CO

emissions (g/kWd), and PM emissions (mg/kWd). Using these metrics, provided in Section A2.1, two air injection patterns were identified that provide low emissions while maintaining high thermal efficiency. These two patterns were chosen for further parametric testing.

A1.5 Parametric Testing Procedure

During the parametric testing phase, only two air injection patterns were tested at air injection flow rates of 21, 28, and 35 LPM (0.75, 1, and 1.25 CFM), while all other design parameters were held constant at the optimal values identified during exploratory testing. Both injection patterns are illustrated in Figure A6 below. The first injection pattern consists of two concentric rows with six holes each. The bottom row is located at the lowest point on the manifold, where the conical portion of the manifold meets the flat mating lip, and the top row is located 13 mm (0.50 inches) below the throat (at the top of the cone). The second air injection pattern is similar, but the bottom row has 9 holes and the top row (with six holes) is located 25 mm (1.0 inch) below the throat. In both patterns, all holes in each row are equally spaced around the circumference of the conical manifold, and have a diameter of 1.59 mm (0.0625 inches).

During parametric testing, the WBT cold start procedure was implemented, including the measurements omitted during exploratory testing. The experimental performance of the MOD stove is evaluated as function of air injection flow rate and velocity (as calculated using Equation A1 below). Residence time in the combustion zone is another valuable parameter commonly investigated in solid biomass combustion studies. However, determination of residence time typically requires accurate measurements of both the primary and secondary air supply flow rates into a closed combustion volume. Since primary air is naturally drafted into the MOD stove through the open fuel feed and air intake, primary air flow rate into the firebox can not be measured accurately, and it is not possible to calculate residence time.

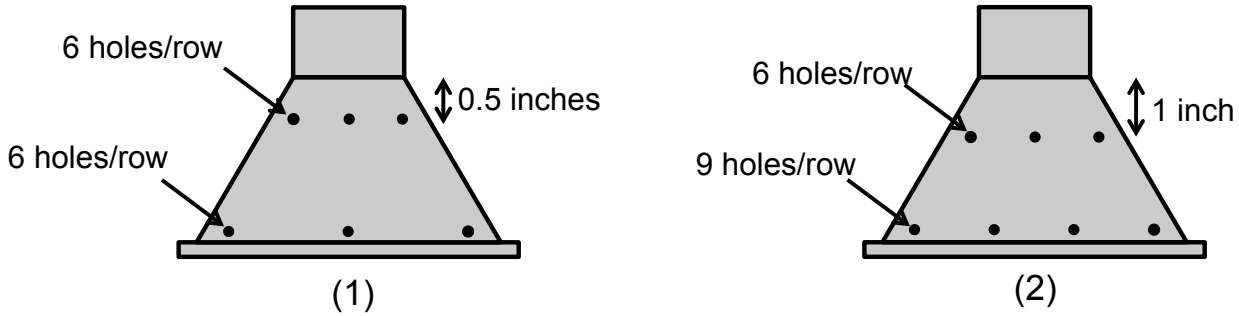

Figure A6. Two air injection patterns implemented during parametric testing: (1) Pattern 1 with 12 holes total; (2) Pattern 2 with 15 holes total. All holes have a diameter of 1.59 mm (0.0625 inches), and are evenly distributed around the circumference of the conical manifold. (Not to scale)

A1.6 Data Analysis

The air injection velocity for each test is calculated as function of the air injection flow rate, and the number and diameter of holes in the air injection pattern. All injection patterns analyzed have equally sized holes throughout. Since these air injection holes are very small relative to the manifold and spaced far apart from one another, it is assumed that the pressure distribution in the manifold is uniform, and that the resulting air flow rate through each hole in

the injection pattern is equal. Using this assumption, the air injection velocity (v) can be calculated as follows,

$$v\left[\frac{m}{sec}\right] = \frac{Q[\frac{m^3}{sec}]}{\frac{1}{4}\times\pi N\times D_h^2[m^2]} \qquad \text{(A1)}$$

where Q is the total air injection flow rate, N is the total number of holes in the air injection pattern, and D_h is the diameter of the holes in the air injection pattern.

The flow rate through the duct is calculated using differential pressure measurements from a calibrated iris damper in the duct. This iris is calibrated according to the methods presented in Appendix A4. Using the discharge coefficient and iris diameter output by this calibration method, Equations A10 and A11 can be used to calculate the volumetric duct flow rate in real time.

Performance metrics, such as firepower, equivalent dry mass of fuel consumed, and thermal efficiency, are calculated using the methods provided in the WBT Protocol 4.2.3.[89] Emission factors, however, are calculated using the equations outlined below, and do not implement the carbon balance or total capture calculation methods presented in the WBT Protocol. The total mass of PM emitted during the cold start phase is calculated using the mass measurement of PM collected on the 47 mm gravimetric filter as follows,

$$PM_{2.5\_tot}[mg] = PM_{2.5\_filter}[mg]\times\frac{\bar{Q}_{duct}[CFM]}{Q_{sample}[CFM]} \qquad \text{(A2)}$$

where $PM_{2.5\_tot}$ is the total mass of PM emitted during the cold start, $\bar{Q}_{duct}$ is the average duct flow rate throughout the test (nominally 5660 LPM, or 200 CFM,), Q_{sample} is the constant sample flow rate through the gravimetric filter (nominally 16.7 LPM, or 0.590 CFM), and $PM_{2.5\_filter}$ is the mass of $PM_{2.5}$ collected on the 47 mm filter, calculated as the difference in the filter's mass before and after testing. The total mass of gaseous emissions (CO and CO_2) are calculated using volumetric concentration measurements from the CAI gas analyzer logged at 1 Hz,

$$m_{gas}[g] = \sum_{t=0}^{t=t_f}\frac{C_{gas}(t)[ppmv]\times MW[\frac{g}{mol}]\times Q_{duct}(t)[m^3/sec]\times P_{amb}[Pa]\times\Delta t[sec]}{R\ [J/(mol\ K)]\times(T_{duct}(t)[^\circ C]+273)} \qquad \text{(A3)}$$

where m_{gas} is the total mass of gaseous emissions, t is the time step, t_f is the duration of the cold start test, C_{gas} is the volumetric gas concentration, MW is the molecular weight of the gas species, Q_{duct} is the flow through the duct measured every second at the iris damper, P_{amb} is the ambient pressure (97.77 KPa at the laboratory's altitude of 300 m MSL), Δt is the sampling period (1 second), R is the ideal gas constant (8.314 J/ (mol K)), and T_{duct} is the temperature in the duct, also logged every second. Similarly, the total mass of BC is calculated using mass concentration measurements from the AE-22 aethalometer logged at 1 Hz,

$$m_{BC}[g] = \sum_{t=0}^{t=t_f} C_{BC}(t)[g/m^3]\times Q_{duct}(t)[m^3/sec\ ]\times\overline{\mathrm{DR}}\times\Delta t[sec] \qquad \text{(A4)}$$

where m_{BC} is the total mass of black carbon, C_{BC} is the black carbon concentration, and $\overline{DR}$ is the mean dilution ratio through the secondary diluter over the course of the test. Throughout each test, the secondary dilution ratio is calculated in real time as the ratio of CO_2 concentrations in the duct and diluted sampled flow, as outlined in Appendix A5.

The total particle number and volume distributions are calculated using $dN/dlog(D_p)$ data from the FMPS and APS, where dN is the PM concentration in units of number of particles per cubic centimeter of air per particle size bin, and $dlog(D_p)$ is the logarithmic width of the corresponding particle size bin in log nanometers. Each instrument has a constant logarithmic bin width throughout their measurement range. The total particle number distribution generated over the course of a cold start test $dN_t/dlog(D_p)$ is calculated for each particle bin using,

$$\left(\frac{dN_t}{dlogD_p}\right)_{D_p}[\#] = \sum_{t=0}^{t=t_f}\left(\frac{dN}{dlogD_p}\right)_{t,D_p}\left[\frac{\#}{cm^3}\right]\times\overline{DR}\times\bar{Q}_{duct}\left[\frac{cm^3}{sec}\right]\times\Delta t\ [sec] \qquad \text{(A5)}$$

where D_p is the particle diameter at which the measurement bin is centered, and $\left(\frac{dN}{dlogD_p}\right)_{t,D_p}$ is the particle number concentration at time t and particle bin diameter D_p. When applied to all particle bins over each instrument's measurement range, this equation yields a distribution of the total number of particles generated by the stove over the test duration as a function of particle diameter.

Using the total number distribution generated with Equation A5, the total particle volume emitted over the cold start test $dV_t/dlog(D_p)$ can be calculated at each measurement bin,

$$\left(\frac{dV_t}{dlogD_p}\right)_{D_p}[cm^3] = \frac{\pi D_p^3}{6}[cm^3]\times\left(\frac{dN_t}{dlogD_p}\right)_{D_p} \qquad \text{(A6)}$$

This equation can be applied at each measurement bin to provide the total volume distribution. This total volume distribution can subsequently be integrated over the particle diameter range to calculate the total volume of particles emitted over the cold start phase,

$$V_t[cm^3] = \sum_{D_p=d_i}^{D_p=d_f}\left(\frac{dV_t}{dlogD_p}\right)_{D_p}[cm^3]\times dlogD_p \qquad \text{(A7)}$$

where d_f and d_i are the upper and lower bounds of the particle diameter range over which to integrate, and $dlogD_p$ is the constant logarithmic bin width inherent to each instrument. For the FMPS, $dlogD_p$ has a constant value of 0.0625, while for APS it has a value of 0.0313. It should be noted that in order to merge data from both the APS and FMPS, the particle concentration distributions from the APS must be converted from aerodynamic diameter to electrical mobility diameter according to the procedure provided in section A1.7 below.

The TSI FMPS outputs PM number concentration measurements for particles with diameters ranging from 5 to 562 nm. However, it was found that the last four measurement bins provided by the instrument (centered at 341, 393, 454, and 525 nm) provide highly variable data at low PM number concentrations. Consequently, for parametric settings with a relatively low

number of replicate tests, the 90% confidence interval can exceed the mean of particle concentration measurements in this diameter range. For example, for the set of 4 tests conducted at an air injection flow rate of 21 LPM (0.75 CFM) and velocity of 15 m/s, the total number of particles emitted during the cold start at a diameter of 341 nm is calculated to be $3.22\times10^{11} \pm 3.65\times10^{11}$ (mean ± 90% confidence interval). Given these highly variable particle concentration measurements, the last four bins of the FMPS measurement range are not reported nor used in calculations.

A1.7 PM Density Correction

The TSI FMPS provides PM concentrations as a function of electrical mobility diameter from 5 to 560 nm. The TSI APS, however, provides PM distributions as function of aerodynamic diameter from 520 to 20,000 nm. In order to combine data from both instruments and create PM distributions that continuously span the entire measured particle diameter range from 5 nm to 2500 nm, aerodynamic diameter measurements from the APS must be converted to electrical mobility diameter. It should be noted that although the APS is capable of measuring particles up to 20,000 nm in diameter, the sample flow for all PM instruments passes through a $PM_{2.5}$ cyclone to remove all particles with aerodynamic diameters greater than 2500 nm.

Aerodynamic diameter can be converted to electrical mobility diameter using [99],

$$D_p = D_a \sqrt{\gamma \frac{C_S(D_a)\rho_o}{C_S(D_p)\rho_p}}. \qquad \text{(A8)}$$

In Equation A8, D_p is the electrical mobility diameter, D_a is the aerodynamic diameter, C_s is the slip correction factor (as a function of particle diameter), Υ is the shape correction factor, ρ_o is the unit density (1 g/cm^3), and ρ_p is the particle density. For the particle diameter and density range under consideration, the slip correction factors can be neglected.[99] Without knowledge of the particle morphology, as might be obtained using microscope images of the PM emitted, the particles are assumed to be spherical and the shape correction factor is set to 1. However, this is a simplifying assumption, as studies show that particles emitted by wood combustion are often not spherical.[92,100] Using this set of assumptions, the aerodynamic diameter conversion equation reduces to Equation A9 below.

$$D_p = \frac{D_a}{\sqrt{\rho_p}} \qquad \text{(A9)}$$

The equation above shows that the aerodynamic diameter can be converted to electrical mobility diameter using only the particle density. Particle density is evaluated as the ratio of the total particle mass and total particle volume emitted over each cold start test. The total mass of particles emitted is calculated using gravimetric measurements and the methods previously provided. Total particle volume, however, must be calculated using the PM distributions provided by the FMPS and the APS. Given that the APS data must be corrected using this same information, the particle density must be calculated implicitly. An iterative loop was implemented in MATLAB with the steps outlined below. During these calculations, the last four measurement bins of the FMPS are omitted from the distribution, as PM concentration data at the limits of the FMPS measurement range is highly variable.

1. Initially assume that the particles have unit density (1 g/cm^3)
2. Combine the FMPS and APS data into a single, continuous distribution. Remove APS concentration data for particle diameters smaller than the largest FMPS bin (393 nm) and larger than 2500 nm.
3. Using this complete distribution spanning from 5 to 2500 nm, calculate the total particle volume emitted during the cold start test using Equation A7.
4. Calculate particle density as the ratio of total particle mass (determined using Equation A2) and total particle volume from Step 3.
5. Using the calculated particle density, convert the APS aerodynamic diameter bins to electrical mobility diameter according to Equation A9.
6. Using the converted APS bins, combine the FMPS and APS distributions according to Step 2 and repeat the process to calculate a new particle density. Evaluate the difference in the density calculated during each iteration loop, and continue to iterate until the error from one iteration to the next is less than 0.1%.

Using this approach it is possible to calculate the effective particle density for each trial, and subsequently use this value to convert the APS distribution to electrical mobility diameter.

A2 – Results and Discussion

A2.1 Exploratory Testing Results

Appendix A4 provides a complete set of data and results for all 71 trials conducted during exploratory testing. During the initial 21 trials, basic visual observations and practical testing considerations were used to identify optimal values for many design parameters (grate height, pot height, and primary air intake). For the remaining 50 exploratory trials, these parameters were generally held constant as 12 distinct air injection patterns were tested. A total of 32 replicate tests were conducted at a flow rate of 28 LPM (1 CFM) for 6 promising injection patterns, listed Table A1 in below. Figure A7 provides bar plots of three performance metrics using each of the six air injection patterns.

Pattern ID	Top Holes	Middle Holes	Bottom Holes
1	0	0	6
2	0	3	6
3	0	3	9
4	0	6	6
5	0	6	9
6	6	0	6

Table A1. Secondary Injection Patterns for Replicate Testing

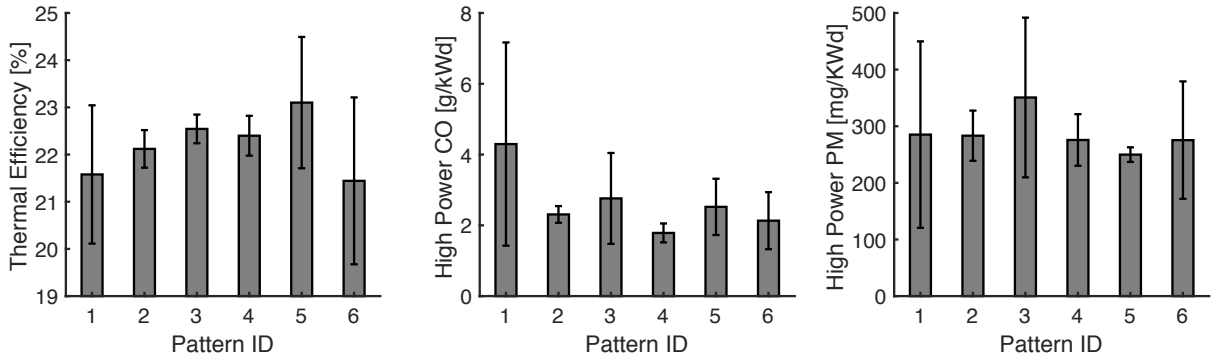

Figure A7. Mean Performance and emissions metrics for replicate testing of six air injection patterns, detailed in Table A1, while all other stove design parameters are held constant. The error bars represent the 90% confidence interval.

Figure A7 allows the six air injection patterns to be compared directly. After considering all three metrics depicted in the figure, patterns 4 and 5 were chosen for further testing. Pattern 4 was chosen because it provides the lowest mean CO emissions in the set, an indication of improved combustion, while maintaining high thermal efficiency and low PM emissions. Pattern 5 was chosen because it emits the least PM in the set and has the highest thermal efficiency. All patterns were considered, but some were not chosen for various reasons. For example, Pattern 1 was not chosen because of its highly variable performance, as evidenced by the large confidence intervals for all metrics. Pattern 2 was omitted because it performs similarly to Pattern 4, but with slightly worst mean results in each metric. Finally, Pattern 3 was excluded because of high PM and CO emissions, while Pattern 6 was removed for low thermal efficiency.

A2.2 Parametric Testing

Parametric testing consisted of 63 trials, in which two injection patterns were tested at three injection flow rates (21, 28, and 35 LPM) while all other design parameters were held constant. The full set of data and results for this phase of testing is provided in Appendix A3.

A2.3 Performance Evaluation: Optimal MOD vs. TSF

Using the experimental optimization presented in this study, it was determined that an air injection flow rate of 28 LPM (1 CFM) at a velocity of 20 m/s (using air injection pattern 1, shown in Figure A6) is the optimal MOD stove configuration. Twelve replicate tests of this configuration were conducted, and compared to ten replicate tests of a traditional Three Stone Fire (TSF). The TSF performance data presented is cited directly from a comparative study of several improved biomass cookstove designs by Rapp et al.[75] Table A2 provides mean performance and emissions metrics for the TSF and optimal MOD stove, and the corresponding percent change from TSF to MOD (with 90% confidence intervals). Table A3 and Table A4 provide performance and emissions metrics for each individual MOD stove and TSF trial, respectively.

	TSF	MOD	Change (%)
Firepower (KW)	5.3 ± 0.4	4.93 ± 0.06	- 7 ± 8
Thermal Efficiency (%)	23.3 ± 0.7	26.2 ± 0.4	12 ± 3
CO (g/KWd)	17 ± 3	2.1 ± 0.2	- 88 ± 2
$PM_{2.5}$ (mg/KWd)	1200 ± 200	130 ± 10	- 89 ± 2
BC (mg/KWd)	530 ± 50	35 ± 3	- 93 ± 1
BC/ $PM_{2.5}$	0.44 ± 0.08	0.27 ± 0.03	- 40 ± 70

Table A2. Mean performance and emissions metrics for a three stone fire (TSF) and the modular stove (MOD), and the percent change of each metric from TSF to MOD.

MOD TRIAL:	1	2	3	4	5	6	7	8	9	10	11	12
Time to boil [min]	23.8	23.6	24.1	24.2	24.6	24.2	25.8	25.6	25.7	26.4	24.4	25.3
Corrected time to boil [min]	25.2	25.5	25.1	26.0	24.0	23.9	26.0	24.9	25.3	26.7	24.3	25.7
Equivalent dry wood consumed [g]	0.378	0.373	0.398	0.389	0.383	0.390	0.403	0.404	0.407	0.402	0.412	0.383
Firepower [KW]	4.96	4.95	5.15	5.03	4.86	5.03	4.88	4.93	4.95	4.77	5.29	4.75
Thermal Efficiency	0.262	0.249	0.252	0.257	0.274	0.263	0.267	0.267	0.261	0.255	0.254	0.275
Combustion Efficiency	0.992	0.992	0.993	0.991	0.993	0.994	0.995	0.993	0.994	0.993	0.993	0.994
CO_2 Total mass [g]	545	512	508	547	570	573	546	595	593	592	582	581
CO Total mass [g]	2.71	2.74	2.19	3.21	2.69	2.17	1.88	2.55	2.15	2.54	2.58	2.11
$PM_{2.5}$ Total mass [g]	0.13	0.19	0.15	0.15	0.24	0.16	0.13	0.19	0.16	0.31	0.18	0.15
BC Total mass [g]	0.048	0.046	0.048	0.048	0.039	0.041	0.042	0.034	0.041	0.071	0.091	0.063
CO/Cooking energy [g/MJd]	1.46	1.57	1.16	1.71	1.37	1.13	0.93	1.26	1.08	1.32	1.31	1.07
$PM_{2.5}$/Cooking energy [mg/MJd]	68.6	111.5	79.1	79.1	124.3	83.6	66.2	94.6	78.5	159.7	92.7	73.4
BC/Cooking energy [mg/MJd]	26.0	26.6	25.5	25.4	20.0	21.2	21.0	16.9	20.6	36.8	46.3	32.0
CO/ cooking emissions [g/KWd]	2.08	2.22	1.69	2.49	2.02	1.65	1.44	1.94	1.66	2.09	1.92	1.62
$PM_{2.5}$/ cooking emissions [mg/KWd]	98.2	157.7	114.6	114.6	183.7	121.5	102.6	145.5	121.0	252.9	135.4	111.1
BC/ cooking emissions [mg/KWd]	37.2	37.6	36.9	36.8	29.6	30.8	32.6	25.9	31.8	58.2	67.7	48.5

Table A3. Performance and emission metric for 12 replicate trials of the MOD in the optimal parametric configuration (flow rate = 28 LPM, velocity = 20 m/s)

TSF TRIAL	1	2	3	4	5	6	7	8	9	10
Time to boil [min]	34.3	25.8	26.5	21.6	27.3	31.2	40.8	35.2	32.7	34.2
Corrected time to boil [min]	32.8	24.6	26.2	23.9	30.9	31.1	38.2	37.4	34.5	33.3
Equivalent dry wood consumed [g]	0.566	0.476	0.491	0.443	0.529	0.429	0.574	0.472	0.602	0.545
Firepower [KW]	5.15	5.77	5.78	6.41	6.07	4.30	4.41	4.19	5.76	4.98
Thermal Efficiency	0.215	0.242	0.242	0.224	0.209	0.280	0.239	0.248	0.194	0.233
Combustion Efficiency	0.962	0.966	0.964	0.958	0.963	0.959	0.955	0.952	0.960	0.952
CO_2 Total mass [g]	780	670	735	599	740	814	908	740	886	834
CO Total mass [g]	19.8	15.2	17.7	16.7	18.2	22.3	27.5	23.9	23.3	26.6
$PM_{2.5}$ Total mass [g]	1.14	1.35	1.27	1.90	1.68	1.72	1.65	1.01	2.03	1.07
BC Total mass [g]	0.651	0.707	0.564	0.547	0.744	0.675	0.586	0.559	0.697	0.625
CO/Cooking energy [g/MJd]	8.7	7.0	7.9	9.0	8.8	9.9	10.7	10.8	10.6	11.1
$PM_{2.5}$/Cooking energy [mg/MJd]	498	623	568	1020	808	760	642	461	928	448
BC/Cooking energy [mg/MJd]	285	327	253	295	358	299	228	254	318	262
CO/ cooking emissions [g/KWd]	17.9	10.9	12.6	11.6	14.3	18.5	26.1	22.9	20.9	22.9
$PM_{2.5}$/ cooking emissions [mg/KWd]	1025	965	904	1321	1323	1422	1569	975	1820	919
BC/ cooking emissions [mg/KWd]	588	506	403	381	586	559	557	537	624	538

Table A4. Performance and emission metric for 10 replicate trials of the TSF

A2.4 Particulate Emissions: Parametric Study

Particulate number concentrations were measured using the FMPS and APS during all parametric testing trials. Using the methods outlined in Section A1, the average particle density from all 63 parametric trials was calculated to be 2.4 ± 0.2 g/cm^3 (mean of all trials and 90% confidence interval). This density value was used to correct all APS data presented in the parametric PM study of the MOD stove. Figure A8 below provides size distributions of total particle number and volume emitted over the cold start, normalized by the average cooking power, for each of the six parametric configurations tested. Each curve represents the mean distribution of all trials conducted at each parametric configuration, and confidence intervals are omitted to enhance plot visibility. Overall, the plot shows that the MOD stove generates the lowest volume (and proportionally, mass) of particles at a flow rate of 28 LPM and injection velocity of 20 m/s, while number generation is minimized at a flow rate of 21 LPM and velocity of 15 m/s.

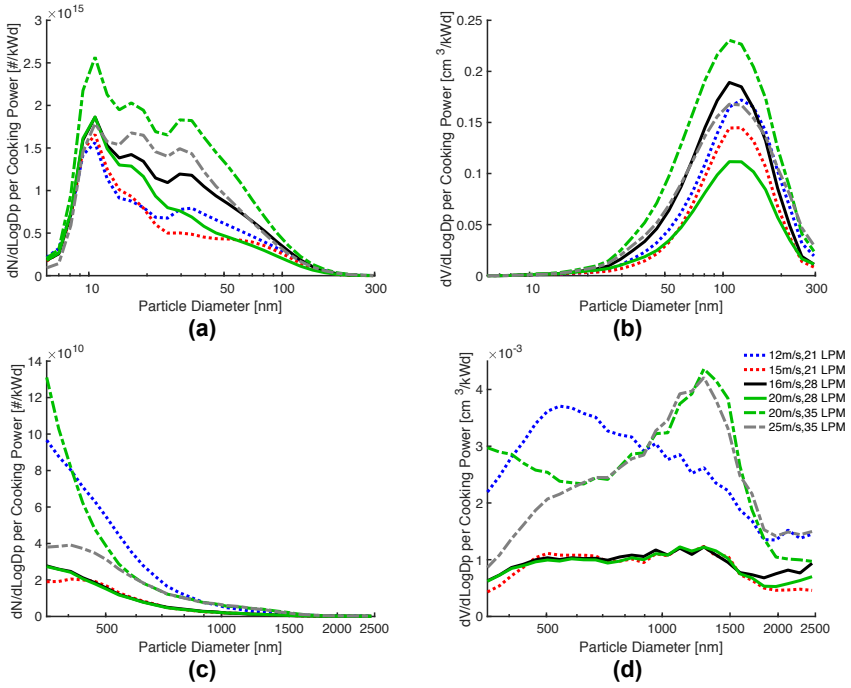

Figure A8. Average size distributions of total particle number and volume emitted over the cold start (normalized by the average cooking power) for all six parametric configurations tested. Distributions are measured by the FMPS (A and B) and APS (C and D).

Figure A9 through Figure A11 below provide total particle number and volume distributions for both velocity settings tested at each of the three air injection flow rates (21, 28, and 35 LPM). In these plots, the curves represent the mean distribution of all trials conducted at each parametric setting, while the shaded areas represent 90% confidence intervals.

The particle distributions emitted at an air injection flow rate of 21 LPM (provided in Figure A9), show that increasing injection velocity generally decreases PM emissions larger than 30 nm. However, size-resolved measurements were only collected during 4 trials at each of the velocity settings tested at 21 LPM. Consequently the distributions' confidence intervals are large and overlap throughout much of the measurement range, making the identification of definitive parametric trends difficult. Similarly, the distributions generated at a flow rate of 35 LPM (shown in Figure A11) also have large confidence intervals because size-resolved measurements were only collected during 3 and 5 trials at the low and high velocity settings, respectively. Many more trials were conducted at a flow rate of 28 LPM, and consequently the confidence intervals in Figure A10 are more constrained.

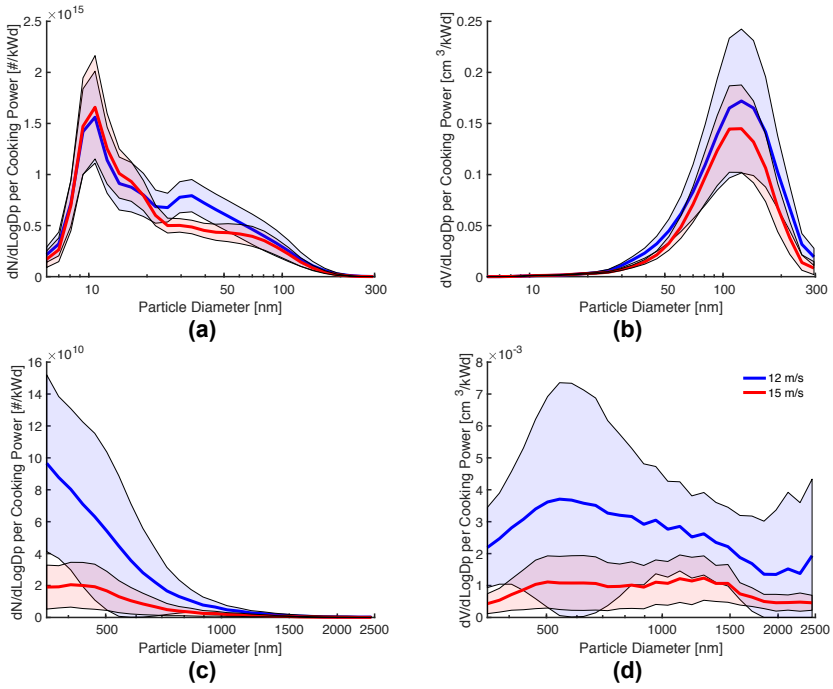

Figure A9. Size distributions of total particle number and volume emitted over the cold start, normalized by the average cooking power, for both air injection velocities tested at a secondary air flow rate of 21 LPM. Distributions are measured by FMPS (A and B) and APS (C and D).

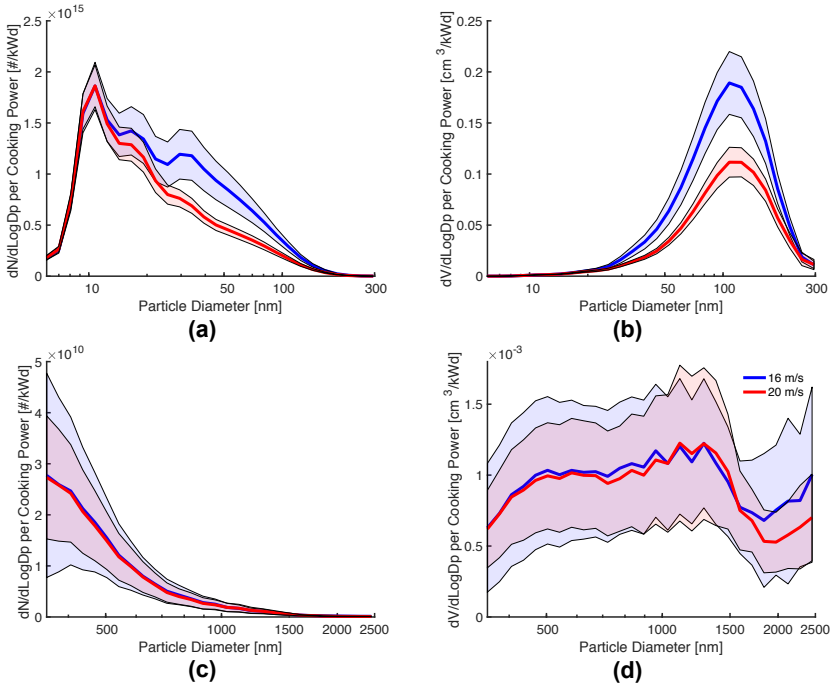

Figure A10. Size distributions of total particle number and volume emitted over the cold start, normalized by the average cooking power, for both air injection velocities tested at a secondary air flow rate of 28 LPM. Distributions are measured by the FMPS (A and B) and APS (C and D).

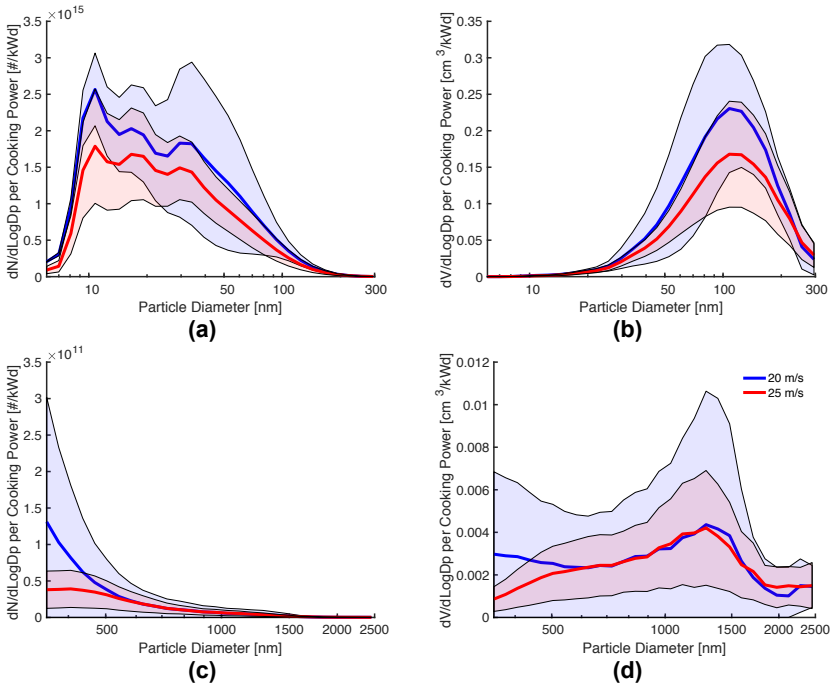

Figure A11. Size distributions of total particle number and volume emitted over the cold start, normalized by the average cooking power, for both air injection velocities tested at a secondary air flow rate of 35 LPM. Distributions are measured by FMPS (A and B) and APS (C and D).

A2.5 Particulate Emissions: Optimal MOD vs. TSF

The parametric particle distributions provided in Figure A8 show that the MOD stove minimizes volumetric PM emissions when operating at an air injection flow rate of 28 LPM, and injection velocity of 20 m/s. This trend supports the analysis of performance metrics, which also show that this configuration minimizes pollutant mass emissions. The total particle number and volume distributions are provided for the optimal MOD stove configuration and traditional TSF in Figure A12. These distributions represent the mean from 12 optimal MOD stove trials and 6 TSF trials. Similarly to the performance metrics presented previously, the size-resolved particle emissions data presented for the TSF are cited directly from a comparative study of several improved biomass cookstoves by Rapp et al.[75] In addition, it should be noted that the particle density correction applied to the APS data is different for the TSF and MOD stove. Using the method outlined in Section A1.7, it was found that the TSF and optimal MOD stove have particle densities of 1.5±0.2 g/cm^3 and 2.3±0.3 g/cm^3, respectively. These density values are used to correct the APS distributions provided below. In addition, it should be noted that during testing of the TSF, data were not collected for the first measurement bin of the APS, due to an instrument logging error. Consequently, the TSF distributions shown in Figure A12(c) and A12(d) begin at a particle diameter of 475 nm, rather than 440 nm (as adjusted for density).

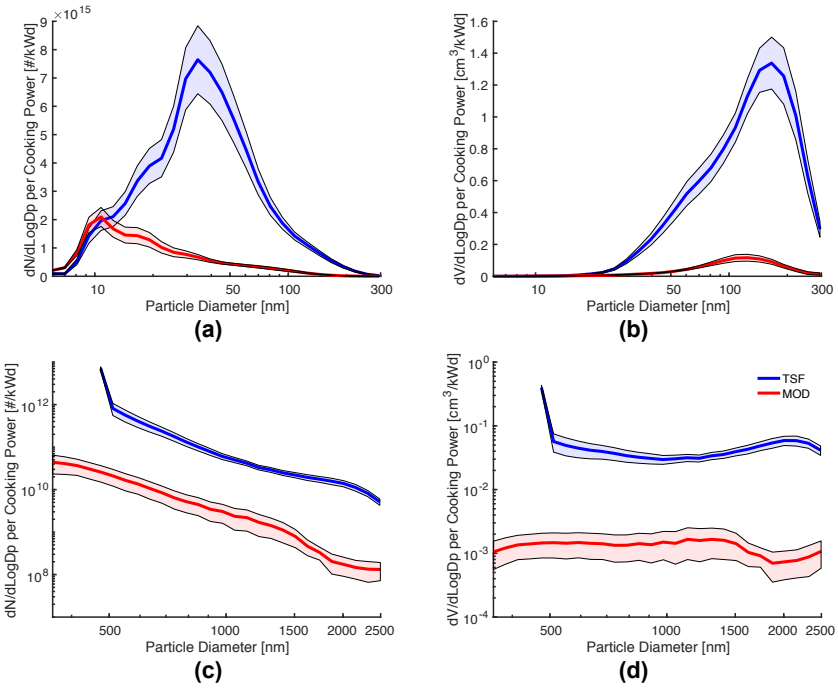

Figure A12. Size distributions of total particle number and volume emitted over the cold start, normalized by the average cooking power, for the traditional TSF and MOD stove in the optimal parametric configuration (flow = 28 LPM, velocity = 20 m/s). Distributions are measured by the FMPS (A and B) and APS (C and D).

Overall, the plots in Figure A12 show that the MOD stove reduces all PM emissions larger than 10 nm in diameter. Furthermore, Figure A12(b) shows that volumetric emissions with a diameter smaller than 500 nm are reduced by roughly an order of magnitude, while Figure A12 (c) and (d) show that particle emissions from about 500 to 2500 nm are reduced by nearly two orders of magnitude throughout.

A3 – Comprehensive Testing Data and Results

A3.1 Exploratory Testing

This section provides complete data and results from the exploratory phase of MOD stove testing. During the initial portion of this testing, incomplete data were often collected, as parametric stove adjustments were often made using experimental observations and practical testing considerations. Data collected for all 71 exploratory trials are provided in Table A5, while the stove design parameters implemented for each trial are provided in Table A6. It should be noted that the first two trials were not completed, as the water could not be brought to a boil within 40 minutes. Six trials were removed from the collected data set due to erroneous data collection resulting from instrumentation malfunctions, or stove operation far below the 5-KW firepower set point.

In the parametric settings presented in Table A6, the grill height is measured as the vertical distance between the top of the fuel feed and the grate, as this distance is convenient for the operator to measure. There is a constant vertical gap of 21 mm (1.25 inches) between the top

of the fuel feed and the bottom of the air injection manifold, which should be added to the recorded values presented if the total vertical distance between the grate and bottom of the manifold is desired. The height of the pot was measured in terms of the number of washers placed under the bolts supporting the pot. Each washer has a thickness of 0.78 mm (0.03125 inches). A pot height of 9 washers corresponds to a roughly constant 15 mm (0.60 inch) gap between the pot and stove skirt.

Table A7 provides a detailed description of each air injection pattern implemented. Generally, the air injection patterns were arranged in three concentric rows along the length of the sloped, conical portion of the removable air injection manifold (known as the 'cone'). The top row of holes was located 25 to 38 mm (1.0 to 1.5 inches) along the cone from the straight pipe 'throat' at the top. The bottom row was generally located 5 to 13 mm (0.25 to 0.50 inches) along the cone from the flat lip at the bottom. The middle row was located at a point equidistant from the top and bottom rows. For the last trials, row location was recorded more carefully as replicability of successful configurations became more important.

Nearly all injection patterns use only a single hole diameter throughout. Only the patterns tested during trials 28 and 29 of this phase used both 1.59 mm (0.0625 inch) and 3.20 mm (0.125 inch) diameter holes. These two patterns are excluded from all comparison analyses. Furthermore, some configurations were tested with a 'spiral' applied to air injection holes. This 'spiral' consists of using a screwdriver to bend the air injection holes in a uniform direction, with the resulting holes resembling the perforations on a cheese grater. These spirals are intended to create a swirled injection pattern that could potentially promote better mixing in the firebox. During experimentation, however, the spirals had no observable effect on the combustion or the air injection patterns' emissions performance, and are consequently treated as trials without spirals.

In order to accelerate stove testing, several experimental measurements were omitted during the initial 21 trials of this testing phase. In order to execute complete calculations, several assumptions were made to account for omitted measurements, as outlined in Section A1. The performance and emissions metrics calculated for each trial in this test phase are provided in Table A8 and Table A9.

Test	Water Initial (°C)	Wood Initial (g)	Wood Final (g)	Start	End	Final Pot/ Water (g)	Empty Pot (g)	Duct Flow (CFM)	Filter Mass (mg)
1	18.8	1018.4	NaN	10:37	NaN	NaN	NaN	NaN	NaN
2	18.7	1036.9	NaN	12:27	NaN	NaN	NaN	NaN	NaN
3	17.1	1060	572	10:28	11:00	NaN	NaN	NaN	NaN
4	18.3	1034.8	606.5	11:29	11:55	NaN	NaN	NaN	NaN
5	21.7	1042.5	585.6	12:57	13:23	NaN	NaN	NaN	NaN
6	23	944	479.2	13:14	13:47	NaN	NaN	NaN	NaN
7	20.5	1017.3	591.6	15:03	15:29	NaN	NaN	NaN	NaN
8	21.1	1002.3	550.6	16:25	16:58	NaN	NaN	NaN	NaN
9	24	932.2	398.3	13:15	13:50	NaN	NaN	NaN	NaN
10	22.7	938.9	441.8	14:13	14:41	NaN	NaN	NaN	NaN
11	23.6	942.2	425.7	14:59	15:26	NaN	NaN	NaN	NaN
12	21.7	924.4	402.4	12:55	13:24	NaN	NaN	NaN	NaN
13	22.4	938.7	376	14:18	14:45	NaN	NaN	NaN	NaN

14	21.9	964.4	402	15:20	15:48	NaN	NaN	NaN	NaN
15	22.2	1065.2	505.8	11:30	11:56	NaN	NaN	NaN	NaN
16	22	979.7	467.1	13:12	13:36	NaN	NaN	NaN	NaN
17	28.1	957.5	467.9	14:27	14:51	NaN	NaN	NaN	NaN
18	24.9	1032.7	495.2	11:43	12:15	NaN	NaN	200	2.5614
19	25.2	1058	526.8	13:12	13:38	NaN	NaN	200	2.0805
20	25.3	937.2	432.9	14:28	14:51	NaN	NaN	200	2.5351
21	24.6	988.9	500.2	15:17	15:39	NaN	NaN	200	2.9315
22	972.6	5001.1	474.3	11:06	11:35	6485.2	1720.4	205	2.135
23	926.2	5002.8	353.9	12:08	12:41	6330	1719.7	207	1.670
24	1022.5	5001.7	394.2	13:36	14:09	6390.1	1720.1	208	1.099
25	974.2	5001	414.5	13:21	13:49	6460	1718.1	210	1.470
26	964.6	5000	499.6	15:08	15:33	6463.2	1718.4	205	0.820
27	972.8	5002.3	528.7	16:29	16:53	6522.7	1718.3	208	0.956
28	946.9	5000.8	492.8	12:28	12:56	6430.5	1716.8	205	2.373
29	953.5	5003.1	507.4	13:59	14:27	6504.3	1717.2	205	2.173
30	960.1	5002.1	483.4	15:33	15:58	6484.1	1716.9	208	0.867
31	961.1	4999.3	457.3	10:57	11:24	6443.9	1715.8	205	0.638
32	957.3	4999.1	404	11:57	12:27	6388.7	1714.9	205	0.412
33	962.6	5001.5	474.8	12:56	13:21	6474.5	1714.3	205	0.965
34	965.1	5002.4	483.9	10:50	11:16	6493.7	1714.6	208	1.494
35	968.1	5002.7	529.3	11:58	12:23	6499.2	1714.4	208	1.076
36	959.9	5001.5	489.6	13:20	13:47	6458.4	1714.7	208	1.129
37	992.5	5000.7	504.7	14:19	14:43	6465.9	1714.1	207	0.726
38	932.6	5000.1	451.6	15:30	15:56	6489.5	1713.2	209	1.681
39	925.7	5000.2	470.9	10:43	11:07	6493.7	1713.7	212	1.477
40	923.9	4998.7	492.7	12:19	12:42	6486	1713.2	212	0.664
41	955.5	5001.2	520	13:31	13:55	6499.5	1713.3	212	1.679
42	923.4	5002.6	454	14:21	14:46	6480.5	1713.5	213	0.989
43	915.4	5007.8	461.8	10:45	11:12	6482.2	1713.4	205	1.154
44	996.6	5000.8	548.9	11:45	12:11	6482.4	1713.2	208	0.974
45	958	5000	487.6	13:00	13:27	6440	1713.3	205	0.880
46	974.6	5000.2	426	12:13	12:47	6337.9	1713.7	208	1.826
47	993.5	5001.5	492.6	13:26	13:54	6409.7	1713.2	210	1.467
48	945.2	5000.2	456	14:26	14:53	6457.9	1712.9	212	1.297
49	915.9	4997	385	11:58	12:29	6369.8	1712.8	214	1.330
50	964.4	5004.1	443.8	13:05	13:36	6390	1713.5	215	0.920
51	991	4999.7	511.3	14:53	15:22	6433	1712.9	206	0.719
52	998.2	4996.9	526.1	10:11	10:40	6497.1	1712.8	210	1.123
53	989.1	5004.6	518.8	11:31	11:58	6476.7	1712.4	205	0.681
54	957.6	5006.1	499.5	12:37	13:04	6491.5	1712.3	212	0.824

55	956.2	5002.5	482.4	14:06	14:33	6486	1712.4	205	0.829
56	1040.6	5007.5	543.9	11:29	11:56	6498.9	1711.8	207	1.245
57	924.9	5000.1	452.6	12:49	13:16	6477.8	1712.1	207	1.171
58	1048.1	5007.3	538.1	13:58	14:24	6459.5	1711.9	210	1.153
59	938.7	4997.9	474.6	15:06	15:35	6509.5	1711.6	210	1.174
60	992.1	5000.9	487.1	12:13	12:42	6466.8	1711.8	200	1.199
61	965.4	5000.7	535.2	13:25	13:50	6482.2	1711.6	199	0.927
62	997	5001	522.4	14:48	15:16	6465.9	1712.1	200	2.079
63	1015	5002.2	500.6	13:31	14:03	6453	1711	200	1.151
64	945.3	5004.4	465.2	14:48	15:17	6445.4	1711.1	200	0.928
65	1085.6	5000.8	568.1	10:56	11:24	6492.7	1710.9	128	1.424
66	959.4	5000.3	480.9	12:59	13:25	6510.7	1710.6	129	1.788
67	950	5002.8	471.9	14:16	14:41	6490.6	1710.4	127	1.666
68	923.8	5004	431.7	11:04	11:32	6473.5	1710.4	198	0.511
69	992.6	5002.6	515.1	12:19	12:44	6504.2	1710.2	200	1.189
70	953.4	5001.6	498.9	13:28	13:54	6479.1	1710.3	200	0.989
71	931.1	5003.6	472.4	15:01	15:28	6490.2	1710.2	200	0.996

Table A5. Exploratory Testing Collected Data

Test	Grill Height (in)	Pot Height (washer #)	Hole Diameter (in)	Top Holes	Middle Holes	Bottom Holes	Flow Rate (CFM)
1	NaN	6	0.125	6	6	6	1
2	0.7	6	0.125	6	6	6	1
3	0.7	6	0.125	6	6	6	1
4	0.7	6	0.125	6	6	6	1.5
5	0.7	6	0.125	6	6	6	2
6	0.7	6	0.125	12	12	12	1
7	0.7	6	0.125	12	12	12	1
8	0.7	6	0.125	12	12	12	1
9	0.7	6	0.125	12	12	12	0.5
10	0.7	6	0.125	12	12	12	0.75
11	0.7	6	0.125	12	12	12	1
12	0.7	6	0.0625	6	6	6	NaN
13	2	6	0.0625	6	6	6	1
14	2	9	0.0625	6	6	6	0.75
15	2	9	0.0625	6	6	12	1
16	2	9	0.0625	6	12	12	1
17	2	9	0.0625	12	12	12	1
18	2	9	0.0625	12	12	12	0.25
19	2	9	0.0625	12	12	12	0.5
20	2	9	0.0625	12	12	12	0.75

21	2	9	0.0625	12	12	12	1
22	2	9	0.0625	12	12	12	1.25
23	2	9	0.0625	12	12	12	1.5
24	2	9	0.0625	12	12	12	1.75
25	1.4	9	0.0625	6	0	6	1
26	1	9	0.0625	6	0	6	1
27	1	9	0.0625	6	0	12	1
28	1	9	0.0625	6	0	12	1
29	1	9	0.0625	6	0	12	1
30	1	9	0.0625	6	0	6	1
31	1	9	0.0625	6	0	6	1.25
32	1	9	0.0625	6	0	6	1.5
33	1	11	0.0625	6	0	6	1
34	1	9	0.0625	0	0	12	1
35	1	9	0.0625	0	0	6	0.75
36	1	9	0.0625	0	0	6	0.5
37	1	9	0.0625	0	0	6	1
38	1	9	0.0625	0	0	6	1.5
39	1	9	0.0625	0	0	6	1.5
40	1	9	0.0625	0	3	6	1
41	1	9	0.0625	0	6	6	1
42	1	9	0.0625	0	6	6	1.5
43	1	9	0.0625	0	3	6	0.5
44	1	9	0.0625	0	3	6	1.5
45	1	9	0.0625	0	3	6	1
46	1	9	0.125	3	0	6	1
47	1	9	0.125	3	0	3	1
48	1	9	0.125	0	0	3	1
49	1	9	0.0625	0	0	6	1
50	1	9	0.0625	0	0	6	1
51	1	9	0.0625	0	3	6	1
52	1	9	0.0625	0	3	6	1
53	1	9	0.0625	0	6	6	1
54	1	9	0.0625	0	6	6	1
55	1	9	0.0625	0	6	6	1
56	1	9	0.0625	0	6	6	1
57	1	9	0.0625	0	6	6	1
58	1	9	0.0625	0	3	6	1
59	1	9	0.0625	0	3	6	1
60	1	9	0.0625	0	3	6	1
61	1	9	0.0625	0	6	6	1

62	1	9	0.0625	0	3	9	1
63	1	9	0.0625	0	3	6	1
64	1	9	0.0625	0	6	6	1
65	1	9	0.0625	0	6	6	1
66	1	9	0.0625	0	3	9	1
67	1	9	0.0625	0	6	9	1
68	1	9	0.0625	0	6	9	1.25
69	1	9	0.0625	0	3	9	1
70	1	9	0.0625	0	6	9	1
71	1	9	0.0625	0	3	9	1

Table A6. Exploratory Testing Parametric Configurations

Test	Pattern Description
1	0.125" , 3 rows , 6 holes for each row
2	0.125" , 3 rows , 6 holes for each row
3	0.125" , 3 rows , 6 holes for each row
4	0.125" , 3 rows , 6 holes for each row
5	0.125" , 3 rows , 6 holes for each row
6	0.125", 3 rows , 12 holes in the bottom row
7	0.125" , 3 rows ,12 holes in the middle & bottom rows
8	0.125" , 3 rows , 12 holes in each row
9	0.125" , 3 rows , 12 holes in each row
10	0.125" , 3 rows , 12 holes in each row
11	0.125" , 3 rows , 12 holes in each row
12	0.0625" , 3 rows , 6 holes in each
13	0.0625" , 3 rows , 6 holes in each
14	0.0625" , 3 rows , 6 holes in each
15	0.0625" , 3 rows , 6 holes in top & middle rows, 12 holes in bottom row
16	0.0625" , 3 rows , 6 holes in top row, 12 holes in middle & bottom row
17	0.0625" , 3 rows , 12 holes in each row
18	0.0625" , 3 rows , 12 holes in each row
19	0.0625" , 3 rows , 12 holes in each row
20	0.0625" , 3 rows , 12 holes in each row
21	0.0625" , 3 rows , 12 holes in each row
22	0.0625" , 3 rows , 12 holes in each row
23	0.0625" , 3 rows , 12 holes in each row
24	0.0625" , 3 rows , 12 holes in each row
25	0.0625", 2 rows (bottom & top), 6 holes in each row
26	0.0625", 2 rows (bottom & top),6 holes in each row
27	0.0625", 2 rows (bottom & top), 12 holes in bottom & 6 in top
28	2 rows (bottom & top), 12 holes in bottom (0.0625") & 6 in top (3 of 0.125" & 3 of 0.0625)

29	2 rows (bottom & top), 12 holes in bottom (0.0625") & 6 in top (0.125")
30	0.0625", 2 rows (bottom & top), 6 holes in each row
31	0.0625", 2 rows (bottom & top), 6 holes in each row
32	0.0625", 2 rows (bottom & top), 6 holes in each row
33	0.0625", 2 rows (bottom & top), 6 holes in each row
34	0.0625" , 1 row (bottom), 12 holes
35	0.0625" , 1 row (bottom), 6 holes
36	0.0625" , 1 row (bottom), 6 holes
37	0.0625" , 1 row (bottom), 6 holes
38	0.0625" , 1 row (bottom), 6 holes
39	0.0625" , 1 row (bottom), 6 holes
40	0.0625", 2 row (bottom & middle), 6 holes in bottom & 3 in middle
41	0.0625", 2 row (bottom & middle), 6 holes in each
42	0.0625", 2 row (bottom & middle), 6 holes in each
43	0.0625", 2 row (bottom & middle), 6 holes in bottom & 3 in middle
44	0.0625", 2 row (bottom & middle), 6 holes in bottom & 3 in middle
45	0.0625", 2 row (bottom & middle), 6 holes in bottom & 3 in middle
46	0.125", 2 rows (top & bottom), 6 holes in bottom & 3 in top
47	0.125", 2 rows (top & bottom), 3 holes in each
48	0.125", 1 rows (bottom), 3 holes
49	0.0625", 1 row (bottom), 6 holes
50	0.0625", 1 row (bottom), 6 holes
51	0.0625", 2 rows (bottom & middle [1" below collar]) 6 holes bottom, 3 holes middle
52	0.0625", 2 rows (bottom & middle [1" below collar]) 6 holes bottom, 3 holes middle
53	0.0625", 2 rows (bottom & middle [1" below collar]) 6 holes bottom, 6 holes middle
54	0.0625", 2 rows (bottom & middle [1" below collar]) 6 holes bottom, 6 holes middle
55	0.0625", 2 rows (bottom & middle [1" below collar]) 6 holes bottom, 6 holes middle (spiraled)
56	0.0625", 2 rows (bottom & middle [1" below collar]) 6 holes bottom, 6 holes middle (spiraled)
57	0.0625", 2 rows (bottom & middle [1" below collar]) 6 holes bottom, 6 holes middle (spiraled)
58	0.0625", 2 rows (bottom & middle [1" below collar]) 6 holes bottom, 3 holes middle (spiraled)
`59	0.0625", 2 rows (bottom & middle [1" below collar]) 6 holes bottom, 3 holes middle (spiraled)
60	0.0625", 2 rows (bottom & middle [1.5" below collar]) 6 holes bottom, 3 holes middle (spiraled)
61	0.0625", 2 rows (bottom & middle [1.5" below collar]) 6 holes bottom, 6 holes middle (spiraled)
62	0.0625", 2 rows (bottom & middle [1" below collar]) 9 holes bottom, 3 holes middle
63	0.0625", 2 rows (bottom & middle [.5" below collar]) 6 holes bottom, 3 holes middle (spiraled)
64	0.0625", 2 rows (bottom & middle [.5" below collar]) 6 holes bottom, 6 holes middle (spiraled)
65	0.0625", 2 rows (bottom & middle [.5" below collar]) 6 holes bottom, 6 holes middle (spiraled)
66	0.0625", 2 rows (bottom & middle [1" below collar]) 9 holes bottom, 3 holes middle
67	0.0625", 2 rows (bottom & middle [1" below collar]) 9 holes bottom, 6 holes middle
68	0.0625", 2 rows (bottom & middle [1" below collar]) 9 holes bottom, 6 holes middle
69	0.0625", 2 rows (bottom & middle [.5" below collar]) 9 holes bottom, 3 holes middle (spiraled)

70	0.0625", 2 rows (bottom & middle [.5" below collar]) 9 holes bottom, 6 holes middle (spiraled)
71	0.0625", 2 rows (bottom & middle [1.5" below collar]) 9 holes bottom, 3 holes middle (spiraled)

Table A7. Exploratory Testing Air Injection Patterns

Test	Time to Boil (min)	Time to Boil Corrected (min)	Moist Fuel (kg)	Eq. Dry Fuel (kg)	Firepower (kW)	Combustion Efficiency (%)	Thermal Efficiency (%)
1	NaN	NaN	NaN	NaN	NaN	NaN	NaN
2	NaN	NaN	NaN	NaN	NaN	NaN	NaN
3	32.7	30.4	0.563	0.510	4.88	98.9	23.6
4	25.4	23.9	0.503	0.456	5.61	99.4	26.2
5	26.8	26.3	0.532	0.482	5.63	99.3	24.0
6	32.5	32.6	0.540	0.489	4.70	98.8	23.3
7	25.7	25.0	0.501	0.454	5.51	99.1	25.7
8	33.2	32.5	0.527	0.477	4.50	98.6	24.3
9	35.4	35.9	0.609	0.552	4.87	98.2	20.5
10	28.9	28.8	0.572	0.518	5.61	98.9	22.1
11	26.6	27.0	0.592	0.536	6.29	99.0	21.1
12	29.4	29.0	0.597	0.541	5.75	98.9	21.3
13	26.5	26.2	0.638	0.578	6.83	99.2	19.9
14	28.3	28.1	0.637	0.578	6.38	99.2	19.9
15	26.5	26.3	0.634	0.575	6.80	99.3	19.9
16	24.3	24.1	0.588	0.532	6.84	98.6	21.6
17	23.6	25.3	0.565	0.512	6.78	98.7	21.2
18	32.1	33.0	0.613	0.555	5.41	98.5	20.2
19	26.6	27.4	0.606	0.549	6.45	98.5	20.3
20	22.8	23.7	0.579	0.525	7.20	97.3	21.2
21	22.4	23.1	0.564	0.511	7.12	96.8	21.9
22	29.1	29.2	0.573	0.519	5.59	98.9	21.5
23	32.5	35.0	0.647	0.587	5.64	99.1	21.3
24	32.4	33.5	0.703	0.637	6.15	99.3	19.0
25	28.3	29.8	0.635	0.575	6.36	99.0	19.2
26	25.0	25.5	0.540	0.489	6.11	99.2	23.1
27	24.6	24.8	0.519	0.470	5.99	99.2	22.7
28	28.4	29.8	0.529	0.479	5.29	99.2	23.8
29	27.7	28.1	0.521	0.472	5.33	98.9	23.0
30	25.2	25.0	0.552	0.500	6.21	99.4	22.5
31	26.7	27.3	0.579	0.524	6.14	99.3	21.9
32	29.8	32.4	0.628	0.569	5.98	99.5	20.4
33	24.9	26.9	0.563	0.510	6.40	99.4	20.9
34	26.0	25.8	0.556	0.504	6.07	98.9	22.1
35	24.5	25.7	0.514	0.466	5.96	99.2	22.7

36	27.2	28.8	0.545	0.494	5.68	98.9	22.3
37	24.2	25.0	0.563	0.510	6.58	99.3	21.8
38	25.5	26.1	0.556	0.504	6.18	99.0	21.6
39	24.1	25.0	0.530	0.480	6.23	99.1	22.3
40	23.5	25.6	0.506	0.459	6.10	99.1	22.7
41	24.2	26.1	0.511	0.463	5.98	98.9	22.4
42	24.5	25.5	0.544	0.493	6.30	99.0	22.0
43	26.9	28.6	0.529	0.479	5.57	99.1	22.5
44	25.5	27.7	0.523	0.474	5.80	98.9	22.2
45	26.7	28.8	0.545	0.494	5.80	99.2	22.4
46	33.7	35.3	0.624	0.565	5.24	99.1	22.1
47	28.0	28.7	0.576	0.522	5.82	98.9	22.7
48	27.1	28.9	0.564	0.511	5.89	99.0	21.4
49	30.9	36.3	0.606	0.549	5.55	98.8	20.4
50	30.8	31.4	0.596	0.540	5.48	98.6	22.5
51	28.7	29.0	0.555	0.503	5.48	99.1	23.1
52	28.2	27.8	0.547	0.496	5.51	98.8	22.2
53	27.3	28.2	0.545	0.494	5.66	99.5	22.2
54	27.2	28.1	0.533	0.483	5.55	99.3	22.5
55	27.2	27.9	0.549	0.497	5.71	99.5	22.0
56	26.5	26.1	0.572	0.518	6.12	99.4	21.5
57	27.2	27.2	0.547	0.496	5.70	99.5	22.6
58	26.1	26.2	0.585	0.530	6.36	99.4	21.6
59	29.3	29.6	0.539	0.488	5.21	99.4	21.9
60	28.9	29.8	0.580	0.526	5.69	99.3	21.0
61	25.4	26.8	0.505	0.458	5.63	99.4	23.4
62	27.6	28.4	0.550	0.498	5.65	98.5	22.3
63	31.3	30.4	0.589	0.534	5.34	99.3	22.0
64	29.4	28.7	0.555	0.503	5.35	99.3	23.5
65	27.5	25.8	0.593	0.537	6.11	99.5	21.5
66	26.0	24.8	0.554	0.502	6.03	99.3	22.3
67	25.1	24.1	0.553	0.501	6.24	99.0	22.8
68	27.8	26.0	0.567	0.514	5.78	99.3	23.1
69	25.2	23.9	0.553	0.501	6.22	99.2	22.6
70	25.7	25.5	0.530	0.480	5.84	99.1	23.4
71	27.2	27.1	0.534	0.484	5.55	99.2	22.9

Table A8. Exploratory Testing Performance Metrics

Test	Total CO2 Mass (g)	Total CO Mass (g)	Total PM Mass (g)	CO/Energy (g/MJd)	CO/Power (g/KWd)	PM/Energy (mg/MJd)	PM/Power (mg/KWd)
1	NaN	NaN	NaN	NaN	NaN	NaN	NaN
2	NaN	NaN	NaN	NaN	NaN	NaN	NaN
3	860.5	4.49	NaN	2.02	3.96	NaN	NaN
4	756.6	2.08	NaN	0.94	1.44	NaN	NaN
5	806.3	2.56	NaN	1.19	1.91	NaN	NaN
6	853.6	4.64	NaN	2.19	4.28	NaN	NaN
7	785.5	3.36	NaN	1.55	2.40	NaN	NaN
8	860.5	5.70	NaN	2.66	5.30	NaN	NaN
9	1005.8	8.70	NaN	4.12	8.76	NaN	NaN
10	893.1	4.93	NaN	2.30	3.99	NaN	NaN
11	878.9	4.30	NaN	2.02	3.23	NaN	NaN
12	917.8	4.20	NaN	1.96	3.45	NaN	NaN
13	896.7	2.81	NaN	1.31	2.09	NaN	NaN
14	937.3	3.51	NaN	1.64	2.79	NaN	NaN
15	885.2	2.65	NaN	1.23	1.96	NaN	NaN
16	830.1	6.10	NaN	2.82	4.11	NaN	NaN
17	795.0	5.15	NaN	2.52	3.57	NaN	NaN
18	1005.8	7.10	0.905	3.35	6.46	430.6	829.7
19	821.2	6.10	0.737	2.87	4.59	351.7	561.9
20	776.7	11.16	0.901	5.31	7.27	432.4	591.9
21	767.4	12.99	1.034	6.15	8.28	493.2	663.9
22	775.9	4.10	0.747	1.96	3.41	356.7	622.2
23	997.7	4.17	0.585	1.78	3.47	249.5	487.0
24	1050.2	3.04	0.390	1.34	2.61	171.8	333.9
25	895.5	4.06	0.520	1.95	3.32	250.6	425.1
26	826.2	2.52	0.289	1.19	1.79	136.5	205.1
27	783.1	2.72	0.336	1.36	2.00	167.7	247.0
28	838.0	3.04	0.833	1.42	2.41	388.2	660.7
29	768.4	3.73	0.765	1.83	3.04	375.4	623.5
30	840.7	2.36	0.306	1.12	1.69	144.7	218.6
31	871.8	2.93	0.225	1.36	2.18	104.6	167.7
32	954.3	2.13	0.144	0.98	1.75	66.3	118.4
33	848.5	2.33	0.339	1.16	1.74	169.2	253.0
34	834.1	4.24	0.523	2.03	3.16	250.7	390.3
35	793.1	3.14	0.378	1.58	2.32	190.4	279.4
36	840.5	4.19	0.397	2.03	3.31	192.2	313.7
37	826.2	2.72	0.254	1.31	1.90	122.2	177.6
38	848.0	4.07	0.590	2.00	3.05	288.8	441.6
39	829.6	3.70	0.527	1.84	2.67	262.4	379.7
40	762.1	3.27	0.235	1.68	2.37	120.6	170.3

41	738.7	3.68	0.596	1.89	2.75	306.6	445.2
42	793.1	3.53	0.351	1.73	2.54	172.1	252.9
43	840.6	3.44	0.410	1.71	2.75	203.4	328.2
44	805.7	4.14	0.346	2.10	3.22	175.7	269.3
45	839.7	3.00	0.311	1.45	2.31	150.2	240.3
46	1027.3	4.03	0.647	1.72	3.47	275.6	557.6
47	870.2	4.38	0.518	1.97	3.31	232.8	391.6
48	882.9	4.25	0.457	2.07	3.37	222.8	362.7
49	1026.2	5.97	0.470	2.83	5.26	223.2	414.0
50	1007.2	7.08	0.326	3.10	5.73	142.8	264.1
51	897.1	3.78	0.256	1.73	2.98	117.3	201.7
52	910.0	4.93	0.399	2.38	4.03	192.7	325.5
53	867.3	2.01	0.241	0.98	1.60	116.6	191.2
54	847.8	2.57	0.293	1.26	2.06	143.9	234.9
55	870.0	1.93	0.293	0.94	1.54	142.9	233.7
56	869.3	2.54	0.440	1.21	1.93	210.6	334.4
57	853.7	1.68	0.414	0.80	1.30	196.9	321.4
58	909.7	2.54	0.408	1.18	1.84	189.3	296.0
59	871.4	2.37	0.417	1.18	2.07	207.9	365.6
60	886.8	2.78	0.404	1.34	2.32	194.8	337.6
61	767.6	1.81	0.313	0.90	1.38	155.8	237.7
62	760.6	5.83	0.703	2.80	4.63	337.2	557.8
63	897.2	2.65	0.387	1.20	2.26	175.5	329.4
64	852.2	2.55	0.310	1.15	2.03	139.8	246.9
65	824.0	1.95	0.310	0.90	1.48	143.3	236.2
66	772.4	2.53	0.389	1.20	1.88	185.2	289.3
67	747.7	3.84	0.359	1.79	2.70	167.7	252.8
68	835.2	2.78	0.171	1.25	2.08	76.7	127.9
69	807.4	3.21	0.406	1.51	2.28	191.3	289.0
70	776.6	3.20	0.338	1.52	2.34	160.2	247.0
71	817.6	2.86	0.340	1.38	2.25	163.4	266.9

Table A9. Exploratory Testing Emissions Metrics

A3.2 Parametric Testing

Table A10 through Table A13 provide the raw collected data, parametric settings, performance metrics, and emissions metrics, respectively, for each test conducted during the parametric testing phase. The cone identification numbers provided in Table A7 correspond to air injection patterns 1 and 2 shown in Figure A6. It should be noted that the first 12 trials do not have BC emission data, as the Magee Scientific AE-22 instrument was out for maintenance and calibration.

Test	Water Initial (°C)	Wood Initial (g)	Wood Final (g)	Water Initial (g)	Wood MC (%)	Start	End	Leftover Wood (g)	Leftover Char (g)	Final Pot/ Water (g)	Empty Pot (g)	Duct Flow (CFM)	Filter Mass (mg)
1	25.7	979.6	499.4	5006	8.3	13:29	13:58	44.3	24.1	6475.6	1711	201	1.3601
2	26.2	871.2	290.8	5002	8.3	14:54	15:26	16.4	45.2	6422.5	1710.7	199	1.681
3	19.7	961.5	169.4	5002	8.0	11:22	12:09	26.4	59	6276.5	1710.5	201	3.1537
4	28.6	986.7	456.9	5287	6.9	12:11	12:36	74.1	27.1	6811.2	1710.8	199	1.2424
5	23.8	959.8	457.8	5001	6.9	13:43	14:08	32.3	28.7	6503.5	1710.8	200	1.1639
6	27.7	1008.3	461.4	5003	7.3	11:34	12:00	32.6	37.2	6502.4	1710.7	195	1.2925
7	27.9	1002.9	485.1	5004	7.3	13:08	13:33	67.5	30.3	6490.2	1711	197	0.9853
8	25.5	961.1	454.3	5004	7.3	14:32	14:57	30.8	32.2	6448.9	1710.7	198	1.1776
9	28.1	980.3	534.7	5005	10.4	10:43	11:04	69.5	22.4	6527.1	1710.6	214	0.8091
10	24	809.3	277.8	5001	7.3	15:46	16:16	42.6	33.5	6471.6	1710.6	197	1.1202
11	32	958.3	522.4	5005	10.4	12:04	12:25	60.4	32.4	6504.6	1710.5	218	0.4293
12	29.9	971.8	500.4	5012	10.4	13:34	13:59	39.5	18.4	6519.8	1710.3	218	0.7117
13	30.8	988.8	562.3	5004	9.0	11:45	12:07	76	32	6526.8	1710.6	200	0.589
14	36.2	935.3	558.3	5004	9.0	13:10	13:29	30.1	22.4	6510.1	1710.8	202	0.8541
15	25.9	937.9	458.7	5008	9.0	14:32	14:57	22.3	27.6	6478.5	1710.9	205	1.2194
16	32.1	985.5	591.0	4999	8.1	10:58	11:19	45.5	4.9	6521.6	1710.7	203	0.5492
17	34.8	983.1	572.3	5001	8.1	12:41	13:02	36	28.8	6529.4	1710.7	205	0.4457
18	25.6	969.6	371.0	5006	8.1	13:58	14:33	11.2	41.4	6354.1	1711	209	1.2637
19	20.5	972.2	510.0	5008	8.1	10:01	10:29	24.2	38.2	6455.7	1710.8	201	1.1054
20	25.4	905.5	433.7	5004	8.1	11:21	11:45	32.2	35.3	6492.1	1710.8	204	1.2097
21	28.7	918.0	324.3	5000	8.1	12:35	13:04	20.7	42	6381.4	1710.9	204	0.9893
22	23.5	933.9	501.0	4999	7.8	11:58	12:24	20.4	15.1	6466.3	1711	203	0.739
23	25.9	904.7	404.4	5007	7.8	13:42	14:08	22.2	6.0	6405.8	1711	204	0.589
24	27.1	944.3	493.6	4999	9.3	13:05	13:25	35.6	43.0	6503.7	1710.2	200	0.708
25	25.3	952.6	434.9	5007	9.3	14:28	14:50	49.9	51.9	6494.4	1710.1	206	0.740
26	24.6	955.7	524.7	5001	8.0	10:57	11:17	44.7	37.8	6542.7	1709.7	204	0.948
27	23.5	984.9	501.1	4999	8.0	12:53	13:14	46	39.6	6501.6	1709.6	204	0.392
28	24.2	994.0	451.1	5001	8.0	14:07	14:33	29.5	56.6	6517.3	1710	202	1.886
29	24.9	946.9	482.6	5002	9.0	10:31	10:53	68.7	34.3	6530.4	1709.8	204	0.476
30	27.4	977.4	440.4	5004	9.0	13:16	13:40	54.2	50.9	6477	1710	203	1.741
31	25.5	936.3	476.4	4996	9.0	11:50	12:12	38	45.9	6497.9	1709.7	205	0.746
32	23.6	940.3	470.2	5005	11.0	11:19	11:45	40.9	30.0	6444.4	1709.7	201	0.554
33	23	945.4	445.9	5004	11.0	12:38	13:04	69.9	16.2	6511.1	1709.7	200	0.657
34	23.3	984.5	425.1	4998	11.0	13:50	14:19	57	32.8	6475	1709.8	201	1.166
35	24.4	960.8	545.2	5001	11.1	11:48	12:12	18.6	28.7	6517.6	1709.5	204	0.747
36	26.9	946.6	482.1	4999	11.1	13:24	13:46	18.9	52.0	6511.3	1709.8	205	1.049
37	25	891.9	380.2	4999	11.1	14:33	14:59	24.6	40.1	6492.7	1710.7	205	0.748
38	22.7	961.9	514.9	4998	10.0	10:51	11:15	15	43.3	6526.7	1709.6	204	0.882
39	26.1	932.6	487.3	4996	10.0	13:01	13:28	4.5	24.3	6451.4	1709.9	203	0.622

40	27.3	958.3	388.3	4999	10.0	14:39	15:10	35.2	38.2	6402.3	1710.5	205	1.781
41	27.8	933.1	515.9	5005	9.7	13:54	14:18	9.3	32.5	6505.2	1709.6	206	0.369
42	30.2	947.9	523.7	5004	9.3	11:09	11:33	28.2	28.9	6482	1709.6	203	0.568
43	26.3	966.6	478.4	4997	9.6	12:32	12:56	51.8	32.7	6484.2	1709.8	205	0.437
44	29	999.7	571.3	4997	9.0	14:15	14:39	14.9	30.5	6487.6	1710	203	0.433
45	21.8	978.3	466.4	5000	8.9	11:00	11:25	73.8	44.8	6497.7	1709.2	204	0.709
46	22.9	921.2	465.8	4996	8.3	12:44	13:08	33.2	35.7	6514.9	1709.5	204	0.467
47	23.2	924.1	442.8	4998	8.6	15:11	15:37	42.6	34.3	6457.6	1709.5	204	0.388
48	21.4	965.7	457.8	5003	9.6	13:18	13:43	56.9	37.3	6475.3	1709.6	205	0.553
49	22.3	961.1	493.2	4999	8.9	14:37	15:02	23.8	35.0	6478.1	1709.7	206	0.453
50	21.2	949.3	505.4	5004	7.9	11:20	11:51	39.8	24.3	6529.7	1709.7	203	1.072
51	21.8	993.3	532.3	5005	8.8	14:09	14:38	19.4	17.7	6511.8	1710.2	206	1.346
52	20.7	945.2	473.4	5002	8.8	12:02	12:32	52.4	36.7	6510.6	1710	203	1.048
53	20.9	927.9	505.7	5000	9.2	13:32	13:59	19	33.4	6502	1710.2	203	0.562
54	22.5	932.6	498.8	5001	9.2	14:50	15:14	27.7	42.7	6524.5	1710.6	203	0.778
55	20.1	928.5	496.7	4999	8.9	10:17	10:44	32.1	16.3	6472.4	1710.2	203	0.463
56	21.2	938.2	511.7	5002	8.8	11:36	12:05	12.1	25.3	6461.5	1710.4	202	0.707
57	22.1	936.6	492.3	5005	8.2	13:08	13:33	28.1	36.0	6544.8	1710.7	203	0.983
58	20.9	954.0	519.3	4996	8.7	11:59	12:30	24.9	15.9	6491.8	1710.5	203	0.905
59	21.8	969.4	544.7	4999	8.9	13:38	14:04	27.5	24.1	6500.3	1710.6	203	0.522
60	23.8	961.7	518.0	5005	8.1	14:51	15:14	44.6	31.0	6513.5	1710.8	203	0.768
61	24.8	935.6	484.7	5001	9.0	10:54	11:21	31	23.2	6494.1	1710.6	201	0.898
62	24	942.6	475.8	5004	8.8	12:19	12:43	42	18.3	6493	1710.7	203	0.529
63	25.3	910.0	453.0	4996	8.9	13:42	14:07	49.5	28.1	6476.9	1710.9	202	0.422

Table A10. Parametric Testing Collected Data

Test	Cone ID	Flow Rate (CFM)
1	1	0.75
2	1	1
3	1	1.25
4	2	0.75
5	2	1
6	2	1.25
7	2	0.75
8	2	1
9	2	0.75
10	2	1.25
11	2	1
12	2	1.25
13	2	0.75
14	2	1

15	2	1.25
16	2	0.75
17	2	1
18	2	1.25
19	2	0.75
20	2	1
21	2	1.25
22	2	0.75
23	2	1
24	1	1
25	1	1.25
26	1	0.75
27	1	1
28	1	1.25
29	1	0.75
30	1	1.25
31	1	1
32	1	0.75
33	1	1
34	1	1.25
35	1	0.75
36	1	1
37	1	1.25
38	1	0.75
39	1	1
40	1	1.25
41	1	1
42	1	1
43	1	1
44	1	1
45	1	1
46	1	1
47	1	1
48	1	1
49	1	1
50	2	1
51	2	1
52	2	1
53	2	1
54	2	1
55	2	1

56	2	1
57	2	1
58	2	1
59	2	1
60	2	1
61	1	1
62	1	1
63	1	1

Table A11. Parametric Testing Parametric Configurations

Test	Time to Boil (min)	Time to Boil Corrected (min)	Moist Fuel (kg)	Eq. Dry Fuel (kg)	Firepower (kW)	Thermal Efficiency (%)	Combustion Efficiency (%)
1	29.1	30.1	0.511	0.429	4.61	25.67	99.30
2	31.6	33.1	0.639	0.512	5.07	22.46	96.96
3	47.1	44.5	0.841	0.677	4.49	20.8	97.6
4	24.8	26.6	0.531	0.449	5.65	23.4	99.4
5	25.3	25.2	0.545	0.460	5.67	23.8	99.5
6	26.3	27.5	0.589	0.485	5.78	21.7	97.8
7	25.0	26.2	0.525	0.437	5.46	24.5	99.4
8	25.2	25.7	0.551	0.458	5.69	24.9	98.8
9	20.1	21.6	0.451	0.368	5.72	27.4	99.1
10	30.5	30.5	0.564	0.468	4.80	24.0	99.5
11	21.3	23.7	0.451	0.351	5.17	28.6	99.6
12	25.4	27.7	0.507	0.424	5.22	23.9	99.0
13	22.3	24.6	0.426	0.335	4.71	29.3	99.4
14	19.6	23.3	0.422	0.347	5.56	27.3	99.0
15	25.6	26.5	0.532	0.439	5.37	25.0	99.2
16	21.1	23.7	0.424	0.380	5.64	25.5	99.6
17	21.2	24.5	0.450	0.366	5.39	25.8	99.1
18	34.9	36.1	0.662	0.541	4.85	23.1	98.1
19	28.0	27.1	0.513	0.409	4.58	28.8	99.3
20	23.5	24.3	0.515	0.415	5.52	25.9	99.0
21	29.2	32.1	0.648	0.527	5.64	22.0	99.3
22	26.4	26.4	0.488	0.424	5.01	26.7	99.5
23	26.6	27.4	0.553	0.498	5.85	23.9	99.6
24	20.5	21.4	0.490	0.375	5.73	27.9	98.4
25	22.4	23.2	0.543	0.409	5.70	26.4	96.9
26	19.3	19.9	0.461	0.363	5.88	28.0	97.7
27	20.8	20.9	0.513	0.407	6.14	26.5	98.5
28	25.4	25.7	0.581	0.443	5.46	28.9	92.5
29	22.3	22.7	0.471	0.373	5.22	27.9	98.8

30	24.8	26.5	0.556	0.424	5.35	13.3	96.7
31	21.4	22.3	0.497	0.378	5.53	27.8	98.5
32	25.5	26.0	0.504	0.400	4.91	28.6	99.4
33	25.4	25.3	0.505	0.422	5.20	25.7	99.2
34	29.1	29.5	0.577	0.461	4.95	24.0	98.9
35	23.7	24.0	0.472	0.373	4.93	28.3	99.3
36	22.1	23.3	0.521	0.380	5.38	27.2	98.7
37	26.1	26.2	0.562	0.435	5.22	25.1	98.9
38	24.0	23.9	0.507	0.387	5.04	27.3	99.1
39	26.8	27.9	0.516	0.424	4.96	26.1	99.3
40	30.5	32.3	0.610	0.487	5.00	23.8	97.9
41	23.9	25.5	0.483	0.383	5.02	27.1	99.2
42	23.6	25.9	0.471	0.380	5.04	27.4	99.2
43	24.1	25.3	0.511	0.409	5.30	26.0	99.3
44	24.2	26.0	0.489	0.395	5.11	26.3	99.1
45	24.8	24.1	0.513	0.395	4.99	28.2	99.3
46	23.8	23.8	0.497	0.398	5.22	26.8	99.9
47	26.0	26.5	0.514	0.414	4.98	27.0	99.5
48	25.7	25.2	0.526	0.415	5.04	27.5	99.3
49	25.6	25.5	0.519	0.416	5.09	26.9	99.5
50	30.8	29.6	0.479	0.401	4.08	27.2	98.5
51	28.7	28.2	0.517	0.441	4.80	24.9	96.4
52	30.5	29.8	0.494	0.391	4.01	28.1	98.7
53	26.4	25.8	0.478	0.380	4.50	29.2	99.0
54	23.6	23.8	0.481	0.368	4.87	28.7	99.0
55	26.7	25.6	0.475	0.405	4.73	28.6	99.5
56	29.0	28.6	0.489	0.405	4.36	28.4	99.4
57	24.2	23.6	0.491	0.393	5.07	27.1	99.2
58	30.7	29.8	0.485	0.416	4.24	27.0	99.2
59	26.1	25.8	0.472	0.390	4.67	28.1	99.5
60	23.1	23.4	0.474	0.385	5.20	27.8	98.9
61	26.7	27.1	0.495	0.412	4.83	26.4	99.3
62	24.5	24.5	0.500	0.425	5.43	26.0	99.3
63	25.3	26.0	0.483	0.394	4.86	27.7	99.4

Table A12. Parametric Testing Performance Metrics

Test	Total CO2 Mass (g)	Total CO Mass (g)	Total PM Mass (g)	Total BC Mass (g)	CO/Energy (g/MJd)	CO/Power (g/KWd)	PM/Energy (mg/MJd)	PM/Power (mg/KWd)	BC/Energy (mg/MJd)	BC/Power (mg/KWd)
1	600.9	2.7	0.464	NaN	1.31	NaN	165.1	391.9	NaN	NaN
2	703.6	13.9	0.573	NaN	6.45	NaN	185.3	503.5	NaN	NaN
3	970.3	15.2	1.074	NaN	5.75	3.96	155.2	1146.3	NaN	NaN

4	593.1	2.40	0.420	NaN	1.22	1.44	180.0	318.0	NaN	NaN
5	628.5	1.89	0.395	NaN	0.92	1.91	82.7	293.2	NaN	NaN
6	679.7	9.68	0.435	NaN	4.89	4.28	135.5	346.6	NaN	NaN
7	606.4	2.40	0.331	NaN	1.20	2.40	110.7	247.9	NaN	NaN
8	642.0	4.87	0.397	NaN	2.28	5.30	166.5	279.7	NaN	NaN
9	502.1	2.84	0.293	NaN	1.50	8.76	204.9	187.2	NaN	NaN
10	666.0	2.28	0.380	NaN	1.08	3.99	103.8	328.8	NaN	NaN
11	500.8	1.15	0.156	NaN	0.61	3.23	86.4	105.4	NaN	NaN
12	584.7	3.84	0.257	NaN	2.02	3.45	187.4	206.4	NaN	NaN
13	468.0	1.88	0.204	0.068	1.02	2.09	172.3	148.0	37.1	49.6
14	471.1	2.87	0.296	0.172	1.62	2.79	207.2	195.3	96.8	113.6
15	623.8	3.39	0.422	0.081	1.64	1.96	157.2	314.3	39.4	60.5
16	480.8	1.30	0.189	0.077	0.71	4.11	119.4	131.4	42.3	53.6
17	490.2	2.84	0.153	0.092	1.60	3.57	91.0	110.1	51.9	66.2
18	768.7	9.44	0.439	0.107	4.03	6.46	124.0	392.6	45.5	95.4
19	639.8	2.69	0.382	0.127	1.21	4.59	126.6	289.2	57.4	96.3
20	599.8	4.01	0.419	0.088	1.98	7.27	170.0	292.3	43.7	61.7
21	740.1	3.26	0.342	0.049	1.50	8.28	66.3	275.6	22.7	39.8
22	600.9	1.83	0.254	0.094	0.86	3.41	83.3	189.3	44.3	70.2
23	716.2	1.80	0.203	0.078	0.81	3.47	129.5	145.3	35.0	55.8
24	515.1	5.42	0.244	0.092	2.76	2.61	88.2	152.4	47.0	57.7
25	575.9	11.83	0.256	0.075	5.85	3.47	110.9	170.4	37.3	50.2
26	498.1	7.62	0.324	0.112	4.00	4.74	191.6	197.0	58.8	68.1
27	546.5	5.18	0.134	0.059	2.55	3.32	130.1	82.6	29.1	36.2
28	559.5	28.92	0.643	0.109	14.56	323.92	55.0	22.2	493.0	83.7
29	514.9	4.11	0.163	0.066	2.10	1.79	186.4	111.4	33.9	45.4
30	613.5	13.26	0.600	0.081	6.61	299.55	40.4	9.8	445.4	60.1
31	534.2	5.26	0.256	0.073	2.66	2.00	125.9	166.3	36.7	47.2
32	575.1	2.39	0.190	0.063	1.11	3.40	153.1	135.1	29.2	44.7
33	563.8	2.85	0.226	0.061	1.40	2.41	103.7	168.9	30.1	45.8
34	646.0	4.58	0.398	0.028	2.21	3.04	284.6	334.9	13.7	23.9
35	524.1	2.44	0.258	0.090	1.23	1.69	65.7	184.6	45.2	64.1
36	538.5	4.56	0.360	0.063	2.36	2.18	99.4	246.7	32.7	43.3
37	588.0	4.25	0.258	0.044	2.07	1.75	74.6	196.9	21.5	33.6
38	545.1	3.29	0.303	0.076	1.66	1.74	75.9	220.5	38.5	55.5
39	614.9	2.82	0.216	0.045	1.36	3.16	116.9	166.5	21.7	34.8
40	661.2	8.89	0.618	0.081	4.10	2.32	80.1	520.1	37.4	68.2
41	545.7	2.74	0.128	0.048	1.41	3.31	63.7	94.1	24.9	35.7
42	512.5	2.74	0.194	0.046	1.40	1.90	89.4	140.7	23.7	33.5
43	508.5	2.19	0.149	0.048	1.10	3.05	74.7	108.1	24.0	34.8
44	546.8	3.21	0.148	0.048	1.65	2.67	180.5	110.0	24.4	35.4

45	554.4	2.66	0.244	0.050	1.27	2.37	225.0	173.5	23.8	35.3
46	455.4	0.25	0.161	0.041	0.12	2.75	174.7	114.5	20.4	29.2
47	548.8	1.87	0.134	0.043	0.89	2.54	92.9	99.3	20.3	31.6
48	597.6	2.53	0.191	0.034	1.19	2.75	135.1	138.1	16.1	24.8
49	567.9	1.83	0.157	0.041	0.87	3.22	73.2	114.5	19.6	30.1
50	540.8	5.16	0.369	0.113	2.52	2.31	112.5	333.2	55.4	102.3
51	588.6	13.73	0.463	0.162	6.67	3.47	169.1	388.0	78.7	135.7
52	584.2	4.88	0.361	0.082	2.36	3.31	146.5	319.6	39.6	72.4
53	552.8	3.45	0.193	0.100	1.66	3.37	86.8	147.1	48.1	76.2
54	544.4	3.36	0.268	0.097	1.70	5.26	130.5	191.5	49.0	69.4
55	605.5	1.76	0.159	0.046	0.81	5.73	150.7	117.5	21.2	34.0
56	570.3	2.13	0.243	0.055	0.99	2.98	87.8	195.9	25.5	44.4
57	577.1	2.78	0.338	0.106	1.39	4.03	70.8	245.6	52.9	76.8
58	519.6	2.56	0.308	0.048	1.22	1.60	116.6	270.0	22.6	41.7
59	564.7	1.91	0.179	0.055	0.93	2.06	143.9	136.2	26.6	41.7
60	503.3	3.59	0.262	0.121	1.79	1.54	142.9	181.2	60.3	83.8
61	601.9	2.58	0.307	0.071	1.27	1.93	210.6	241.4	35.1	56.2
62	587.6	2.55	0.182	0.092	1.23	1.30	196.9	129.0	44.5	65.4
63	582.5	2.16	0.145	0.064	1.05	1.84	189.3	107.6	31.1	47.2

Table A13. Parametric Testing Emissions Metrics

A4 – Duct Flow Rate Calibration

Cookstoves are tested under a steel exhaust hood that completely captures pollutant emissions. Electric blowers exhaust all captured emissions outside the building using a steel duct system. Accurate volumetric flow rate measurements of the exhaust passing through this duct are required to calculate the mass of pollutants emitted by the cookstoves. Volumetric flow rate is calculated using differential pressure measurements across a Fantech IR Series iris damper installed in the 152-mm (6-inch) diameter ducting. This iris damper is adjustable, and set to a diameter of 110 mm (4.5 inches). Differential pressure measurements are taken at static ports on either side of the iris using pressure sensors integrated into the Energy Conservatory Automated Performance Testing System (APT-8) unit.

In order to convert differential pressure measurements across the iris to volumetric flow measurements, a calibrated equation is required. The basic calibration method presented in this Appendix is adapted from ISO 5167, which provides standard hardware configurations and empirical equations for the measurement of fluid flow rates using differential pressure devices.[195] In this calibration method, the volumetric flow rate of air aspirated into the exhaust duct is measured using a Minneapolis Duct Blaster while differential pressure measurements are recorded across the iris. The Minneapolis Duct Blaster is operated in accordance with the procedures outlined in the manual and instructional video cited in the References below. [196,197]

Using this set of experimental measurements, it is possible to generate a calibration equation for the iris. This procedure is repeated over four trials, as the temperature of the duct flow is modulated. The duct flow was heated using a large propane burner upstream of the Duct

Blaster instrument, which is connected directly to the duct. The collected data from these four trials is provided in Table A14.

Trial	Duct Temp [°C]	Duct Flow [m^3/min]	Pressure Diff [Pa]
1	23.7	6.9093	125.9
2	38.0	6.6261	123.8
3	52.3	6.4138	119.5
4	68.4	6.2155	112.7

Table A14. Duct Flow Rate Calibration Data

Using the experimental data from Table A14, the differential pressure measurements across the iris can be used to calculate the volumetric flow of air through the duct iris according to the governing equation,

$$Q_{duct}\left[\frac{m^3}{sec}\right] = A[m^2]C\sqrt{\frac{2\Delta P[Pa]}{\rho\left[\frac{kg}{m^3}\right]\left(1-\left(\frac{D_o}{D}\right)^4\right)}} \qquad \text{(A10)}$$

where ΔP is the pressure differential measured across the iris, A is the area of the duct (0.0182 m^2), D is the diameter of the duct (0.152 m), Do is the diameter of the iris, and C is the discharge coefficient.[198] The air density, ρ, is calculated as a function of temperature using the equation,

$$\rho[\frac{kg}{m^3}] = \frac{P_{amb}[Pa]}{(T_{duct}[°C]+273)\cdot Ra\left[\frac{J}{K}\cdot Kg\right]} \qquad \text{(A11)}$$

where P_{amb} is the ambient pressure (97.77 KPa at the laboratory's altitude of 300 m MSL), T_{duct} is the temperature in the duct, and Ra is the gas constant (286.9 J/Kg K for air).[199] All inputs to equations A10 and A11 are known experimental measurements, except for the discharge coefficient and iris diameter. Although the iris diameter can be measured directly, this procedure calculates the effective iris diameter for added calibration accuracy. Equation A10 can be rearranged to yield the discharge coefficient as follows,

$$C = \frac{Q_{duct}\left[\frac{m^3}{sec}\right]}{A[m^2]}\sqrt{\frac{\rho\left[\frac{kg}{m^3}\right]\left(1-\left(\frac{D_o}{D}\right)^4\right)}{2\Delta P[Pa]}} \qquad \text{(A12)}$$

In addition, the ISO 1057 Standard defines the discharge coefficient through a concentric iris in a pipe flow using the following empirical function,

$$C = 0.5959 + 0.312\left(\frac{D_o}{D}\right)^{2.1} - 0.184\left(\frac{D_o}{D}\right)^{8} + 0.0029\left(\frac{D_o}{D}\right)^{2.5}\left(\frac{10^6}{Re}\right)^{0.75} \quad \text{(A13)}$$

where Re is the dimensionless Reynolds number.[195] The Reynolds number is calculated using,

$$Re = \frac{4Q_{duct}\left[\frac{m^3}{sec}\right]}{\pi\upsilon\left[\frac{m^2}{sec}\right]D[m]} \quad \text{(A14)}$$

where ν is the kinematic viscosity of air. The kinematic viscosity is calculated as a function of duct airflow temperature using Equation A15.[198]

$$\nu = \frac{1}{\rho}\left(\frac{1.458\times10^{-6}(T_{duct}[°C] + 273)^{1.5}}{(T_{duct}[°C] + 273) + 110.4}\right) \quad \text{(A15)}$$

Overall, Equations A12 and A13 form a system of two equations with two unknowns. Using MATLAB, this system of equation is solved implicitly to yield values of the discharge coefficient and effective iris diameter for each trial, as provided in Table A15 below.

Trial	Density (kg/m^3)	Kinematic Viscosity (m^2/s)	Reynolds Number	Coefficient of Discharge	Iris Diameter (m)
1	1.148	1.60×10^{-5}	6.25×10^{4}	0.6042	0.1163
2	1.095	1.73×10^{-5}	5.78×10^{4}	0.6053	0.1159
3	1.047	1.88×10^{-5}	5.41×10^{4}	0.6056	0.1162
4	0.998	2.04×10^{-5}	5.06×10^{4}	0.6056	0.1171

Table A15. Calibration Procedure Results

Table A15 shows that the iris has a discharge coefficient of 0.6052 ± 0.0007 and effective iris diameter of 0.1164 ± 0.0005 m (both results represent the mean and 90% confidence interval from the four trial results). Using these calibration factors and governing equation A10, it is possible to calculate volumetric flow rate through the 152 mm (6-inch) diameter duct as a function of differential pressure across the iris and air flow temperature in the duct.

The Minneapolis Duct Blaster and Fantech iris damper are rated to measure volumetric air flow rate with ± 3% and ± 5% accuracy, respectively.[196,200] The APT-8 measures pressure with ±1% accuracy and temperature with ± 0.25 °C accuracy (or a maximum error of around ± 1%, given an ambient temperature of ~25 °C).[201] Combining these sources of measurement error (by taking the root of sum of squares), it can be estimated that the flow rate measurements are recorded with a nominal accuracy of around ± 6%.

A5 – Secondary Diluter Overview

Real time particulate matter (PM) concentrations in the exhaust duct are measured and recorded at a frequency of 1 Hz using a suite instruments. However, PM concentrations in the

duct are typically an order of magnitude greater than the ambient concentrations for which the instruments are intended. Consequently, a custom secondary diluter was designed and constructed to reduce emission concentrations to levels that the instruments can safely measure, while maintaining isokinetic sampling conditions that prevent distortion of the particle size distribution collected.

The secondary diluter, schematically illustrated in Figure A13, samples cookstove emissions using a stainless steel tube (known as the sampling probe) mounted in the 254 mm (10-inch) diameter exhaust duct. This sampling probe is parallel to the longitudinal axis of the duct (with the opening facing directly into the flow), and located on the horizontal plane at the center of the duct, offset by about 50 mm (2 inches) from the duct's central axis. The sample flow from the duct subsequently enters the secondary diluter, shown in Figure A14.

The secondary diluter consists of a long cylindrical mixing volume equipped with plumbing fittings at either end. The sample is diluted using ultra-zero air (O_2 19.5% - 23.5%, water < 2 ppm, hydrocarbons < 0.1 ppm, CO_2 < 0.5 ppm, CO < 0.5 ppm) injected at the top of the diluter. The sample probe extends 57 mm (2.25 inches) into the diluter body so the secondary dilution air can develop a flow profile parallel to the sample flow prior to mixing, thereby preventing the impaction of particles onto the walls of the diluter. The sample flow and secondary dilution air are subsequently allowed to mix through two succeeding tubes: the first is 58 mm (2.0 inches) long in a tube with an internal diameter of 12 mm (0.46 inches), while the second is 89 mm (3.5 inches) long with an internal diameter of 4.9 mm (0.19 inches). This two stage mixing section provides about 25 characteristic turbulent mixing lengths, fully ensuring that the duct sample and secondary dilution air are well mixed prior to sampling by the instruments. Excess flow is purged at the bottom of the diluter using a splitter. The diluted flow from the diluter subsequently passes through a BGI Very Sharp Cut Cyclone (VSCC) with a nominal particle size cutoff of 2.5 μm prior to sampling by the suite of PM instruments. Flow rate through this cyclone must be maintained at a constant 16.7 LPM in order to ensure effective particle removal from the sample flow.

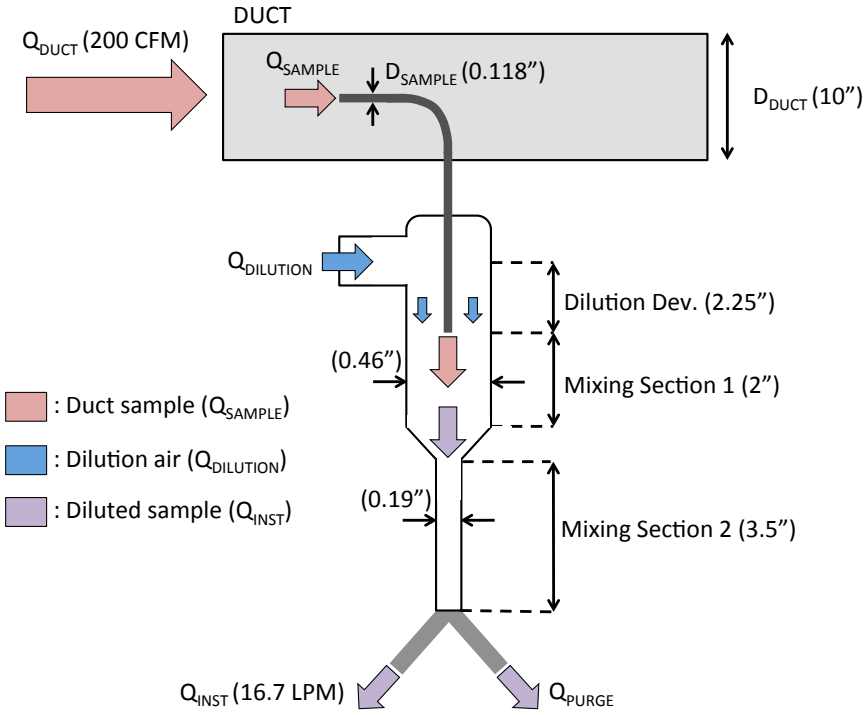

Figure A13. Schematic of secondary diluter

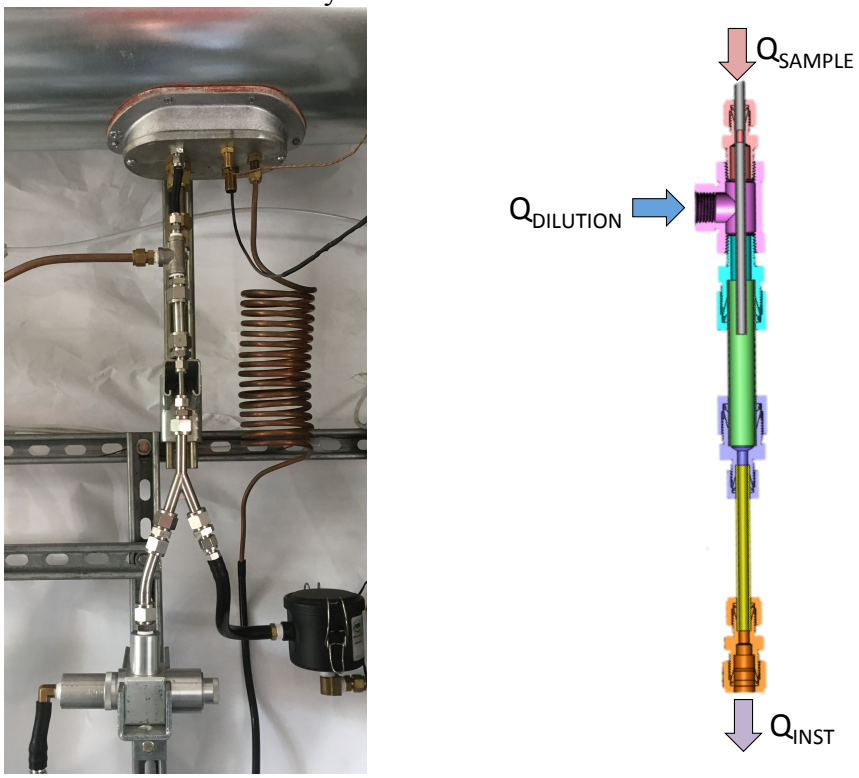

Figure A14. Photograph of secondary diluter at Lawrence Berkeley National Laboratory (left) and cut-section of the diluter as built (right). The diluter is entirely constructed from plumbing parts, and volumetric flow rates are controlled using Alicat Scientific mass flow controllers

The flow rates of dilution and purge air are controlled using Alicat Scientific mass flow controllers to adjust the secondary dilution ratio through the tunnel while maintaining isokinetic sampling conditions. Flow rate settings are calculated using the methods outlined below. Firstly, the secondary dilution ratio is defined as,

$$DR = \frac{Q_s[LPM] + Q_{dil}[LPM]}{Q_s[LPM]} \qquad \text{(A16)}$$

where Q_s is the sample flow rate and Q_{dil} is the dilution flow rate. Given isokinetic sampling conditions at the nominal duct flow rate of 200 CFM (5660 LPM), the sample flow can be calculated as,

$$Q_s[LPM] = Q_{duct}[LPM]\left(\frac{D_s[mm]}{D_{duct}[mm]}\right)^2 \qquad \text{(A17)}$$

where Q_{duct} is the duct flow rate, D_s is the inner diameter of the sampling probe (3.00 mm, or 0.118 inches), and D_d is the duct diameter (254 mm, or 10 inches). Given these values, the sample flow is calculated to equal 0.789 LPM for isokinetic sampling conditions. Using equations A16 and A17, it is possible to calculate the dilution flow rate as a function of the desired secondary dilution ratio. The purge flow rate can be calculated by balancing the mass flows of air entering and exiting the secondary diluter,

$$Q_P[LPM] = Q_{dil}[LPM] + Q_s[LPM] - Q_{inst}[LPM] \qquad \text{(A18)}$$

where Q_{inst} is the flow rate sampled by the suite of instruments (set to a constant 16.7 LPM to accommodate the nominal flow rate of the $PM_{2.5}$ cyclone). Using these three equations, it is possible to calculate dilution and purge flow rates to sample PM from the duct isokinetically over a range of secondary dilution ratios. It should be noted, however, that there exists a minimum dilution ratio below which isokinetic sampling conditions cannot be achieved. This minimum secondary dilution ratio occurs when the purge flow is set to zero, and the sum of the dilution and sample flow rates is equal to 16.7 LPM (the total flow rate sampled by the suite of instruments). For the design parameters provided above, a minimum secondary dilution ratio of 21.5 maintains isokinetic sampling.

Although the secondary diluter is initially set using the calculations above, the dilution ratio is also validated and monitored in real time. CO_2 concentrations in the duct are measured with a CAI gas analyzer, while concentrations in the diluted flow are measured using with a PP Systems SBA-5 NDIR gas analyzer. Given that the ultra-zero air used for secondary dilution does not contain CO_2, the dilution ratio can be calculated as the ratio of CO_2 concentrations in the duct and diluted flows. Prior to each day of testing, volumetric sample and instrument flow rates are measured using a Gillian Gillibrator. In conjunction with the volumetric dilution and purge flow measurements from the Alicat Scientific flow controllers, these measurements are used to validate and calibrate the secondary diluter's operation.

The PM instrument suite consists of six instruments, as illustrated in Figure A15. In order to accommodate the $PM_{2.5}$ cyclone, the combined sample flow rate from all the instruments in the suite is set to 16.7 LPM. A purge line was installed to allow the secondary diluter to operate with any combination of instruments. Flow through the purge line is driven by a vacuum pump and controlled by an Alicat Scientific mass flow controller such that the total sample flow rate is

maintained at the 16.7 LPM setting. In addition, it should be noted that the TSI 3330 OPS particle sizer is particularly sensitive to high PM concentrations. Consequently the OPS sample flow is provided with additional (tertiary) dilution using a TSI 3332 Aerosol Diluter. This diluter provides an additional 10:1 dilution ratio, further decreasing sampled PM concentrations to levels that the OPS can measure accurately.

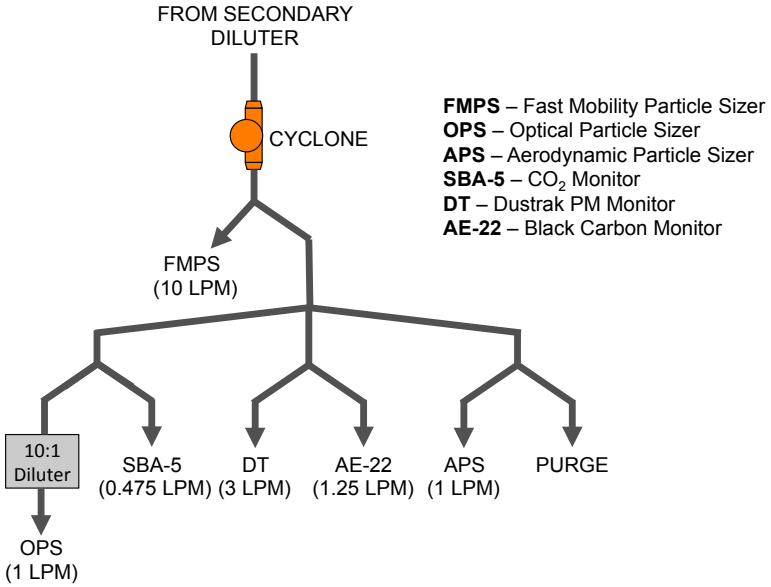

Figure A15. PM instrument suite at Lawrence Berkeley National Laboratory. The suite consists of three particle sizers (TSI 3091 FMPS, TSI 3330 OPS, and TSI 3321 APS), black carbon monitor (Magee Scientific AE-22), PM monitor (TSI 8532 Dustrak II), and CO_2 gas analyzer (PP Systems SBA-5). The system also has a purge line to ensure that the entire system draws a constant 16.7 LPM flow rate of air through the cyclone regardless of which instruments are in use. Flow through the purge line is driven by a vacuum pump and controlled by an Alicat Scientific mass flow controller.

Appendix B – Supporting Information: Practical Design Considerations for Secondary Air Injection in a Wood-Burning Cookstove

B1 – Materials and Methods

B1.1 Modular Air Injection Cookstove Design: Version 2 (MOD2)

The MOD2 stove is a wood-burning cookstove that enables the experimental optimization of secondary air injection design parameters. Figure B1 and Figure B2 below provide a rear and top view of the MOD2 stove, respectively, showing the location of the secondary air supply line, thermocouples, and manifold pressure port. Figure B2 also shows the junctures at the top of the manifold that leaked during testing. The outer juncture was sealed with a high-temperature graphite gasket (Figure B3(b)), but the thin top plate warped over extended use and thermal cycling (Figure B3(a)), resulting in leakage. Figure B1 shows that secondary air is injected into the manifold through a removable access port, which can be easily modified to accommodate a small electric fan or blower in future studies.

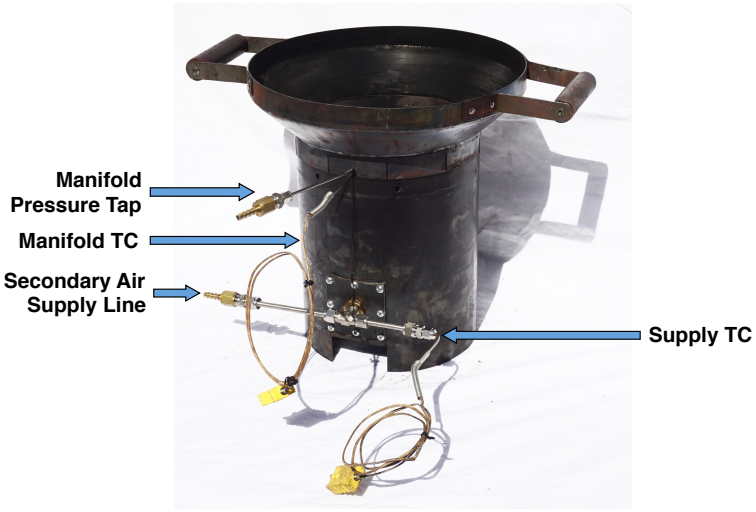

Figure B1. Rear view of the MOD2 stove, showing the secondary air inlet, thermocouples (TC), and manifold pressure port.

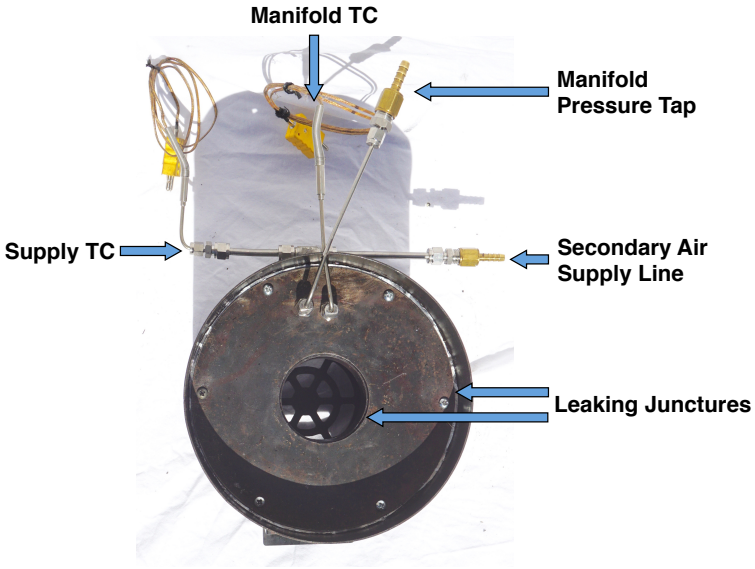

Figure B2. Top view of the MOD2 stove, showing the secondary air inlet, thermocouples (TC), manifold pressure port, and the leaky manifold junctures. The pot skirt and pot supports were removed so as to expose the top of the manifold assembly.

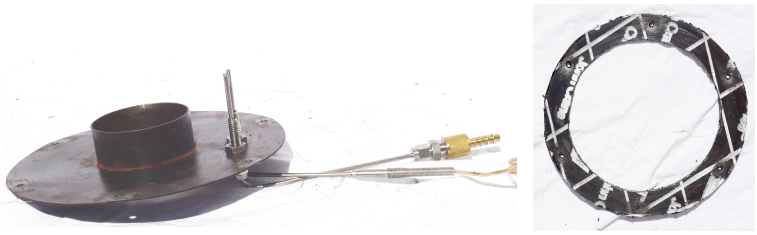

Figure B3. (a) Top of the manifold assembly, showing the thermocouple and pressure port that extend into the manifold. (b) High temperature graphite gasket, used to seal the outer juncture between the top of the manifold assembly and the stove body.

B1.2 Parametric Testing Procedure

Over the course of 52 preliminary tests, a total of 7 injection patterns were evaluated at secondary flow rates ranging from 14 to 43 SLPM (the total flow into the stove manifold), and two promising air injection patterns were identified for further parametric testing (Figure B4). Pattern 1 consists of two concentric rows, each with three orifices evenly spaced around the circumference of the conical chimney. The bottom row of orifices is located ~6.4 mm (0.25 inch) above the juncture of the conical chimney and firebox, while the top row is located ~25 mm (1.0 inch) below the throat. The orifices in each row are offset, such that orifices in the top row are exactly above the midpoint between two orifices in the bottom row. Pattern 2 is identical to the Pattern 1, except that the bottom row has six evenly spaced orifices, rather than three. The two rows in Pattern 2 are vertically aligned, such that orifices in the top row are directly above every other orifice in the bottom row. In both patterns, all air injection orifices have a diameter of 1.59 mm (0.0625 in).

In order to increase the height of the pot above the chimney throat, 2.5-mm (0.10-inch) thick washers were added under the three bolts that serve as pot supports. Primary air flow was controlled using adjustable intakes located under the grate. After initial tests showed that the combustion lacked primary air, these adjustable intakes were left fully open throughout. The stove was not fitted with a pot skirt or thermocouples during preliminary testing. As a result, no secondary air temperature data was collected.

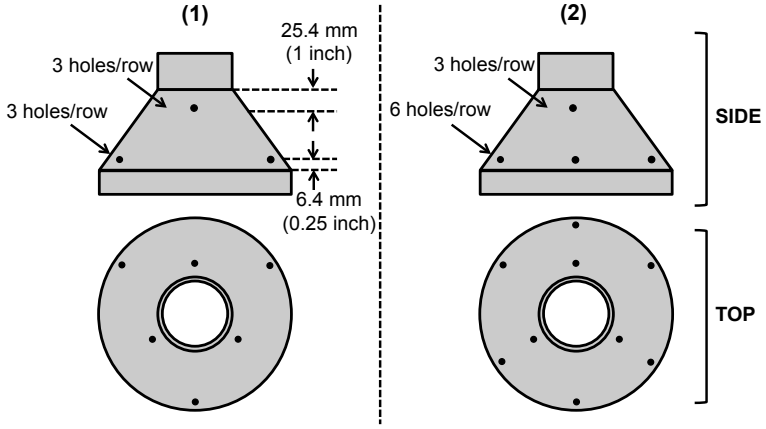

Figure B4. Schematic representation of the two injection patterns (Pattern 1 and Pattern 2) identified during preliminary testing, and evaluated through parametric testing. All air injection orifices have a diameter of 1.59 mm (0.0625 inch). Schematic is not drawn to scale.

B1.3 Manifold Leakage Correction

The MOD2 stove's integrated manifold had some faulty juncture seals (Figure B2), and so a portion of the secondary air systematically leaked to the environment, rather than flowing through the orifices in the injection pattern and into the combustion chamber (firebox). In order to calculate the portion of the secondary flow injected through the orifices, the stove manifold was completely sealed using hot glue, as shown in Figure B5. For the two air injection patterns identified during preliminary testing, Figure B5 shows the manifold pressure at secondary flow rates ranging from 14 to 57 SLPM, with the manifold both in the normal operating configuration (leaking) and fully sealed using hot glue. Manifold pressure measurements were collected with the stove at ambient conditions throughout. Figure B6 shows that for both air injection patterns, the manifold pressure is much greater once the junctures are sealed with hot glue.

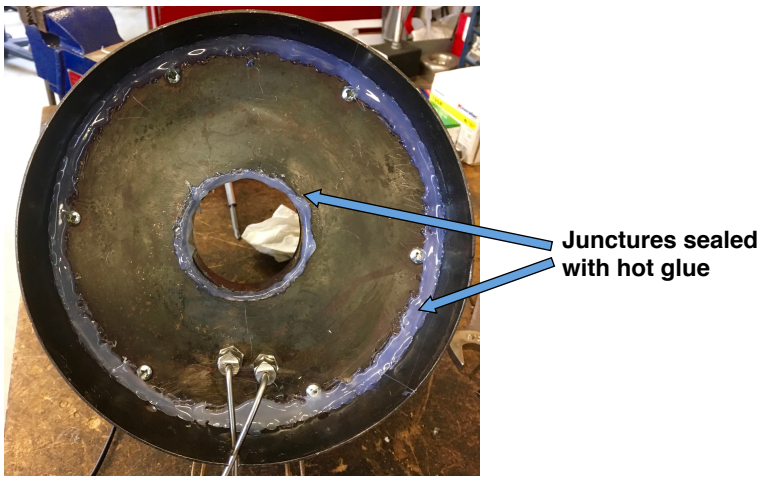

Figure B5. Top of the manifold assembly, sealed with hot glue.

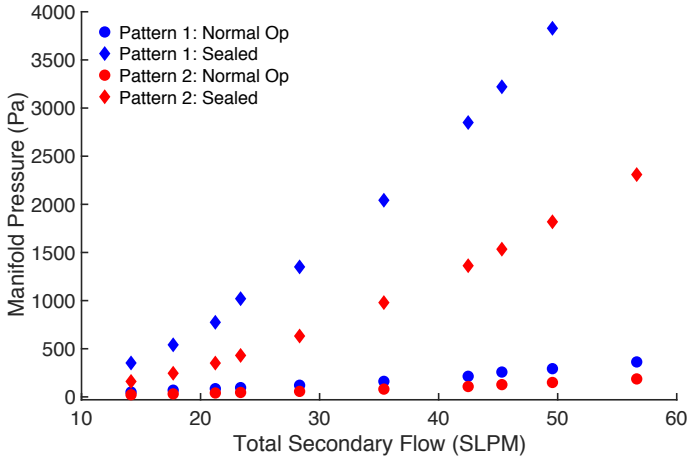

Figure B6. Manifold pressure as a function of secondary air flow rate for two injection patterns, with the manifold in both the normal operating configuration (leaking) and fully sealed using hot glue.

With the stove manifold completely sealed and all the secondary air passing through the injection pattern, it is possible to use the corresponding pressure and flow rate measurements to calculate the coefficient of discharge (C_d) through the orifices using Equation B1,

$$C_d = \left(\frac{4Q}{N\pi D^2}\right)\sqrt{\frac{\rho_{STP}}{2\Delta P}} \qquad \text{(B1)}$$

where Q is the standard volumetric flow rate of secondary air (SLPM), ρ_{STP} is the density of air at standard conditions (1.225 kg/m^3), ΔP is gauge pressure in the manifold (Pa), N is the number of orifices in the injection pattern, and D is the orifice diameter (1.59 mm).[198] The standard volumetric flow rate of secondary air into the manifold was measured with a rotameter (SLPM), and so must correspondingly be converted to mass flow rate using the density of air at standard conditions. Figure B7 below shows the coefficient of discharge calculated at each parametric setting (with the manifold fully sealed). The coefficient of discharge remains relatively constant throughout, ranging from 0.82 to 0.88, and has an average value of 0.846 ± 0.008 (mean of C_d at all parametric configurations ± 90% confidence interval). This value of discharge coefficient agrees closely with that derived in other experimental studies of turbulent air discharge through small orifices. [202,203]

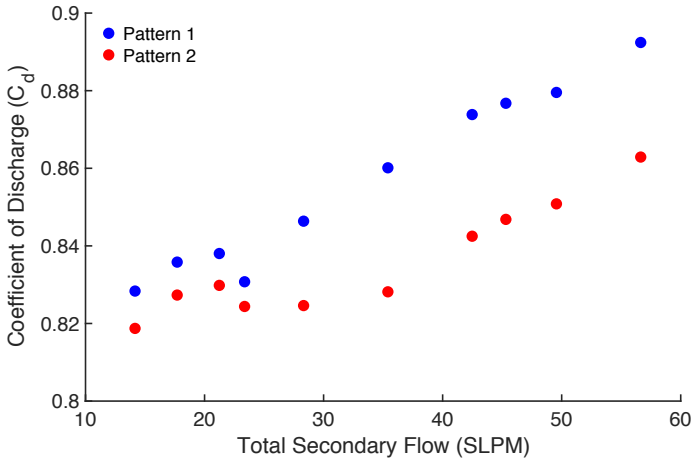

Figure B7. Coefficient of discharge (C_d) calculated at each parametric configuration, using pressure and flow rate measurements collected with the MOD2 stove manifold fully sealed, such that all the secondary air passes through each of the two patterns presented.

Using the average coefficient of discharge calculated above (0.846 ± 0.008) and the manifold pressure measurements collected in the normal operating configuration (with the leakage), it is possible to determine the standard volumetric flow rate of secondary air passing through each injection pattern as follows,

$$Q = \left(\frac{C_d N \pi D^2}{4}\right)\sqrt{\frac{2\Delta P}{\rho_{air}}}. \qquad \text{(B2)}$$

For each combination of secondary flow rate (the total flow into the manifold) and injection pattern, Figure B8 and Figure B9 show the standard volumetric flow rate (SLPM) and fraction (%) of secondary air injected into the firebox, respectively. The flow rate of injected air increases linearly with total secondary flow, and is generally consistent between the two patterns at each setting. As total secondary flow increases, the fraction of injected air initially decreases from around 39% to 27%, presumably because higher manifold pressures push against the top of the

manifold assembly and expand the cracks through which air is leaking. However, the leakage stabilizes for flow rates > 40 SLPM, as the cracks can expand no further.

Using these calculations, it is possible to present the stove performance results in terms of the standard volumetric flow injected through the patterns, rather than the total secondary flow into the manifold. Since secondary air leaked mostly through the outer juncture at the top of the manifold assembly, away from the firebox, it is unlikely that the leakage significantly impacted the stove's combustion performance. However, it should be acknowledged that the leakage of cold secondary air near the pot of water (the thermal load) may have hampered heat transfer from the hot exhaust flow, and restricted the stove's thermal performance. Future iterations of the MOD stove should rectify the leakages, and manifold pressure measurements should be collected in real time throughout testing (as was done for temperature).

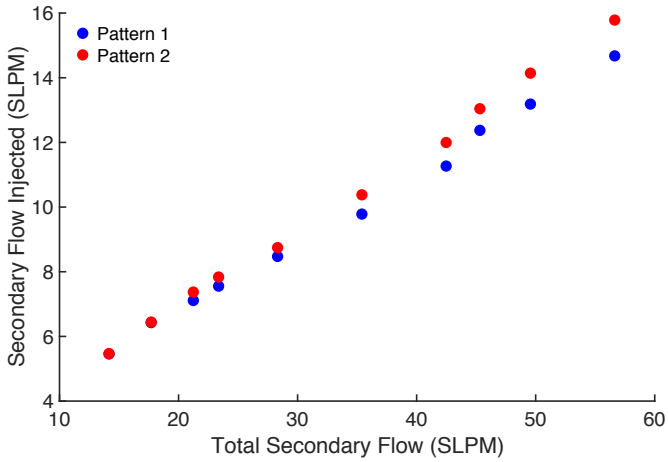

Figure B8. Standard volumetric flow rate of air injected through the orifices in each pattern, calculated using Equation B2, as a function of total secondary flow rate into the manifold.

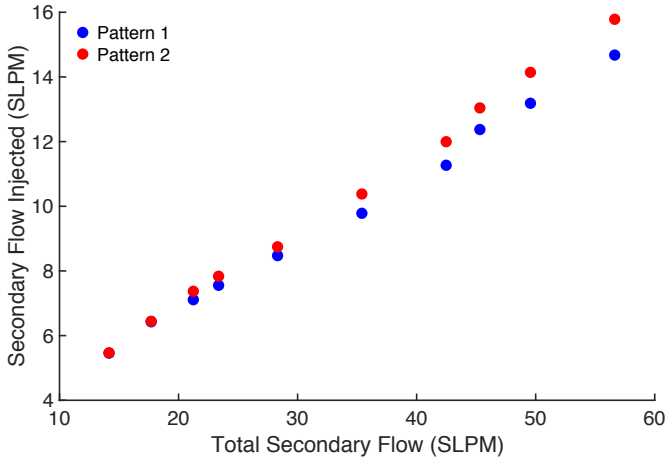

Figure B9. Fraction of the total secondary flow rate injected through the orifices in each pattern.

B1.4 Data Analysis and Performance Metrics

Performance metrics, such as firepower, equivalent dry mass of fuel consumed, and thermal efficiency, are calculated for each test using the methods provided in the WBT Protocol 4.2.3.[89] Emission factors are calculated according to the methods outlined by Caubel et al.,[105] and some additional methods are presented below. Size-resolved particle concentration measurements from the TSI 3321 APS instrument are corrected using a particle density of 1.90 ± 0.05 g/cm^3 (mean of particle density calculated at all parametric tests ± 90% confidence interval).[99] The total mass of gaseous emissions emitted (CO, CO_2) or consumed (O_2) is calculated using Equation B3 below,

$$m_{gas} = \sum_{t=0}^{t=t_f} \frac{MW(C_{gas}(t) - C_{gas,bkg})Q_{duct}(t)P_{amb}\Delta t}{R(T_{duct}(t) + 273)} \qquad \text{(B3)}$$

where m_{gas} (g) is the total mass of gaseous emissions, t is the time step, t_f is the duration of the cold start test (sec), C_{gas} is the volumetric gas concentration (ppmv), $C_{gas,bkg}$ is the background gas concentration (ppmv), MW is the molecular weight of the gas species (g/mol), Q_{duct} is the duct flow rate (m^3/sec), P_{amb} is the ambient pressure (97150 Pa at the laboratory's altitude of ~300 m MSL), Δt is the sampling period (1 sec), R is the ideal gas constant (8.314 J/ (mol K)), and T_{duct} is the temperature in the duct (°C). The background levels of each gas species are calculated by taking the average of concentration measurements collected for 1 min prior to the start of the test phase (ignition of the kindling), while the system is sampling ambient air. Background concentrations of $PM_{2.5}$ and BC are always assumed to be exactly 0 μg/m^3.

The average standard volumetric flow rate of air stoichiometrically consumed by the combustion (Q_{stoich}, SLPM) is calculated using Equation B4 below,

$$Q_{stoich} = \frac{4.76 m_{O_2}(MW_{air}/MW_{O_2})}{\rho_{STP} ttb} \qquad \text{(B4)}$$

where m_{O2} is the total mass of O_2 consumed over the cold start (g, calculated using Equation B3), MW_{air} is the molecular of air (28.97 g/mol), MW_{O2} is the molecular mass of O_2 (32.0 g/mol), and ttb is the time to boil (min). Throughout the cold start test, the air injection velocity (v, m/s) is calculated at every time step (t) using Equation B5,

$$v(t) = \frac{4\rho_{STP}Q}{\rho(t)\pi N D^2} = \frac{4\rho_{STP}Q(T_{man}(t) + 273)R_{air}}{P_{man}\pi N D^2} \qquad \text{(B5)}$$

where ρ is the density of air in the manifold (kg/m^3), T_{man} is the air temperature in the manifold (°C), R_{air} is the ideal gas constant for air (287 J/Kg K), and P_{man} is the absolute pressure in the manifold (roughly equal to the local ambient pressure, 97150 Pa). Similarly, the manifold gauge pressure (ΔP, Pa) is calculated as follows,

$$\Delta P(t) = \Delta P_{STP}\left(\frac{\rho_{STP}}{\rho(t)}\right) = \frac{\Delta P_{STP}\rho_{STP}(T_{man}(t) + 273)R_{air}}{P_{man}} \qquad \text{(B6)}$$

where ΔP_{STP} (Pa) is the manifold gauge pressure measured at ambient (standard) conditions, show in Figure B6. The average secondary air velocity and manifold pressure are evaluated using measurements calculated over the length of the cold start air. The average rate of heat transferred to the secondary air in the manifold (H_{man}, kW) is calculated using,

$$H_{man} = \rho_{STP} Q \left(C_p (T_{man,avg} - T_{in,avg}) + \frac{1}{2} (4\rho_{STP} Q R_{air})^2 \left(\left(\frac{(T_{man,avg} + 273)}{P_{amb}(N\pi D^2)} \right)^2 - \left(\frac{(T_{in,avg} + 273)}{P_{man}(\pi D_{in}^2)} \right)^2 \right) \right) \quad \text{(B7)}$$

where C_p is the specific heat of air (1.055 KJ/Kg K), D_{in} is the secondary air inlet diameter (4.6 mm), and $T_{man,avg}$ and $T_{in,avg}$ are the average secondary air temperatures in the manifold and inlet (°C), respectively, over the length of the test.[204]

Multiple tests were conducted for each parametric stove design configuration (unique combination of secondary air injection pattern and flow rate), and the first and third quartiles (*Q1* and *Q3*) were calculated for each replicate set of results. Outliers in each replicate set are defined as,

$$Q1 - 1.5IQR > \text{outlier} > Q3 + 1.5IQR \quad \text{(B8)}$$

where *IQR* is the interquartile range (= *Q3* – *Q1*).[205] Outliers are removed from the replicate set according to this criterion, and for each stove design configuration, the mean and 90% confidence interval of the remaining measurements (or calculated metrics) is evaluated.

B2 – Results and Discussion

B2.1 Preliminary Testing Results

Manifold pressure measurements were only collected with air injection patterns 1 and 2, and so some operational metrics are unavailable for the remaining patterns (e.g. the calculated portion of secondary flow rate of air injected into the firebox). Figure B10 and Figure B11 below summarizes the preliminary testing results collected with air injection patterns 1 and 2. For Pattern 1, 5 to 8 replicate tests were conducted at four flow rate settings, ranging from 7.2 to 12 SLPM. Only 1 or 2 tests were conduced at each of five flow rate settings using Pattern 2, and so the corresponding confidence intervals are large or non-existent. When comparing results from the preliminary and parametric testing phases, only results collected with Pattern 1 should be considered, as insufficient trials were conducted with Pattern 2. Since thermocouples were not installed during preliminary testing, some temperature dependent parameters are omitted, such as average air injection velocity.

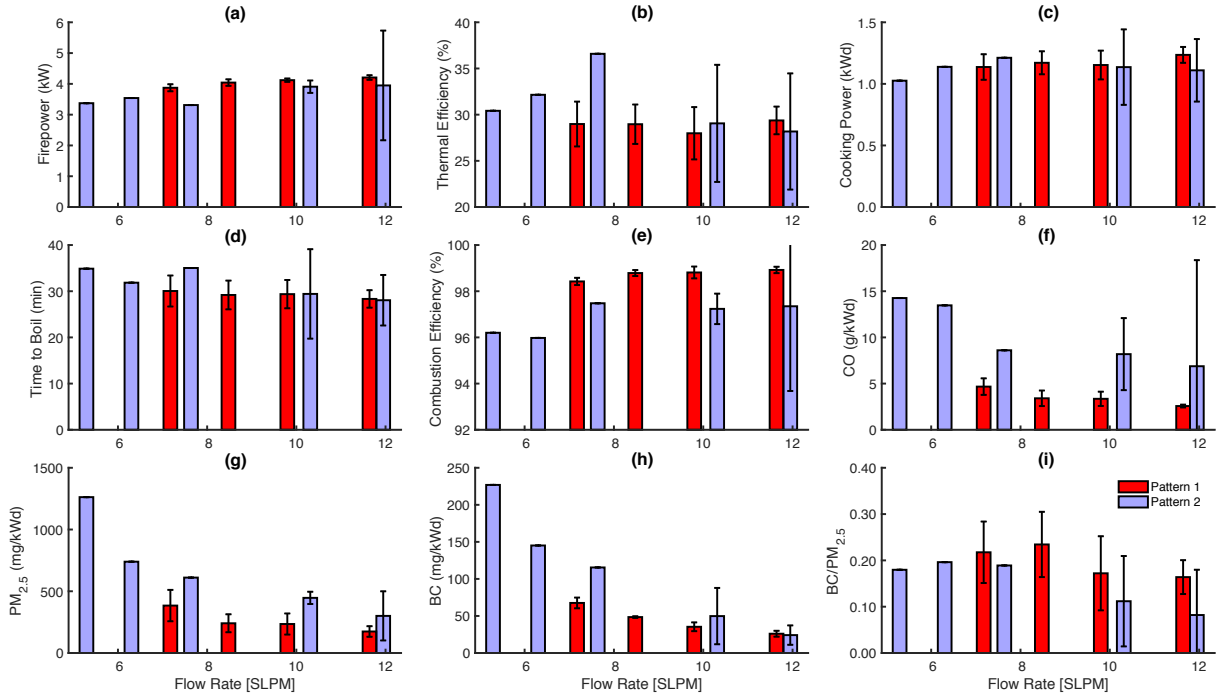

Figure B10. MOD2 stove performance, emissions, and operational metrics during high-power cold start testing (preliminary tests), presented as function of secondary air injection flow rate and pattern: (a) Firepower (kW); (b) Thermal Efficiency (%); (c) Cooking Power (kWd); (d) Time to boil (min); (e) Combustion Efficiency (%); (f) CO emissions (g/KWd); (g) $PM_{2.5}$ emissions (mg/KWd); (h) BC emissions (mg/KWd); (i) BC/ $PM_{2.5}$ ratio. Bars represent the mean of replicate test data collected for each stove configuration, while error bars represent the corresponding 90% confidence interval. Only 1 test was conducted for some configurations (Pattern 1), and so confidence intervals are not shown.

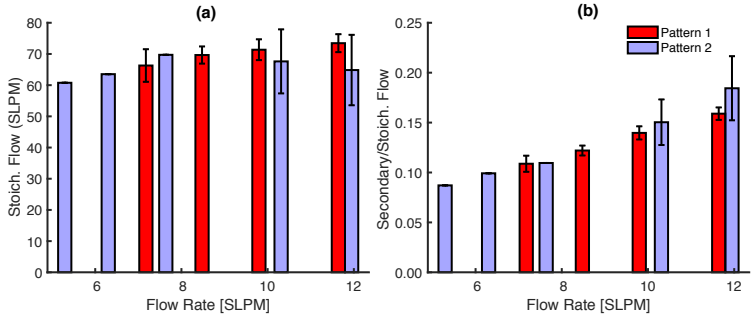

Figure B11. MOD2 stove operational metrics during high-power cold start testing (preliminary tests), presented as function of secondary air injection flow rate and pattern: (a) Stoichiometric flow rate of air into the combustion (SLPM); (b) Ratio of the secondary to stoichiometric flow rate of air. Bars represent the mean of replicate test data collected for each stove configuration, while error bars represent the corresponding 90% confidence interval. Only 1 test was conducted for some configurations (Pattern 1), and so confidence intervals are not shown.

B2.2 Parametric Testing Results

During parametric testing, two air injection patterns were evaluated at six flow rate settings. In addition to Figure 2 in the manuscript, Figure B12 summarizes the stove's performance at all twelve parametric design configurations.

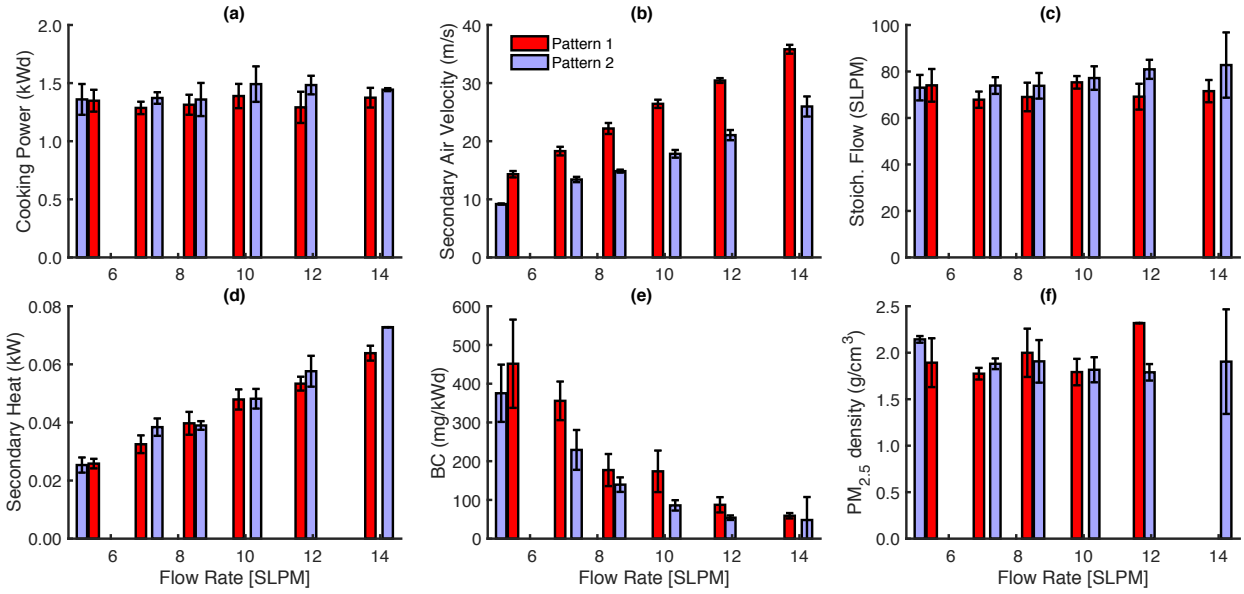

Figure B12. MOD2 stove performance, emissions, and operational metrics during high-power cold start testing, presented as function of secondary air injection flow rate and pattern: (a) Cooking Power (kWd); (b) Average secondary air injection velocity (m/s); (c) Stoichiometric flow rate of air into the combustion (SLPM); (d) Average rate of heat transfer to secondary air in the manifold (kW); (e) Black carbon (BC) emissions (mg/kWd); (f) $PM_{2.5}$ density (g/cm^3). Bars represent the mean of replicate test data collected for each stove configuration, while error bars represent the corresponding 90% confidence interval. Error bars necessarily are omitted for metrics calculated from a single data point.

B2.3 Optimal MOD2 Stove and TSF Comparison

During parametric testing, MOD2 stove performance was found to be optimal using secondary air injection Pattern 2 at a flow rate of 12 SLPM. Table B1 below summarizes the performance of the MOD2 stove in this optimal design configuration, and compares it to a traditional three stone fire (TSF). Testing results for the TSF are provided by Rapp et al., and were collected using the same experimental set up and methods as that used during MOD2 stove testing.[75]

	TSF	MOD2	Difference (%)
Number of Tests	10	4	N/A
Firepower (kW)	5.3 (0.4)	4.7 (0.2)	-11 (8)
Time to boil (min)	31 (3)	24 (2)	-20 (10)
Cooking Power (kW)	1.22 (0.08)	1.48 (0.08)	21 (9)
Thermal Efficiency (%)	23 (1)	31 (1)	34 (6)
Combustion Efficiency (%)	95.9 (0.3)	98.95 (0.07)	3.2 (0.3)
CO (g/kWd)	18 (3)	1.7 (0.3)	-90 (20)
PM2.5 (mg/kWd)	1200 (200)	90 (20)	-90 (20)
BC (mg/kWd)	550 (40)	54 (6)	-90 (10)

Table B1. Performance and emissions metrics for a traditional three-stone fire (TSF) and the MOD2 stove in the optimal configuration (air injection Pattern 2 at 12 SLPM). The mean and 90% confidence interval (in parentheses) are provided for each metric, and the corresponding number of replicate tests is indicated for each stove. The table also provides the percent change in MOD2 performance relative to the TSF.

B2.4 $PM_{2.5}$ Generation: Additional Plots and Results

Size-resolved PM measurements were collected during parametric testing of air injection Pattern 2. For each secondary flow rate setting, Figure B13 presents the mean and 90% confidence interval of $PM_{2.5}$ emission metrics from each set of replicate cold start tests. The metrics presented in Figure B13 are identical to that shown in Figure 4 except that the emission contributions from each particle size range have been rearranged such that confidence intervals can be displayed clearly. Similarly, Figure B14 and Figure B15 present the same time-resolved $PM_{2.5}$ accumulation measurements as that shown in Figure 5, but the data from the six parametric design configurations is split up over two Figures, such that 90% confidence intervals are clearly discernible. It should be noted that only 2 tests were conducted at a secondary flow rate of 14 SLPM, and so the corresponding 90% confidence intervals are much larger than shown at other secondary flow settings, for which 4 to 8 replicate tests were conducted.

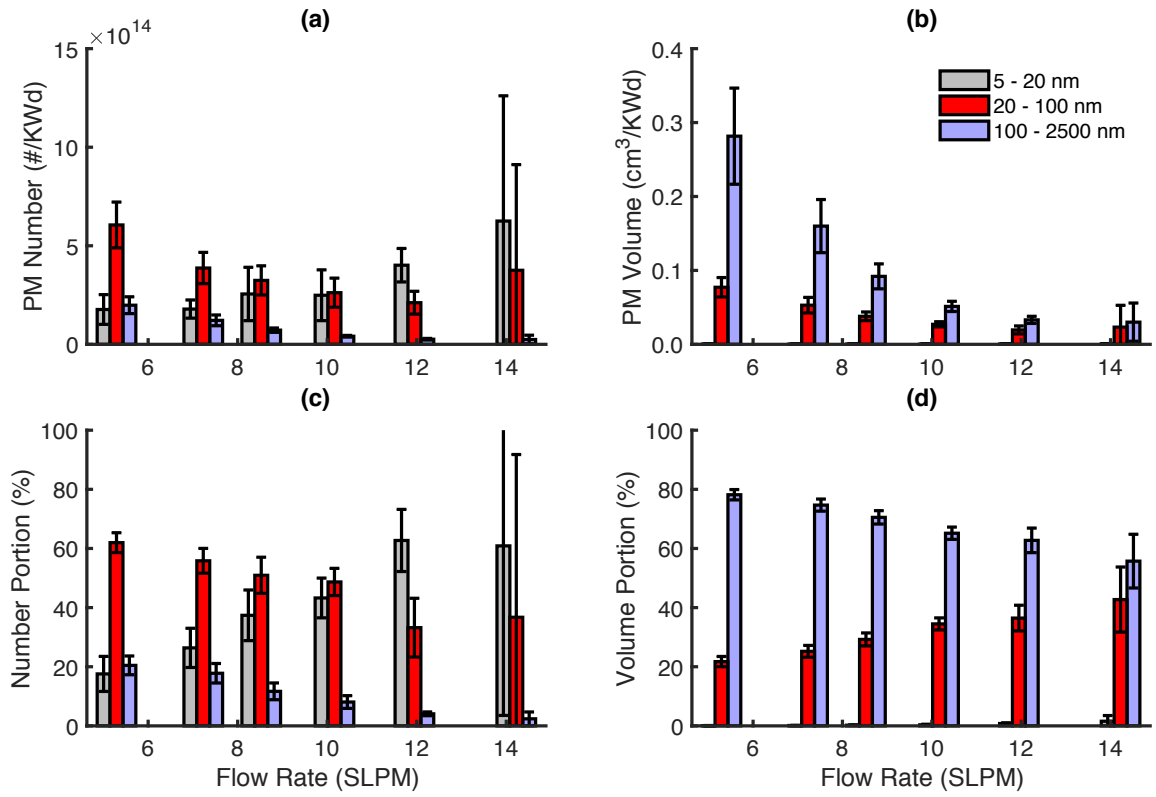

Figure B13. (a) Total $PM_{2.5}$ number and (b) volume emissions from the MOD2 stove over the cold start (normalized by cooking power), as a function of secondary air flow rate through injection Pattern 2 for three particle size ranges: 5 to 20 nm, 20 to 100 nm, and 100 to 2500 nm. (c) Portion of the total number, and (b) volume of particles emitted in each of the three particle size ranges. Each bar represents the mean of replicate test data collected for each stove configuration, and error bars represent the corresponding 90% confidence interval.

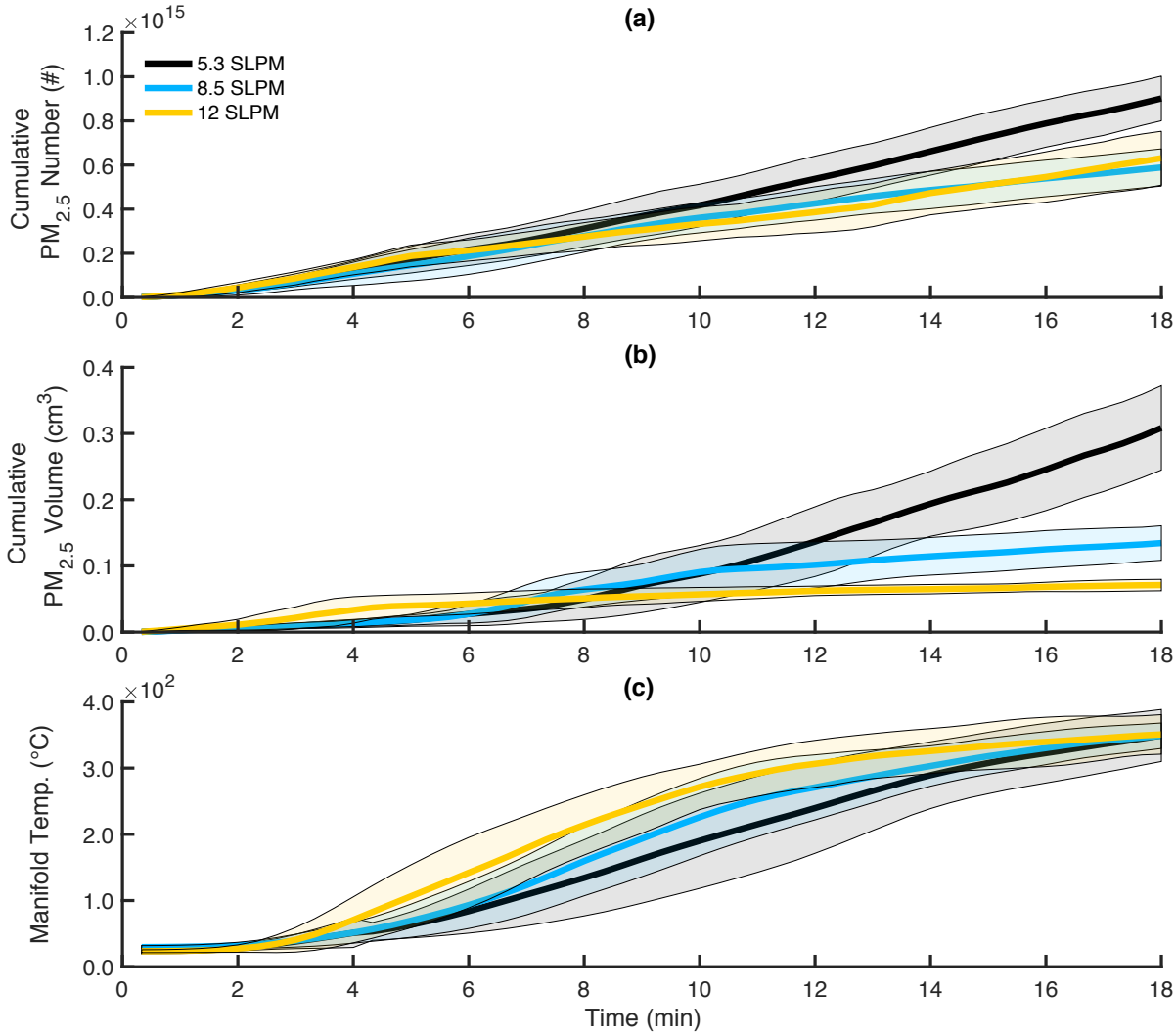

Figure B14. (a) Accumulation of $PM_{2.5}$ number and (b) volume emissions from the MOD2 stove over the first 18 minute of the cold start. (c) Temperature of secondary air in the MOD2 stove manifold over the first 18 minute of the cold start. Each bold line represents the mean of replicate test measurements collected at secondary flow settings of 5.3, 8.5, and 12 SLPM (using air injection Pattern 2), while shaded areas represent the corresponding 90% confidence interval. All data presented is block-averaged on a 20-sec time base.

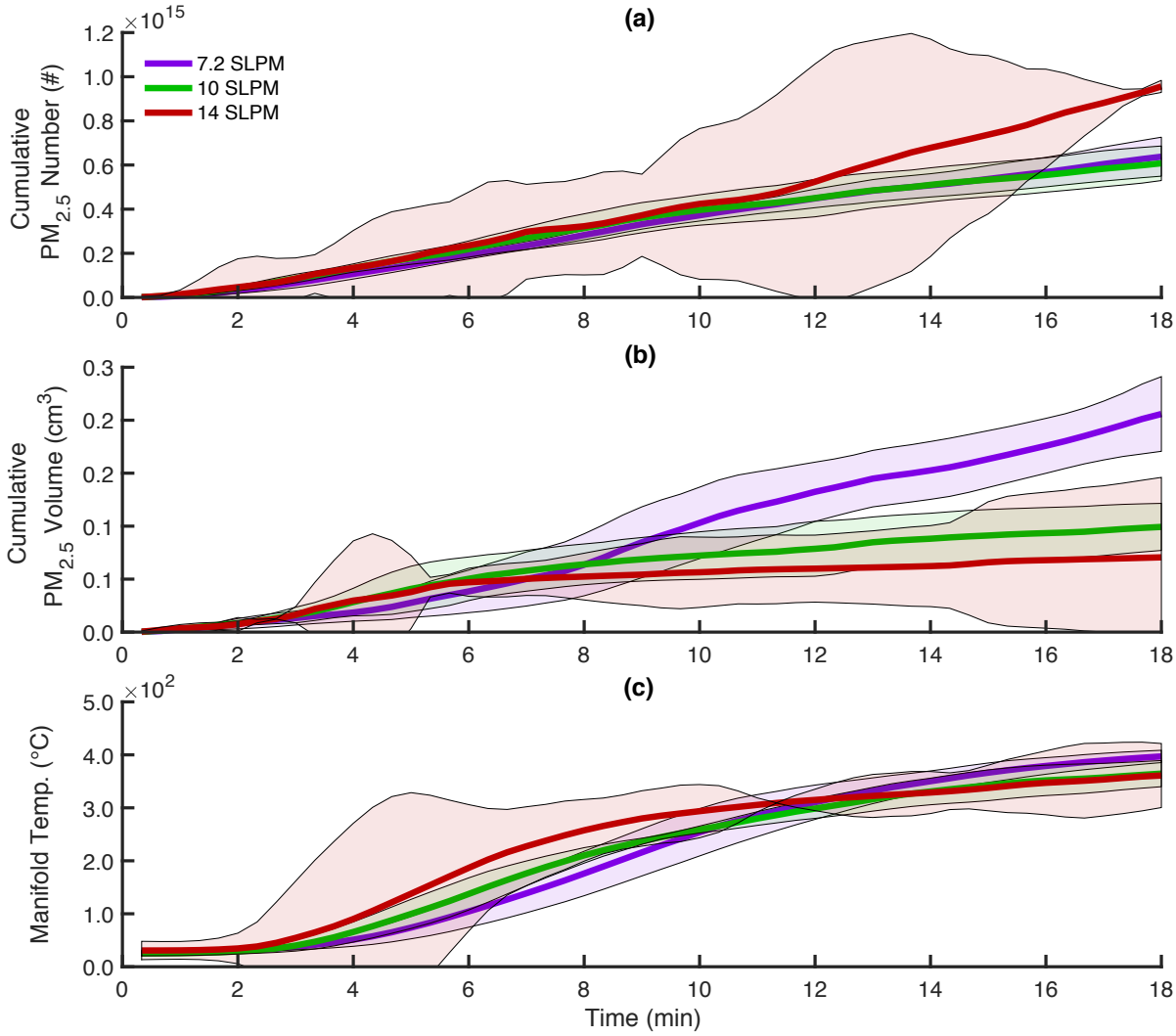

Figure B15. (a) Accumulation of $PM_{2.5}$ number and (b) volume emissions from the MOD2 stove over the first 18 minute of the cold start. (c) Temperature of secondary air in the MOD2 stove manifold over the first 18 minute of the cold start. Each bold line represents the mean of replicate test measurements collected at secondary flow settings of 7.2, 10, and 14 SLPM (using air injection Pattern 2), while shaded areas represent the corresponding 90% confidence interval. All data presented is block-averaged on a 20-sec time base.

For each secondary flow rate setting, Figure B16 provides the size distributions of total $PM_{2.5}$ number and volume emissions from the MOD2 stove during the cold start. Figure B17 shows the count median diameter (CMD) and volume median diameter (VMD) of $PM_{2.5}$ emissions over the first 18 minutes of the cold start. Figure B18 and Figure B19 present the same time-resolved median particle diameter data as that shown in Figure B17, but include the corresponding 90% confidence intervals at each stove configuration.

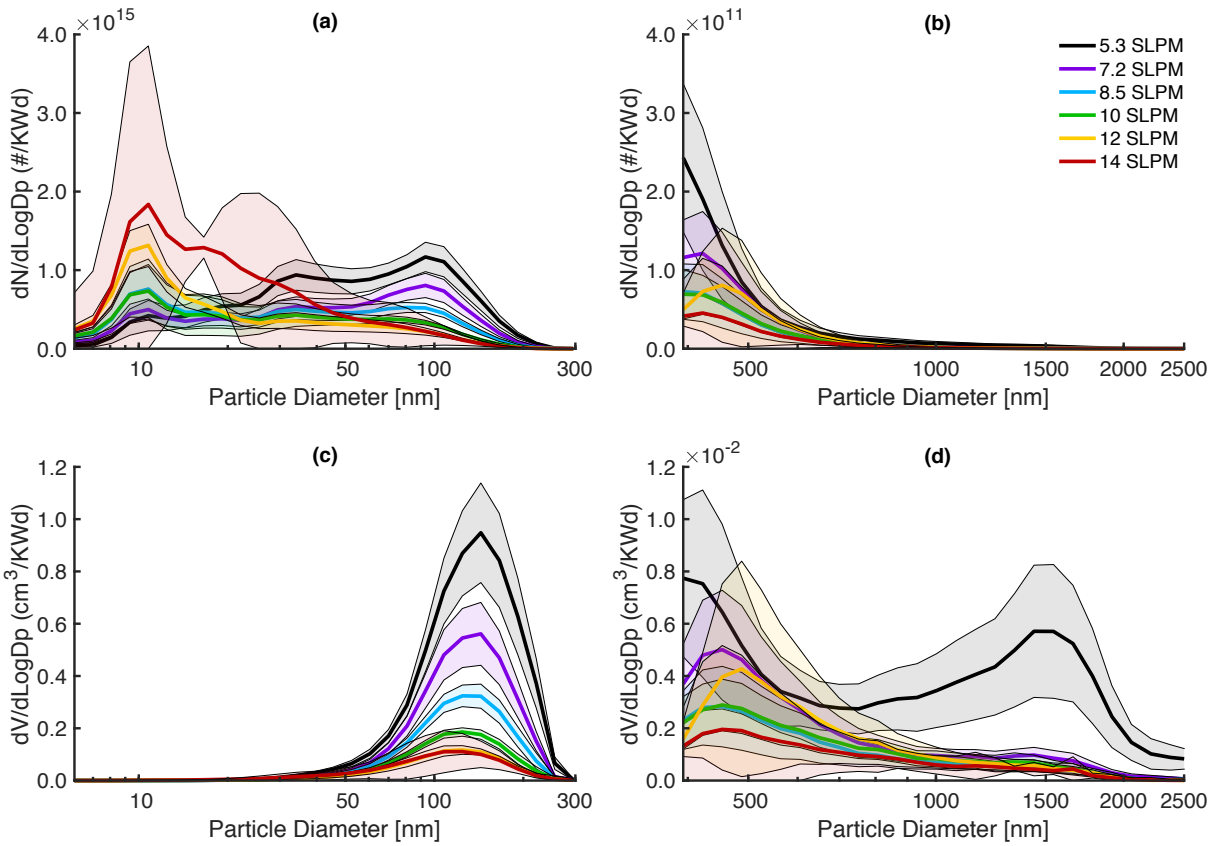

Figure B16. Size-resolved distribution of total particle number or volume emitted during the cold start, normalized by the average cooking power, for each secondary flow rate setting (using injection Pattern 2): (a) FMPS particle number distribution; (b) FMPS particle volume distribution; (c) APS particle number distribution; (d) APS particle volume distribution.

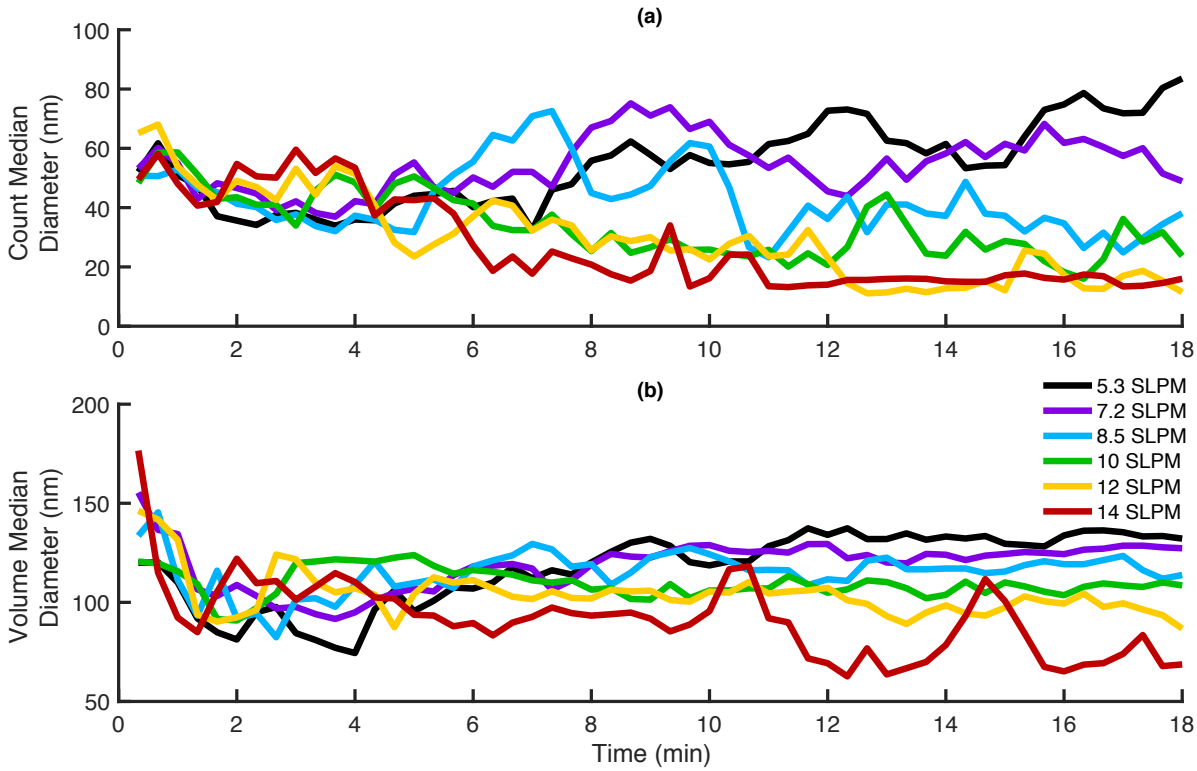

Figure B17. (a) Count median diameter and (b) count volume diameter of $PM_{2.5}$ emissions from the MOD2 stove over the first 18 minute of the cold start. Each line represents the mean of replicate test measurements collected at each of the six secondary flow rate settings (using injection Pattern 2). Confidence are omitted here for clarity, and instead provided in Figure B18 and Figure B19 for all secondary flow rate settings. All data presented is block-averaged on a 20-sec time base.

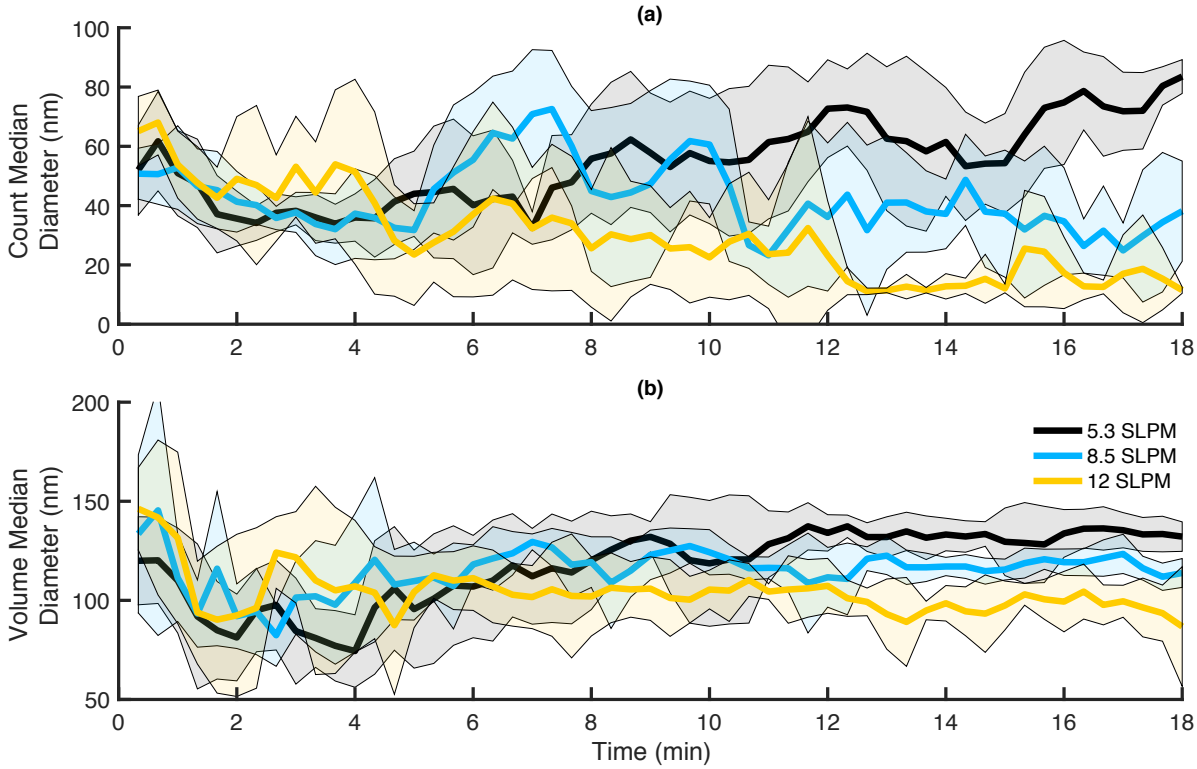

Figure B18. (a) Count median diameter and (b) count volume diameter of $PM_{2.5}$ emissions from the MOD2 stove over the first 18 minute of the cold start. Each bold line represents the mean of replicate test measurements collected at secondary flow rate settings of 5.3, 8.5, and 12 SLPM (using air injection Pattern 2), while shaded areas represent the corresponding 90% confidence interval. All data presented is block-averaged on a 20-sec time base.

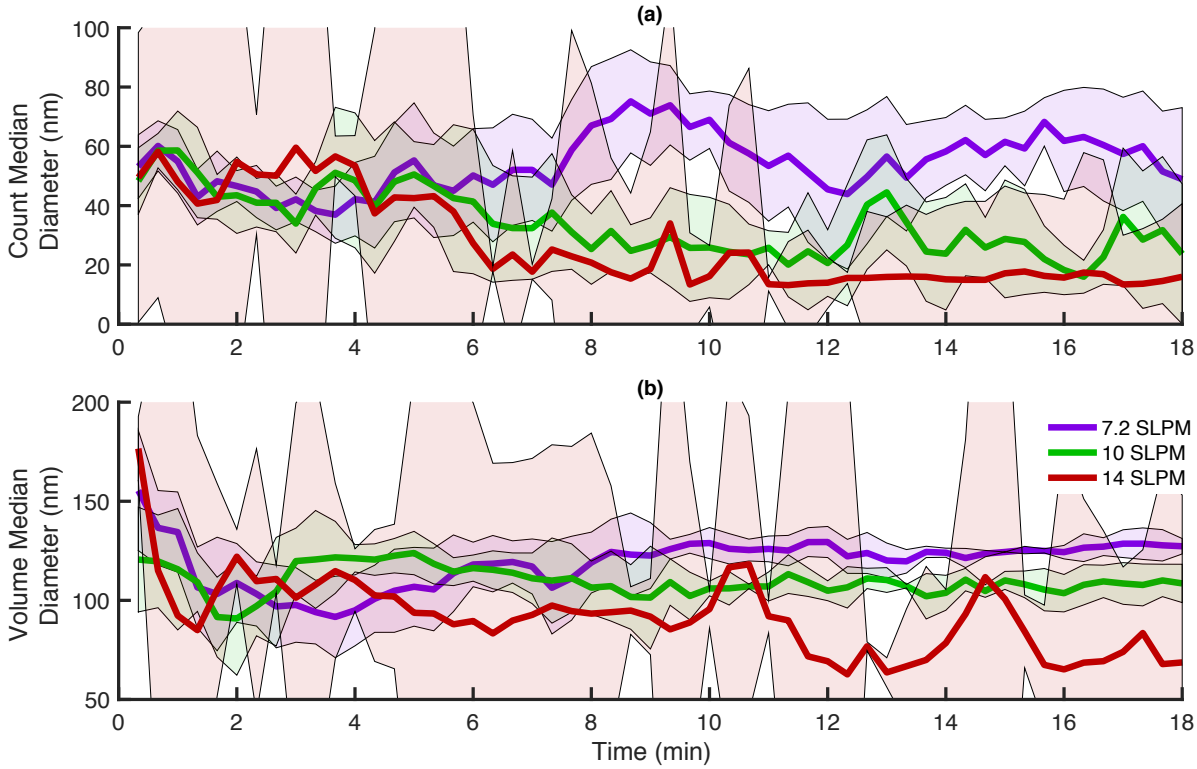

Figure B19. (a) Count median diameter and (b) count volume diameter of $PM_{2.5}$ emissions from the MOD2 stove over the first 18 minute of the cold start. Each bold line represents the mean of replicate test measurements collected at secondary flow settings of 7.2, 10, and 14 SLPM (using air injection Pattern 2), while shaded areas represent the corresponding 90% confidence interval. All data presented is block-averaged on a 20-sec time base.

Appendix C – Supporting Information: A New Black Carbon Sensor for Dense Air Quality Monitoring Networks

C1 – Field Validation Site

During field validation, Aerosol Black Carbon Detector (ABCD) units were deployed on the roof of the Bay Area Air Quality Management District (BAAQMD) roadside monitoring station, located near Laney College and Highway 880 in Oakland, California (as shown in Figure C1).

(a) (b)

Figure C1. (a) Over 60 Aerosol Black Carbon Detector (ABCD) units hung from the railing of the Bay Area Air Quality Management District (BAAQMD) roadside monitoring station in Oakland, California; (b) Close up view of ABCD units deployed at the monitoring station, with California Highway 880 in background.

C2 – Sensor Principle of Operation

The Aerosol Black Carbon Detector (ABCD) calculates black carbon (*BC*) mass concentrations (μg m^{-3}) at each measurement time interval using the sample and reference voltage outputs from the optical cell, and flow rate measurements from the differential pressure sensor:

$$BC(t_i) = \frac{A}{Q(t_i) \cdot MAC \cdot (t_i - t_{i-1})} \cdot \ln\left(\frac{V_{ref}(t_i)}{V_{smpl}(t_i)} \cdot \frac{V_{smpl}(t_{i-1})}{V_{ref}(t_{i-1})}\right). \qquad (C1)$$

where t_{i-1} and t_i are the time stamps of two consecutive measurements, V_{smpl} and V_{ref} (V) are the optical cell's sample and reference voltage outputs, respectively, and A (m^2) is the surface area of each filter orifice. In the ABCD optical cell, both circular orifices have a diameter of 0.003175 m (0.125 in), and corresponding area of 7.87×10^{-6} m^2. Q (m^3 s^{-1}) is the volumetric flow rate of air through the instrument, as measured by the differential pressure sensor downstream of the optical

cell (see Appendix C). The ABCD's flow rate is set between 1.67×10^{-6} and 4.17×10^{-6} m^3 s^{-1} (100 and 250 cc min^{-1}), and held constant. MAC (m^2 g^{-1}) is the mass attenuation coefficient of BC, which is set at 12.5 m^2 g^{-1}. The ABCD uses Teflon-coated glass filters (Pallflex® Emfab™) and LEDs centered at a wavelength of 880 nm. Other BC instruments using similar fibrous filter materials at this incident wavelength use the same MAC value. [206] Throughout this study, the ABCD operated at a sampling frequency of 0.5 Hz, so $\Delta t = t_i - t_{i-1} = 2$ seconds.

C3 – Flow Rate Sensor Calibration

The flow rate of air sampled through the Aerosol Black Carbon Detector (ABCD) is measured using an Omron D6F differential pressure sensor installed inline between the optical cell and vacuum pump (as illustrated in Figure 15). The sensor outputs an analog voltage that is dependent on the volumetric flow rate of air through the sensor. The MCU digitizes the analog voltage using an integrated, 10-bit analog-to-digital converter (ADC), so it can be used to calculate BC mass concentrations. To calibrate the differential pressure sensor, the analog voltage output is recorded while the ABCD's sample flow rate (at the inlet, with clean filters loaded in the optical cell) is simultaneously measured with a bubble meter (Gilian Gilibrator). Flow calibration data was collected using four different sensor units, as shown in Figure C2, and a least-squares regression was used to generate the quadratic calibration equation:

$$FR = 77.1(V_{FR})^2 + 72.6(V_{FR}) - 48.0. \qquad (C2)$$

where FR (cc min^{-1}) is the sample flow rate at the inlet, and V_{FR} (V) is the analog voltage output by the differential pressure sensor. Figure C2 shows that the calibration data is repeatable between sensor units, and that the empirical equation generated from the aggregate data set has a coefficient of determination (R^2) of 0.992.

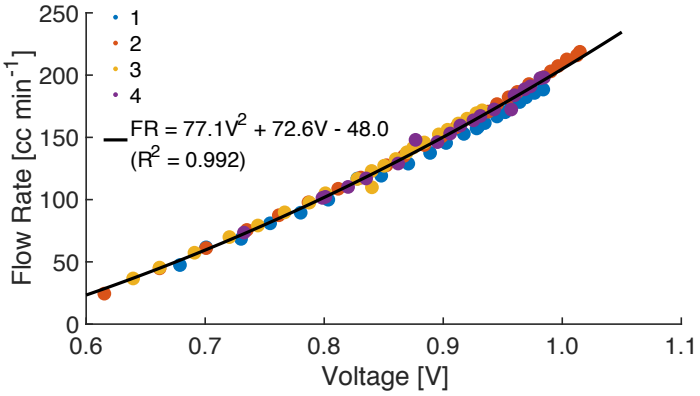

Figure C2. Flow sensor calibration data. Volumetric flow rate of air sampled through ABCD plotted as function of voltage output from four different Omron D6F differential pressure sensor units. A quadratic regression equation is derived for the aggregate data collected from all four sensors, and is shown with the corresponding coefficient of determination (R^2).

C4 – Sensor Components List

Table C1 below lists the major components shown in the ABCD functional diagram (Figure 15), the corresponding material cost, and the component manufacturer and model where applicable. The prices listed represent the approximate cost of each component when ordering 150 units, and do not reflect the costs associated with the assembly, calibration, and validation of each ABCD. The total material cost of the components listed is $430.

Component	Manufacturer / Model	Approximate Material Cost (USD)
Optical Cell	N/A	100
AUX Board	N/A	80
Pump	Schwartzer / 135 FZ	125
Flow Sensor	Omron / D6F	40
Battery	KXD / 12V, 10AH	35
Photovoltaic Panel	Shine Solar / 18V, 8W	20
Packaging	BUD Industries / NBF-32002	20
Miscellaneous[1]	N/A	10

[1]Miscellaneous components include electrical connectors, packaging insulation, and other minor items.

Table C1. Major components of the Aerosol Black Carbon Detector.

C5 – Data Processing and Quality Assurance

The ABCD generates BC data that is stored directly on the onboard memory card (SD card) every 2 seconds. After zero-response trials, 2-second data is collected from the SD cards and used for temperature compensation calculations, without any data correction or filtering. During field validation, the ABCD transmits one-minute time base data to an online server every hour, where it is cataloged and stored. SD card data is also collected manually to supplement the wireless data set during periods when the sensor is operating but unable to communicate with the online server. The 2-second time base data from the SD card is averaged down to a one-minute time base (with time stamps synchronized to calendar minutes) and concatenated with the wireless data set downloaded from the online server.

The aggregated field validation data is filtered to remove erroneous measurements resulting from hardware errors or unsuitable operating conditions. Three data filters are implemented on the one-minute time base data:

1. **BC Outlier Filter:** Remove all data points where the absolute value of the BC measurement is greater than 100 μg m^{-3}. BC concentrations on this order of magnitude are improbable while sampling ambient air, and instead usually result from hardware errors, such as disconnection or disturbance of the optical cell during field maintenance (changing of filters or batteries).

2. **High Attenuation Filter:** Remove data when measured optical attenuation is greater than 100 units to avoid possible optical saturation effects. Attenuation is mathematically defined

as 100 times the natural log ratio of the reference to sample voltage outputs from the ABCD optical cell ($ATN = 100\ln(V_{smpl}/V_{ref})$).

3. **Flow Rate Filter:** Remove all data generated when the ABCD is operating at a flow rate that deviates by more than 5 cc min^{-1} from the nominal set point (usually 110 cc min^{-1}). It was found that some rotary vane pumps failed during deployment, so the flow rate through the ABCD could not be steadily maintained. Consequently, all data with non-nominal sample flow is discarded to account for pump failures and potentially inaccurate flow rate measurements.

Hourly average values are calculated by taking the simple mean of all filtered one-minute measurements collected within a calendar hour. Hourly average values calculated using less than 48 measurements (less than 80% of the 60 one-minute time base measurements that should ideally be collected every hour) are discarded. This filtering accounts for periods when the ABCD is operating intermittently, and may consequently provide inaccurate or erroneous data.
The ABCD's performance is quantified using hourly average BC measurements. The Mean Absolute Error (MAE (μg m^{-3})) of the hourly BC measurements when sampling with HEPA-filtered inlets is calculated as:

$$MAE = \frac{\sum_{t_i}^{t_f}\left|BC(t) - BC_{ref}\right|}{N} = \frac{\sum_{t_i}^{t_f}|BC(t)|}{N}, \qquad (C3)$$

where $BC(t)$ (μg m^{-3}) represents hourly BC concentrations during the zero-response tests, from t = t_i to t = t_f, and N is the total number of hourly measurements collected. Since the ABCD is operated with a filtered inlet, the reference measurement (BC_{ref}(μg m^{-3})) is 0 μg m^{-3} throughout, and the MAE expression reduces to the simple mean of the absolute BC data.

During field validation, the ABCDs are operated in collocation with a commercial BC instrument, the Magee Scientific AE33. The Mean Absolute Percent Error (MAPE (%)) of hourly BC measurements from the ABCD is evaluated relative to hourly reference measurements from the Magee Scientific AE33 ($BC_{AE33(t)}$ (μg m^{-3})):

$$MAPE = \frac{100}{N}\sum_{t_i}^{t_f}\left|\frac{BC(t) - BC_{AE33}(t)}{BC_{AE33}(t)}\right|, \qquad (C4)$$

where $BC(t)$ (μg m^{-3}) represents hourly BC concentrations during the field validation, from t = t_i to t = t_f, and N is the total number of hourly measurements collected.

C6 – Performance Evaluation of Commercial BC Instrument

Over a period of 20 days, two Magee Scientific AE33 instruments were operated side-by-side inside the Bay Area Air Quality Management District monitoring station in Oakland, California. The instruments sampled ambient air at the same flow rate through two adjacent inlets extending out of the monitoring station roof. Figure C3a provides a time series of the black carbon (BC) mass concentration data collected, and Figure C3b is a scatter plot that illustrates

precision. Over the 20-day period, both instruments exhibit a mean absolute percent error (MAPE) of roughly 9% relative to the mean of their measurements.

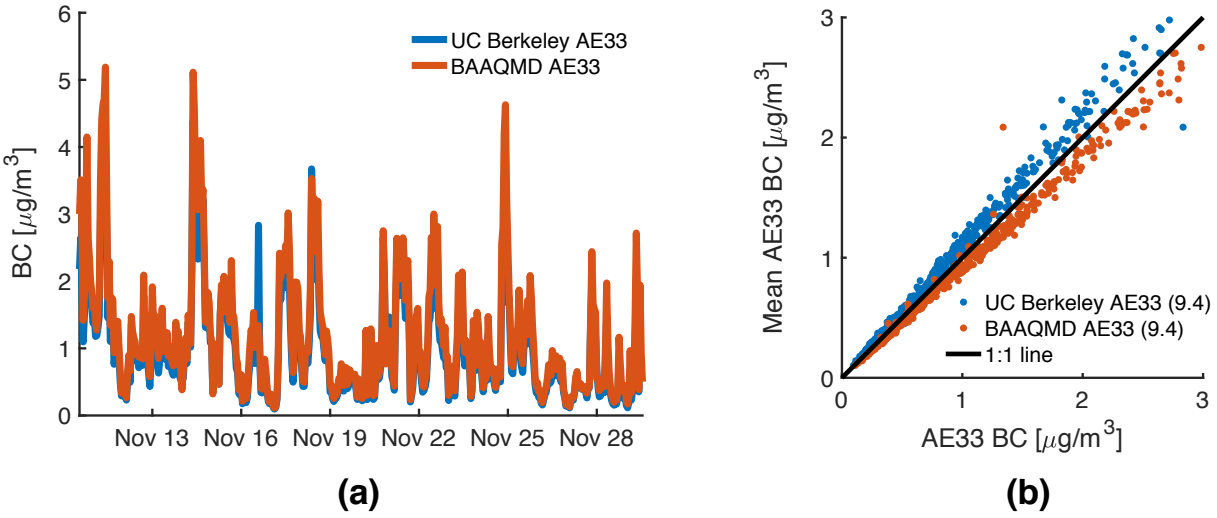

Figure C3. Two Magee Scientific AE33 instruments operating inside the Bay Area Air Quality Management District roadside monitoring station: (a) Time series of black carbon (BC) mass concentration measurements; (b) Precision of black carbon (BC) concentrations. All data is provided on a 60-minute time base. Precision error is evaluated relative to the mean of BC measurements from both AE33 units, and is provided in the legend.

Appendix D – Supplementary Information: A Distributed Network of 100 Black Carbon Sensors for 100 Days of Air Quality Monitoring in West Oakland, California

D1 – Materials and Methods

D1.1 Aerosol Black Carbon Detector (ABCD)

Figure D1 shows an Aerosol Black Carbon Detector (ABCD) deployed to a sampling site in West Oakland. The figure demonstrates how the ABCD is mounted using zip ties and shows the instrument's photovoltaic panel and sample flow inlet.

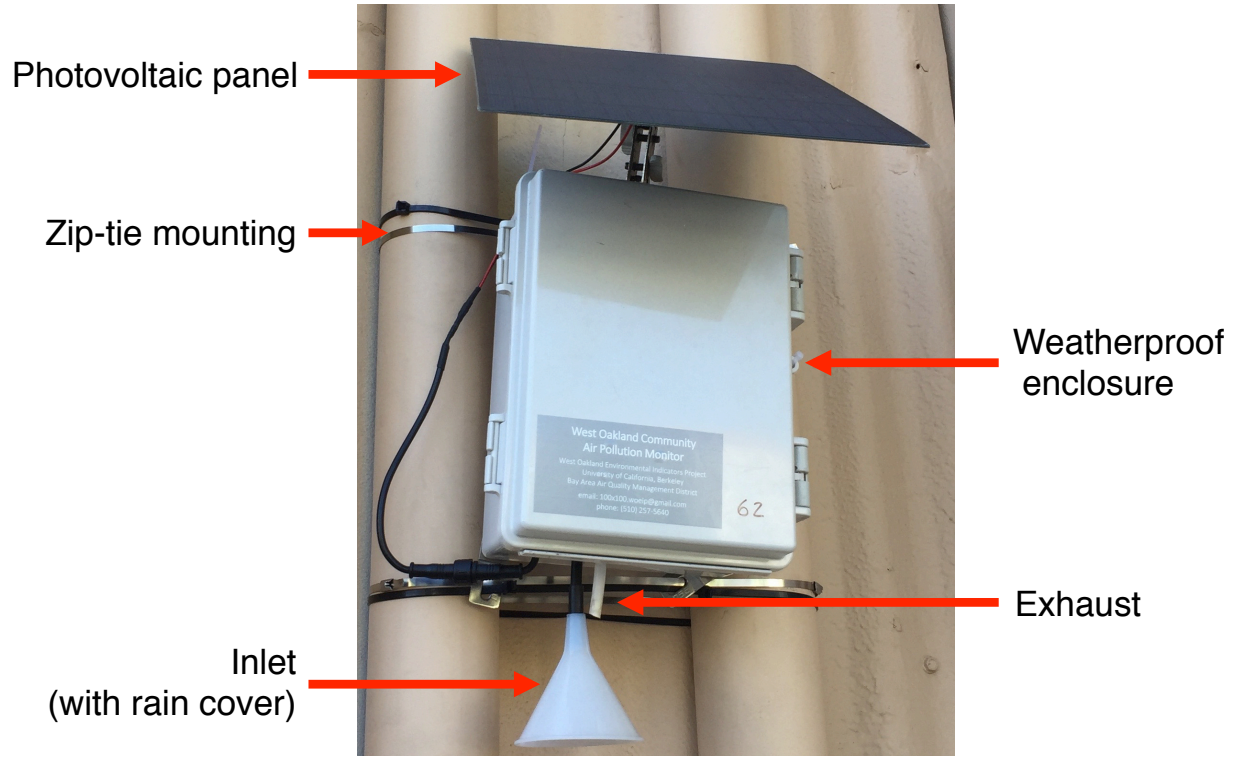

Figure D1. An Aerosol Black Carbon Detector (ABCD) deployed outdoors

Prior to deployment in the 100×100 Network, each ABCD was validated outdoors at one of three sampling sites in Oakland, California. At each validation site, groups of ABCD units were deployed for 2 to 7 days and collocated with a commercial BC monitor (Model AE33, Magee Scientific) that was housed inside an air-conditioned station. Using the data from the collocated ABCD units and AE33, the precision and accuracy of each ABCD was evaluated in terms of mean average percent error (MAPE):

$$MAPE = \frac{100}{N} \sum_{t_i}^{t_f} \left| \frac{BC(t) - BC_{ref}(t)}{BC_{ref}(t)} \right| \qquad \text{(D1)}$$

where BC(t) represents the hourly average BC mass concentration measurements (μg m^{-3}) collected by the ABCD during the field validation, from $t = t_i$ to $t = t_f$, and N is the total number of hourly measurements collected. When evaluating sensor precision, $BC_{ref}(t)$ represents the mean of hourly measurements (μg m^{-3}) from all ABCDs at the validation site at time "t". Similarly, accuracy MAPE is evaluated by setting $BC_{ref}(t)$ equal to hourly BC measurements from the collocated AE33. Figure D2 provides histograms of the precision and accuracy MAPEs for 115 ABCD units operated during the study.

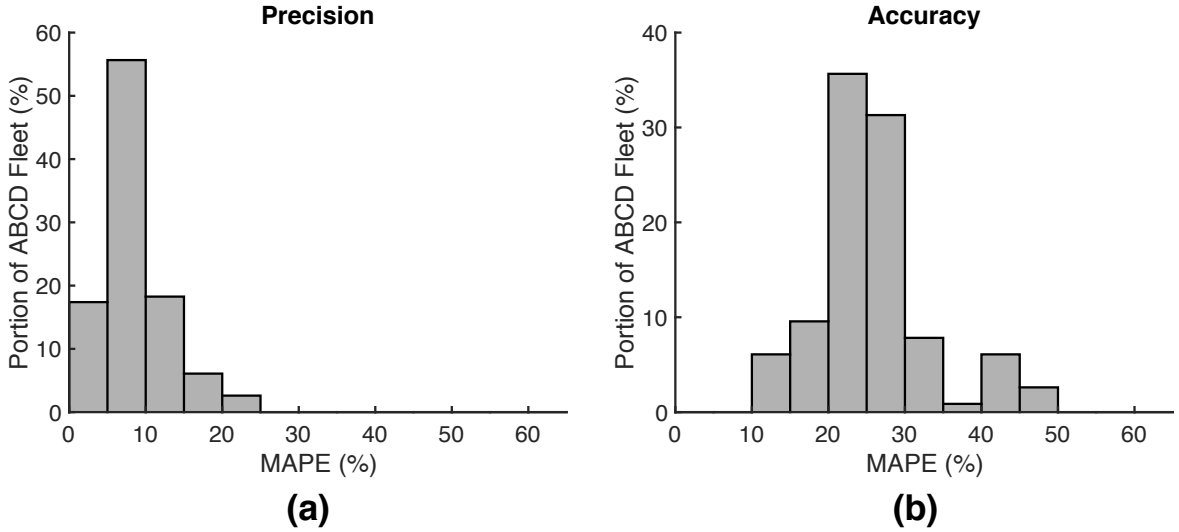

Figure D2. Measurement performance of 115 ABCD units during field validation (prior to deployment in the 100×100 Network): (a) Precision MAPE, evaluated relative to the ABCD fleet average data; (b) Accuracy MAPE, evaluated relative to the AE33 data.

Figure D2 shows that > 75% of ABCD units demonstrate precision MAPEs < 10% and accuracy MAPEs < 27% during the validation period. Following investigation, the remaining ~25% of ABCD units exceeding these MAPE values were shown to have miscalibrated flow rate sensors, resulting in BC measurements proportionally offset from the corresponding reference values. Flow rate sensors were re-calibrated in the field. At the end of the 100-day campaign, any remaining measurements errors resulting from the miscalibration of flow rate sensors were corrected according to the methods described in Section D-1.6. In addition, it should be noted that Figure D2 only represents the validation performance of 115 ABCD units, although a total of 128 units were constructed for the study. Validation data from the remaining 13 ABCD units was either lost during the development of the network's database or invalidated by erroneous AE33 measurements. Overall, the validated fleet of 115 sensors demonstrated average precision and accuracy MAPEs of 8.5 ± 0.7% and 26 ± 1%, respectively (fleet-average ± 90% confidence interval). These performance metrics are derived from 115 of the 128 ABCD units used in the study because the AE33 monitors sometimes provided invalid measurements and some ABCD data was lost during early development of the network's custom database.

D1.2 Network Deployment

Figure D3 shows all 100 sampling sites in the 100×100 BC Network categorized by the type of host who accommodated the sensor (e.g., residents, businesses, etc.). One ABCD sensor was deployed to most sampling sites in the network, a pair of ABCD units were operated at 12 sampling sites, and four ABCD units were collocated with a commercial BC monitor (Model AE33, Magee Scientific) at three sites. Figure D4 shows the location of the 3 validation and 8 collocation sites in the 100×100 Network, labeled with their corresponding site ID numbers. Validation sites 1 and 3 are the Bay Area Air Quality Monitoring District's (BAAQMD) air quality monitoring stations at West Oakland and Laney College, respectively, while validation site 2 is the West Oakland Environmental Indicators Project (WOEIP) office. The map in Figure D4 also provides the names of major roads and freeways in West Oakland.

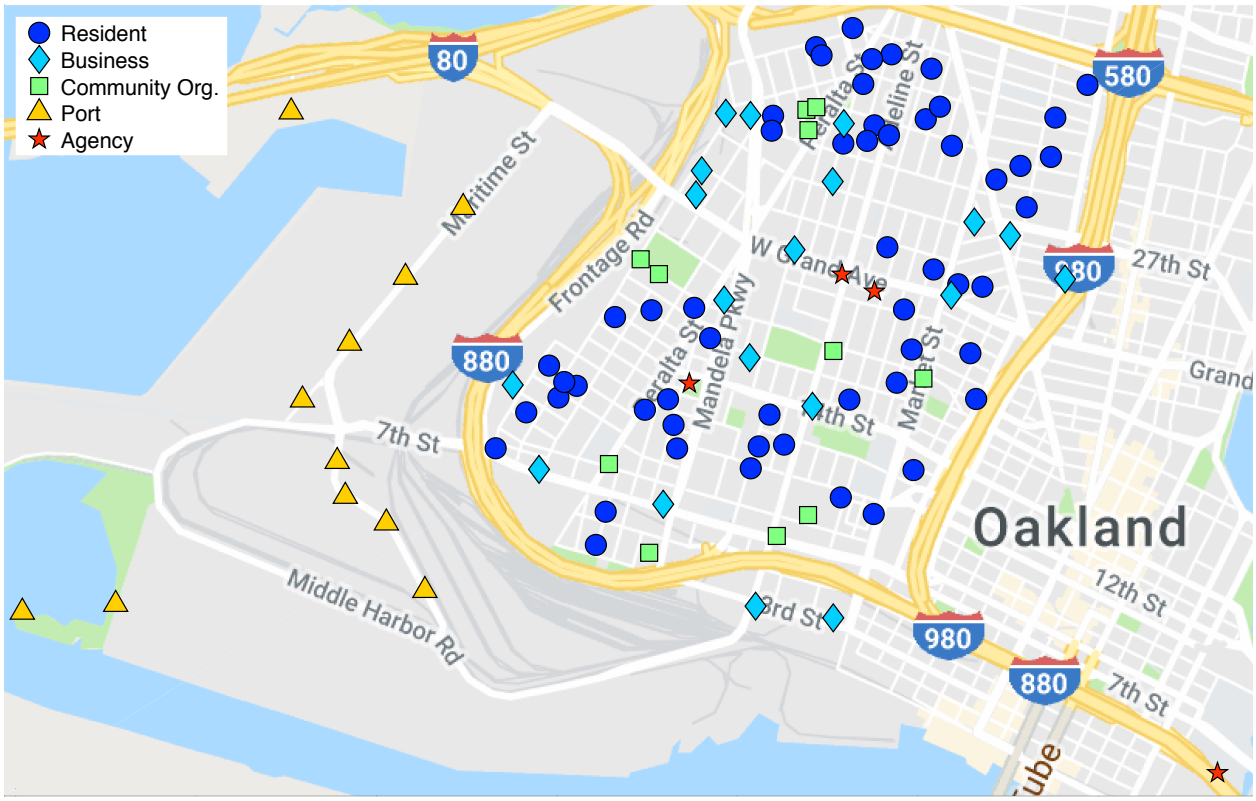

Figure D3. All 100 sampling locations in the 100×100 BC Network, categorized by host type. Major roads and highways are also labeled for reference.

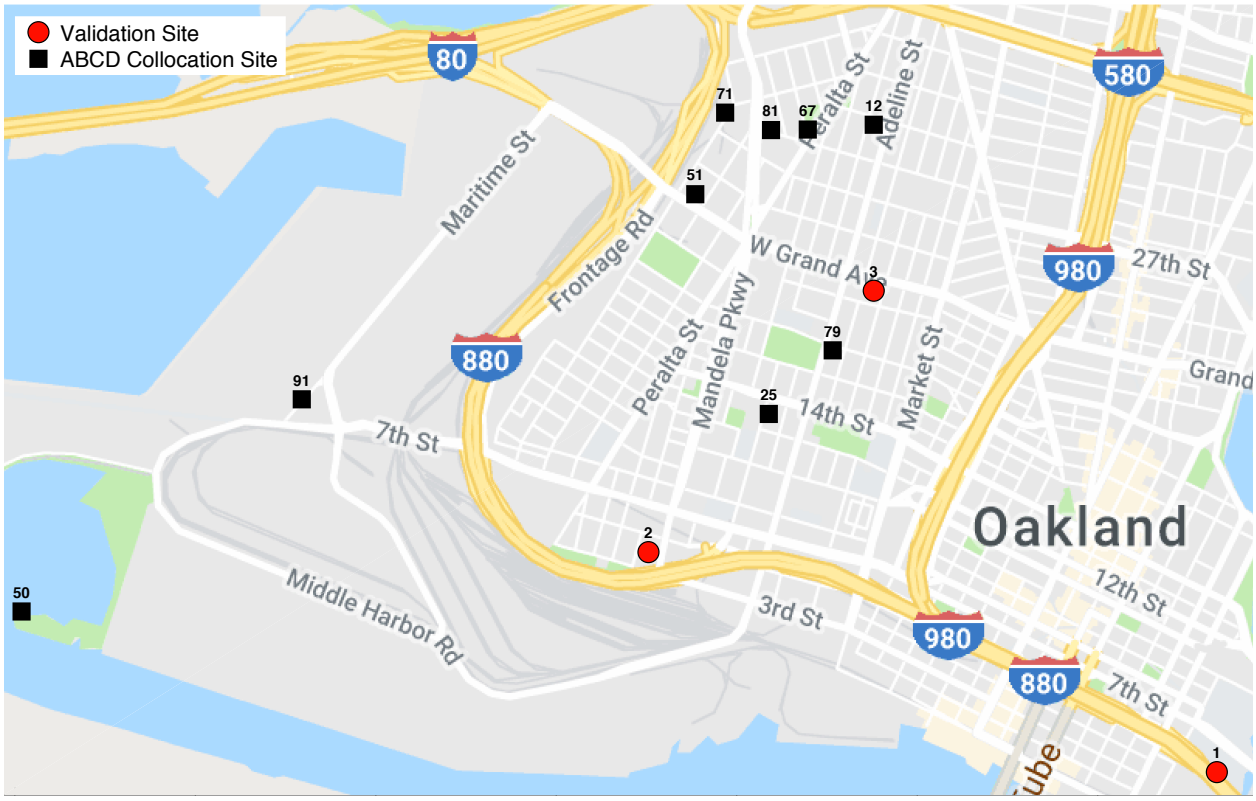

Figure D4. ABCD collocation sites in the 100×100 Network. At validation sites, four ABCD units were deployed in collocation with a commercial BC monitor (Model AE33, Magee Scientific). At collocation sites, ABCD units were deployed in pairs. Major roads and highways are also labeled for reference.

D1.3 Network Data Aggregation

Data from the 100×100 network is aggregated from two distinct sources: (1) An online database containing 1-minute average measurements wirelessly transmitted by each ABCD and stored in a custom SQL database online, and (2) SD cards collected manually from each ABCD in the field, containing 2-second time base data that was downloaded and stored in a separate Google drive database (Figure D5). The first ABCD units were deployed to the validation sites (sites 1, 2, and 3) on February 16, 2017, and the last sensors were removed from their sampling sites in West Oakland on September 22, 2017. All wireless and SD card data collected during this period was filtered according to the methods outlined below. However, only the data collected over the official 100-day campaign, from May 19 to August 27, are presented in this study. Data collected at the validation sites prior to May 19 is used to quantify and validate each sensor's accuracy and precision. Data collected after August 27 is used to evaluate the filter loading artifact at some collocation sites.

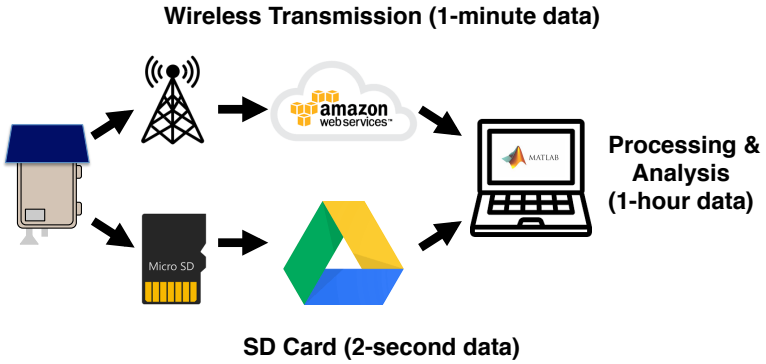

Figure D5. Schematic representation of data collection and analysis from the 100×100 Network

The data was extracted as custom data objects in MATLAB, where each individual object represented a unique combination of sensor ID and sampling site ID (e.g., ABCD 5 at site 67 is its own data object, containing the corresponding data stream). The SD card data was averaged down to a 1-minute time base and combined with the data collected wirelessly. During time periods when data was collected both wirelessly and on the SD card, SD card data was retained. The final combined data set had 329 distinct data objects (each representing a unique combination of sensor and sampling site ID) and contained a total of over 22 million 1-minute time base measurements. The data set collected during the 100-day campaign consisted of 155 data objects containing ~15 million 1-minute time base measurements.

D1.4 Programmatic Data Filtering

During sensor deployment, technical and procedural errors sometimes resulted in the collection of invalid or inaccurate BC mass concentration measurements. Consequently, a program was written in MATLAB to automatically detect and remove these invalid measurements. In order to facilitate error detection, the complete set of 329 data objects described above were split up such that each object only contained data collected during the loading of a single aerosol filter, henceforth referred to as a 'loading event'. A loading event began when an ABCD's clean fibrous filter first sampled ambient air and ended when the BC-loaded filter was replaced (typically after sampling for 5 to 7 days). By splitting up the data into discrete loading events using the method outlined below, invalid BC concentration measurements were detected more robustly and efficiently.

1. Each data object in the raw aggregated set represented a particular ABCD unit at a single sampling site. In order to keep track of optical cells during maintenance, the ID of the optical cell housed inside each ABCD was logged continuously. Using this log, each data object was divided up to contain data from only a single optical cell, such that each object then represented a unique combination of sensor, location, and optical cell ID. Over 1900 data objects resulted from splitting up the data this way.
2. All data objects containing < 500 valid 1-minute data points (where BC mass concentration is a non-NaN value) were deleted.
3. All data objects using optical cell 32 were deleted, as this cell was shown to be faulty.
4. During periods of intermittent ABCD operation, when sensors transmitted data for less than 30 minutes continuously (interruptions shorter than 5 minutes), all collected measurements were assigned a value of NaN.

5. Some ABCD units may have received the same optical cell multiple times over the course of campaign. In order to split up individual filter loading events, the MATLAB program also analyzed the sensor's attenuation (ATN) signal. The program detects abrupt changes in the optical attenuation's mean and linearity that occur during filter replacement. In order to validate that break points resulted from filter replacements, rather than interruptions in data collection, the program also checked that the reference and sample voltage signals changed by ≥ 0.3 V at each break point. This reason is that clean filters do not have identical optical depth, and so transmitted light intensity signals typically changed appreciably when filters were replaced.
6. Following these data filtering operations, all data objects containing < 500 valid 1-minute data points (where BC mass concentration is a non-NaN value) were again deleted.

By splitting up the data in this way, over 2000 data objects were created, each representing a single loading event. This set of data objects was then programmatically filtered for invalid BC mass concentration measurements according to the procedure outlined below. When a measurement met a filtering criterion, all measurements collected at that time stamp were assigned a value of NaN. For example, if attenuation exceeded the set limit of 100 units, all measurements collected at that time (BC concentration, sample flow rate, optical signal voltages, etc.) were assigned a value for NaN. In this way, the final data set allows for differentiation between data that is missing (never collected), and data that was removed during filtering. In addition, a log was created for each data object to catalog the data points discarded by each programmatic filtering criterion.

1. Data transmissions where the absolute value of the BC mass concentration measurements were > 100 $\mu g/m^3$ are removed. 1-minute average BC concentrations on this order of magnitude are improbable while sampling ambient air and usually result from hardware errors, such as disconnection or disturbance of the sensors' optical components during field maintenance (changing of filters or batteries).
2. It was found that many rotary vane pumps failed during deployment, so the flow rate through the ABCD could not be steadily maintained. Data points where the flow rate was < 50 cc min^{-1} were removed. Since sample flow rate was never set below 90 cc min^{-1} during the field campaign, flow rate measurements in this range indicated a failing pump.
3. The nominal flow rate of the loading event was determined (90, 100, 110, 135, 150, 220 or 250 cc min^{-1}). Data points where the flow rate deviated by more than 3 cc min^{-1} from this nominal set point were removed, as this too indicated a failing pump or flow sensor and, thus, untrustworthy data.
4. The optical cells' electrical connections were sometimes faulty, resulting in highly scattered optical voltage signals. Data was removed during intervals when consecutive reference voltage measurements changed by more than 0.0025 V. Periods when data was missing for > 5 minutes were not considered, ensuring that the voltage fluctuations detected resulted from faulty connectors rather than interruptions in data transmission.
5. The LEDs were sometimes set too brightly, such that photodetectors became saturated. All data points where the reference or sample voltage was ≥ 2.5 V were removed. Similarly, all data points where the reference or sample voltage was ≤ 0 V were also removed, as this indicated that the optical cell was disconnected or inoperative.

6. Optical cells were occasionally installed inside the ABCD sensor backwards ('flipped'), resulting in negative BC concentration measurements that exactly mirrored the correct measurements. For each data object, if the mean of all BC measurements collected during the loading event was < -0.1 $\mu g/m^3$, the sensor was considered flipped. In this case, the reference and signal voltage measurement logs were switched, and the attenuation and BC measurements were both mirrored about the zero axis.
7. By definition, a clean filter (free of light-absorbing PM deposits) has an optical attenuation (ATN) value of zero. For all data objects, each representing a single loading event, the mean of the first 3 valid ATN measurements was subtracted from the ATN time series, such that ATN = 0 when clean filters are initially loaded.
8. With ATN values reset to zero at each filter replacement, all data points where ATN > 100 units were removed to avoid optical saturation effects.
9. When data was removed according to the filters above, this may result in intermittent data periods. Intervals when data was collected for less than 10 minutes continuously (containing data interruptions shorter than 2 minutes) were removed.
10. Following these data filtering operations, data objects containing < 500 valid 1-minute data points (where BC mass concentration is a non-NaN value) were again deleted.

With the data filtered programmatically, there were still over 2000 data objects in the set. In order to facilitate subsequent analyses, the sensor objects were re-aggregated such that each object represents a unique sensor and location ID, containing multiple optical cells (if applicable). The result is 326 unique data objects, containing a total of 19.3 million filtered data points collected from February to September 2017.

D1.5 Manual Data Filtering and Quality Assurance

After programmatic filtering, the 326 data objects were manually inspected using a custom graphical user interface (GUI) written in MATLAB (Figure D6). The GUI displayed each data object's BC mass concentration, attenuation, sample flow rate, and optical voltage measurements on a 1-minute time base, exactly as they were stored. For reference and comparison, the GUI also provided the BC mass concentration measurements collected by the ABCD on an hourly time base, overlaid with BC measurements from the AE33 housed in the BAAQMD's West Oakland monitoring station. After inspecting the data displayed, the user was presented with three options: (1) Trim: One of the six displayed variables was chosen and plotted in a new window. The user was then prompted to select the beginning/end points of the data period to be removed (Figure D7a), and both the resulting trimmed data and original data sets were shown together (Figure D7b). At this juncture, the user could select another interval to remove, or revert to the original data set and repeat the trimming process. After trimming was complete, the data was saved, and the next data object was loaded/displayed for inspection; (2) Remove: The entire data object was deleted, as all measurements contained were invalid; (3) Next: All measurements shown were valid; the data object was saved without modification, and the next object was loaded/displayed. In this way, each data object was inspected, and any remaining erroneous measurements were removed. When data was trimmed using the GUI, the time stamp of the measurements removed and the data variable used during the trimming (which is usually indicative of the error mode) were both logged for analysis.

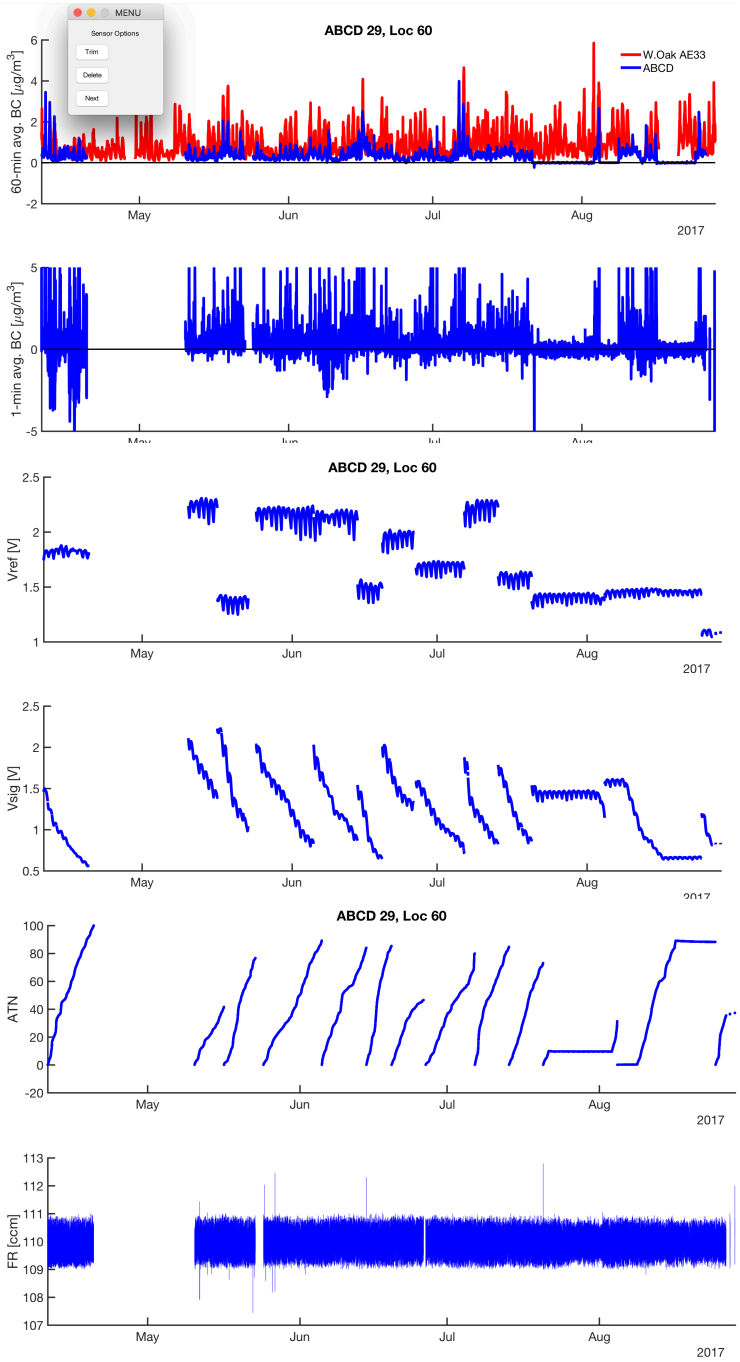

Figure D6. Screenshot of the Graphical User Interface (GUI) used for quality assurance screening of data collected by the 100×100 Network. The GUI is presented with data collected by ABCD unit 29 at sampling site 60, and provides the corresponding BC mass concentration, attenuation, sample flow rate, and optical voltage measurements on a 1-minute time base, exactly as they are stored in the data object. The GUI also presents BC mass concentration measurements on an hourly time base, overlaid with BC measurements from the commercial BC monitor (Magee Scientific, Model AE33) housed in the BAAQMD's West Oakland monitoring station. The three GUI options (Trim, Delete, Next) are shown in the top left of the figure.

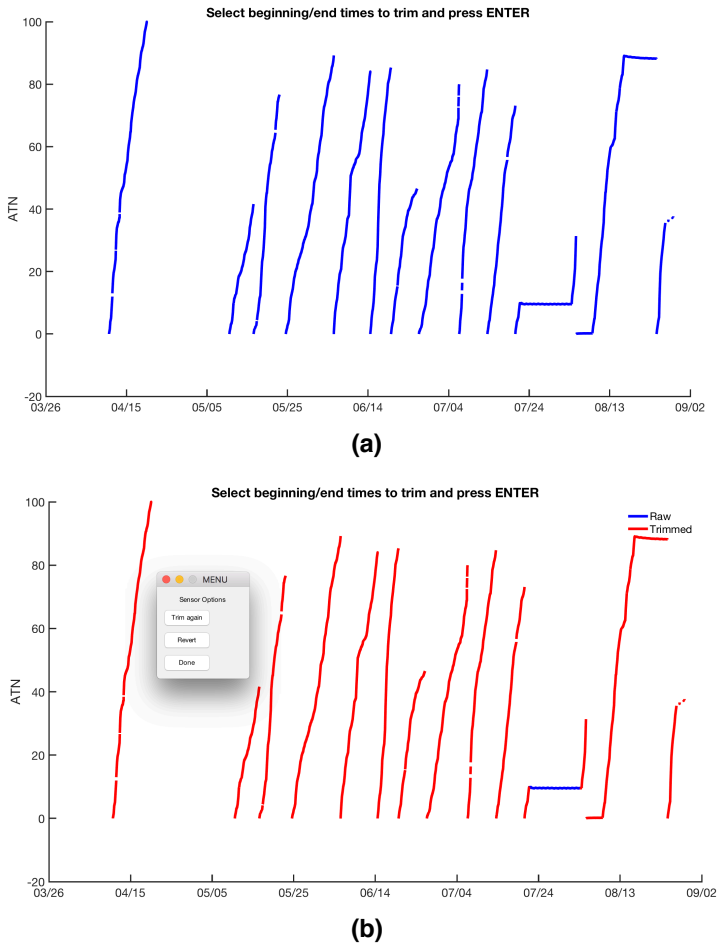

Figure D7. Trimming data using the GUI: (a) Selecting the beginning/end points of the data interval to be removed. In this case, the interval during which the attenuation remains constant was trimmed, as this suggested that disconnected tubing is preventing the sensor's optical cell from sampling ambient air or that a HEPA filter had been installed on the sensor inlet during zero calibration; (b) Trimmed and original ('Raw') data shown together for comparison. The GUI presents the user with three options: (1) Trim again: Select more data to remove from the set; (2) Revert: Return to the original data set and repeat the trimming process; or (3) Done: Accept and save the trimmed data set.

D1.6 Sample Flow Rate Correction

Following the 100-day measurement campaign, 96 operational units (out of the 128 originally deployed) were taken down from their assigned sampling sites and brought back to the laboratory. In order to help validate the accuracy of collected BC measurements, the sample flow rate of each ABCD was measured using a wet bubble cell flow calibrator (Gillian Gilibrator) and compared to measurements from the ABCD's onboard flow rate sensor. Figure D8 shows that nearly 70% of ABCD units in the fleet had flow rate measurement errors $\leq$ 5%. This degree of flow rate measurement error was accepted and data from these units was not corrected. However, for each ABCD unit with a flow rate error > 5 %, BC concentrations were scaled by the ratio of the sample flow rate measured by the onboard flow sensor to that measured using the Gilibrator

during the post-deployment calibration. This flow rate correction was applied to BC concentrations collected after June 15th, as flow rate calibrations were conducted in the field from June 10th to June 15th. Data collected prior to this date could not be flow rate corrected.

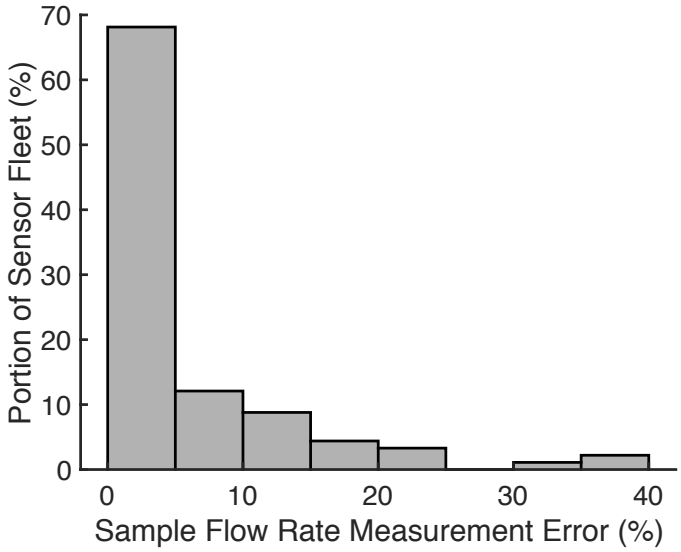

Figure D8. Flow rate measurement error in the ABCD fleet collected at the end of the 100-day campaign.

D1.7 Filter Loading Correction

The ABCD, like other aerosol photometers, increasingly underestimates BC mass concentrations as light-absorbing PM accumulates on the filter. This measurement bias, commonly known as the 'filter loading artifact', is corrected using the following function[167]:

$$BC_c = \frac{BC}{a \times \exp(-ATN/100) + (1-a)} \qquad \text{(D2)}$$

where BC and BC_c are the uncorrected and corrected BC measurements (μg m^{-3}), respectively, ATN is the corresponding optical attenuation measurement, and a is the filter loading correction factor (FLCF). The FCLF is dependent on many factors, including the composition of PM sampled and the type of fibrous filter used (e.g., quartz, glass fiber, etc.). Consequently, a FLCF was derived specifically for the ABCD units deployed in the 100×100 Network as follows.

Pairs of ABCD units were collocated at 12 sampling sites, as shown in Figure D4. For each collocated pair, one ABCD was set to a flow rate of 110 cc min^{-1} ("low flow"), while the other was set to either 150 or 220 cc min^{-1} ("high flow"). Henceforth, ABCD 1 and ABCD 2 will refer to the "low flow" and "high flow" sensors in a collocated pair, respectively. Figure D9 shows the hourly-average BC, ATN, and sample flow rate measurements collected by a collocated pair of ABCD units. The figure shows that the sensors' BC measurements agreed closely when both their filters were lightly loaded. However, as ABCD 2 accumulated BC more rapidly than ABCD 1, ABCD 2 increasingly underestimated BC mass concentrations relative to ABCD 1. In order to model this measurement artifact, we only analyzed measurement trials

when filters in both collocated sensors were changed simultaneously. This method ensures that BC measurement disparities result mainly from differences in filter loading, as all other experimental factors are constant for both sensors. At each filter replacement, ABCD attenuation reset to a value of zero units (by definition, ATN = 0 for clean filters).

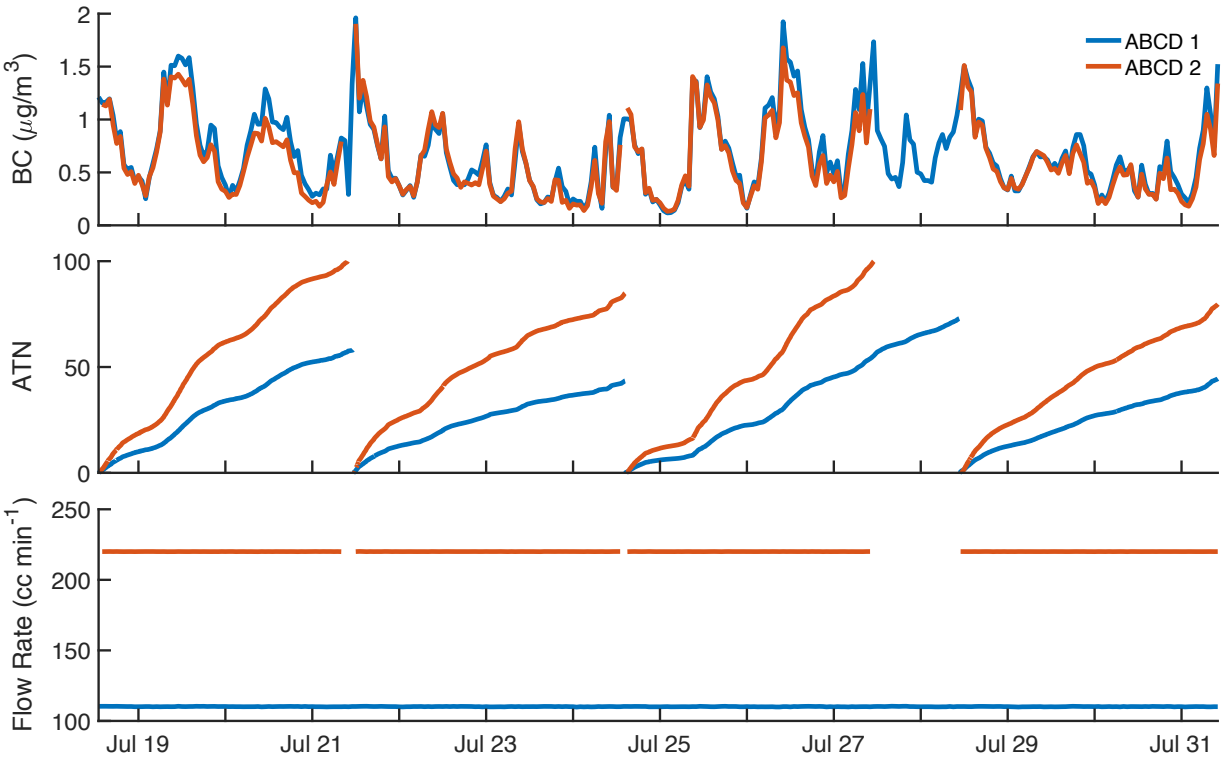

Figure D9. Hourly-average black carbon (BC), optical attenuation (ATN), and sample flow rate measurements collected by a pair of collocated ABCD units deployed at sampling site 1 from July 18 to August 1, 2017.

For each collocated pair of ABCD units, it is possible to determine a FLCF that minimizes the observed BC measurement bias. Throughout the collocated deployment, we calculated the ratio of the hourly-average attenuation rates measured by the high and low flow ABCD units: $(dATN_2/dt)/(dATN_1/dt)$. Since the change in attenuation was evaluated over the same time period for each collocated sensor, this ratio reduces simply to $dATN_2/dATN_1$. We compared the $dATN_2/dATN_1$ ratio to the corresponding difference in the sensors' optical attenuation measurements at each hour: $ATN_2 - ATN_1$. Ideally (when $BC_1 = BC_2$), the ratio of the attenuation rates should always equal the ratio of the sensors' sample flow rates (FR_2/FR_1),

$$\frac{dATN_2/dt}{dATN_1/dt} = \frac{dATN_2}{dATN_1} = \frac{(BC_2 \times FR_2 \times \sigma)/A}{(BC_1 \times FR_1 \times \sigma)/A} = \frac{FR_2}{FR_1} \qquad \text{(D3)}$$

where all ABCD units utilize the same mass absorption coefficient (σ, $m^2\ g^{-1}$) and filter orifice area (A, m^2), and so these factors cancel. Figure D10 shows the ratio of the attenuation rates

($dATN_2/dATN_1$) plotted as a function of the attenuation difference ($ATN_2 - ATN_1$) between collocated ABCD units at three sampling sites. For each collocated ABCD pair, a reference line was provided at $dATN_2/dATN_1 = FR_2/FR_1$. For these same sites, Figure D11 compares the BC measurements collected by each collocated ABCD. As expected, the figure shows that uncorrected BC concentrations measured by "low flow" ABCD 1 systematically exceeded those measured by "high flow" ABCD 2, whose fibrous filters were more heavily loaded with BC.

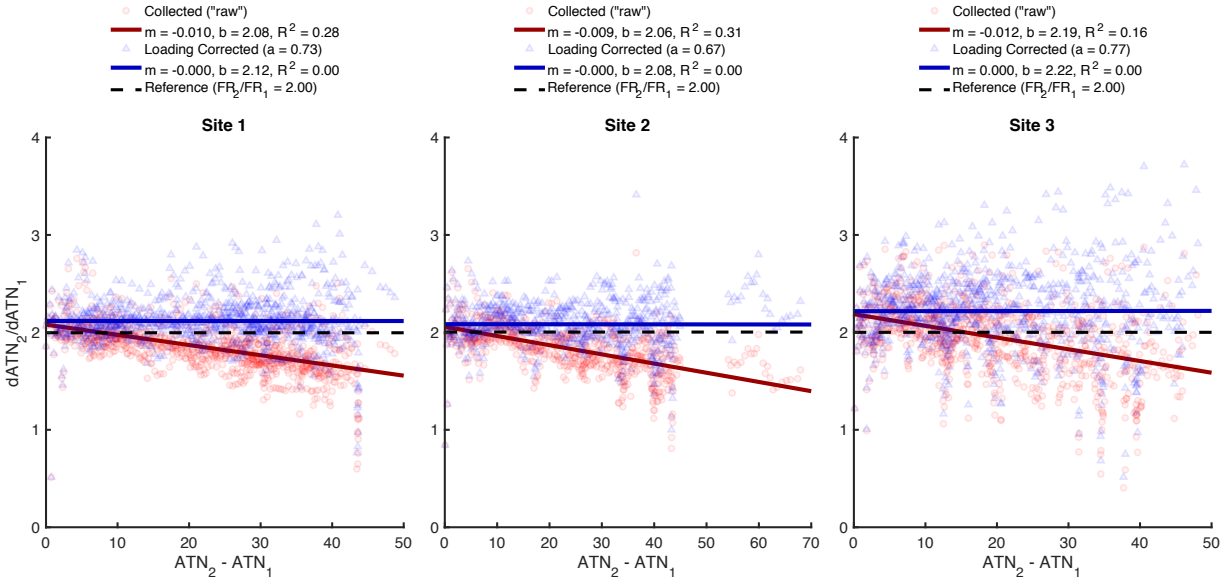

Figure D10. Ratio of the hourly-average attenuation rates ($dATN_2/dATN_1$) measured by collocated pairs of ABCD units at sampling sites 1, 2, and 3, plotted as a function of attenuation difference ($ATN_2 - ATN_1$). At each site presented, ABCD units 1 and 2 were set to sample flow rates of 110 and 220 cc min^{-1}, respectively. Both the uncorrected (red) and filter loading corrected (blue) $dATN_2/dATN_1$ measurements are shown, with the slope (m), intercept (b), and correlation coefficient (R^2) of the corresponding linear regression provided in the legend. The legend also provides the FLCF (*a*) calculated and applied to each pair of ABCD units.

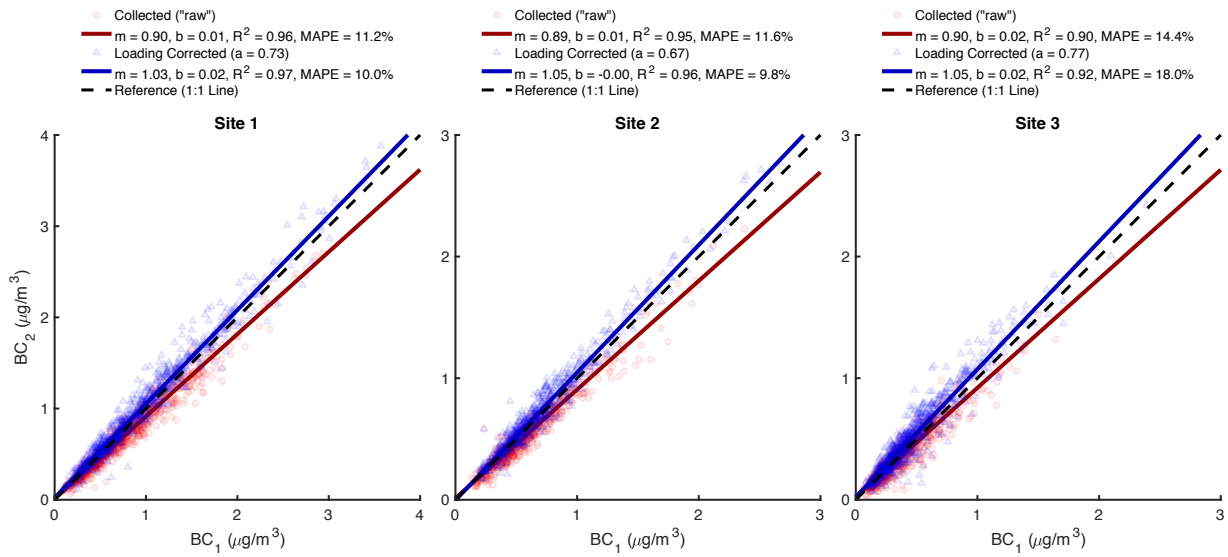

Figure D11. Comparison of hourly-average black carbon (BC) mass concentration measurements collected by collocated ABCD units at sampling sites 1, 2, and 3. Both uncorrected (red) and filter loading corrected (blue) BC measurements are shown, with the slope (m), intercept (b), and correlation coefficient (R^2) of the corresponding least-square linear regressions provided in the legend. The legend also provides the FLCF (a) applied to each pair of ABCD units and the mean average percent error (MAPE) for each set of collocated BC measurements.

As a result of the filter loading artifact, the data collected from all three sites show that $dATN_2/dATN_1$ decreased linearly as the attenuation difference between the collocated sensors increased. A FLCF factor was iteratively calculated to minimize this linear dependence. At each possible LCFL value (ranging from 0 to 1), both collocated sensors' attenuation rate measurements were corrected for filter loading using Equation D2. The ratio of the corrected attenuation rates was calculated and the linear dependence on attenuation difference (slope and intercept) was determined using a least-squares regression. The LCFL value providing a linear regression slope closest to zero was identified and used to correct the data, as shown in Figure D10. The figure shows that for each site, the ratio of the corrected attenuation rates was no longer linearly dependent on the attenuation difference between the two sensors (slope = 0).

Following the filter loading correction, Figure D10 shows that the ratio of the attenuation rates still did not equal FR_2/FR_1 throughout the trial, as would be expected. For the three sampling sites shown, the linear regression of corrected $dATN_2/dATN_1$ measurements always exceeded the FR_2/FR_1 ratio. As a result, Figure D11 shows that corrected BC measurements from the high flow sensor ($BC_{2,c}$) generally exceeded those from the low flow sensor ($BC_{1,c}$). This bias is the result of errors in the sensors' flow rate measurements (when miscalibrated, ABCD flow rate measurements were proportionally offset from the actual value). Since the ratio of the corrected attenuation rates reflects the real flow rate ratio, we used the intercept of the corresponding linear regression to compensate for the flow rate measurement error. Arbitrarily, we assumed that low flow sensors were accurate and only compensated measurements collected by the high flow sensors in each collocated pair:

$$BC_{2,FRc} = BC_{2,c} \times \frac{(FR_2/FR_1)}{b} \qquad \text{(D4)}$$

where $BC_{2,FRc}$ represents high flow BC measurements corrected for both the filter loading artifact and flow rate measurement error (μg m^{-3}), and b represents the intercept of the linear regression derived for the filter loading corrected $dATN_2/dATN_1$ measurements as function of attenuation difference (Figure D10). For each collocated ABCD at the three sites, Figure D12 compares filter loading corrected BC measurements both before and after compensation for the flow rate measurement error. Overall, the figure shows that BC measurements from the collocated sensors generally agreed closely when corrected for both the filter loading artifact and the flow rate measurement error.

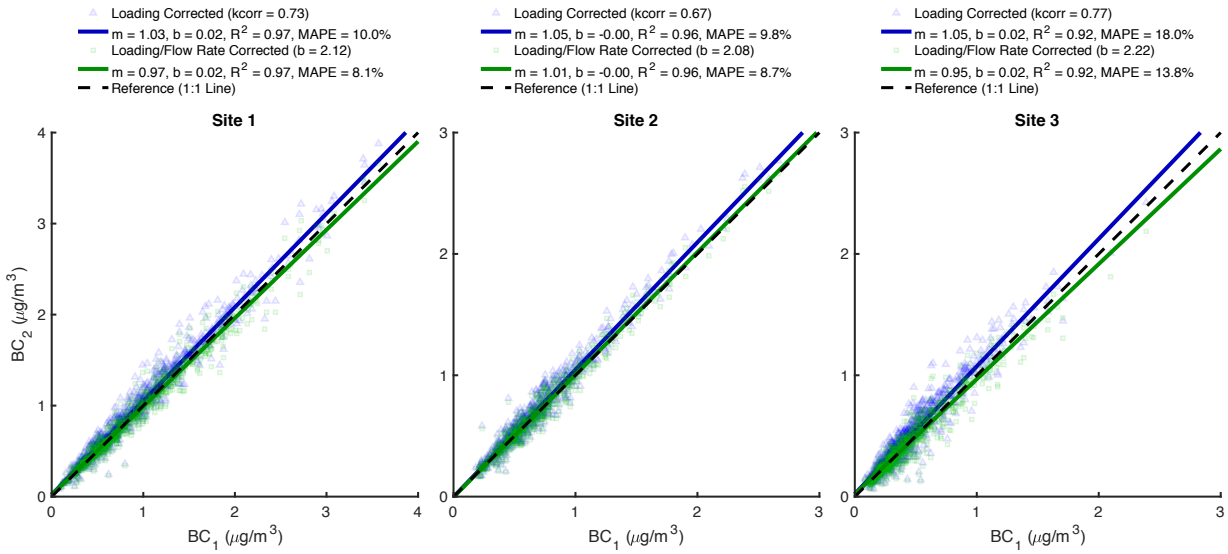

Figure D12. Comparison of hourly-average black carbon (BC) mass concentration measurements collected by collocated ABCD units at sampling sites 1, 2, and 3, and corrected for the filter loading artifact. BC measurements are presented both before (blue) and after (green) flow rate correction, with the slope (m), intercept (b), and correlation coefficient (R^2) of the corresponding least-square linear regressions provided in the legend. The legend also provides the FLCF (a) and linear intercept (b) applied to each pair of ABCD units, and the mean average percent error (MAPE) for each resulting set of collocated BC measurements.

The procedure outlined above was repeated for 28 pairs of ABCD units collocated at 12 sampling sites. At sites where high flow sensors were operated at both 150 and 220 cc min^{-1}, the data was analyzed separately, such that the measured flow rate ratio (FR_2/FR_1) remained constant for each collocated dataset. For six of the collocated pairs analyzed, the data collected was erroneous or insufficient to calculate a valid FLCF. Table D1 provides the FLCF (a) calculated for each of the remaining 22 collocated ABCD pairs at 11 sampling sites (the data collected at collocation site 50 could not be analyzed). The calculated FLCF ranged from 0.47 to 0.77, with an average value of 0.64 ± 0.03 (mean ± 90% confidence interval). This derived FLCF agrees roughly with that derived by Good et al. (~0.73) for ambient BC measurements collected with a commercial portable aethalometer (Model AE51, AethLabs)[166]. Exact agreement with this

published value is not expected due to variations in the composition of PM sampled during each study and the different fibrous filter material utilized by the AE51. However, it should be noted that the FLCF value calculated using the collocated ABCD units were highly consistent (small confidence interval), suggesting that this correction factor is applicable across the 100 x 100 BC Network. Consequently, the average FLCF of 0.64 ± 0.03 is used to correct all BC measurements for filter loading (using Equation D2).

Table D1 also provides the mean average percent error (MAPE) between each set of collocated BC measurements. The table shows that the filter loading correction often increased the MAPE of hourly BC measurements, as a result of the flow rate measurement error outlined above. The linear intercepts (b) derived to correct the relative error in collocated flow rate measurements are also shown in Table D1. This relative flow measurement error was unique to each pair of ABCD units, and thus the intercept values cannot be used to correct data from the ABCD fleet as a whole. However, Table D1 shows that the MAPE of hourly BC measurements always improved when corrected for both filter loading and flow rate error. These results illustrate that the filter loading correction was effective and that the remaining measurement errors were largely due to miscalibrated flow rate sensors (which were corrected separately according to the methods outlined in Section D1.6).

It should also be noted that the MAPE of uncorrected BC measurements was ~10% for most collocated sensors, suggesting that the filter loading artifact and miscalibrated flow rate sensors did not significantly diminish the accuracy of most BC measurements. However, some ABCD units were subject to significant errors from these sources (up to ~40%), therefore justifying the effort dedicated to their correction. For example, the MAPE of collocated measurements at site 67 was reduced from 28% to 10% using the correction methods outlined above.

Site ID	FR_1 (cc min^{-1})	FR_2 (cc min^{-1})	a	b	MAPE (%)	$MAPE_c$ (%)	$MAPE_{FRc}$ (%)
1	129	220	0.71	1.86	7.4	10.7	5.5
1	110	150	0.73	1.51	5.9	11.4	4.3
1	110	220	0.74	2.12	11.2	10.0	8.1
2	110	150	0.66	1.37	7.1	5.7	5.7
2	110	220	0.77	2.13	11.0	10.1	8.0
2	110	220	0.68	2.23	12.0	14.7	10.4
3	110	150	0.67	1.54	9.8	14.7	8.2
3	110	220	0.72	2.17	14.4	17.1	14.1
3	110	220	0.64	2.01	14.3	12.0	12.0
12	110	127	0.72	1.38	13.6	19.5	7.9
25	110	150	0.73	1.45	5.7	8.1	4.7
51	110	150	0.51	1.41	6.1	6.8	5.9
51	110	220	0.66	2.30	9.0	17.2	6.5
67	110	220	0.47	2.37	12.8	19.9	6.0
67	72	150	0.64	1.67	27.5	21.5	9.5
71	110	150	0.56	1.53	10.2	15.0	7.4
71	110	220	0.68	2.54	13.2	25.3	6.2
79	110	150	0.57	1.48	7.7	10.4	7.1
79	110	141	0.53	1.47	10.0	14.4	4.1
81	110	150	0.71	1.56	11.9	17.1	9.6
81	110	220	0.51	2.17	9.6	11.8	8.3
91	110	150	0.57	1.31	15.5	14.2	13.8

Table D1. Sampling site ID, low/high flow rate settings (FR_1/FR_2), and the FLCF (*a*) and linear intercept (*b*) derived for each collocated pair of ABCD units. The table also provides the mean absolute percent error of the uncorrected (MAPE), filter loading corrected ($MAPE_c$), and filter loading/flow rate corrected ($MAPE_{FRc}$) BC measurements.

D1.8 Site Categorization

In total, 68 sampling sites in the 100×100 BC Network were assigned to represent six location categories: (1) Upwind, (2) Residential, (3) Industrial, (4) Near Highway, (5) Truck Route, and (6) Port. The land use designation map in Figure D13 was used to identify residential sites in areas designated "Mixed Housing Type Residential" use, which contain "a mix of single-family, townhomes and small, multi-unit buildings along with small-scale neighborhooDserving businesses."[207] Similarly, industrial sampling sites were selected in "Business Mix" areas, primarily allocated for "a wide variety of businesses, and related commercial and industrial establishments."[207] Most uncategorized sites in the network did not meet any of the criteria detailed above, such as those located in areas designated for "Community Commercial" or "Urban Residential" use. Sampling sites located near the border between two land use designations were also excluded from the analysis to ensure that sites are fully representative of their assigned location category. For example, sampling site 23 is in a "Mixed Housing Type

Residential" area, but remained unassigned because it so closely borders an "Urban Residential" area. Furthermore, some sampling sites met the criteria for multiple location categories, such as sites 60 and 71, which were categorized as industrial but also lie within 150 meters of I-880. In these cases, categorizations were chosen to ensure that a representative set of sampling sites was assigned to each location category. Since large portions of "Business Mix" areas are located near highways, sampling sites 60 and 71 were classified as industrial to accurately represent BC concentrations in this category.

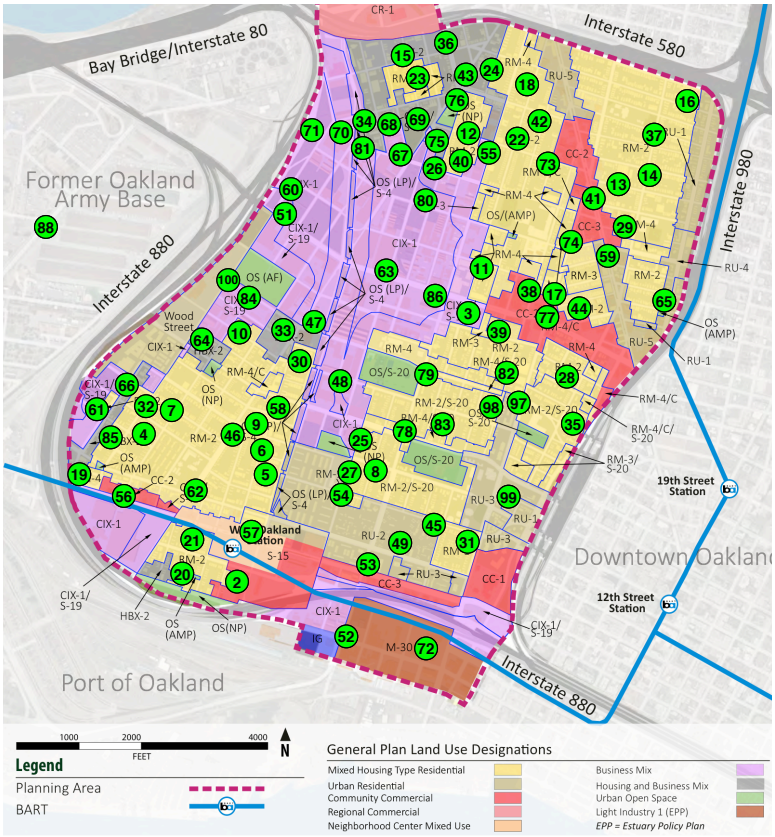

Figure D13. Land use designations in West Oakland.[207] The 100×100 Network's sampling sites are shown in green and labeled.

D2 – Results and Discussion

D2.1 Network and Sensor Performance

While Figure 27 presents the aggregated data collection performance of the entire 100×100 network, Figure D14 the same performance data broken down by sampling site. For each site, the percentage of missing hourly data was evaluated relative to the 2400 hourly BC measurements that should have ideally been collected during the 100-day campaign. Figure D15 shows each sampling site's data collection status at each hour of the measurement campaign (from May 19 to August 27, 2017).

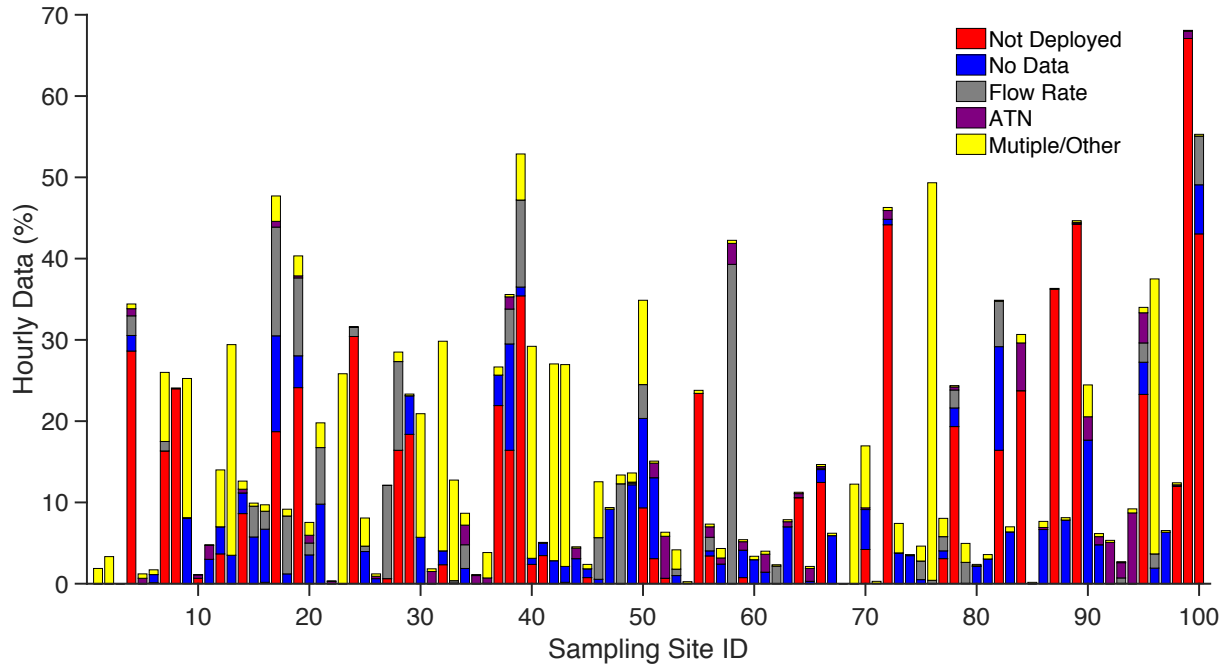

Figure D14. Data collection performance of each sampling site in the 100×100 Network.

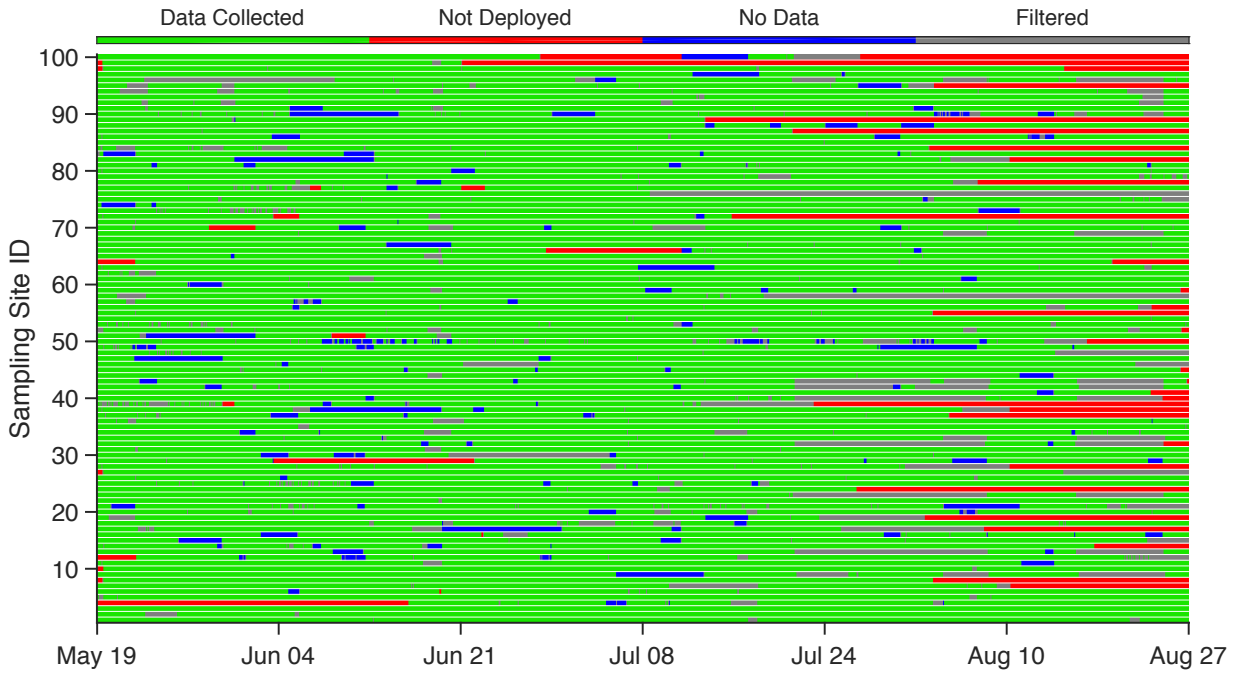

Figure D15. Hourly data collection status of each sampling site in the 100×100 Network.

D2.2 Black Carbon Concentrations in West Oakland: Spatiotemporal Trends and Outliers

For each of the 100 sampling sites in the network, hourly- and daily-average BC concentrations (and corresponding 90% confidence intervals) were calculated over the diurnal

and weekly cycles using all hourly BC measurements collected during the 100-day campaign. Using the diurnal and weekly trends calculated at each site, the bold lines in Figure 28 represent the mean of the hourly- and daily-average BC concentrations calculated at all sites assigned to each category. For example, the dark red line in Figure 28(a) represents the mean of hourly-average BC concentrations measured at the 8 Port sites. Measurement error was propagated through the site-averaging operation, such that the confidence intervals shown in Figure 28 represent the root-sum-square of the confidence intervals associated with all sampling sites in each category, divided by the corresponding number of sites. As such, the dark red shaded area in Figure 28(a) represents the root-sum-square of the hourly-average confidence intervals at the 8 Port sites, divided by 8.

Figure D16 provides a satellite image of the area surrounding sampling site 94 along the outer boundary of the Port of Oakland and shows trucks parked in the middle lane of Maritime Street. Figure D17, on the other hand, shows a section of Maritime Street that does not have a middle lane (near sampling site 88) so trucks cannot park.

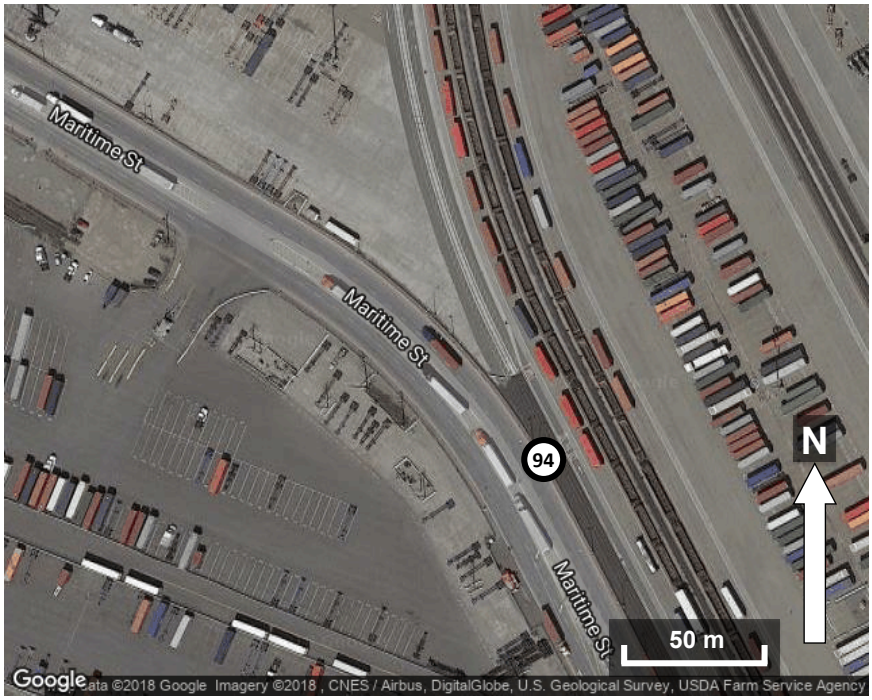

Figure D16. Satellite image of the area surrounding sampling site 94 on Maritime Street along the outer boundary of the Port of Oakland, showing trucks parked along the middle lane of the road.

Figure D17. Satellite image of the area surrounding sampling site 88 on Maritime Street along the outer boundary of the Port of Oakland, showing that trucks cannot park along this stretch of road where there is no middle lane.

Figure D18 shows the diurnal wind speed and direction trends in West Oakland, calculated using hourly wind speed and direction measurements collected at the BAAQMD monitoring station (site 3) over the 100-day campaign (from May 19 to August 27, 2017).

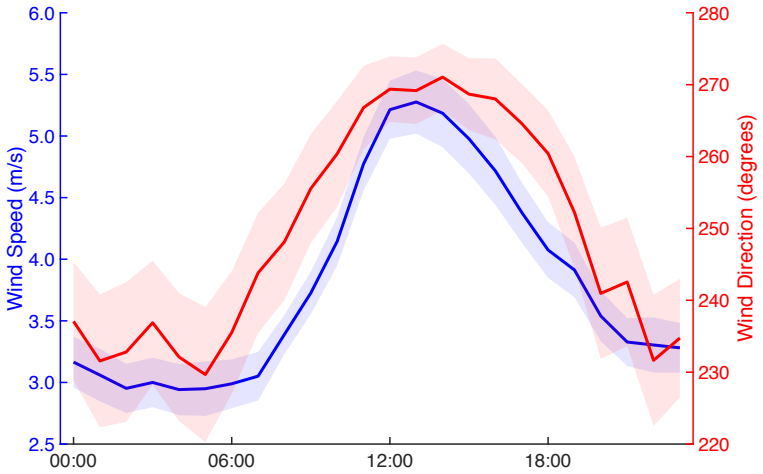

Figure D18. Hourly-average wind speed and direction trends in West Oakland over the diurnal cycle. Bold lines represent average values, and shaded areas represent the corresponding 90% confidence intervals.

Figure D19 and Figure D20 provide satellite images of the areas surrounding the two outlier sites where unusually elevated BC concentrations were detected during the 100-day

measurement campaign. Each figure shows the location of the outlier site, likely emission source nearby, and surrounding sampling sites where BC concentration trends were more typical of general trends observed across the neighborhood.

Figure D19. Satellite image of the area surrounding outlier site 84 (purple). The ABCD was mounted to the fence surrounding the public park, directly across from the street from a trucking company. Site 100 (white) is located at the southwest corner of the park (~100 meters away), and does not detect the elevated concentrations measured at site 84.

Figure D20. Satellite image of the area surrounding outlier site 26 (purple). The ABCD was mounted to a fence outside a small business. A metals recycling plant occupies the block across the street, and the block directly to the southwest. Sampling sites 40 and 75 (white) are located at a residence and business, respectively, and do not detect the elevated concentrations measured at site 26.

From April 25 to May 29, the sensor at industrial sampling site 70 was mounted to a fence < 5 m from Mandela Parkway. After the sensor was stolen, a replacement unit was mounted to the façade of a building ~ 20 m further from the roadway, and operated at this location for the remainder of the study (June 2 to August 26). Both sensor locations at site 70 are shown in Figure D21. Figure D22 provides the diurnal and weekly BC trends measured at both sensor locations, and shows that hourly- and daily-average concentrations at sampling site 70 were clearly much higher when the sensor was mounted closer to the roadway.

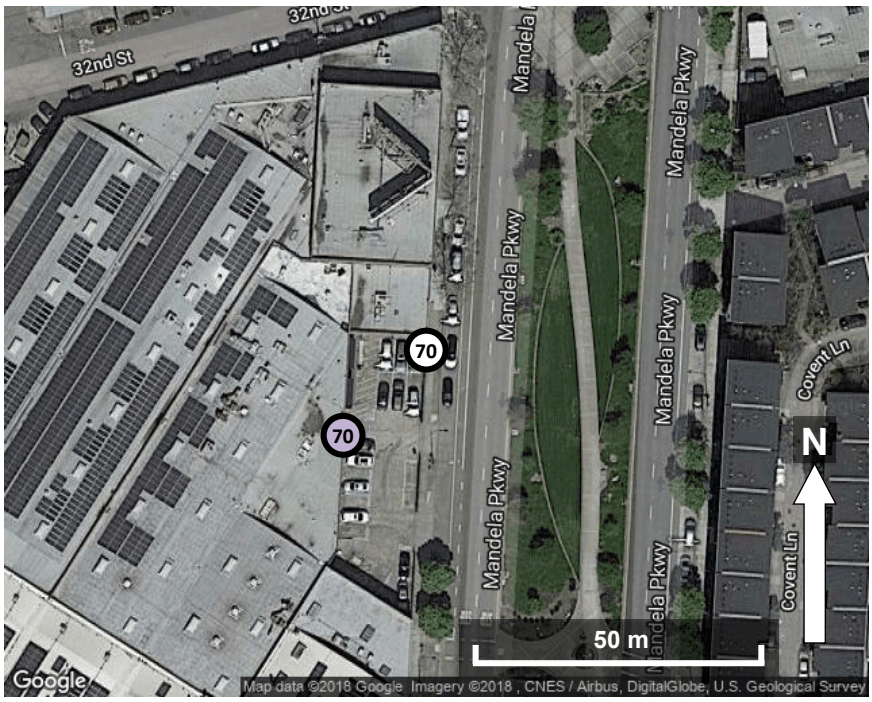

Figure D21. Satellite image of the area surrounding industrial site 70. From April 25 to May 29, the ABCD was originally mounted to a fence near Mandela Parkway, shown in white. From June 2 to August 26, the ABCD was mounted to a building façade ~25 m away, shown in purple.

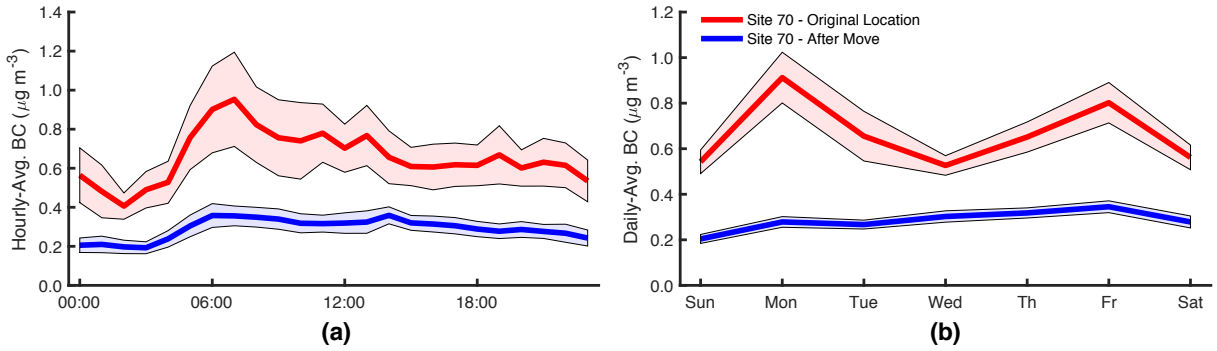

Figure D22. Average BC concentration trends at industrial site 70 before and after the sensor was moved ~20 m further from the nearby roadway: (a) Hourly-average BC concentrations over the diurnal cycle, (b) Daily-average concentrations over the weekly cycle. Bold lines represent the mean of hourly- or daily-average BC concentrations measured at each sensor location, with shaded areas representing the corresponding 90% confidence intervals.

D2.3 Air Quality Monitoring Networks: Lessons Learned and Future Approaches

Figure D23 presents diurnal and weekly BC concentration trends derived using data collected at site 62 (located in a residential area) over 2, 4, and 6 weeks of continuous sampling, and compares these trends to those derived using data collected over the entire 100-day campaign (~14 weeks). Figure D24 provides the same analysis for site 53 (located near 7th Street, a busy truck route). Both figures show that after 2 weeks of sampling, the BC concentration

trends (and associated 90% confidence intervals) were similar to those derived over the entire campaign. Although a more thorough sensitivity analysis should be conducted that comprises all network sites, these results illustrate that several weeks of continuous monitoring may be sufficient to accurately characterize BC concentration trends at each sampling location. Sites 62 and 53 were chosen for this sensitivity analysis to show that BC concentrations were highly repeatable and consistent both in residential areas, where concentrations were typically low and stable, and near emissions from trucks along designated routes, where concentrations were generally higher and more variable. Otherwise, the choice of sites was arbitrary, with similar trends generated at all other network sites investigated for this analysis.

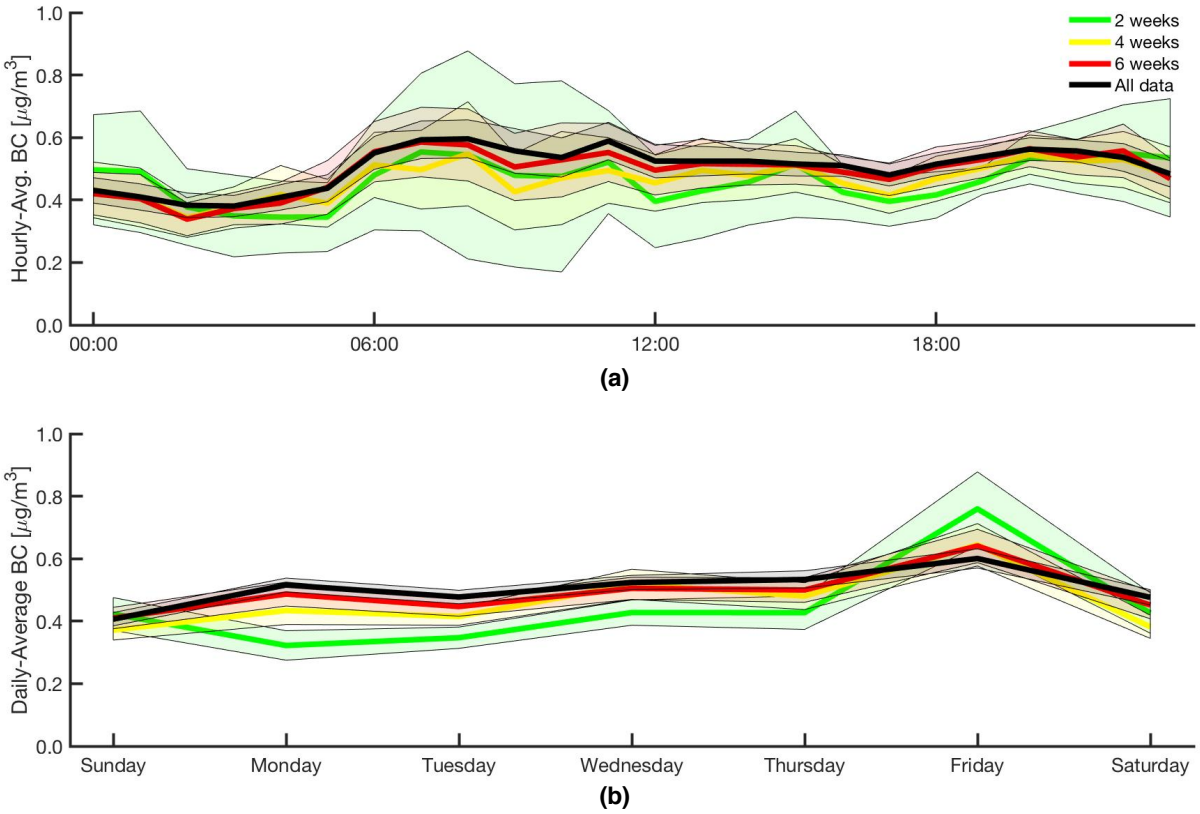

Figure D23. BC concentration trends at site 62 (located in a residential area): (a) Hourly-average BC concentrations over the diurnal cycle, (b) Daily-average concentrations over the weekly cycle. Colored lines represent trends derived using data collected over 2, 4, and 6 weeks, while the black line represents the trends derived using all available measurements (collected over ~14 weeks of sampling). Shaded areas represent the corresponding 90% confidence intervals.

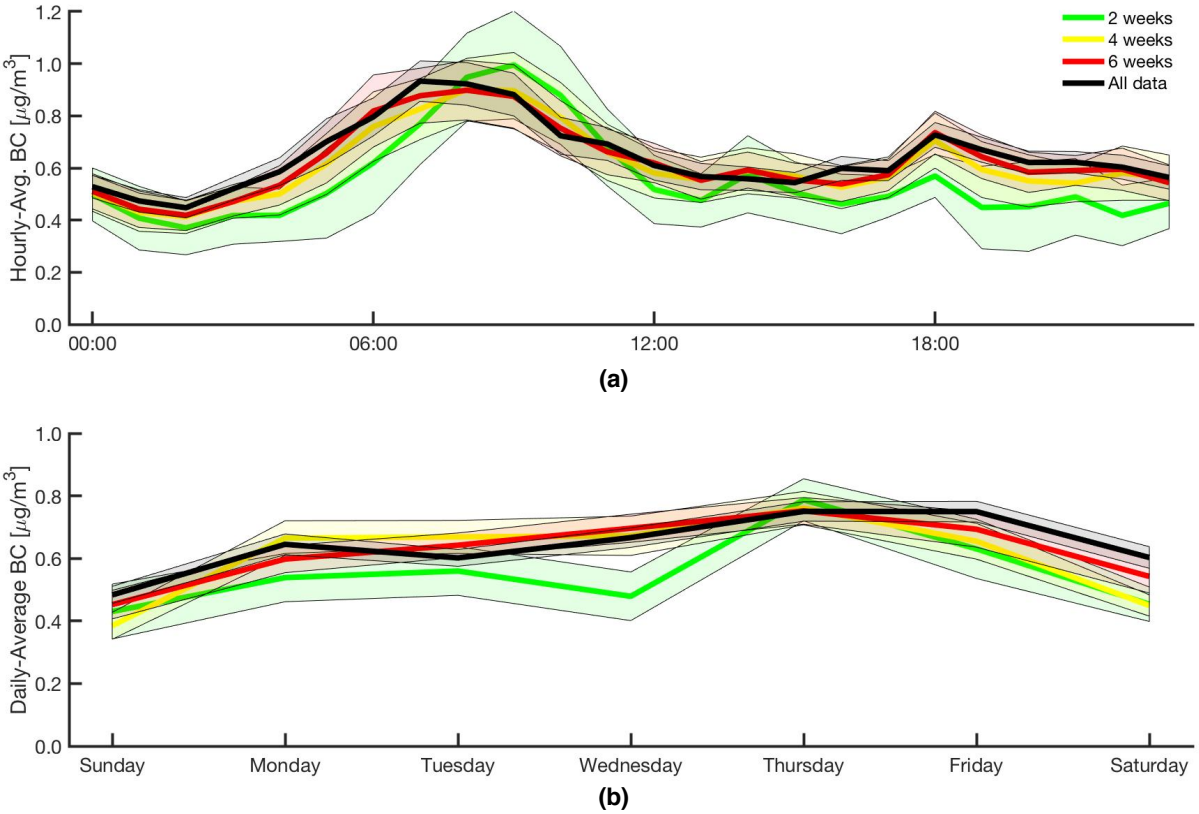

Figure D24. BC concentration trends at site 53 (located near a designated truck route): (a) Hourly-average BC concentrations over the diurnal cycle, (b) Daily-average concentrations over the weekly cycle. Colored lines represent trends derived using data collected over 2, 4, and 6 weeks, while the black line represents the trends derived using all available measurements (collected over ~14 weeks of sampling). Shaded areas represent the corresponding 90% confidence intervals.